DNS and Lie Group Analysis of Zero Pressure Gradient Turbulent Boundary Layer Flow

Für den Fachbereich Maschinenbau
an der Technischen Universität Darmstadt

zur
Erlangung des Grades eines Doktor-Ingenieurs (Dr.-Ing.)
genehmigte

D i s s e r t a t i o n

vorgelegt von

MSc. George Khujadze
aus Tbilisi, Georgien

Berichterstatter:	Prof. Dr.-Ing. M. Oberlack
Mitberichterstatter:	Prof. Dr.-Ing. R. Friedrich
Tag der Einreichung:	06.12.2005
Tag der mündlichen Prüfung:	24.01.2006

D17
Darmstadt, 2005

To my daughter, Mariam

Kurzzusammenfassung

Die Methode der Lie-Symmetrie-Gruppen und ihre Anwendung auf Turbulenz entwickelt von Oberlack (siehe z.B. Oberlack (2001) und die dort referenzierten Quellen),wird verwendet um neue Skalengesetze für eine Vielzahl von Parametern einer turbulenten Grenzschichtströmung ohne Druckgradienten herzuleiten. Die verwendete Methode baut auf den Vorarbeiten von Oberlack für die mittlere Geschwindigkeit einer stationären parallelen turbulenten Scherströmung auf und erweitert sie maßgeblich. Die Symmetrien der Zwei-Punkt-Korrelations(ZPK) Gleichungen ermöglichen die Herleitung einer Vielzahl von invarianten Lösungen (Skalengesetze) für turbulente Strömungen. Eine davon ist das exponentielle Geschwindigkeitsprofil, welches im Außnbereich (wake region) der Grenzschicht gefunden wurde. Im weiteren konnte eine dritte Symmetriegruppe mithilfe der ZPK-Gleichungen für eine turbulente Grenzschicht berechnet werden. Diese steht im Gegensatz zu den Navier-Stokes- und Eulergleichungen, die nur ein bzw. zwei Skalengruppen besitzen. Direkte Numerische Simulationen (DNS) einer ebenen turbulenten Grenzschicht ohne Druckgradienten wurden für drei Reynoldszahlen $Re_\theta = 750, 2240, 2500$ durchgeführt. Dazu wurden die Navier-Stokes-Gleichungen numerisch mittels einer Spektralmethode für 32, 140, bzw. 270 Millionen Gitterpunkte gelöst. Das Hauptziel der Simulation war die Validierung der vorgenannten exponentiellen Gesetze, der Reynoldsspannungen und der ZPK-Funktionen. Die numerische Simulation weist eine gute Übereinstimmung mit den theoretischen Ergebnissen auf. In der vorliegenden Arbeit werden die Ergebnisse aller Simulationen präsentiert. Alle klassischen statistischen Parameter wurden während der Simulation aufgenommen. Der Zeitraum der Statistik war in allen Fällen hinreichend, um eine gute Statistik zu erhalten. Es wurden außerdem Geschwindigkeits- und Wirbelfelder zu einem festen Zeitpunkt untersucht. Eindimensionale turbulente Signale der Geschwindigkeitsfluktuationen in Hauptströmungsrichtung wurden an verschiedenen Positionen (viscous sublayer, buffer layer, log-region und exponentieller Bereich) mittels Wavelets untersucht. Es wurden sowohl kontinuierliche als auch diskrete Wavelettransformationen angesetzt. Für die kontinuierliche Transformation wurden Coiflets Wavelets und für die diskrete Daubechies Wavelets verwendet.

Abstract

The Lie group or symmetry approach applied to turbulence as developed by Oberlack (see e.g. Oberlack (2001) and references therein) is used to derive *new scaling laws* for various quantities of a zero pressure gradient turbulent boundary layer flow. The approach unifies and extends the work done by Oberlack for the mean velocity of stationary parallel turbulent shear flows. From the two-point correlation (TPC) equations the knowledge of the symmetries allows us to derive a variety of invariant solutions (scaling laws) for turbulent flows, one of which is the new exponential mean velocity profile that is found in the mid-wake region of flat-plate boundary layers. Further, a third scaling group was found in the TPC equations for the one-dimensional turbulent boundary layer. This is in contrast to the Navier-Stokes and Euler equations which has one and two scaling groups respectively.

A direct numerical simulation (DNS) of a flat plate turbulent boundary layer with zero pressure gradient (ZPG) was performed at three different Reynolds numbers $Re_\theta = 750, 2240, 2500$ at different resolutions. The Navier-Stokes equations were numerically solved using a spectral method with $32, 140, 270$ million grid points. The main aim of the simulations were to validate the new exponential laws for mean velocity profile, Reynolds stresses and TPC functions. The numerical simulations show good agreement with the theoretical results. DNS results for each simulations are presented. All classical statistical quantities were accumulated during the simulations. Statistics accumulation time in all cases was large enough to get smooth statistics. Instantaneous velocity and vorticity fields were analysed.

Wavelet analysis was done for one-dimensional turbulent signals of the streamwise velocity fluctuation in streamwise direction for different (viscous sublayer, buffer layer, log-region and exponential region) positions in wall-normal directions. Both, the continuous and the discrete wavelet transformations were done using Daubechies (for discrete) and Coiflets wavelets (for continuous).

Acknowledgements

First of all I would like to thank my supervisor Prof. Dr.-Ing. M. Oberlack for accepting me as his PhD student and for his valuable and interesting discussions during my work in his group. It is his great merit to bring the symmetry methods into my work. His scientific support and everyday encouragement helped me to finish this work.

I am thankful to Prof. Johansson and Prof. Henningson from the department of Mechanics (KTH) for their hospitality during my visit at KTH. I would like to thank Martin Skote, Mathias Shevalier and Luca Brandt from the Department of Mechanics (KTH) for their help in the beginning of my work on the code.

Andreas Schönfeld and Norbert Conrad from HHLR, TU Darmstadt helped me to run the code on the IBM supercomputer. I express my gratitude to both for their continuing help during my work on the project.

I would like to express my gratitude to Dr. Mathias Brehm and Dr. Richard Patra from the Leibniz-Rechenzentrum of the Bavarian Academy of Sciences and Humanities for their help.

Finally, I would like to address my sincere gratitude to my family, to my wife Tamara and daughter Mariam, for their patience and love.

Darmstadt, Germany — George Khujadze
06.12.2005

Contents

Nomenclature

$-\rho\overline{u_i u_j}$	Reynolds stress tensor
$\delta(x_1)$	boundary-layer thickness
$\delta^*(x_1)$	boundary layer displacement thickness
Δx^+	resolution in streamwise direction in plus units
Δy^+	resolution in wall-normal direction in plus units
Δz^+	resolution in spanwise direction in plus units
Δ	Rotta-Clauser length scale
η	Kolmogorov length scale
λ	Taylor microscale
$\theta(x_1)$	boundary layer momentum thickness
ε	viscous dissipation of the turbulent kinetic energy
$^+$	superscript denoting plus, or inner scaling
c_f	friction coefficient
H	shape factor of boundary layer
$k(\boldsymbol{x}, t)$	turbulent kinetic energy
l	integral length scale
l_x, l_y, l_z	size of structures in streamwise, wall-normal and spanwise directions respectively
N	number of grid points
$R_{i(jk)}, R_{(ik)j}$	triple correlations
$R_{ij}(\boldsymbol{x}, \boldsymbol{r}, t)$	two-point correlation tensor
Re	Reynolds number
Re_δ	Reynolds number based on boundary layer thickness
Re_θ	Reynolds number based on boundary layer momentum thickness

Re_L	Reynolds number based on L, size of the physical problem domain
Re_l	'turbulent' Reynolds number
$Re_{\delta^\star}$	Reynolds number based on boundary layer displacement thickness
Re_λ	Reynolds number based on Taylor microscale
S_{ij}	Strain rate tensor
t_c	'convective' time scale
t_d	'diffusive' time scale
u_∞	free stream velocity
u_τ	mean 'friction velocity
x_2^+	wall-normal coordinate in plus units
$\bar{u}_{rms}$	*root-mean-square* of a fluctuating velocity
$\boldsymbol{\xi}(\boldsymbol{x},\boldsymbol{y})$, $\boldsymbol{\eta}(\boldsymbol{x},\boldsymbol{y})$	infinitesimals of Lie transformations
$\boldsymbol{r}(r_1, r_2, r_3)$	vector in correlation space
$\boldsymbol{x}(x_1, x_2, x_3)$	vector in physical space
$\mathcal{D}$	turbulent kinetic energy spatial redistribution
$\mathcal{P}$	production of turbulent energy
$\overline{pu_j}$	pressure-velocity two-point correlations

When you follow two separate chains of thought, Watson, you will find some point of intersection which should approximate the truth.

Sherlock Holmes

1 Introduction

Turbulence is the invention of the Devil on the seventh day of creation.
P. Bradshaw

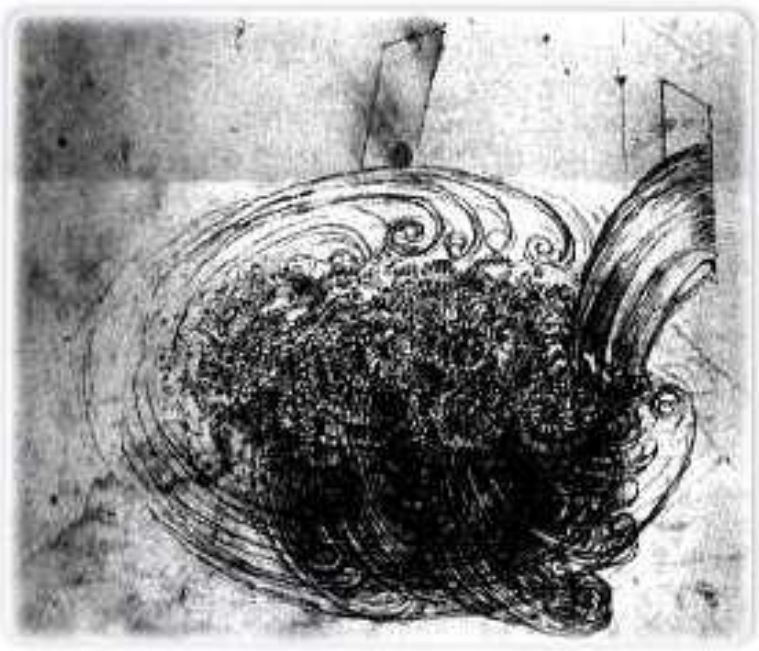

Figure 1.1: da Vinci sketch of turbulent flow.

Turbulence was recognized by da Vinci as a distinct phenomenon and termed by him as the 'turbolenca', and hence the origin of our modern word for this type of fluid flow (see Figure 1). It is often claimed that there is no good definition of turbulence, but one of the best known definitions is due to Richardson (Richardson 1922):
We realise that big whirls have little whirls that feed on their velocity, and little whirls have lesser whirls and so on to viscosity.

Is there a 'theory of turbulence' arises the question. **Unfortunately, after a century of concerted effort, involving engineers, physicist, and mathematicians, no such theory has emerged** answers Davidson (2004).

Most flows occurring in nature and in industrial applications are turbulent: the boundary layers in the earth's atmosphere (see Figure 1.2), in laboratory experiments (Figure 1.3) and numerical simulations (Figure 1.4); the flow over the wing of an aircraft and the flow of blood through our veins; The air flowing in and out of our lungs is turbulent. The drag on cars, aeroplanes, and bridges is controlled by turbulence. It dictates the weather through its influence on atmospheric and oceanic flows. Solar flares are manifestation of turbulence. Turbulence holds a unique place in the field of classical mechanics. The understanding of turbulent behavior in flowing fluids is one of the most intriguing problem in all of classical physics.

The turbulent flow phenomena can also occur in turbomachineries (for details see (Oertel 2004)). In Figure 1.5 a fan jet engine is shown to consider the flow processes. The fanjet engine is a flow machine in which almost all phenomena of fluid mechanics occur that have to be taken into account in the development of such machinery.

Turbulent flow appears random in time and in space and is not experimentally reproducible. In this thesis incompressible, Newtonian fluids, whose viscosity and density are taken constant, and which are not acted on by body forces, are considered. These approximations are commonly accepted and with them the velocity and pressure are described by the celebrated Navier-Stokes equations which are now almost universally believed to embody the physics of all Newtonian fluid flows within the continuum hypothesis, including turbulent flows

$$\frac{\partial U_i}{\partial t} + U_j \frac{\partial U_i}{\partial x_j} = -\frac{1}{\rho}\frac{\partial P}{\partial x_i} + \nu \frac{\partial^2 U_i}{\partial x_j \partial x_j}, \tag{1.1}$$

and the incompressibility condition

$$\frac{\partial U_i}{\partial x_i} = 0, \tag{1.2}$$

which should be supplemented by appropriate boundary and initial conditions. In these equations x_i are Cartesian spatial coordinates and ρ, ν are the constant density and kinematic viscosity of the fluid. U_i is the velocity vector which in general depends on all three spatial coordinates. **These equations are nonlinear because of the convection term and non-local due to the pressure and hence difficult to solve.** It is well known that there are only few exact solutions, and all of these have been obtained at the expense of introducing simplifying, often physically unrealistic assumptions.

Reynolds (1894) was the first to systematically investigate the transition from laminar to turbulent flow by injecting a dye streak into the flow through a pipe with

Figure 1.2: Kelvin-Helmholtz roll-ups as seen in a cloud formation. From the National Center for Atmospheric Research.

Figure 1.3: Side view of the large eddies in a turbulent boundary layer. Prof. M. Gad-el-Hak, University of Notre Dame

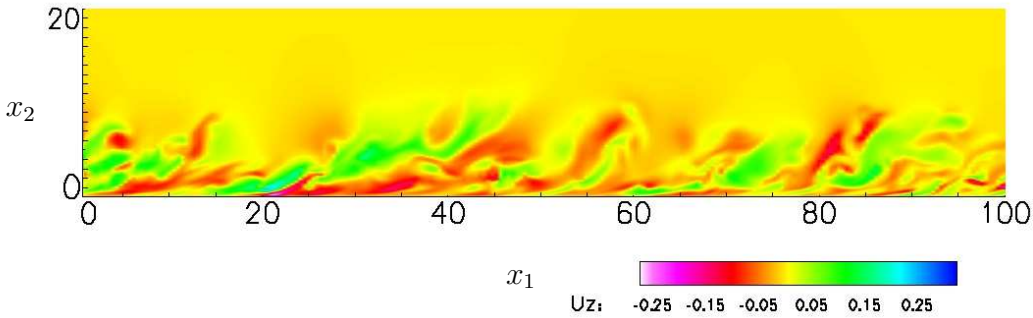

Figure 1.4: Boundary layer at $Re_\theta = 2240$ from the present DNS.

smooth walls. His observations led to the identification of a single dimensionless parameter, now called the Reynolds number:

$$Re = \frac{UL}{\nu}, \tag{1.3}$$

that completely describes the global flow behavior in this situation. U is the velocity scale (typical velocity), L is the typical length scale (for example, the

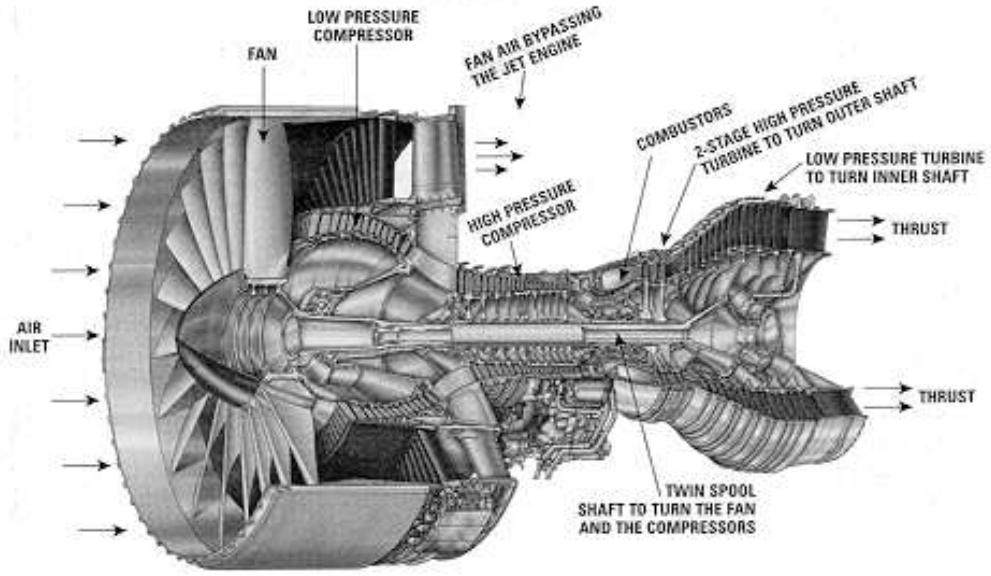

Figure 1.5: Fan jet engine.

pipe radius in the case of pipe flow). It is worthwhile to give here the rescaled Navier-Stokes equations:

$$\frac{\partial U_i}{\partial t} + U_j \frac{\partial U_i}{\partial x_j} = -\frac{1}{\rho}\frac{\partial P}{\partial x_i} + \frac{1}{Re}\frac{\partial^2 U_i}{\partial x_j \partial x_j}, \tag{1.4}$$

where the variables have been nondimensionalized.

Due to the great mathematical difficulties of these equations, no general approach had been found to the general mathematical treatment of viscous flows. Despite the fact that the governing equations have been known since 1845, there is still surprisingly little we can predict with relative certainty. There are a few exact solutions that are obtained by simplifying the system and introducing physically unrealistic assumptions.

In general the Navier-Stokes equations are satisfied by an infinite number of solutions - realizations of turbulent flows. Exact integration of the equations for a turbulent flow is not possible. The alternative way to solve them is DNS of the original equations. DNS of the original Navier-Stokes equations requires a numerical discretization which should resolve even the smallest scales in a flow. Because of the large demand on computer resources, DNS is at present time limited to relatively low Reynolds numbers and simple geometries.

Turbulence by its nature is an irregular, non-stationary, three-dimensional, non-

linear, non-local and a stochastic phenomenon. Because of the inability to describe turbulence analytically in real flows, physical intuition supported by similarity arguments and dimensional analysis have been used to characterize turbulence and its properties in various flows. Experiments, DNS and LES play a crucial role in verifying the findings. Such analysis allowed to establish some general conclusions about the turbulence structure and its behavior (characteristic turbulent time, length and velocity scales, etc.).

1.0.1 Turbulence time- and length scales

One of the main characteristics of turbulence is its wide range of length and time scales. This is the reason why the 'turbulence problem' is not solved yet. This feature of turbulent flow precludes the use of DNS in most realistic flow situations.

There are, in general, four main sets of scales in a turbulent flow (if heat transfer and combustion phenomena are not taken into account):

1. the large scale, based on the problem domain geometry;
2. the integral scale: $\mathcal{O}(1)$ fraction (~ 0.2) of the large scale;
3. the Taylor microscale (intermediate scale);
4. the Kolmogorov (or 'dissipation') scale which is the smallest of all the turbulence scales.

Increasing Re has little effect on the integral and large scales, because they are defined by the size and shape of the flow domain. On the other hand the beginning of the dissipation region is strongly influenced by the Reynolds number. Let us discuss all subregions (scales) in detail.

In the **large scale** region a 'convective' time scale is given by

$$t_c = \frac{L}{U}, \tag{1.5}$$

where L is the size of the physical problem domain, and U is the characteristic velocity (e.g. mean, or centerline velocity in the pipe flow, free-stream velocity in the case of boundary layer flow.)

The second time scale is the 'diffusive' time scale, based on the kinematic viscosity:

$$t_d = \frac{L^2}{\nu}. \tag{1.6}$$

The ratio of these time scales shows the rate at which flow properties are transferred by (molecular) diffusion and (macroscopic) convection:

$$\frac{t_d}{t_c} = Re_L. \tag{1.7}$$

Thus, if Re_L is large, the time for diffusion is long compared to the convection time, and diffusion effects are essentially negligible for large scales.

The **integral scales** do not cover a wide range. They are sometimes associated with a single wavenumber, which corresponds to the maximum in turbulent energy. The integral length scale can be obtained as follows:

$$l = \frac{1}{||u||_{L^2}^2} \int_{-\infty}^{\infty} u(\boldsymbol{x}, t) u(\boldsymbol{x} + \boldsymbol{r}, t) d\boldsymbol{r}, \tag{1.8}$$

where $u = U - \bar{u}$ ($\bar{u}$ is the mean) is the turbulent fluctuating velocity, $||u||_{L^2}^2$ is the inner product that induces a norm on the spatial domain Ω.

$L^2(\Omega)$ is the Hilbert space, which is a complete, normed, linear space with an inner product that induces the norm of the space:

$$||u||_{L^2}^2 = \int_{-\infty}^{\infty} u(\boldsymbol{x}) u(\boldsymbol{x}) d\boldsymbol{x}, \tag{1.9}$$

$Re_l = \dfrac{|u|l}{\nu}$ is often called the 'turbulent' Reynolds number and u is usually taken to be the square root of the turbulent kinetic energy, i.e. $|u| = \sqrt{k}$, with $k = \dfrac{1}{2}(u^2 + v^2 + w^2)$.

Length and time scales associated with the **Taylor microscale**:
The Taylor microscale is (see for example (Lesieur 1990)) defined as

$$\lambda = \frac{\overline{|u|^2}}{\overline{||\boldsymbol{S}||^2}}, \tag{1.10}$$

where $\boldsymbol{S}$ is the strain rate tensor

$$S_{ij} \equiv \frac{1}{2}\left(\frac{\partial u_i}{\partial x_j} + \frac{\partial u_j}{\partial x_i}\right),$$

which is connected to turbulence energy dissipation rate ε as follows:

$$\varepsilon = 2\nu\overline{||\boldsymbol{S}||^2}, \tag{1.11}$$

which in turn gives the Taylor microscale in the following expression:

$$\lambda = \left[\frac{\nu\overline{|u|^2}}{\varepsilon}\right]^{(1/2)} . \tag{1.12}$$

The corresponding Taylor microscale Reynolds number is calculated as

$$Re_\lambda = \frac{|u|\lambda}{\nu}. \tag{1.13}$$

The smallest scales of turbulence are the **Kolmogorov scales**. At these scales mainly dissipation is important, as it was assumed by Kolmogorov. Thus ν and the dissipation rate ε are enough to describe these scales:

$$\eta = \left(\frac{\nu^3}{\varepsilon}\right)^{1/4}, \tag{1.14}$$

Kolmogorov time scale:

$$\tau = \left(\frac{\nu}{\varepsilon}\right)^{1/2}, \tag{1.15}$$

Kolmogorov scale velocity:

$$v = (\nu\varepsilon)^{1/4}. \tag{1.16}$$

Kolmogorov Reynolds number:

$$Re_\eta = \frac{v\eta}{\nu} = 1. \tag{1.17}$$

Scale relations:

$$\frac{\eta}{l} \sim Re_l^{-3/4}; \frac{\eta}{\lambda} \sim Re_\lambda^{-1/2}; \tag{1.18}$$

$$Re_\lambda = \frac{\lambda}{l} Re_l; Re_\lambda \sim Re_l^{1/2}. \tag{1.19}$$

$$\eta \ll \lambda \ll l \tag{1.20}$$

2 Basic equations

Turbulence is the last unsolved problem of classical physics.
R. P. Feynman

2.1 Turbulence and the Navier-Stokes equations

The equations of motion for a Newtonian fluid (Navier-Stokes equations) in general have the form:

$$\rho\left[\frac{\partial U_i}{\partial t}+U_j\frac{\partial U_i}{\partial x_j}\right]+\frac{\partial P}{\partial x_i}=\frac{\partial}{\partial x_j}\left[\mu\left(\frac{\partial U_i}{\partial x_j}+\frac{\partial U_j}{\partial x_i}\right)\right]+\frac{\partial}{\partial x_j}\left[\lambda\left(\frac{\partial U_k}{\partial x_k}\right)\right], \quad (2.1)$$

where μ and λ are shear/dynamic viscosity and the second coefficient of viscosity, P is the static pressure and the equation of continuity is given by

$$\frac{d\rho}{dt}+\frac{\partial \rho U_j}{\partial x_j}=0. \quad (2.2)$$

in the case of incompressibility the Newtonian fluid equation 2.1 reduces to the equations (1.1) and (1.2).

The pressure P satisfies the Poisson equation:

$$\nabla^2 P=-\rho\frac{\partial U_i}{\partial x_j}\frac{\partial U_j}{\partial x_i} \quad (2.3)$$

Mathematically the solution of these equations with given initial and boundary conditions is unique. Unfortunately, this does not automatically guarantee that the solutions to those equations satisfy the given physics. In fact, it is not even guaranteed a priori that a satisfactory solution exists (for details of mathematical theory of Navier-Stokes equations see (Foias, Manley, Rosa & Temam 2001)). It is very important to know the nature of the solutions to the Navier-Stokes equations because the equations must be solved by numerical methods and the nature of the solutions directly influences which type of method will be effective and which not.

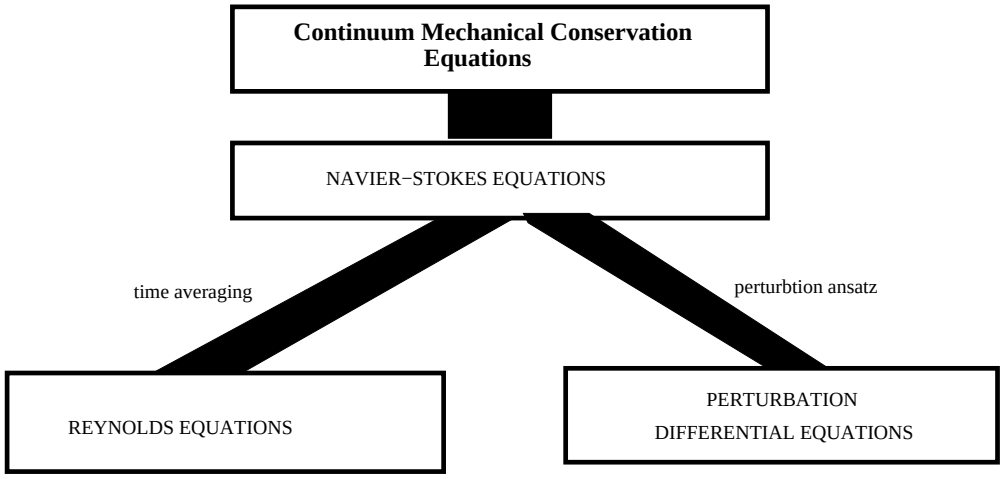

Figure 2.1: Hierarchy of fluid-mechanical fundamental equations (from (Oertel 2004))

Results for the Navier-Stokes equations can be classified as pertaining to $2D$ and $3D$ flows, and as to whether they relate to weak or strong solutions. For the $2D$ case, existence and uniqueness of solutions, both weak and strong, have been proven for all physically reasonable problems. As for the $3D$ case, long-time existence can be demonstrated for weak solutions, but uniqueness has not been proven for this case (Foias et al. 2001).

Since it is widely accepted that turbulence is three-dimensional, the inability to prove the long-time existence of strong solutions, might cast some doubt on the acceptance of these equations as the correct representation of turbulent flows. In particular without long-time existence it is difficult to state that stationary solutions even exist. However, it is generally accepted that the lack of proof of the long-time existence more reflects the inadequacy of current mathematics. The general success of DNS of turbulent flows is the support of the fact that the Navier-Stokes equations correctly describe turbulent fluid flows.

The Navier-Stokes equations are obtained for Newtonian media, and time averaging leads to the Reynolds equations (discussed below) for turbulent flows (see Figure 2.1).

2.2 Statistical description of turbulence

The characteristic feature of the turbulent motion is the presence of disordered fluctuations of the fluid dynamic variables of the flow. Hence, spatial and temporal dependence of the instantaneous values of the fluid dynamic fields have a very complex nature. Due to this disorder of the different flow quantities, in the study of turbulence it is necessary to use some method of averaging which will enable us to pass to smoother, more regular *mean values* of the flow variables. In choosing some particular *averaging rule*, one must first formulate the general requirements for these rules. Reynolds (1894) formulated the following five relationships that must be satisfied:

$$\overline{f+g} = \bar{f} + \bar{g}, \tag{2.4}$$

$$\overline{af} = a\bar{f}, \qquad \text{if} \qquad a = const. \tag{2.5}$$

$$\overline{a} = a, \qquad \text{if} \qquad a = const, \tag{2.6}$$

$$\overline{\frac{\partial f}{\partial s}} = \frac{\partial \bar{f}}{\partial s}, \qquad \text{where } s \text{ is} \qquad x_1, x_2, x_3, t, \tag{2.7}$$

$$\overline{\bar{f}g} = \bar{f}\bar{g}, \tag{2.8}$$

At present these conditions are known as the **Reynolds conditions**.

2.2.1 One-point statistics: Reynolds equations

Statistical averaging methods for turbulent flows introduced by (Reynolds 1894) over a century ago may be used to study mean values involving any number of points in space and time; however simplest are single-point, single-time averages (mean velocities, root-mean-squared fluctuations) which simplify the flow description. However one-point statistics do not encompass the full statistics of the flow. Even so, one-point averages include many important physical measures, for example, mean-flow velocity and turbulent kinetic energy per unit mass. The Reynolds decomposition of the velocity $\boldsymbol{U}(\boldsymbol{x}, t)$ into mean and the fluctuation parts (see Figure 2.2) has the following form

$$\boldsymbol{U}(\boldsymbol{x}, t) \equiv \bar{\boldsymbol{u}}(\boldsymbol{x}, t) + \boldsymbol{u}(\boldsymbol{x}, t). \tag{2.9}$$

The mean-flow equation has the form

$$\frac{\partial \bar{u}_i}{\partial t} + \bar{u}_j \frac{\partial \bar{u}_i}{\partial x_j} = -\frac{1}{\rho}\frac{\partial \bar{p}}{\partial x_i} + \nu \frac{\partial^2 \bar{u}_i}{\partial x_j \partial x_j} - \frac{\partial \overline{u_i u_j}}{\partial x_j} \tag{2.10}$$

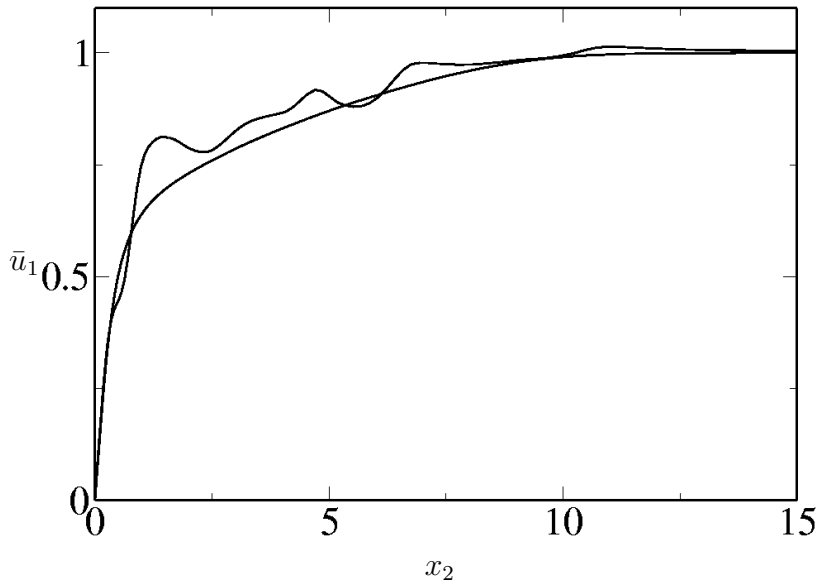

Figure 2.2: Instantaneous velocity profile of turbulent boundary layer flow and its mean.

$$\frac{\partial \bar{u}_i}{\partial x_i} = 0, \tag{2.11}$$

where $\bar{u}_i$ and $\bar{p}$ are one-point averages of velocity and pressure. These equations contain only smoothly varying averaged quantities, and their use does not give rise to any difficulties connected with the complexity and irregularity of the fluid dynamic variables of turbulent flows. However, another difficultyes arise in the equations. It is connected with the presence in the Reynolds equations of the new unknowns $-\rho\overline{u_i u_j}$, by which the fluctuating part of the flow interacts with the mean flow. The appearance of these new unknowns is due to the nonlinearity of the Navier-Stokes equations. These additional stresses are called *Reynolds stresses* in turbulence theory. In the turbulent flows, in addition to the exchange of momentum between fluid particles due to the forces of molecular viscosity, the transport of momentum from one volume to the other occurs, induced by the mixing caused by the velocity fluctuations (see, for example (Monin & Yaglom 1971)).

The second order tensor $\overline{u_i u_j}$ is symmetric, i.e., $\overline{u_i u_j} = \overline{u_j u_i}$. The diagonal components $\overline{u_1^2}$, $\overline{u_2^2}$ and $\overline{u_3^2}$ are called **normal stresses**, while the off-diagonal components (for example $\overline{u_1 u_2}$) are the **shear stresses**. The Reynolds stress tensor is one of the most important basic concepts in the theory of turbulence.

The turbulent kinetic energy $k(\boldsymbol{x}, t)$ is defined as

$$k \equiv \frac{1}{2}\overline{u_i u_i} \tag{2.12}$$

The Reynolds equations plus the mean continuity equation or the Poisson equation for the mean pressure $\bar{p}$ are the governing equations for a general statistically three-dimensional flow. However, these four equations contain more than four unknowns in addition to $\bar{u}_i$ and $\bar{p}$, there are also the Reynolds stresses. This is the manifestation of the **closure problem**. The statistical equations are unclosed.

The mean pressure satisfies a Poisson equation:

$$-\frac{1}{\rho}\nabla^2\bar{p} = \frac{\partial \bar{u}_i}{\partial x_j}\frac{\partial \bar{u}_j}{\partial x_i} + \frac{\partial^2 \overline{u_i u_j}}{\partial x_j \partial x_i} \tag{2.13}$$

A useful measure of turbulence is the *root-mean-square* of a fluctuating velocity, defined as

$$\bar{u}_{rms} = \sqrt{\overline{u_i^2}}. \tag{2.14}$$

2.2.2 Reynolds stress budget and turbulent kinetic energy

The equation for the time evolution of the Reynolds stress tensor has the form

$$\frac{\partial \overline{u_i u_j}}{\partial t} + \bar{u}_k \frac{\partial \overline{u_i u_j}}{\partial x_k} = P_{ij} + \Pi_{ij} + D_{ij} - \varepsilon_{ij} + T_{ij}^{(u)} \tag{2.15}$$

where

$$P_{ij} \equiv -\overline{u_i u_k}\frac{\partial \bar{u}_j}{\partial x_k} - \overline{u_j u_k}\frac{\partial \bar{u}_i}{\partial x_k} \qquad \text{Production} \tag{2.16}$$

$$\Pi_{ij} \equiv -\frac{1}{\rho}\left(\overline{u_i \frac{\partial p}{\partial x_j} + u_j \frac{\partial p}{\partial x_i}}\right) \qquad \text{Velocity-pressure gradient} \tag{2.17}$$

$$\varepsilon_{ij} \equiv 2\nu \overline{\frac{\partial u_i}{\partial x_k}\frac{\partial u_j}{\partial x_k}} \qquad \text{Turbulent dissipation} \tag{2.18}$$

$$T_{ij}^{(u)} \equiv -\frac{\partial \overline{u_i u_j u_k}}{\partial x_k}, \qquad \text{Turbulent transport} \tag{2.19}$$

$$D_{ij} \equiv \nu \nabla^2 \overline{u_i u_j} \qquad \text{Viscous diffusion} \tag{2.20}$$

It is easy to show that $\Pi_{ij} = \Phi_{ij} + T_{ij}^{(p)}$, where

$$\Phi_{ij} \equiv \overline{\frac{p}{\rho}\left(\frac{\partial u_i}{\partial x_j} + \frac{\partial u_j}{\partial x_i}\right)}, \qquad \text{Pressure-rate-of-strain tensor} \qquad (2.21)$$

$$T_{ij}^{(p)} \equiv -\frac{1}{\rho}\frac{\partial}{\partial x_k}(\overline{u_i p}\delta_{jk} + \overline{u_j p}\delta_{ik}). \qquad \text{Pressure transport tensor} \qquad (2.22)$$

and the equation 2.15 can be rewritten in the form:

$$\frac{\partial \overline{u_i u_j}}{\partial t} + \bar{u}_k \frac{\partial \overline{u_i u_j}}{\partial x_k} = P_{ij} + \Phi_{ij} + T_{ij}^{(p)} + D_{ij} - \varepsilon_{ij} + T_{ij}^{(u)}. \qquad (2.23)$$

- P_{ij} is the production due to the mean field gradients;
- $T_{ij}^{(u)}$ is the divergence of the triple correlation tensor, acting as a spatial redistribution term;
- $T_{ij}^{(p)}$ is the divergence of pressure-velocity correlations. It represents transport driven by pressure fluctuations;
- ε is the dissipation rate tensor (destruction of turbulent kinetic energy);
- D_{ij} is the diffusion tensor (molecular diffusion term);
- Φ_{ij} is the traceless pressure-strain rate tensor. It represents inter-component transfer between Reynolds stress terms.

From the equation (2.23) we can get the equation for the turbulent kinetic energy:

$$\frac{\partial k}{\partial t} + \bar{u}_k \frac{\partial k}{\partial x_k} = \mathcal{P} - \varepsilon + \mathcal{D}, \qquad (2.24)$$

$\mathcal{P} \equiv 1/2 P_{ii}$ represents production of turbulent energy, the transfer of energy from the mean flow to the turbulent fluctuation;
$\mathcal{D} \equiv (T_{ii}^{(u)} + T_{ii}^{(p)} + D_{ii})/2$ is the term that acts as a turbulent kinetic energy spatial redistribution;
$\varepsilon \equiv 1/2 \varepsilon_{ii}$ is the viscous dissipation.

2.2.3 Higher order statistics: two-point correlations

Because of the complex nature of turbulent flows it is not sufficient to study only one-point statistics. Much insight into the problem can be gained by investigating simultaneous measurements of more than one velocity component in different

points. The two-point correlation (TPC) is generally defined as the covariance between velocity components measured at two different points:

$$R_{ij}(\boldsymbol{x},\boldsymbol{r},t)=\overline{u_i(\boldsymbol{x},t)u_j(\boldsymbol{x}+\boldsymbol{r},t)} \tag{2.25}$$

In its most general form the TPC equation reads in mixed physical-correlation $(\boldsymbol{x},\boldsymbol{r})$-space:

$$\begin{aligned}\frac{\bar{D}R_{ij}}{\bar{D}t}+R_{kj}\frac{\partial\bar{u}_i(\boldsymbol{x},t)}{\partial x_k}+R_{ik}\frac{\partial\bar{u}_j(\boldsymbol{x},t)}{\partial x_k}\bigg|_{\boldsymbol{x}+\boldsymbol{r}}+[\bar{u}_k(\boldsymbol{x}+\boldsymbol{r},t)-\bar{u}_k(\boldsymbol{x},t)]\frac{\partial R_{ij}}{\partial r_k}\\ +\frac{\partial\overline{pu}_j}{\partial x_i}-\frac{\partial\overline{pu}_j}{\partial r_i}+\frac{\partial\overline{u_ip}}{\partial r_j}-\nu\left[\frac{\partial^2R_{ij}}{\partial x_k\partial x_k}-2\frac{\partial^2R_{ij}}{\partial x_k\partial r_k}+\frac{\partial^2R_{ij}}{\partial r_k\partial r_k}\right]\\ +\frac{\partial R_{(ik)j}}{\partial x_k}-\frac{\partial}{\partial r_k}[R_{(ik)j}-R_{i(jk)}]=0,\end{aligned} \tag{2.26}$$

where correlation vectors and tensors are defined as

$$\begin{aligned}\overline{pu_j}&=\overline{p(\boldsymbol{x},t)u_j(\boldsymbol{x}+\boldsymbol{r},t)},\\ \overline{u_ip}&=\overline{u_i(\boldsymbol{x},t)p_j(\boldsymbol{x}+\boldsymbol{r},t)},\\ R_{(ik)j}&=\overline{u_i(\boldsymbol{x},t)u_k(\boldsymbol{x},t)u_j(\boldsymbol{x}+\boldsymbol{r},t)},\\ R_{i(jk)}&=\overline{u_i(\boldsymbol{x},t)u_j(\boldsymbol{x}+\boldsymbol{r},t)u_k(\boldsymbol{x}+\boldsymbol{r},t)}.\end{aligned}$$

and $\frac{\bar{D}}{Dt}=\left(\frac{\partial}{\partial t}+\bar{u}_k\frac{\partial}{\partial x_k}\right)$ is the mean substantial derivative. $\boldsymbol{x}$ and $\boldsymbol{r}=\boldsymbol{x}'-\boldsymbol{x}$ are coordinates in the physical and the correlation spaces respectively. All of the vectors and tensors in equation (2.26) obey additional constraints derived from continuity (see (Oberlack 2002)).

$$\frac{\partial R_{ij}}{\partial x_i}-\frac{\partial R_{ij}}{\partial r_i}=0;\quad\frac{\partial R_{ij}}{\partial r_j}=0;\quad\frac{\partial\overline{pu_i}}{\partial r_i}=0;\quad\frac{\partial\overline{u_jp}}{\partial x_j}-\frac{\partial\overline{u_jp}}{\partial r_j}=0. \tag{2.27}$$

In some cases it is useful to employ equation (2.26) written in the physical $(\boldsymbol{x}',\boldsymbol{x}'')$-space:

$$\begin{aligned}\frac{\partial R_{ij}(\boldsymbol{x}',\boldsymbol{x}'')}{\partial t}+\bar{u}_k(\boldsymbol{x}')\frac{\partial R_{ij}(\boldsymbol{x}',\boldsymbol{x}'')}{\partial x'_k}+\bar{u}_k(\boldsymbol{x}'')\frac{\partial R_{ij}(\boldsymbol{x}',\boldsymbol{x}'')}{\partial x''_k}+\\ R_{ik}(\boldsymbol{x}',\boldsymbol{x}'')\frac{\partial\bar{u}_j(\boldsymbol{x}'')}{\partial x''_k}+R_{kj}(\boldsymbol{x}',\boldsymbol{x}'')\frac{\partial\bar{u}_i(\boldsymbol{x}')}{\partial x'_k}+\frac{\partial\overline{u_ip}(\boldsymbol{x}',\boldsymbol{x}'')}{\partial x''_j}+\frac{\partial\overline{pu_j}(\boldsymbol{x}',\boldsymbol{x}'')}{\partial x'_i}+\\ \frac{\partial R_{i(jk)}(\boldsymbol{x}',\boldsymbol{x}'')}{\partial x''_i}+\frac{\partial R_{(ik)j}(\boldsymbol{x}',\boldsymbol{x}'')}{\partial x'_i}=0,\end{aligned} \tag{2.28}$$

$$\frac{\partial \overline{u_i p}(\boldsymbol{x}', \boldsymbol{x}'')}{\partial x_i'} = 0; \quad \frac{\partial \overline{p u_i}(\boldsymbol{x}', \boldsymbol{x}'')}{\partial x_i''} = 0; \quad \frac{\partial R_{ij}(\boldsymbol{x}', \boldsymbol{x}'')}{\partial x_i'} = 0; \quad \frac{\partial R_{ij}(\boldsymbol{x}', \boldsymbol{x}'')}{\partial x_i''} = 0, \tag{2.29}$$

where $\boldsymbol{x}' = \boldsymbol{x}$ and $\boldsymbol{x}'' = \boldsymbol{x} + \boldsymbol{r}$.

3 ZPG turbulent boundary layer flow

The simplest case of a turbulent boundary layer occurs on a flat plate at zero pressure gradient. The velocity outside the layer (free stream velocity) is constant and the external pressure gradient is zero. The results of such a flow can be applied with some approximation to the estimation of the skin friction drag of ships, airplane bodies, etc.

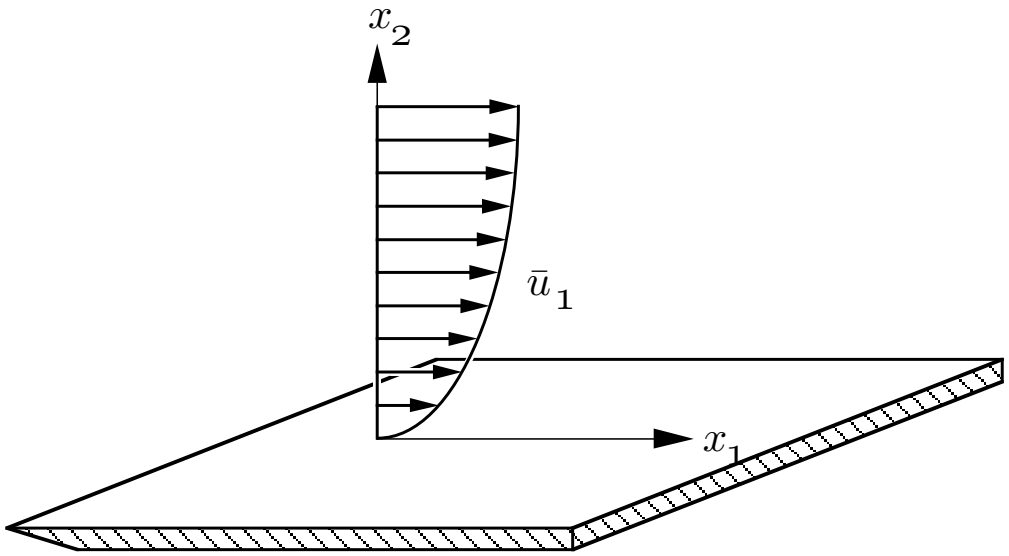

Figure 3.1: Sketch of the coordinate system and the mean velocity field of boundary layer flow.

3.1 Classical theory of turbulent boundary layer flows

In his lecture 'On fluid motion with very small friction' at the Heidelberg mathematical congress Prandtl (1904), using theoretical considerations together with

some simple experiments, showed that the flow past a body can be divided into two regions: a very thin layer close to the body (boundary layer) where the viscosity is important and the remaining region outside this layer where the viscosity can be neglected. Very soon it was discovered that the flow within the boundary layer can either be turbulent or laminar, which are generally known as the boundary layer flow. Since that time a huge number of experimental and theoretical investigations about boundary layer flow have been published. The theory of the **Prandtl boundary layer** has proved to be exceptionally useful and has given stimulation to research into fluid mechanics since the beginning of this century.

One of the most important applications of boundary-layer theory is the calculation of the friction drag of bodies in a flow, e.g. the drag of a flat plate at ZPG, the friction drag of a ship, an airfoil, the body of an airplane, or a turbine blade. The simplest boundary layer is the one which is formed by uniform-velocity non-turbulent stream flows over a smooth flat plate (see Figure 3.1). The boundary layer develops continuously in the flow direction, so that statistics depend on x_1 and x_2 coordinates. The free stream pressure $p_0(x_1)$ satisfies Bernoulli's equation:

$$-\frac{dp_0}{dx_1} = \rho\bar{u}_1\frac{d\bar{u}_1}{dx_1}, \tag{3.1}$$

Accelerating flow $\dfrac{d\bar{u}_1}{dx_1} > 0$ corresponds to a negative and decelerating flow to a positive, adverse pressure gradient. Our attention is focused only on ZPG turbulent boundary layer flow:

$$\frac{dp_0}{dx_1} = 0. \tag{3.2}$$

Because the flow develops slowly in streamwise direction, the boundary-layer approximation $Re \to \infty, \bar{u}_2 \ll \bar{u}_{1\infty}, \partial/\partial x_1 \ll \partial/\partial x_2$ can be applied to equations (2.11) and (2.10). As a result one gets the following equations for steady two-dimensional boundary layer flow:

$$\frac{\partial\bar{u}_1}{\partial x_1} + \frac{\partial\bar{u}_2}{\partial x_2} = 0, \tag{3.3}$$

$$\bar{u}_1\frac{\partial\bar{u}_1}{\partial x_1} + \bar{u}_2\frac{\partial\bar{u}_1}{\partial x_2} = -\frac{1}{\rho}\frac{dP}{dx_1} + \nu\frac{\partial^2\bar{u}_1}{\partial x_2^2} - \frac{\partial\overline{u_1u_2}}{\partial x_2} \tag{3.4}$$

where $\bar{u}_1$ is the mean streamwise velocity, $\bar{u}_2$ is the mean wall-normal velocity.

3.1.1 The inner part of boundary layer flow

The analysis of the near wall boundary layer flow is very important. Here the fluid motion is restricted by the presence of the wall so that viscous dissipation increases

and consequently the velocity fluctuations decrease when the wall is approached. As a result, the fraction of shear stress achieved by direct action of the viscosity grows more and more while the Reynolds shearing stress $-\overline{u_1 u_2}$ decreases. All derivatives of mean values with respect x_1 are negligible for sufficiently small values of x_2. With this suppositions it follows from the continuity equation that $\bar{u}_2 = 0$ and the equation (3.4) for this region can be rewritten in the following way:

$$0 = \nu \frac{\partial^2 \bar{u}_1}{\partial x_2^2} - \frac{\partial \overline{u_1 u_2}}{\partial x_2} \equiv \frac{1}{\rho} \frac{\partial \tau}{\partial x_2}, \tag{3.5}$$

where τ is the total shear stress. The rhs of the equation is interpreted as the gradient of the shear stress τ. One of the most important quantities characterizing a turbulent boundary layer is the mean 'friction velocity' u_τ is defined as

$$u_\tau \equiv \sqrt{\nu \left. \frac{\partial \bar{u}_1}{\partial x_2} \right|_{x_2=0}}. \tag{3.6}$$

If we use the viscous scaling (or plus units) given by

$$x_2^+ \equiv \frac{x_2 u_\tau}{\nu}, \qquad \bar{u}_1^+ \equiv \frac{\bar{u}_1}{u_\tau} \tag{3.7}$$

then equation (3.5) can be written in the following form:

$$\frac{d\bar{u}_1^+}{dx_2^+} - \overline{u_1 u_2}^+ = 1. \tag{3.8}$$

The dependences on x_1 are included in u_τ. Equation (3.8) expresses constancy of total shear stress, consisting of a sum of the viscous shear stress, $\dfrac{d\bar{u}_1^+}{dx_2^+}$, and Reynolds shear stress, $-\overline{u_1 u_2}^+$. At the wall, the Reynolds shear stress is zero and $\tau_{wall} = \rho u_\tau^2$, while as one leaves the viscous sublayer and enters the inertial layer, viscosity becomes unimportant and we have $-\overline{u_1 u_2} = u_\tau$ in the inertial layer.

The **boundary-layer thickness** $\delta(x_1)$ is defined as the value of x_2 at which $\bar{u}_1(x_1, x_2)$ equals 99% of the free-stream velocity $U_0(x_1)$. There are also integral measures defined

$$\text{displacement thickness :} \qquad \delta^*(x_1) \equiv \int_0^\infty \left(1 - \frac{\bar{u}_1}{U_0}\right) dx_2, \tag{3.9}$$

$$\text{momentum thickness :} \qquad \theta(x_1) \equiv \int_0^\infty \frac{\bar{u}_1}{U_0} \left(1 - \frac{\bar{u}_1}{U_0}\right) dx_2. \tag{3.10}$$

Based on these thicknesses various Reynolds numbers are defined

$$Re_\delta = \frac{U_0\delta}{\nu}, \quad Re_{\delta^*} = \frac{U_0\delta^*}{\nu}, \quad Re_\theta = \frac{U_0\theta}{\nu} \tag{3.11}$$

ZPG turbulent boundary layer flow is formed when a uniform-velocity stream flows over a smooth flat plate in a semi-infinite domain. In spite of the simple geometry of the flow, its statistical behavior is not fully understood. There is no complete theoretical approach from first principles describing the entire flow. The most comprehensive and useful description of a turbulent boundary layer flow is the classical one in terms of an inner and outer region. This fact was first recognized by Kármán (1930) and Prandtl (1932) and many experiments were conducted to validate the theoretical results. An early experiment at high Reynolds number was done by Nikuradse (1932). The region near the wall, where the viscous forces are dominant, is called the viscous sublayer. The scaling law for this region was first proposed by Prandtl (1932). Because of the fact that in fully developed turbulence sufficiently far from the wall the turbulent stresses are dominant, one can neglect the influence of the viscous forces. Hence, the velocity scaling should not depend on viscosity. The layer where these conditions are valid is called the logarithmic layer. The logarithmic law was first derived by Kármán (1930) using a semi-empirical model and dimensional arguments. Later Millikan (1939) derived the law of the wall differently using the so-called 'velocity defect law', which was also introduced by Kármán (1930). Millikan's arguments were founded on an overlap region between the outer and the inner region. From an extensive study of boundary layer data, Coles (1956) showed that the mean velocity profile over the whole boundary layer is well represented by the sum of two functions. The first is the law of the wall, which depends on the viscous length scale, the second function called the *law of the wake*, depends on the outer scale. The representation can be written in the form of a velocity defect law:

$$\frac{\bar{u}_\infty - \bar{u}_1}{u_\tau} = \frac{1}{\kappa}\left\{-ln\left(\frac{x_2}{\delta}\right) + \Pi\left[2 - w\left(\frac{x_2}{\delta}\right)\right]\right\}, \tag{3.12}$$

where Π is called the **wake strength parameter** and its value depends on the flow. The *wake function* $w(x_2/\delta)$ was tabulated by (Coles 1956) based on the experiment, but a more convenient approximation is

$$w\left(\frac{x_2}{\delta}\right) = 2\sin^2\left(\frac{\pi}{2}\frac{x_2}{\delta}\right) \tag{3.13}$$

One of the fundamental ideas of turbulent boundary layer flow and analogous canonical flows is that statistical quantities at different Reynolds numbers should

collapse to a single profile, when the quantities are nondimensionalized with the proper velocity and length scales and Reynolds number tends to infinity. The mean velocity profile described by the universal logarithmic law and located between inner and outer layers, is a good example of the implementation of the idea.

In recent years there has been a large number of publications describing alternative functional forms of the mean velocity distribution in this region (see for example, (Barenblatt & Prostokishin 2000), (George & Castillo 1997) and (Zagarola, Perry & Smits 1997)) some of which were rather controversial. Nevertheless, high quality data such as by Österlund, Johansson, Nagib & Hites (2000a) show that the classical theory gives the most accurate description of the data.

For sufficiently small values of x_2, the viscous stresses will be considerably greater in magnitude than the Reynolds stress $\overline{uv}$. This layer is usually called the **viscous sublayer**.

The scaling law for the near wall region (inner region) has the following form

$$\frac{\bar{u}_1}{u_\tau} = f\left(\frac{x_2 u_\tau}{\nu}\right), \quad \Longrightarrow \quad \bar{u}_1^+ = f(x_2^+) \tag{3.14}$$

It remains now to determine the function $f(x_2^+)$. In the viscous sublayer the viscous force is dominant over the inertial force, hence the parameters related to mass must disappear from the expression for the nondimensional velocity. The only form of the function f which ensures that u_1 is independent of density is $f = 1$. Using this assumption we get the following equation for the velocity distribution law in the viscous sublayer:

$$\bar{u}_1^+ = x_2^+. \tag{3.15}$$

3.1.2 The outer part of boundary layer flow

Leaving the viscous sublayer and entering the region of negligible viscosity equation (3.4) reduces to the following one in the outer region:

$$\bar{u}_1 \frac{\partial \bar{u}_1}{\partial x_1} + \bar{u}_2 \frac{\partial \bar{u}_1}{\partial x_2} = -\frac{1}{\rho}\frac{dP}{dx_1} - \frac{\partial \overline{u_1 u_2}}{\partial x_2}. \tag{3.16}$$

Equation (3.16) describes the development of $\bar{u}_1$ in the outer region of the boundary layer flow.

The universal log-profile describes the mean velocity in the overlap region between the inner and outer layers of any-wall bounded flow and is the best known result

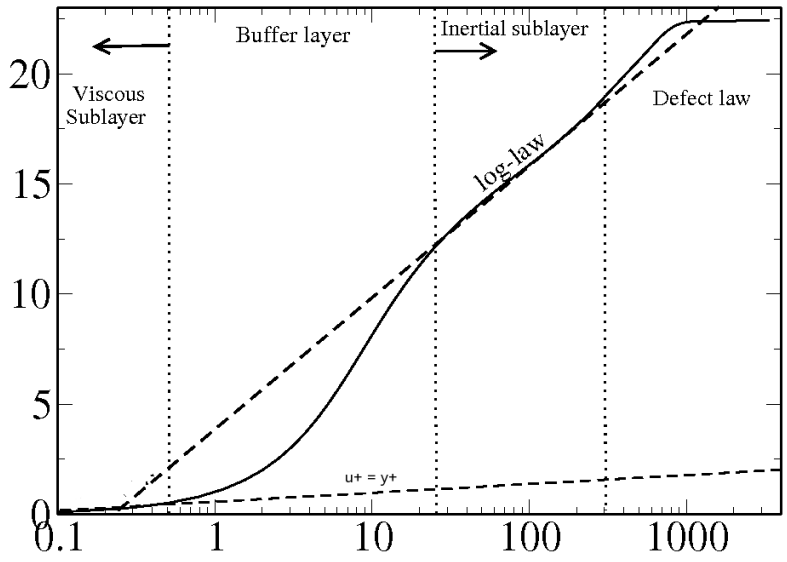

Figure 3.2: Different regions in turbulent boundary layer flow. --- shows the theoretical results for the mean velocity scaling in these regions. — DNS.

of the stated classical idea:

$$\bar{u}_1^+ = -\frac{1}{\kappa}\ln(x_2^+) + C. \tag{3.17}$$

For the outer region of the turbulent boundary layer experimental results have shown that the consideration of the velocity difference $(U_\infty - \bar{u}_1)$, gives a scaling law for its distribution, if this difference is rescaled by u_τ and the distance is normalized by the boundary layer thickness δ. A measure of the boundary layer thickness is the wall distance (e.g. δ_{99}) at which $\bar{u}_1 = 0.99\bar{u}_\infty$ holds. Thus, in the outer part of the boundary layer flow the mean velocity is represented by the equation

$$\frac{\bar{u}_\infty - \bar{u}_1}{u_\tau} = f\left(\frac{x_2}{\delta}\right). \tag{3.18}$$

The classical treatment of the overlap region according to Millikan (1939) gives the following law for the mean velocity behavior

$$\frac{\bar{u}_\infty - \bar{u}_1}{u_\tau} = -\frac{1}{\kappa}\ln\left(\frac{x_2}{\delta}\right) + C, \tag{3.19}$$

where κ, C are constants, which have to be determined from experiments. As it was mentioned above only recently doubts about the validity of the classical logarithmic law begun to arise. However, except for a few authors this law is still generally accepted as the universal profile of the mean velocity in the inner region

of a turbulent boundary layer. Extended logarithmic scaling obtained by Oberlack (2001) using first principles once again confirmed the validity of the law. Let us represent here the logarithmic mean velocity profile in a slightly more general form as it was derived in Oberlack (2001)

$$\bar{u}_1^+ = \frac{1}{\kappa} \ln({x_2}^+ + A^+) + C^+ \tag{3.20}$$

for a comparison with the classical one. Apparently equation (3.20) is an extension of the classical logarithmic law with an extra constant A^+. This scaling law was tested by Lindgren, Österlund & Johansson (2004) using the experimental data of the KTH data-base for turbulent boundary layers for a wide range of Reynolds numbers. They found that with the extra constant A^+, numerically fixed to $A^+ \approx 5$, the modified law describes the experimental data down to $x_2^+ \approx 100$ instead of $x_2^+ \approx 200$ for the classical logarithmic law. The influence of the new constant A^+ decreases rapidly away from the wall (for detailed discussion see Chapter 10.2).

The logarithmic velocity distribution appears to be universal in character, determined only by the wall condition and the distance from the wall. The law has been revised in Oberlack (2001) using a new theoretical approach based on Lie group analysis. Beside an extended form of the logarithmic law the set of mean velocity profiles obtained by Oberlack includes an algebraic law in the center of a turbulent channel flow and in the near wall region, the viscous sublayer, the linear mean velocity in the center of a turbulent Couette flow, the linear mean velocity in the center of rotating channel flow and an exponential mean velocity profile. The latter is very important in our case, because it describes the mean velocity distribution in the wake region (outer region) of the turbulent boundary layer flow over a flat plate and it is in fact an explicit form of the velocity defect law. This exponential law has not previously been reported in the literature.

3.2 Experiments and Numerics

Beginning with the ZPG boundary layer benchmark investigations along a flat plate by Klebanoff (1955), turbulent boundary layers have been examined extensively because of their technological importance, their significance in development of fundamental turbulent models and for the validation of numerical flow simulations. In the paper of Klebanoff (1955) the results of experimental investigations of a boundary layer with ZPG were presented. The measurements of turbulent kinetic energy and turbulent shear stress, probability density and many other useful variables were measured with the hot-wire anemometer. Beside the difficulties associated with the measurement techniques, nearly all experimental boundary

layer investigations are faced with the problem of generation of a fully-developed, turbulent boundary layer flow of large extent and range of scales due to the limited wind-tunnel dimensions.

In 1995 it was decided to build a new low-speed closed return circuit wind-tunnel at the Department of Mechanics, KTH. They performed experiments on ZPG turbulent boundary layer flow for Reynolds numbers based on the momentum thickness ranging from 2500 to 27000 (see (Lindgren et al. 2004), (Lindgren 2002) and (Österlund 1999)). There are several other scientific groups performing similar experiments on ZPG turbulent boundary layer flow. For example, the group of Hassan Nagib at IIT, Chicago, USA, has performed measurements at Reynolds numbers based on momentum thickness up to 70000 (Nagib, Christophorou, Monkewitz & Österlund 2002). Experiments have also been performed in the commercial DNW tunnel in the Netherlands by Hans H. Fernholz's group from TU Berlin, Germany (see (Fernholz & Finley 1996), (Fernholz, Krause, Nockemann & Schrober 1995) and (Knobloch & Fernholz 2002)). In Melbourne, Australia, measurements on a wind-tunnel floor were performed in an open tunnel with a 27 m long test section covering a Reynolds number range up to 60000 (Jones, Nishizawa & Marusic 2002). Kähler (2004) has made experiments at fairly high Reynolds numbers using Particle Image velocimetry. DeGraaff & Eaton (2000) performed experiments using a low-speed, high-Reynolds-number facility and a high-resolution laser-Doppler anemometer. They measured Reynolds stresses and velocity profiles for a flat-plate turbulent boundary layer.

One of the first DNS on ZPG turbulent boundary layer was done by Spalart (1988). The flow at four stations between $Re_\theta = 225$ and $Re_\theta = 1410$ was simulated. Spalart used a spectral method with up to about 10^7 grid points. In the paper a multiple-scale procedure was applied to approximate the slow streamwise growth of the boundary layer. The flow was studied mainly from a statistical point of view and the solutions were compared to the experiments performed by Klebanoff (1955) and Murlis, Tsai & Bradshow (1982). The higher Reynolds number case ($Re_\theta = 1410$) was studied in detail. It was found that in this case the low-Reynods-number effects are weak. The numerical method is fully spectral in space, based on Fourier series in the parallel directions to the plate, and an exponential mapping with Jacobi polynomials in the wall-normal direction. The periods in the streamwise and spanwise directions were $100\delta^\star$ and $25\delta^\star$. The spacings between collocation points, in wall units, were $\triangle x_1^+ \approx 20$ and $\triangle x_3^+ \approx 6.7$. It was concluded that 'near the wall the normal Reynolds stresses $\overline{u_1 u_1}$ and $\overline{u_3 u_3}$ do not collapse when normalized with ν and u_τ.' More recently other contributions have been made including also simulations with adverse pressure gradient, see *e.g.* Spalart & Watmuff (1993), Spalart & Coleman (1997), Skote (2001). Na & Moin (1998) have

performed DNS of a separation bubble and they presented the Reynolds stresses and turbulent energy budgets.

Part I

Lie Groups

4 Lie groups and turbulence

4.1 History of Lie group analysis

Marius Sophus Lie was born in vicarage at Eid in Nordfjord, Norway, on December 17, 1842. He published his first paper in Kristiana (Oslo) in 1869. In 1873, Lie began his research on continuous transformation groups with applications to differential equations and geometry. Lie devoted the reminder of his life to the development and applications of his theory of the continuous groups. The adjective 'continuous' in the name of Lie groups underscores that the transformations can be changed continuously by alterations of the parameters determining particular element of the group.

I noticed that the majority of ordinary differential equations which were integrable by the old methods were left invariant under certain transformations, and that these integration methods consisted in using that property. Once I had thus represented many old integration methods from a common viewpoint, I set myself the natural problem: to develop a general theory of integration for all ordinary differential equations admitting finite or infinitesimal transformations (Lie 2004).

In the biography of Lie and Klein, Yaglom states (Yaglom 1988):
It is my firm belief that of all of the general scientific ideas which arose in the 19th century and were inherited by our century, none contributed so much to the intellectual atmosphere of our time as the idea of symmetry.

One of the crucial point of Lie's theory was that one could assign to each continuous group a much simpler algebraic object, its Lie algebra. Lie analysed in detail the relationship between Lie groups and Lie algebras. The complete solution of the classification problem for simple Lie groups is now attributed to Cartan (1869-1951), who, while a lecturer at the University of Montpellier, substantially advanced the theory of Lie groups and Lie algebras.

In 1892 to 1893, the Kazan physicomathematical society created the international Lobachevsky prize. The first prize was awarded in 1898 to Sophus Lie.

4.2 Lie group analysis

A symmetry of a system of differential equations is a transformation that maps any solution to another solution of the system. These groups played an important role in the development of various areas of mathematics, as well as physics. The applications of these groups include algebraic topology, differential geometry, special functions, relativity, etc.

Typical examples of such groups are the groups of translations, rotations or scaling. Since the ideas of Lie symmetries are not widely known to many readers in the following we give a short introduction to the topic. If a system of partial differential equations is given as follows

$$\boldsymbol{F}(\boldsymbol{x}, \boldsymbol{y}, \boldsymbol{y}^{(1)}, \boldsymbol{y}^{(2)}, ...) = 0, \tag{4.1}$$

where $\boldsymbol{x}$ and $\boldsymbol{y}$ are the independent and dependent variables respectively, a transformation

$$\boldsymbol{x} = \boldsymbol{\Phi}(\boldsymbol{x}^*, \boldsymbol{y}^*), \qquad \boldsymbol{y} = \boldsymbol{\Psi}(\boldsymbol{x}^*, \boldsymbol{y}^*) \tag{4.2}$$

is called a symmetry transformation of equation (4.1) if

$$\boldsymbol{F}(\boldsymbol{x}, \boldsymbol{y}, \boldsymbol{y}^{(1)}, \boldsymbol{y}^{(2)}, ...) = 0, \Longleftrightarrow \boldsymbol{F}(\boldsymbol{x}^*, \boldsymbol{y}^*, \boldsymbol{y}^{*(1)}, \boldsymbol{y}^{*(2)}, ...) = 0, \tag{4.3}$$

holds. $\boldsymbol{y}^{(n)}$ refers to the set of all n^{th} order derivatives of $\boldsymbol{y}$ with respect to $\boldsymbol{x}$.

The primary purpose of the symmetry analysis is to find all Lie symmetries

$$\boldsymbol{x} = \boldsymbol{\Phi}(\boldsymbol{x}, \boldsymbol{y}; \epsilon), \qquad \boldsymbol{y} = \boldsymbol{\Psi}(\boldsymbol{x}, \boldsymbol{y}; \epsilon) \tag{4.4}$$

where ϵ is called the group parameter. Since ϵ may take any value $\epsilon \in R$, equation (4.4) is also called continuous groups in contrast to finite groups such as reflections.

Lie's first theorem shows that if a transformation has group properties it can be represented by its infinitesimal form which contains the essential information. This means that the transformation can be expanded for the small parameter ε :

$$\boldsymbol{x}^* = \boldsymbol{x} + \epsilon \boldsymbol{\xi}(\boldsymbol{x}, \boldsymbol{y}) + \mathcal{O}(\epsilon^2), \tag{4.5}$$

$$\boldsymbol{y}^* = \boldsymbol{y} + \epsilon \boldsymbol{\eta}(\boldsymbol{x}, \boldsymbol{y}) + \mathcal{O}(\epsilon^2), \tag{4.6}$$

where

$$\boldsymbol{\xi}(\boldsymbol{x},\boldsymbol{y}) = \left.\frac{\partial \boldsymbol{\Phi}}{\partial \epsilon}\right|_{\epsilon=0}, \quad \boldsymbol{\eta}(\boldsymbol{x},\boldsymbol{y}) = \left.\frac{\partial \boldsymbol{\Psi}}{\partial \epsilon}\right|_{\epsilon=0}. \tag{4.7}$$

If the infinitesimal of a transformation is given, then their global form can be determined by integrating the first order system using Lie's first theorem (Bluman & Anco 2002):

$$\frac{d\boldsymbol{x}^*(\epsilon)}{d\epsilon} = \boldsymbol{\xi}(\boldsymbol{x}^*(\epsilon),\boldsymbol{y}^*(\epsilon)), \qquad \frac{d\boldsymbol{y}^*(\epsilon)}{d\epsilon} = \boldsymbol{\eta}(\boldsymbol{x}^*(\epsilon),\boldsymbol{y}^*(\epsilon)) \tag{4.8}$$

with the initial conditions:

$$\epsilon = 0 : \boldsymbol{x}^*(\epsilon) = \boldsymbol{x} \text{ and } \boldsymbol{y}^*(\epsilon) = \boldsymbol{y}.$$

The advantage of Lie groups and in turn constructing explicit solutions for them, is that they can be found using computational methods. There are different computer programs (for detailled information see (Ibragimov 1996)) that allows to find continuous symmetry groups for essentially every differential equation. Once the symmetry groups of a system of differential equations are obtained, a wide variety of methods become available to analyze the system. First, one can use symmetry groups to construct new solutions from old ones. Further one can use groups to perform a classification of families of differential equations and their solutions depending on arbitrary parameters or functions. Another possibility is to determine which type of equations admits a given group of symmetry. A mathematically rigorous description of the problem can be found e.g. in Olver (1993) or Bluman & Anco (2002).

4.3 Lie group analysis of TPC equations

The present analysis is based on TPC equations with the limited mean velocity profile $\bar{u}_1 \equiv \bar{u}_1(x_2)$ i.e. the parallel flow assumption, where x_2 is the wall normal coordinate. Figure 3.1 shows the sketch of the coordinate system and mean velocity field. The TPC equations will be considered in the outer part of the boundary layer flow i.e. sufficiently apart from the viscous sublayer, and hence viscosity is negligible.

In order to distinguish between viscosity dominated small-scale quantities and inertia dominated large-scale quantities an asymptotic expansion was introduced in Oberlack & Peters (1993). The matched asymptotic expansion for locally isotropic turbulence in correlation space in Oberlack & Peters (1993) may readily be extended to inhomogeneous flows such as wall-bounded shear flows (Oberlack 2002).

Therein the two-sets of equations for the large and small scales are derived. The former (outer layer in correlation space (r-space)) gives the TPC equations with $\nu = 0$. The outer part of the asymptotic expansion in r-space is obtained by taking the limit $\nu \to 0$ in equation (2.26) yielding

$$\begin{aligned}\frac{\bar{D}R_{ij}}{\bar{D}t} + R_{kj}\frac{\partial \bar{u}_i(\boldsymbol{x})}{\partial x_k} + R_{ik}\frac{\partial \bar{u}_j(\boldsymbol{x})}{\partial x_k}\bigg|_{\boldsymbol{x}+\boldsymbol{r}} + [\bar{u}_k(\boldsymbol{x}+\boldsymbol{r}) - \bar{u}_k(\boldsymbol{x})]\frac{\partial R_{ij}}{\partial r_k} \\ + \frac{\partial \overline{pu}_j}{\partial x_i} - \frac{\partial \overline{pu}_j}{\partial r_i} + \frac{\partial \overline{u_i p}}{\partial r_j} + \frac{\partial R_{(ik)j}}{\partial x_k} - \frac{\partial}{\partial r_k}[R_{(ik)j} - R_{i(jk)}] = 0.\end{aligned} \tag{4.9}$$

It is apparent that the latter equation is not valid in the limit $r \to 0$ since no dissipation is contained which becomes important when r is of the order of the Kolmogorov length-scale.

In the small-scale equations (inner layer in correlation space) we have the expansion

$$\begin{aligned}R_{ij} &= \overline{u_i u_j}(\boldsymbol{x}) - Re_t^{-\frac{1}{2}} R^{(1)}_{ij}(\boldsymbol{x}, \hat{\boldsymbol{r}}) - \mathcal{O}(Re_t^{\frac{3}{4}}) \\ R_{(ik)j} &= \overline{u_i u_j u_k}(\boldsymbol{x}) - Re_t^{-\frac{3}{4}} R^{(1)}_{(ik)j}(\boldsymbol{x}, \hat{\boldsymbol{r}}) - \mathcal{O}(Re_t^{-1}) \\ R_{i(jk)} &= \overline{u_i u_j u_k}(\boldsymbol{x}) - Re_t^{-\frac{3}{4}} R^{(1)}_{i(jk)}(\boldsymbol{x}, \hat{\boldsymbol{r}}) - \mathcal{O}(Re_t^{-1})\end{aligned} \tag{4.10}$$

where the small scales scale like

$$\hat{\boldsymbol{r}} = Re_t^{\frac{3}{4}} \boldsymbol{r},$$

and Re_t is the turbulent Reynolds number.

Introducing the latter expansion into equation (2.26) we get the small-scale equations:

$$\begin{aligned}\frac{\bar{D}\overline{u_i u_j}}{\bar{D}t} + \overline{u_j u_k}\frac{\partial \bar{u}_i(\boldsymbol{x},t)}{\partial x_k} + \overline{u_i u_k}\frac{\partial \bar{u}_j(\boldsymbol{x},t)}{\partial x_k} - \frac{\partial \bar{u}_k(\boldsymbol{x},t)}{\partial x_l}\hat{r}_l \frac{R^{(1)}_{ij}}{\partial \hat{r}_k} + \left[\frac{\overline{pu_j}}{\partial x_i} - \frac{\overline{pu_j}}{\partial r_i} + \frac{\overline{u_i p}}{\partial r_j}\right]\bigg|_{\boldsymbol{r}=0} \\ + 2\frac{\partial^2 R^{(1)}_{ij}}{\partial \hat{r}_k \partial \hat{r}_k} + \frac{\partial \overline{u_i u_j u_k}}{\partial x_k} - \frac{\partial}{\partial \hat{r}_k}\left[R^{(1)}_{i(kj)} - R^{(1)}_{i(jk)}\right] = 0.\end{aligned} \tag{4.11}$$

The pressure-velocity correlations are determined by the Poisson equation and hence they are not independent of the velocity correlations. Figure 4.1 shows a sketch of the overlap region where the small-scale and the large-scale correlations have the same functional behavior: $\lim_{r\to 0} R^{outer}_{ij} = \lim_{r\to\infty} R^{inner}_{ij}$. It is important to note that in the subsequent analysis only the large-scale equations (4.9) are

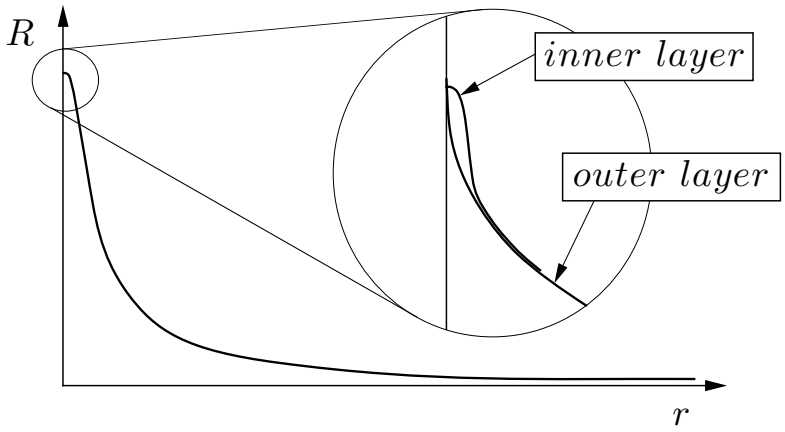

Figure 4.1: Sketch of the TPC function in the overlap region of the r-space asymptotics.

investigated and hence only large-scale quantities such as the mean velocity or the Reynolds stresses are determined. Small scale quantities such as dissipation (the first term in the second line of equation (4.11)) can be formally obtained once the large scale quantities are derived.

The approach developed in Oberlack (2000) and Oberlack (2001) applied to the fluctuation equations will presently be applied to the TPC equations to find their symmetry groups.

In the present study Lie's procedure is used to find symmetry transformations and self-similar solutions of equation (4.9). Lie's procedure to find symmetry transformations and the derivation of self-similar solutions may be divided into three parts. The first one, the computation of the determining system, is completely algorithmic (this is one of the important advantages of the method) and has been aided by the Lie group software package by Carminati & Vu (2000). The package is written for the computer algebra system (CAS) MAPLE. It computes the system of 'determining equations', which consist of a coupled, linear, homogeneous and overdetermined system of partial differential equations for the infinitesimals $\boldsymbol{\xi}(\boldsymbol{x},\boldsymbol{y})$, $\boldsymbol{\eta}(\boldsymbol{x},\boldsymbol{y})$. Typically, such systems vary between ten to several hundred equations. The second part, the solution of the system, may also be solved by CAS, however complete solution under all circumstances may not be expected. The last part of the procedure, the computation of the similarity variables is a rather straightforward process.

In the first step of the present approach the infinitesimal generators ($\boldsymbol{\xi}(\boldsymbol{x},\boldsymbol{y})$, $\boldsymbol{\eta}(\boldsymbol{x},\boldsymbol{y})$) must be determined from equation (4.9). As a result, an over-determined set of ~ 700 linear partial differential equations are obtained. A partial solution

has been derived partly using CAS. The remaining part of the system was solved by hand. Imposing the reduction of a parallel flow, the solution of the system for the desired symmetries is given below:

$$\xi_{x_2} = c_1 x_2 + c_4, \tag{4.12}$$
$$\xi_{r_1} = c_1 r_1, \tag{4.13}$$
$$\xi_{r_2} = c_1 r_2, \tag{4.14}$$
$$\xi_{r_3} = c_1 r_3, \tag{4.15}$$
$$\eta_{\bar{u}_1} = (c_1 - c_2)\bar{u}_1 + c_5, \tag{4.16}$$
$$\eta_{R_{ij}} = [2(c_1 - c_2) + c_3]\, R_{ij}, \tag{4.17}$$
$$\eta_{\overline{u_i p}} = [3(c_1 - c_2) + c_3]\overline{u_i p} \tag{4.18}$$
$$\eta_{\overline{p u_i}} = [3(c_1 - c_2) + c_3]\overline{p u_i}, \tag{4.19}$$
$$\eta_{Z_{ij}} = [2c_1 - 3c_2 - c_3]\, Z_{ij}. \tag{4.20}$$

Z_{ij} is the sum of derivatives of the triple correlation functions in equation 4.9 and c_i are group parameters. Beside the symmetry groups given in equations (4.12-4.15) two other symmetries were obtained to be discussed in the following. The infinitesimal of the mean velocity $\eta_{\bar{u}_1}$ contains one undetermined function, not shown here, which depends on $\boldsymbol{r}$. Since the mean velocity $\bar{u}_1(x_2)$ depends only on x_2 it means that the function does not dependent on $\boldsymbol{r}$. Hence this arbitrary function has to be limited to a constant, while we have denoted by c_5 in equation (4.16).

Beside the latter another symmetry has been obtained which has no physical meaning. We obtained a translation group in $\boldsymbol{r}$-space which means that correlation functions can be translated in $\boldsymbol{r}$-space ($R_{ij}(\boldsymbol{x}, \boldsymbol{r}; t) = R_{ij}(\boldsymbol{x}, \boldsymbol{r} + \boldsymbol{b}; t)$). Though this group of symmetry is mathematically correct, it has no physical meaning. Due to Schwarz' inequality the maximum value of the TPC function is at $\boldsymbol{r} = 0$ ($R_{ij}(\boldsymbol{x}, 0; t) = \overline{u_i(\boldsymbol{x}, t) u_j(\boldsymbol{x}, t)}$). Using this symmetry we obtain $\overline{u_i(\boldsymbol{x}, t) u_j(\boldsymbol{x}, t)} = \overline{u_i(\boldsymbol{x}, t) u_j(\boldsymbol{x} + \boldsymbol{b}, t)}$ which is untrue for arbitrary turbulence. Thus, this newly found symmetry group has no physical meaning and has to be abandoned.

For the present problem we focus only on the scaling symmetries, Galilean invariance and the translation groups (in equations (4.12-4.15)). For all latter groups

the generators may be written as:

$$
\begin{aligned}
X_1 &= x_2\frac{\partial}{\partial x_2} + r_i\frac{\partial}{\partial r_i} + \bar{u}_1\frac{\partial}{\partial \bar{u}_1} + 2R_{ij}\frac{\partial}{\partial R_{ij}} + 3\overline{u_ip}\frac{\partial}{\partial \overline{u_ip}} + 3\overline{pu}_i\frac{\partial}{\partial \overline{pu}_i}\cdots, \\
X_2 &= -\bar{u}_1\frac{\partial}{\partial \bar{u}_1} - 2R_{ij}\frac{\partial}{\partial R_{ij}} - 3\overline{u_ip}\frac{\partial}{\partial \overline{u_ip}} - 3\overline{pu}_i\frac{\partial}{\partial \overline{pu}_i}, \\
X_3 &= R_{ij}\frac{\partial}{\partial R_{ij}} + \overline{u_ip}\frac{\partial}{\partial \overline{u_ip}} + \overline{pu}_i\frac{\partial}{\partial \overline{pu}_i} + \cdots, \\
X_4 &= \frac{\partial}{\partial x_2}, \\
X_5 &= \frac{\partial}{\partial \bar{u}_1},
\end{aligned}
\tag{4.21}
$$

where the dots denote that also higher order correlations are involved in the corresponding symmetry. The numbering of the c_i corresponds to the X_i. Employing Lie's differential equations (4.8), the global transformations for all groups are given by

$$
\begin{aligned}
\boldsymbol{G}_{s1}&: \tilde{x}_2 = x_2e^{a_1},\ \tilde{r}_i = r_ie^{a_1},\ \tilde{\bar{u}}_1 = \bar{u}_1e^{a_1},\ \tilde{R}_{ij} = R_{ij}e^{2a_1},\ \widetilde{\overline{pu_i}} = \overline{pu_i}e^{3a_1},\ \widetilde{\overline{u_ip}} = \overline{u_ip}e^{3a_1}, \cdots \\
\boldsymbol{G}_{s2}&: \tilde{x}_2 = x_2,\ \tilde{r}_i = r_i,\ \tilde{\bar{u}}_1 = \bar{u}_1e^{-a_2},\ \tilde{R}_{ij} = R_{ij}e^{-2a_2},\ \widetilde{\overline{pu_i}} = \overline{pu_i}e^{-3a_2},\ \widetilde{\overline{u_ip}} = \overline{u_ip}e^{-3a_2}, \cdots \\
\boldsymbol{G}_{s3}&: \tilde{x}_2 = x_2,\ \ \tilde{r}_i = r_i,\ \ \tilde{\bar{u}}_1 = \bar{u}_1,\ \ \tilde{R}_{ij} = R_{ij}e^{-a_3},\ \ \widetilde{\overline{pu_i}} = \overline{pu_i}e^{-a_3},\ \ \widetilde{\overline{u_ip}} = \overline{u_ip}e^{-a_3}, \cdots \\
\boldsymbol{G}_{transl}&: \tilde{x}_2 = x_2 + a_4,\ \ \tilde{r}_i = r_i,\ \ \tilde{\bar{u}}_1 = \bar{u}_1,\ \ \tilde{R}_{ij} = R_{ij},\ \ \widetilde{\overline{pu_i}} = \overline{pu_i},\ \ \widetilde{\overline{u_ip}} = \overline{u_ip}, \cdots \\
\boldsymbol{G}_{galil}&: \tilde{x}_2 = x_2,\ \ \tilde{r}_i = r_i,\ \ \tilde{\bar{u}}_1 = \bar{u}_1 + a_5,\ \ \tilde{R}_{ij} = R_{ij},\ \ \widetilde{\overline{pu_i}} = \overline{pu_i},\ \ \widetilde{\overline{u_ip}} = \overline{u_ip}, \cdots .
\end{aligned}
\tag{4.22}
$$

The variables a_1 – a_5 are the group parameters of the corresponding transformations X_1 – X_5 or the parameter c_1 – c_5 in the infinitesimals.

The most interesting fact with respect to the latter groups is that *three independent scaling groups* $\boldsymbol{G}_{s1}$, $\boldsymbol{G}_{s2}$, $\boldsymbol{G}_{s3}$ have been computed. Two symmetry groups correspond to the scaling symmetries of the Euler equations. The first one is the scaling in space, the second one scaling in time. The third group (G_{s3}) is a new scaling group that is a characteristic feature only of the one-dimensional turbulent boundary layer flow. It is a new scaling symmetry not obtained before. This is in striking contrast to the Euler and Navier-Stokes equations, which only admit two and one scaling groups, respectively. $\boldsymbol{G}_{transl}$ and $\boldsymbol{G}_{galil}$ represent the translation symmetry in space and the Galilean transformation, respectively.

The corresponding characteristic equations for the invariant solutions (Oberlack

2001) read

$$\frac{dx_2}{c_1x_2+c_4}=\frac{dr_i}{c_1r_i}=\frac{d\bar{u}_1}{(c_1-c_2)\bar{u}_1+c_5}=\frac{dR_{ij}}{[2(c_1-c_2)+c_3]R_{ij}}= \\ \frac{d\overline{pu_i}}{[3(c_1-c_2)+c_3]\overline{pu_i}}=\frac{d\overline{u_ip}}{[3(c_1-c_2)+c_3]\overline{u_ip}}=\cdots. \tag{4.23}$$

In Oberlack (2001) it has been shown that the symmetry breaking of the scaling of space leads to a new exponential scaling law. Therein it was argued that physically it corresponds to the outer part of a boundary layer flow, the wake region.

Thus, imposing the assumption of symmetry breaking of the scaling of space ($c_1 = 0$), the characteristic equation for the velocity will get the following form:

$$\frac{dx_2}{c_4}=\frac{d\bar{u}_1}{-c_2\bar{u}_1+c_5}, \tag{4.24}$$

integrating this equation we obtain an extended set of scaling laws for the mean velocity and TPC function as follows:

$$\bar{u}_1(x_2)=k_1+k_2e^{-k_3x_2}, \tag{4.25}$$

where

$$k_1\equiv\frac{c_5}{c_2},\qquad k_3\equiv\frac{c_2}{c_4}$$

and k_2 is a constant of integration.

As for the TPC functions R_{ij} we have the equation:

$$\frac{dx_2}{c_4}=\frac{dR_{ij}}{(-2c_2+c_3)R_{ij}}, \tag{4.26}$$

The solution of the equation is the following:

$$R_{ij}(x_2,\boldsymbol{r})=e^{-k_4x_2}B_{ij}(\boldsymbol{r}), \tag{4.27}$$

In full analogy with the case of mean velocity and TPC functions, one can obtain from the equation (4.23) the following laws for the pressure-velocity correlations:

$$\overline{u_ip}(x_2,\boldsymbol{r})=e^{-(k_3+k_4)x_2}E_i(\boldsymbol{r}),\qquad \overline{pu_i}(x_2,\boldsymbol{r})=e^{-(k_3+k_4)x_2}F_i(\boldsymbol{r}),\cdots, \tag{4.28}$$

where $k_4\equiv\frac{2c_2-c_3}{c_4}$ is a constant comprising several group parameters and constants of integration and B_{ij}, E_i, F_i are functions of $\boldsymbol{r}$ only.

For positive k_3 the velocity law (4.25) converges to a constant velocity for $x_2\to\infty$ ($k_1=\bar{u}_\infty$). For a plane shear flow this may only be applicable to a boundary layer

type of flow. In this flow the symmetry breaking length scale is the boundary layer thickness.

In normalized and non-dimensional variables the exponential scaling law (4.25) may be re-written in the following form

$$\frac{\bar{u}_\infty - \bar{u}_1}{u_\tau} = \alpha \, \exp\left(-\beta \frac{x_2}{\Delta}\right). \tag{4.29}$$

One can derive the scaling laws for the Reynolds stresses from 4.27 when $\boldsymbol{r} = 0$:

$$\frac{\overline{u_i u_j}(x_2)}{u_\tau^2} = b_{ij} \, \exp\left(-a \frac{x_2}{\Delta}\right), \tag{4.30}$$

where $\alpha = k_2/u_\tau$ and $\beta = k_3\Delta$. b_{ij} and a are universal constants that should be found from DNS or experimental data. Δ is the Rotta-Clauser length scale

$$\Delta \equiv \int_0^\infty \frac{\bar{u}_\infty - \bar{u}_1}{u_\tau} dx_2 = \frac{\bar{u}_\infty}{u_\tau}\delta^*,$$

while δ^* is the boundary layer displacement thickness.

Note that in the limit $\boldsymbol{r} = 0$ the expansion (4.10) has to be considered according to the sketch in Figure 4.1. Therein we see that in the latter limit $\overline{u_i u_j}$ is obtained with an error $\mathcal{O}(Re_t^{-\frac{1}{2}})$.

Recently the law 4.27 was validated in detail using high Reynolds number experimental data from the KTH data-base for zero pressure-gradient turbulent boundary layers by Lindgren et al. (2004). The range of Reynolds number based on momentum-loss thickness was from 2500 to 27000. It was found that the exponential scaling law of the mean velocity defect in the outer or wake region fits well with the experimental data over a large part of the boundary layer thickness. Still in the outermost part of the boundary layer the velocity defect decreases more rapidly than the exponential law. This can be caused by intermittency in the outermost part of the boundary layer, or non-parallel effects may became dominant which are not taken into account in the derivation of the exponential law.

Part II

DNS

5 Numerical method and basic parameters of the flow

The most appealing approach to the numerical simulation of turbulent flows is DNS, i.e. solving the three-dimensional Navier-Stokes equations numerically without any simplification. Direct simulation allows to perform such numerical experiments that can not be realized in a laboratory, and gives detailed information about the flow field, that is not possible to get in the laboratory experiments. DNS provides benchmarks against less costly simulation methods, because it does not involve approximations, other than those due to discretization (which is inherent in any numerical solution of partial differential equations). However, the continuum of different spatial and temporal scales in a turbulent flow leads to huge computer time and storage requirements which increase with increasing Reynolds number of the flow. Because of this fact, DNS is limited to relatively low Reynolds numbers in practice. To simulate most of the industrial and naturally occurring flows at real/high Reynolds numbers is not feasible at present.

The DNS-type computations are able to take the organized character of the flow into account. Since the available information is very rich, compared with experimental data, it is necessary to extract the relevant information. This extraordinary advantage (full access to the three velocity components, pressure, etc.) of DNS computations can be a drawback when the choice of the more appropriate parameter has to be selected. A main characteristic of DNS simulation is that a wide range of scales is explicitly computed. The largest scales of the flow are imposed by the flow configuration, through its external geometry (channel width, boundary layer thickness, etc.). As for the homogeneous directions, the length of computational domain must contain at least several integral scales or similarly, must lead to a complete spatial decorrelation of the data along a distance smaller than half the domain. Concerning the smallest resolved scales, it is commonly accepted that the Kolmogorov length scale, η, is a good estimate of the minimal scale that needs to be resolved. It is worthwhile to note to note that this constraint is only indicative, since reliable DNS results can be obtained with computational grids based on mesh size Δx equal to several times the Kolmogorov length. Hence, the condition $\Delta x = \mathcal{O}(\eta)$ seems to be sufficient for many cases. The DNS resolution requirement is naturally directly conditioned by the accuracy of the numerical method. For any

computational grid, a fraction of the computed solution is inevitably corrupted by the numerical errors introduced by the discretizations.

There are many different methods of solving partial differential equations numerically, such as finite elements, finite differences or spectral methods. The latter are used in our work for the numerical simulations of turbulent boundary layer flow. Spectral methods are based on global functions, and each function is expanded in a sum of basis functions,

$$u(x) \approx \sum_{n=0}^{N} a_n \psi_n(x),$$

This series is substituted into the equation

$$Lu = f(x),$$

where L is an operator describing the differential equation. A residual is defined as

$$R(x, a_0, a_1, ..., a_N) = Lu_N - f \tag{5.1}$$

The goal is to minimise the residual function by choosing suitable base functions ψ_n and expansion coefficients a_n.

One great advantage of spectral methods as compared to finite difference or finite volume methods is their minimal phase error. From the error analysis for the spectral methods one can deduce that for an infinitely differentiable function, the approximation error is smaller than any power of $1/N$: **the convergence is exponential**. **This behavior is commonly called "spectral" or "infinite" accuracy** (for details see (Peyret 2002)). For a sufficiently large number of Fourier modes, the error depends only on the regularity of the function under consideration. Such behavior has to be compared to the $\mathcal{O}(1/N^p)$ error of a finite-difference approximation where $1/N$ is the mesh size and p, which depends on the scheme, is essentially finite and even relatively small. More details about the algorithm used in the spectral methods can be found in the appendix (A).

In the review of Moin & Mahesh (1998) the authors discuss the DNS Reynolds number for which the simulations have to be done. They ask two questions: 'How high a Reynolds number is high enough?' and 'What are the objectives of the computations?' The answers to these questions give the Reynolds number which is necessary in every special case. In the case of incompressible ZPG turbulent boundary layer flow, the Reynolds number dependence is commonly emphasized by noting that turbulence statistics in inner and outer scaling do not collapse at different Reynolds numbers. But this could be a consequence of scaling used. For example, recently in the paper DeGraaff & Eaton (2000) a new scaling was

introduced for the streamwise component of the Reynolds stress tensor and better collapse of data was observed.

Some of the most important contributions of DNS have been in the modeling of turbulence. The Reynolds stress equations contain several terms that must be modeled but are difficult to measure experimentally. DNS comes to help in this situation: All terms in the Reynolds stress equations can be directly computed. Rogallo's DNS of homogeneous turbulence (Rogallo 1981) was the first numerical experiment that provided complete Reynolds stress budgets involving the pressure-strain correlation and dissipation.

An important contribution of DNS to a better understanding of turbulent boundary layers is in providing a more realistic view of its structure. In the early 1980s most of what was known about the boundary layer structure was deduced from experiments with extrapolation from incomplete data. The three-dimensional fields of velocity, pressure and vorticity obtained from DNS fill the gaps in boundary layer structure theory.

DNS of high Reynolds number turbulent flows requires huge computer resources. Because of this fact DNS Reynolds numbers were limited to low values compared to experiments. However in a recent paper by Jimenez (2003) the author discusses if numerical simulations will ever replace experiments. For a long time it was stated that experiments can be run at higher Reynolds numbers than simulations. The author discusses DNS cost for different turbulent flows and makes a conclusion that even today simulations are comparable to experiments in many aspects, including Reynolds number. There are several cases in which DNS or LES will reach asymptotic Reynolds numbers in one or two decades, and other cases in which conceptual experiments have already given answers to questions which would be difficult to test in the laboratory.

The resolution problem of DNS has been discussed in many papers and books (a recent summary can be found in Pope (2000)). A wide spectrum of turbulence scales require to account for all eddies in the full description and computation of turbulence field. From equation (1.18) it follows that the range of scales increases with the turbulence Reynolds number, .i.e. $l/\eta \sim Re_l^{3/4}$. DNS require that the numerical grid (Δ_{cell}) resolves the smallest, dissipative, eddies so that the average size of a grid cell must be smaller that the Kolmogorov length scale $\Delta_{cell} < \eta$. The large scale eddies are usually of the size comparable with the characteristic flow dimension L and turbulent velocity fluctuations $k^{1/2}$ is of the same order of magnitude as the characteristic mean flow velocity, $l \approx L, k^{1/2} \approx \bar{u}$. Thus, the mean flow Reynolds number is proportional to the turbulence Reynolds number, i.e. $Re \approx Re_l$. Hence, for a three dimensional turbulent flow, the minimum number

of grid points is

$$N \approx \frac{L}{l} \approx Re^{9/4}, \tag{5.2}$$

where N is the total number of modes. Re is the Reynolds number based on the lengthscale characterizing large eddies.

The first DNS on a zero-pressure gradient turbulent boundary layer flow was performed by Spalart (1988) at four different Reynolds numbers between $Re_\theta = 225$ and $Re_\theta = 1410$. The periods in the x_1- and x_3-directions were $100\delta^*$ and $25\delta^*$ respectively. The resolution was $\Delta x_1^+ \approx 20, \Delta x_3^+ \approx 6.5$. The number of grid points for the higher Reynolds number was $1.1 \cdot 10^7$. The time sample for the statistics was $200\delta^*/U_\infty$.

5.1 Spectral code

The DNS code was developed at KTH, Stockholm (for details see (Lundbladh, Berlin, Skote, Hildings, Choi, Kim & Henningson 1999) and (Skote 2001)) using a spectral method with Fourier decomposition in the horizontal directions and Chebyshev discretization in the wall normal direction. Time integration is performed using a third order Runge-Kutta scheme for the advective and forcing terms (necessary for the fringe region) and Crank-Nicolson for the viscous terms. The transformation between physical and spectral space is done by Fast Fourier Transform (FFT): *By cutting from n^2 to nlogn the number of computations necessary to compute a Fourier transform, the fast Fourier transform transformed entire industries, as well as areas of research - like crystallography - that rely on the Fourier transform* (Hubbard 1998).
The spectral method as a computational tool has evolved vigorously in the early 1970's. Kreiss (1972) and Orszag (1972) applied this method to partial differential equations for spatially periodic problems. Orszag called it a pseudo-spectral method, because of the occurrence of the non-linear terms, which are calculated in physical space. The first unifying mathematical treatment of the theory of spectral methods was done by Gottlieb & Orszag (1977). In this monograph the state of the art in the theory and application of spectral methods is summarized. The methods became widely used during the 1980's. Turbulent boundary layers are almost never homogeneous in the streamwise direction. The first spatially developing, non-parallel approximation of the adverse pressure gradient turbulent boundary layer flow was considered by Spalart & Watmuff (1993). They used a method different from that of Spalart (1988) where the growth-term approach was developed. This strategy was successful in the sink flow (Spalart 1986) and in zero pressure-gradient turbulent boundary layer (Spalart 1988) where the growth

of the boundary layer thickness in streamwise direction is small. If the pressure gradient is adverse or strong, the assumption of weak inhomogeneity fails. Spalart & Watmuff (1993) used a fringe region method in case of the pressure gradient flows. This method is similar to that described in Bertolotti & Spalart (1992) and further details are given below.

The algorithm used in our DNS is similar to that for the channel geometry of Kim, Moin & Moser (1987). The original algorithm (Lundbladh, Henningson & Johansson 1992) has been developed for the incompressible flow equations in a channel flow geometry. The implementation of the method for the turbulent boundary has been used in a number of investigations. Skote, Henningson & Henkes (1998) used it for the numerical simulation of the adverse pressure gradient turbulent boundary layer. DNS of separating turbulent boundary layer was done in Skote & Henningson (2002). Recently the model of turbulence generation in the wall region based on varicose instability of a streak was studied by Skote, Haritonidis & Henningson (2002). Since the boundary layer is spatially developing in the downstream direction, it is necessary to use non-periodic boundary conditions in the streamwise direction. To overcome the difficulties with boundary conditions and simplify the usage of spectral methods in this direction the fringe region technique has been used in DNS of turbulent boundary layer flow. The method allows to rescale the boundary layer growth normal to the wall. In this way the physical domain and the fringe region together satisfy periodic boundary conditions. An extra forcing function is added to the Navier-Stokes equations in the fringe region which is non-zero only in this region:

$$\frac{\partial u_i}{\partial t} + u_j \frac{\partial u_i}{\partial x_j} = -\frac{1}{\rho}\frac{\partial p}{\partial x_i} + \nu \frac{\partial^2 u_i}{\partial x_j^2} + F_i, \tag{5.3}$$

where

$$F_i = \lambda(x)(\tilde{u}_i - u_i),$$

$\lambda(x)$ is a non-negative fringe function which is significantly non-zero only within the fringe region (see Equation (5.4)), $\tilde{u}_i$ is the laminar inflow velocity profile to which the solution u_i is forced. The form of $\lambda(x)$ is defined to minimize the upstream influence.

$$\lambda(x) = \lambda_{max}\left[S\left(\frac{x - x_{start}}{\Delta_{rise}}\right) - S\left(\frac{x - x_{end}}{\Delta_{fall}} + 1\right)\right] \tag{5.4}$$

$\lambda_{max}, x_{start}, x_{end}$ are maximum strength of the damping, start and end of the region were the damping function is non-zero; $S(x)$ is a smooth step function. The computational box is divided into a useful and a fringe region. The non-physical phenomena occurring in the fringe region do not invalidate the solution in the

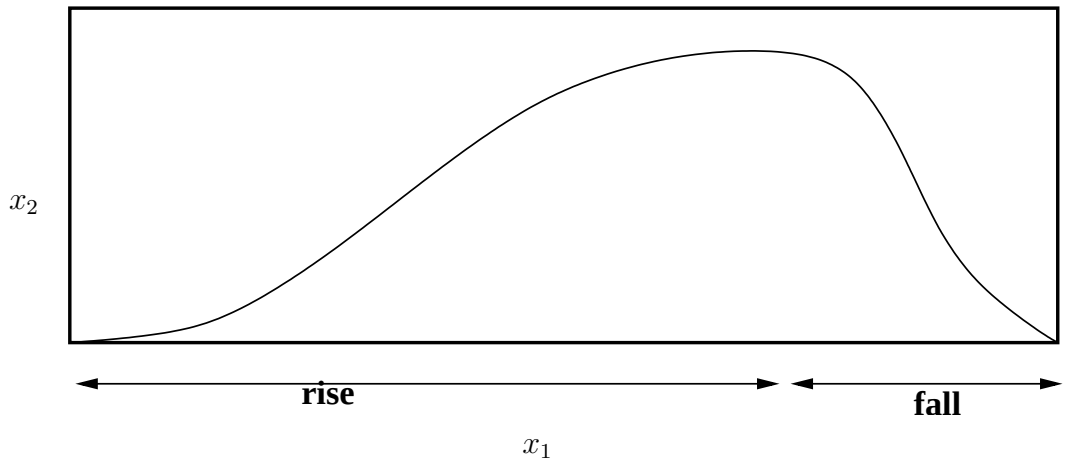

Figure 5.1: Structure of the fringe region.

physically useful part of the computational domain. As it was proved in Nördstrom, Nordin & Henningson (1999), it is possible to force the periodic solutions computed by the fringe region technique toward the exact solution (for the theoretical verification see (Nördstrom et al. 1999)). Figure 5.2 shows the initial part of simulation box that contains laminar boundary layer flow (left plot); The right plot on the same figure shows the end of the simulation box with the fringe region where the flow is forced to the laminar one.

To generate turbulence forcing of a volume force trip strip at the wall running in the spanwise direction was used in the simulations. The volume force has a continuous time derivative and it is independent of the time discretization.

5.2 Performed Simulations

All simulation starts with a laminar boundary layer as inflow which is triggered to transition by a random volume force near the wall. All quantities are non-dimensionalized by the free-stream velocity u_∞ and the displacement thickness δ^* at $x = 0$ where the flow is laminar. The size of the computational box (in these units) in one case was $450 \times 30 \times 34$ (including the fringe region) and $1000 \times 30 \times 34$ in another (with respect to the size of the simulation box, two different simulations were performed, but with the same Reynolds number).

Simulations were run at three different Reynolds numbers (in the inflow plane

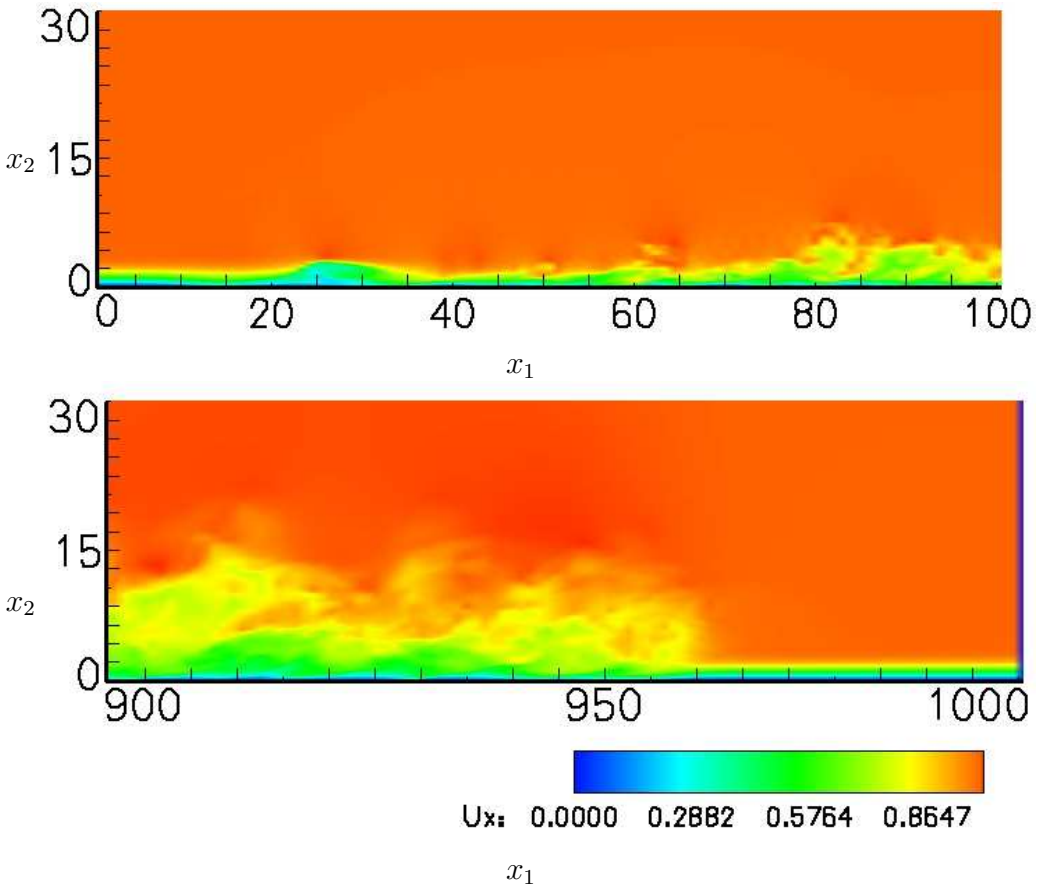

Figure 5.2: Initial (upper plot) and final (bottom plot) part of simulation box.

where the flow is laminar)

$$Re_{\delta^*}|_{x=0} = 600, \quad Re_{\delta^*}|_{x=0} = 2000, \quad Re_{\delta^*}|_{x=0} = 2500.$$

which corresponds to the following turbulent Reynolds numbers:

$$Re_\theta = 810, \quad Re_\theta = 2240, \quad Re_\theta = 2500.$$

The code is parallelized with OpenMP and MPI.
Simulations $DNS600(a-d)$ and $DNS2000(a,b)$ were performed on the IBM computer with 32 parallel processors (Regatta-H) at Technische Universität Darmstadt.
The last simulation, DNS2500, was performed on the Hitachi Supercomputer in Munich using 256 processors. For details about the performed simulations see table 5.1. Figure 5.3 shows scaling of the OpenMP version of the code, which was run on IBM, Regatta-H, in Darmstadt University.

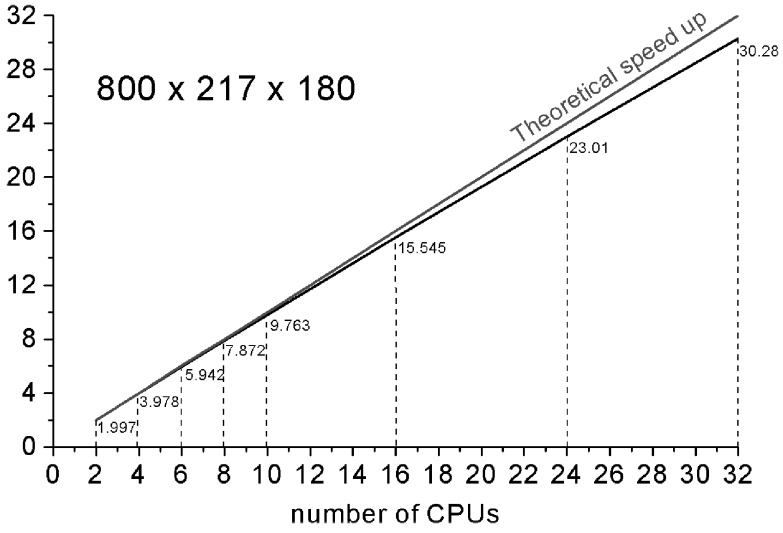

Figure 5.3: Code scaling on different number of CPUs.

DNS in the cases $DNS600(a-c)$ will be called below as *the low Reynolds number DNS with small simulation box*;
$DNS600(d,e)$ - *low Reynolds number DNS with long simulation box*;
$DNS2000(a,b)$ - *high Reynolds number DNS - case I*;
$DNS2500$ - *high Reynolds number DNS - Case II.*

The DNS results presented in the thesis were published in journals and presented on different conferences:
Khujadze & Oberlack (2002, 2003(a,b), 2004(a,b,c,d), 2005(a,b)) and Oberlack & Khujadze (2003, 2005).

	$Re_{\delta^\star}$	$N_x \times N_y \times N_z$	$L_x \times L_y \times L_z$	CPUs	$N \times 10^6$
$DNS600a$	600	$480 \times 129 \times 128$	$450 \times 30 \times 34$	32	7.9
$DNS600b$	600	$800 \times 217 \times 180$	$450 \times 30 \times 34$	32	31.2
$DNS600c$	600	$800 \times 361 \times 256$	$450 \times 30 \times 34$	32	74
$DNS600d$	600	$1024 \times 513 \times 256$	$1000 \times 60 \times 34$	8	134.5
$DNS600e$	600	$2048 \times 513 \times 256$	$1000 \times 60 \times 34$	8	269.
$DNS2000a$	2000	$2500 \times 217 \times 256$	$450 \times 30 \times 34$	32	138.9
$DNS2000b$	2000	$2500 \times 361 \times 256$	$450 \times 30 \times 34$	32	231.
$DNS2500$	2500	$2048 \times 513 \times 256$	$450 \times 30 \times 34$	256	269

Table 5.1: Parameters of performed simulations.

6 Low Reynolds number case

6.1 Small box simulations

The first simulations were performed at three different resolutions (number of grid points 7.9, 31.2 and 73.9 millions respectively). The simulations for low Reynolds number were run for a total of 22000 time units (δ^*/u_∞) and the sampling for the statistics was performed during the last 15000 time units. The useful region was confined to $150 - 350\delta^*|_{x=0}$ which corresponds to Re_{δ^*} from 800 to 1180 or Re_θ from 540 to 810.

The resolution in streamwise and spanwise directions were: $\Delta x^+ \approx 16$ and $\Delta z^+ \approx 5.5$. As for the resolution in wall-normal direction it is $\Delta y^+ \approx 0.04$ near the wall, and it becomes more and more coarse away from the wall because of Chebychev discretization in this direction. Thus, for the resolution in wall-normal directions we have $\Delta y^+ \approx 0.04 - 5$.

The non-dimensional timestep is $\Delta t u_\infty/\delta^*|_{x=0} = 0.11$. In wall units it is $\Delta t u_\tau^2/\nu = 0.15$.

The simulation box of the boundary layer flow in the present DNS is shown in Figure 6.1. The wall-normal component of velocity is presented in the figure.

The comparison between two resolutions (for $u_{i,rms}$) is shown in Figure 6.2. The difference between them is small even though the number of points in each direction for the coarser grid is reduced by a factor of 1.59. Thus we decided that the coarser

	Re_θ	Re_δ	u_∞/u_τ	$u_\tau \times 10^{-2}$	Δ	$c_f \times 10^{-3}$	θ	$\delta^\star$
100	470	700	18.70	5.34	21.72	5.71	0.78	1.16
150	540	800	19.58	5.12	26.16	5.20	0.90	1.33
200	615	910	20.19	4.97	30.58	4.90	1.02	1.51
250	690	1015	20.50	4.89	34.53	4.75	1.14	1.68
300	755	1110	20.80	4.82	38.27	4.61	1.25	1.84
350	810	1180	20.65	4.90	40.04	4.69	1.33	1.94

Table 6.1: Flow parameters at $Re_\theta = 810$

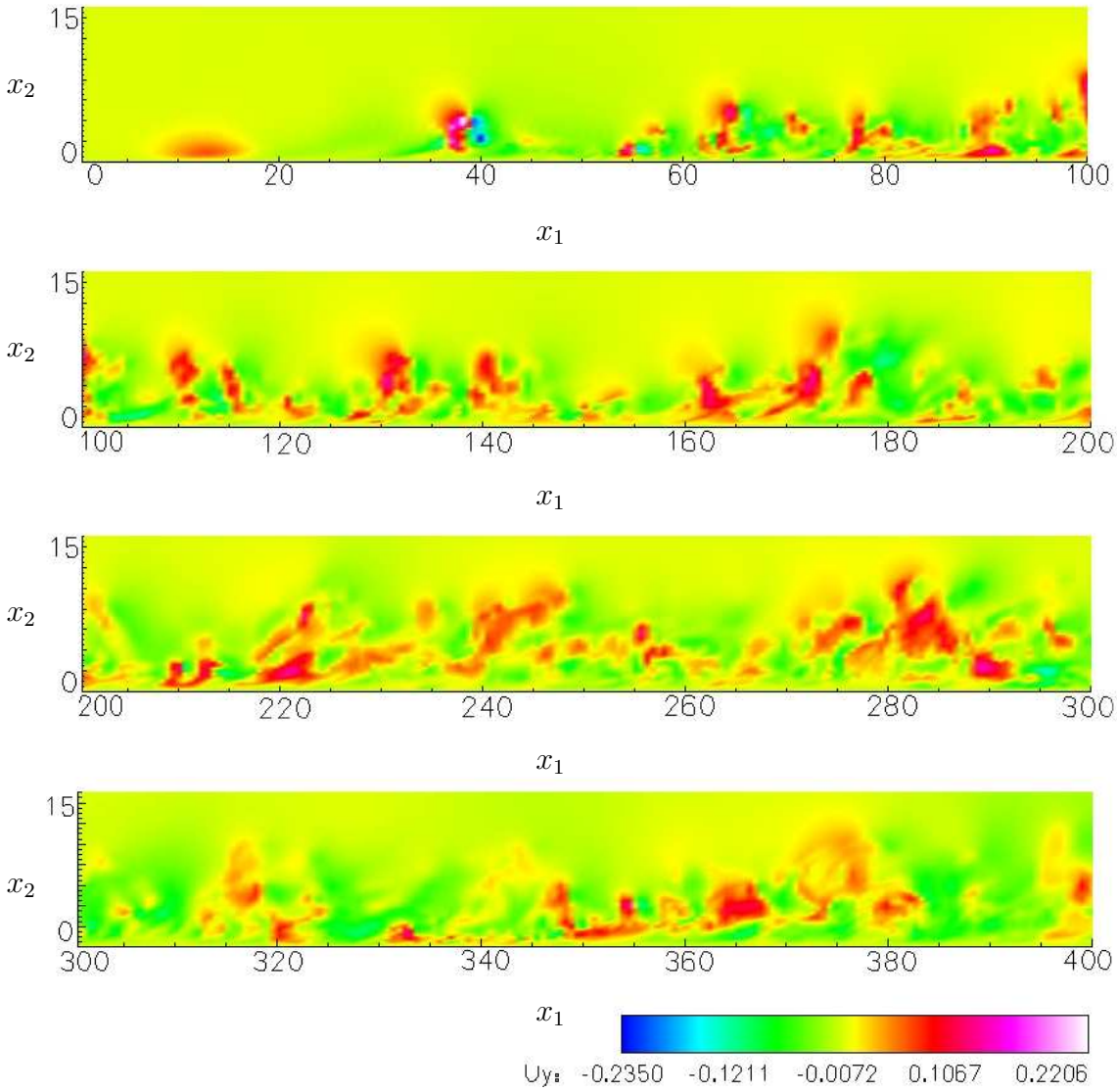

Figure 6.1: Simulation box of boundary layer flow developing in the streamwise direction. The wall-normal component velocity is presented.

grid is sufficient to resolve the flow with this Reynolds number and it has to be used as the starting point for the calculation of the number of grid points for the higher Reynolds number flows. The small difference between different simulations is observed in the case of lower number of grid points. The plots for the second (31.2 million) and third simulations (74 million) collapse. The results from the DNS performed with 31.2 million grid points are presented below.

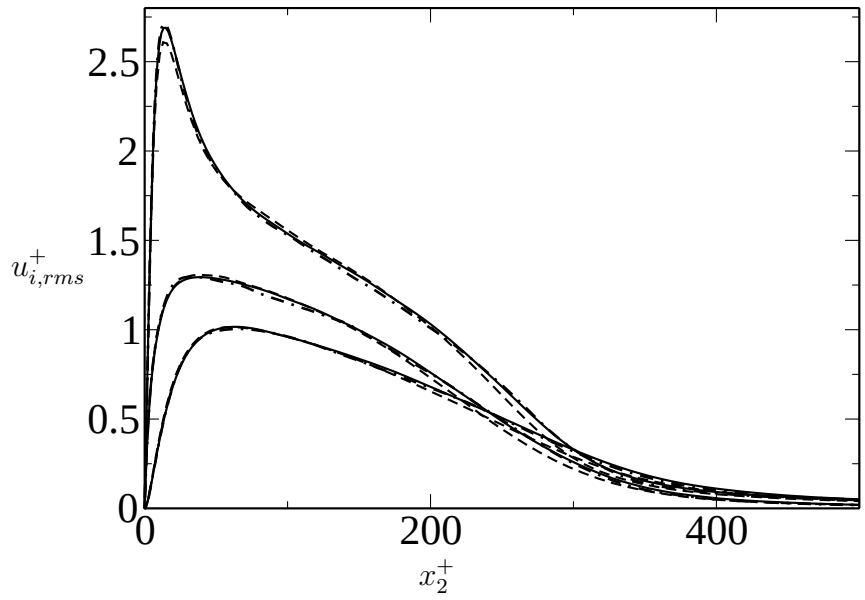

Figure 6.2: $u^+_{i,rms}$: --- 7.9 ($480\times129\times128$), — 31.2 ($800\times217\times180$) and —·— 74 ($800\times361\times280$) million grid points.

Friction coefficient vs. Re_θ is shown in Figure 6.3. As Re_θ increases, c_f decreases slightly. For the turbulent region it changes from 5.7 to 4.6.

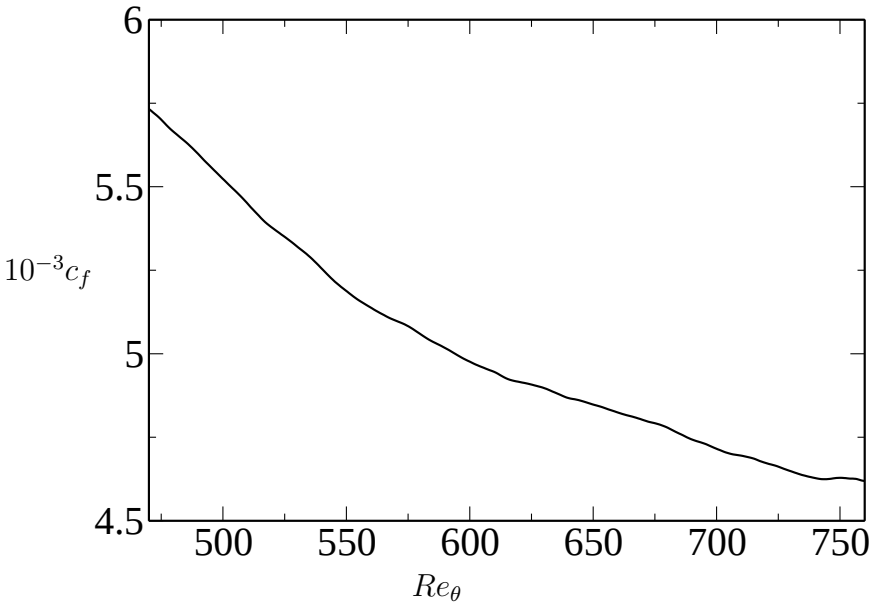

Figure 6.3: Friction coefficient c_f versus momentum-thickness Reynolds number.

The shape factor H (the ratio of the displacement and momentum thicknesses) of the boundary layer flow is displayed in Figure 6.4 (see equation (6.1)).

$$H \equiv \frac{\delta^\star}{\theta} \tag{6.1}$$

Figure 6.5 shows shape factor in turbulent region between $Re_\theta = 470$ and $Re_\theta = 760$. The H is varying in the limits $1.47 - 1.485$. For the comparison, the shape factor for the Blasius profile is $H \approx 2.6$.

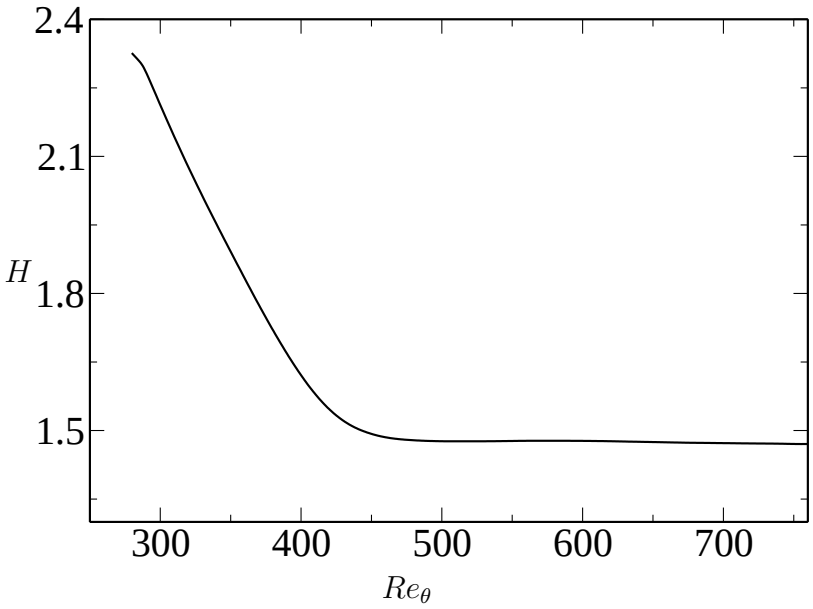

Figure 6.4: Shape factor H in the whole simulation box including the transition region.

The Reynolds stresses obtained from our computation (at $Re_\theta \approx 755$) are compared with the results from Spalart's DNS ($Re_\theta \approx 670$) ((Spalart 1988)). The result of comparison is shown in Figure 6.6. One can see differences between the two DNS data, that could be caused by the following three factors. First, resolution in plus units in our and Spalart's DNS were rather different, namely $\Delta x^+ \approx 15$, $\Delta z^+ \approx 5.5$ and $\Delta x^+ \approx 20$, $\Delta z^+ \approx 6.7$, respectively, which may cause differences, particularly in the near wall region. Second, Spalart's computational box was considerably smaller compared to our one, that means that certain large-scale quantities may not have been fully resolved. Finally, we took great care for the accumulation of the statistics which in our case covered more then $20000\delta^*/u_\infty$ time units, while Spalart used only $200\delta^*/u_\infty$ time units.

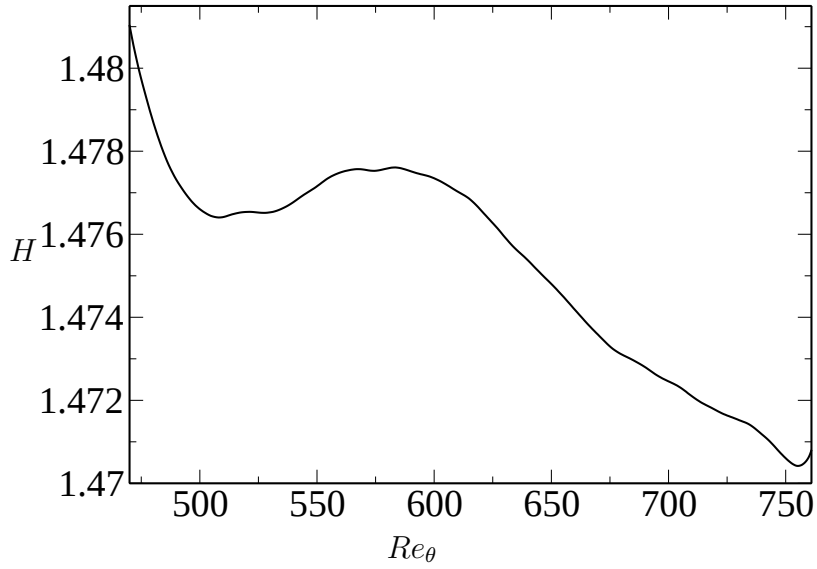

Figure 6.5: Shape factor H in the region of fully developed boundary layer flow.

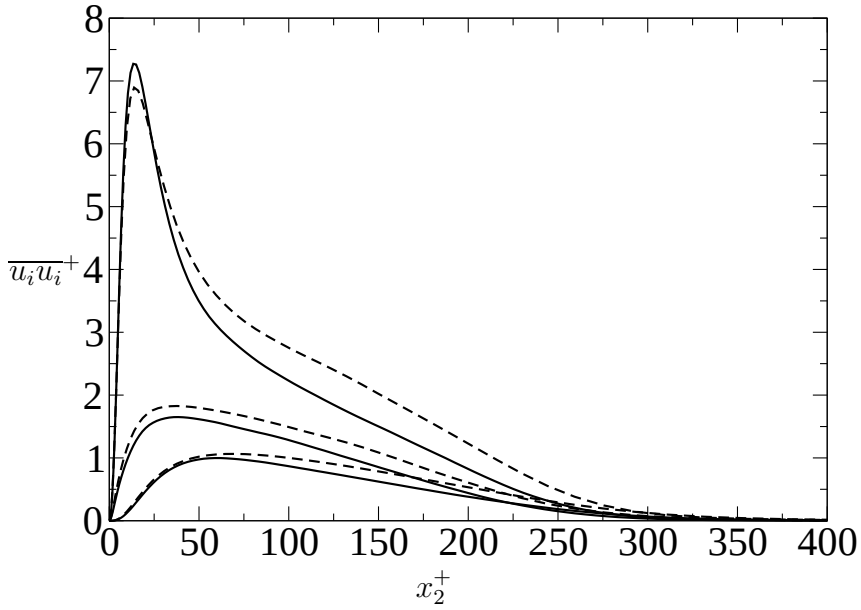

Figure 6.6: Reynolds stresses $\overline{u_i u_i}$. --- Spalart's data (1988), —— DNS ($Re_\theta \approx 755$).

6.1.1 Mean velocity profiles

Mean velocity profiles for different local Reynolds numbers taken at different points of the simulation box $x_1 = 150, 200, 250, 300$ that correspond to $Re_\theta = 540, 615, 690, 755$ are shown in Figures 6.7 and 6.8.

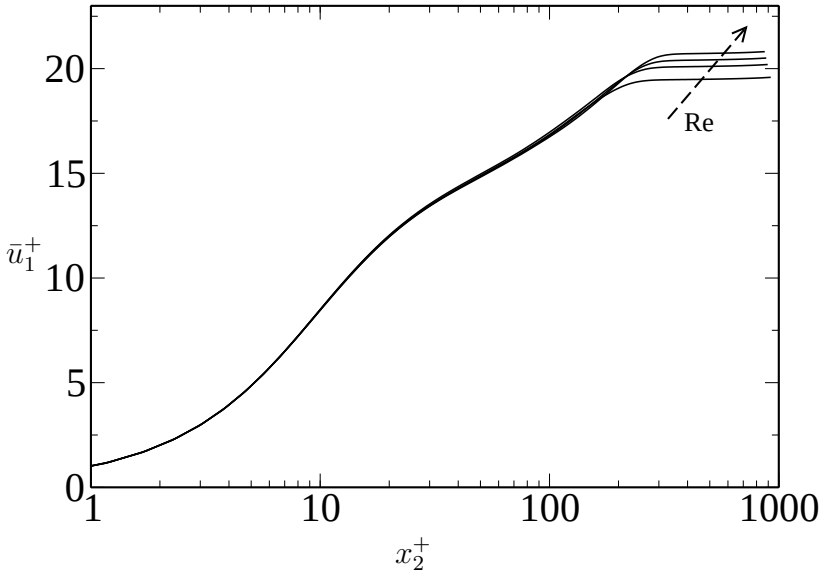

Figure 6.7: Mean velocity profiles for different Reynolds numbers $Re_\theta = 540, 615, 690, 755$.

The behavior of the mean velocity in the near-wall region is shown in Figure 6.7. The straight line corresponds to the linear law of mean velocity profile ($\bar{u}_1^+ = x_2^+$). As one can see from the figure the law is in good agreement with the DNS data up to $x_2^+ \approx 5$. Close-up view of the mean velocity profiles from the plot 6.7 are shown in Figure 6.8.

Figure 6.9 shows mean velocity profiles for the low Reynolds number case (low Reynolds number simulation), Spalart's DNS and the Eaton-DeGraaff experiment. As we see, Spalart's low Reynolds number simulation is very close to our low Reynolds number simulation (small box). The velocity defect law in inner-outer scaling is shown in Figure 6.10 for different points in the streamwise direction. As one can see they collapse onto one line as it should be because of self-similarity of the boundary layer flow.

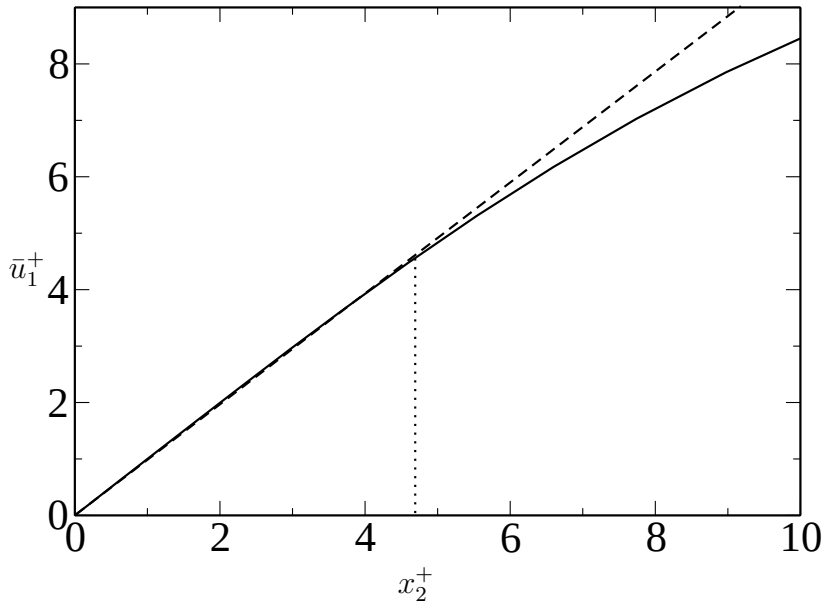

Figure 6.8: Close-up view of the mean velocity profiles from the plot 6.7.

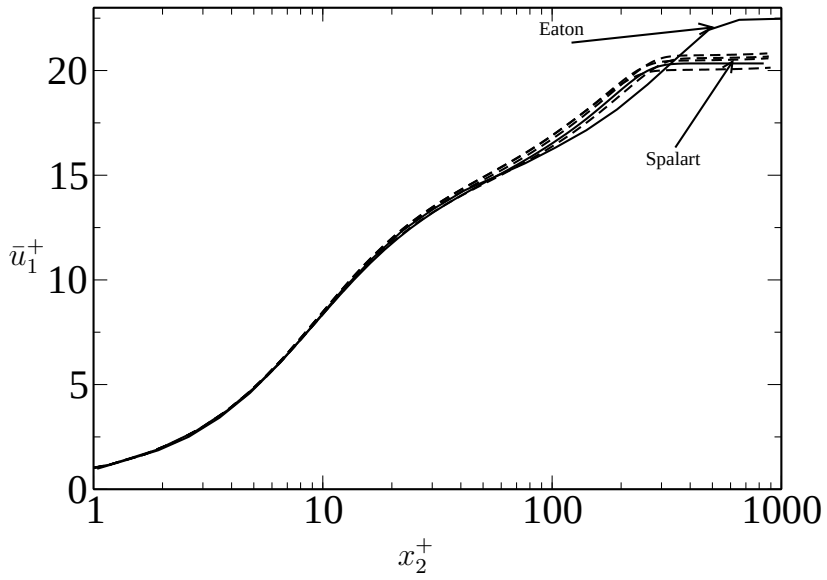

Figure 6.9: Mean velocity profiles —— correspond to Spalart's DNS ($Re_\theta = 670$) and Eaton's experiment ($Re_\theta = 1430$), - - - our DNS at different Reynolds numbers.

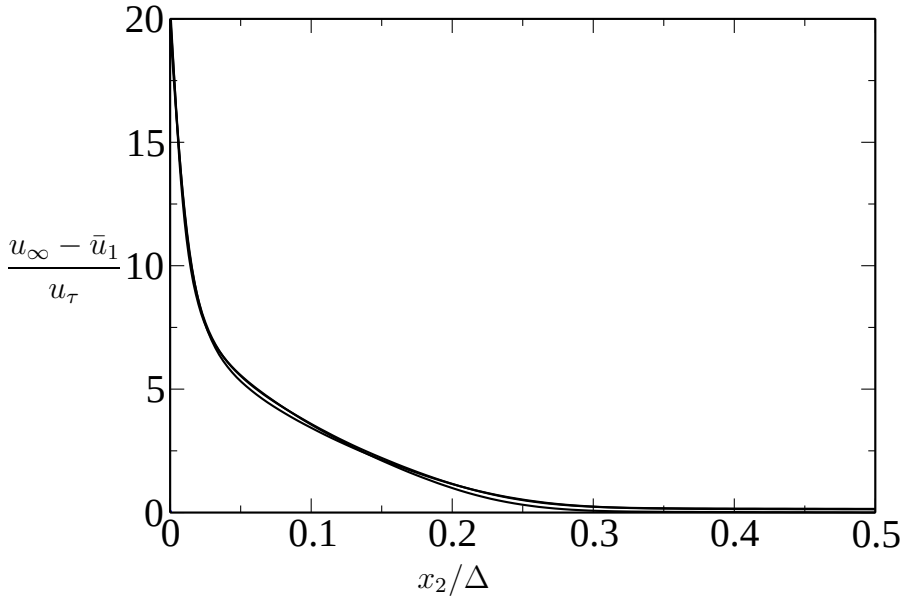

Figure 6.10: Mean velocity profiles in outer scaling for $Re_\theta = 540, 615, 690, 755$.

6.1.2 Instantaneous velocity and vorticity fields

Streamwise velocity fluctuations are shown in Figure 6.11 at the three different spanwise positions $x_3 = 5, 0, -5$. Two contours are plotted in each figure for two different levels $-0.5, 0.5$. Dashed contours correspond to the fluctuations with negative level. As one can see there is no symmetry in spanwise direction (real, 3D boundary layer simulation was performed, no statistics independence on the spanwise direction was taken into account during the simulation). In the figure very long streamwise streaks are observed. Near wall streak length is about $l_x \approx 400$ in plus units. In the upper plot (Figure 6.11) at the beginning of the box a coherent structure with negative value starts to develop at the wall, and increases in wall-normal direction up to $x_2^+ \approx 200$. In general for low Reynolds numbers, there are big structures in the flow.

Streamwise velocity fluctuations for two different levels -0.05 and 0.05 are presented in Figures 6.12 and 6.13 in x_1x_3 and x_2x_3 planes respectively. The figure 6.12 is homogeneously populated with positive and negative streaks of different length in streamwise direction ($l_x^+ \approx 580, 1015$). While in spanwise direction its thickness is $l_z^+ \approx 70$. l_x^+, l_z^+ are the size of streaks in streamwise and spanwise directions respectively.

Streamwise velocity fluctuations are shown in Figure 6.13 for the same parameters as in the two previous figures but in the x_2x_3 plane. The small positive valued

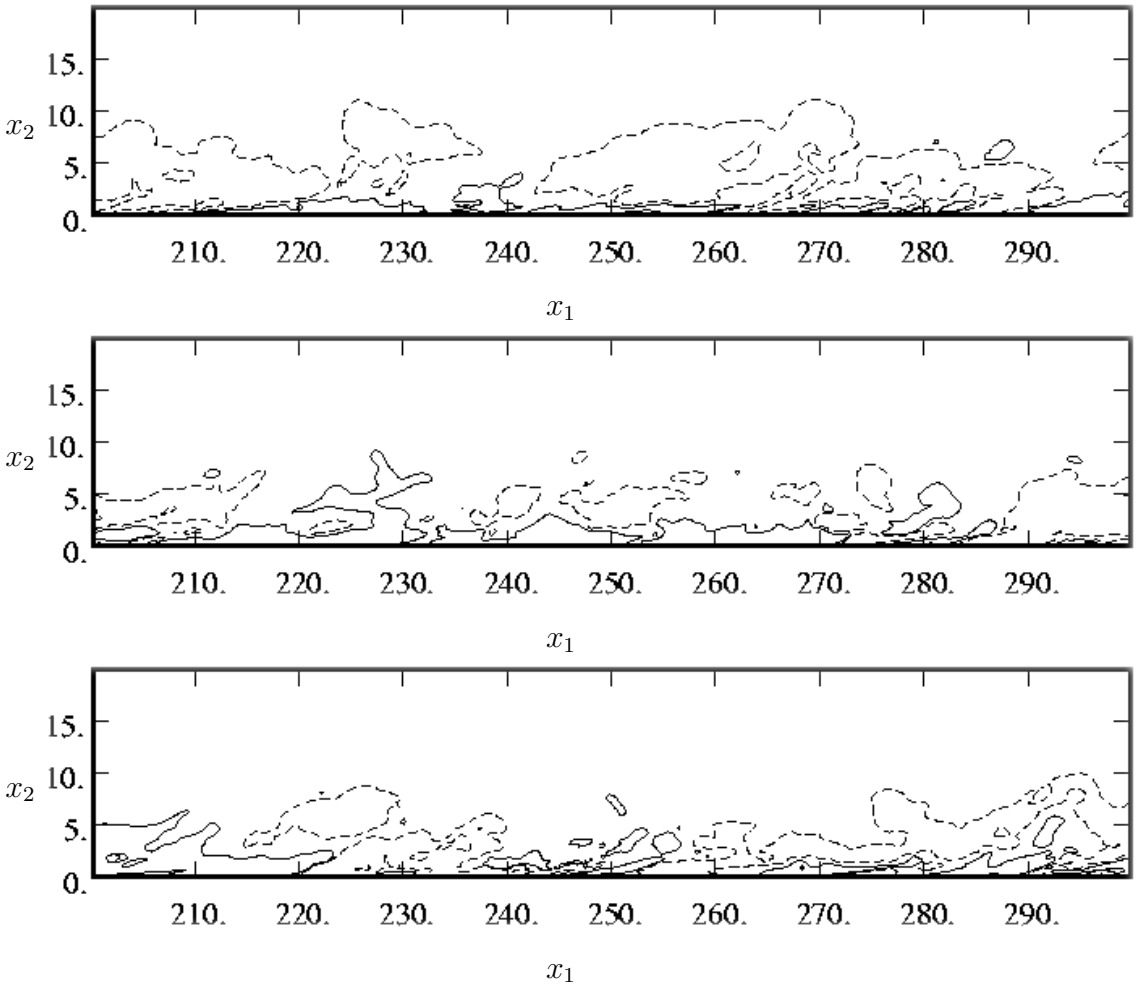

Figure 6.11: Streamwise velocity fluctuations in x_1x_2 plane; Levels of contours: -0.05 and 0.05 at different positions in spanwise direction at $x_3 = 5$ (top plot), $x_3 = 0$ (middle plot) and $x_3 = -5$ (bottom plot).

streaks are located near the wall with $l_x^+ \approx 80, 200$ and $l_y^+ \approx 30, 58$. Structures with negative value are large in comparison with the positive ones with $l_x^+ \approx 435; l_y^+ \approx 260$.

In Figures 6.14 and 6.15 streamwise and wall-normal components of vorticity are displayed in x_1x_3 plane. The vorticity levels were $\omega_x = 20$ and $\omega_y = -0.26, 0.28$. Long streamwise streaks are dominant (up to a length of ≈ 900 in plus units).

In Figure 6.16 isosurfaces of the wall-normal vorticity component are shown at values $\omega_y = -5.087, 5.111$. As it is observed from these figures, long streamwise

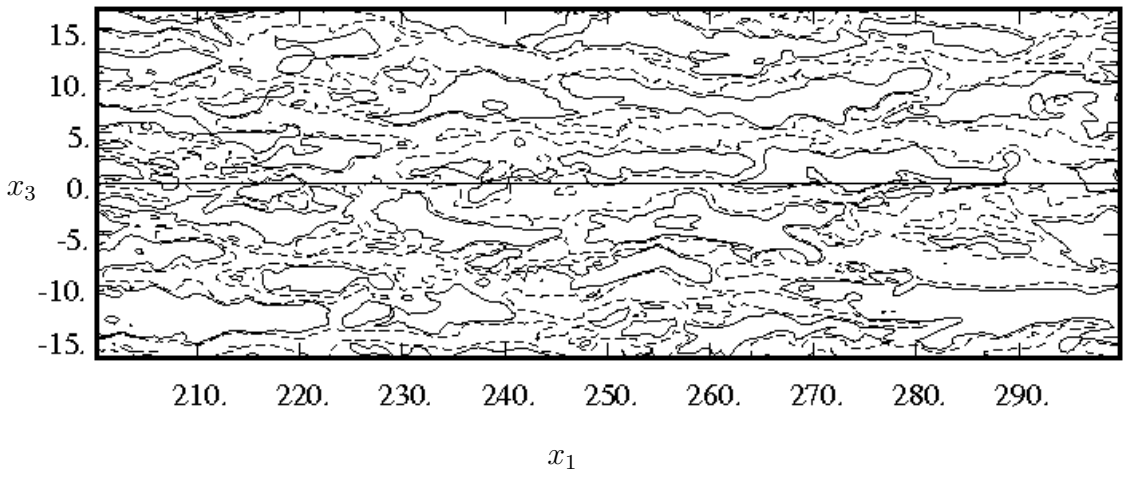

Figure 6.12: Streamwise velocity fluctuations are presented in x_1x_3 plane. Levels of contours: -0.05 and 0.05.

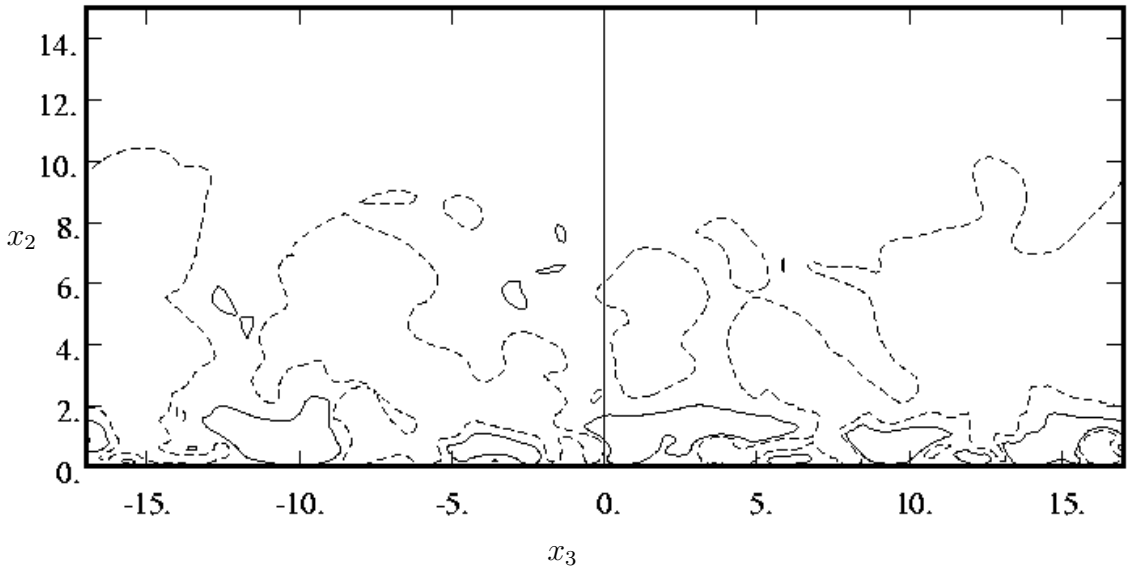

Figure 6.13: Streamwise velocity fluctuations are presented in x_2x_3 plane. Levels of contours: -0.05 and 0.05.

streaks are the common structures in the flow at the low Reynolds number.

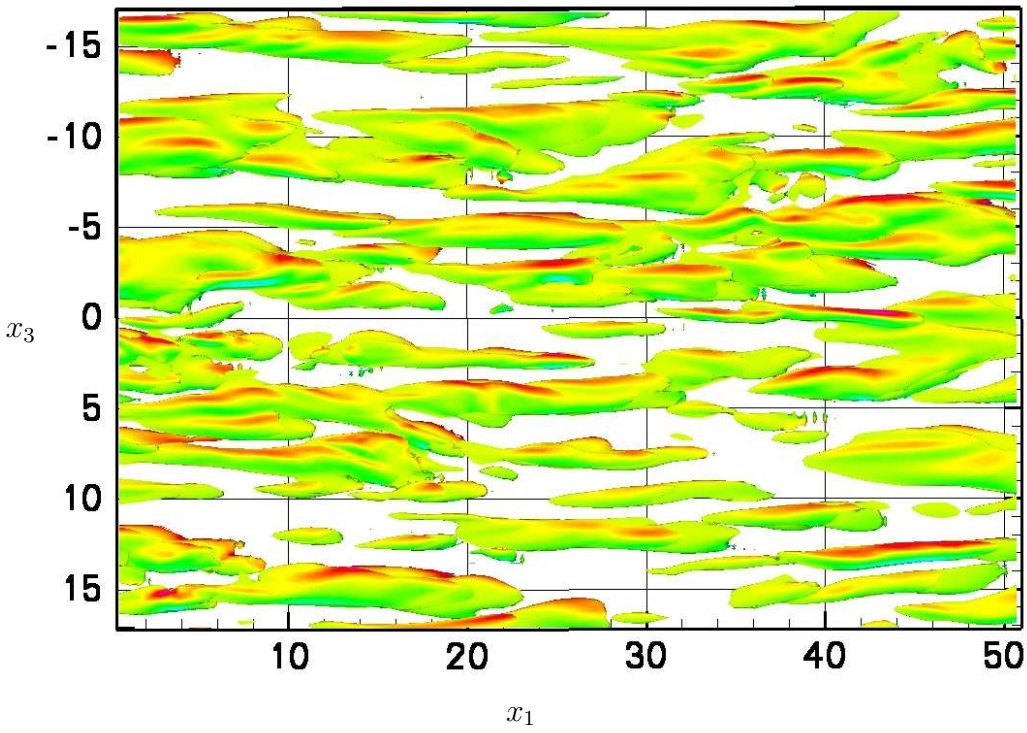

Figure 6.14: Streamwise component of vorticity in x_1x_3 plane.

6.2 Large box simulation

The simulations in this case were performed for two different number of grid points $1024 \times 513 \times 256$ and $2048 \times 513 \times 256$, simulations $DNS600d$ and DNS600e respectively, at the same Reynolds number as in the previous simulations (see Chapter 6). In the second case ($DNS600e$) the resolution in streamwise direction was doubled.

The simulations were run for a total of 1300 and 1700 time units (δ^*/u_∞). The useful region was confined to $100 - 800\delta^*|_{x=0}$ which corresponds to Re_{δ^*} from 870 to 2208 or Re_θ from 634 to 1500. The resolution in the streamwise and spanwise directions is: $\Delta x^+ \approx 24$ and $\Delta z^+ \approx 3.3$. As for the resolution in wall-normal direction it is $\Delta y^+ \approx 0.015 - 5$. The resolution in this case is coarser in the streamwise direction than in the other cases, but it is much finer in spanwise and wall-normal directions. Wall-normal direction is very important for the turbulent boundary layer flow. The non-dimensional timestep was chosen to be $\Delta t u_\infty/\delta^*|_{x=0} = 0.069$. In wall units this is $\Delta t u_\tau^2/\nu = 0.071$.

Figure 6.17 shows comparison of the rms of velocities for different grid. As it is

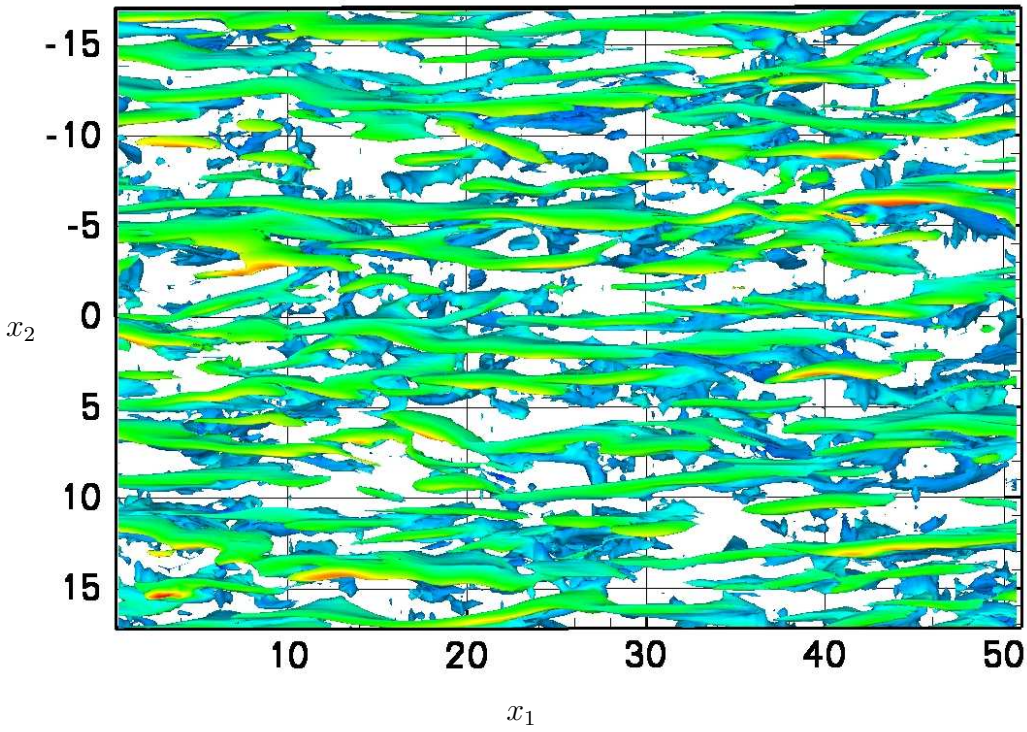

Figure 6.15: Wall-normal component of vorticity in x_1x_3 plane.

seen from this figure the resolution for the both cases is good. $u^+_{i,rms}$ show very little dependence on the number of grid points. We can state that the number of grid points from the simulation $DNS600d$ is enough to resolve the flow for this box and the Reynolds number. The longer box allows us to achieve a higher Reynolds number ($Re_\theta = 1500$) than in the smaller box simulation ($Re_\theta = 810$, see Section 6) with the same initial laminar Reynolds number. The aim for this simulation also was to check the dependence of the results of simulations on the box length in streamwise direction.

The shape factor H is shown in the Figures 6.18 and 6.19 vs. the Reynolds number based on momentum thickness. 6.19 shows a close up view of H. The first figure shows H in the full simulation box. In transition region, where the flow is not turbulent shape factor decreases very fast to the value, which is almost constant in the turbulent region. However, in the next figure (see 6.19) it changes in the range of $1.40 - 1.47$ in the turbulent region of the flow $Re_\theta = 750 - 1500$.

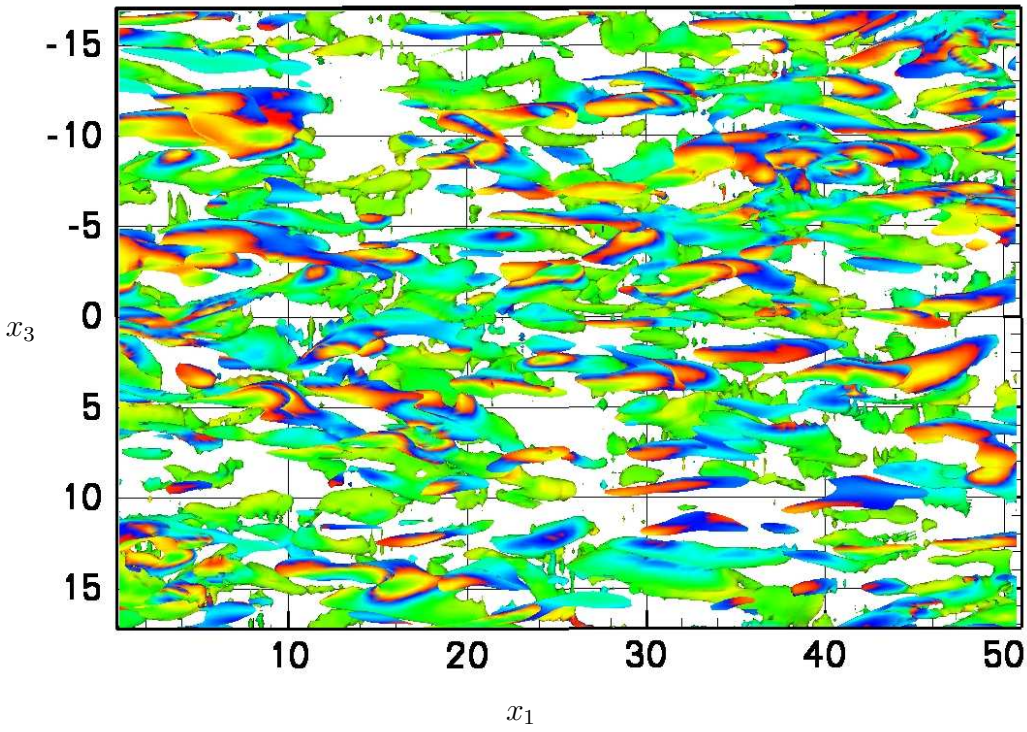

Figure 6.16: Spanwise vorticity component in the XZ plane.

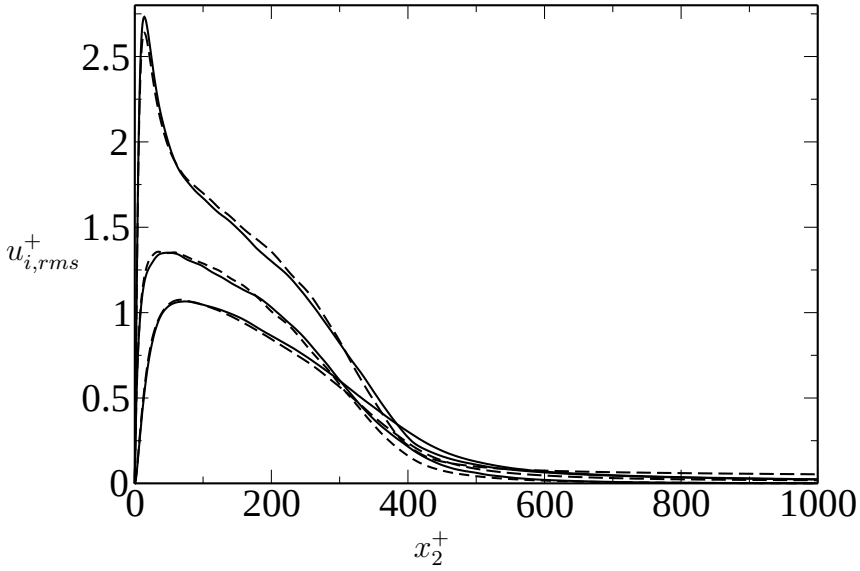

Figure 6.17: $u^+_{i,rms}$. —— $2048 \times 513 \times 256$ and - - - $2048 \times 513 \times 256$.

	Re_θ	Re_δ	u_∞/u_τ	$u_\tau \times 10^{-2}$	$c_f \times 10^{-3}$	θ	$\delta^\star$
100	634.6	872	18.71	5.37	5.71	1.05	1.44
200	754	1068	20.34	4.95	4.84	1.25	1.76
300	882	1262	21.09	4.78	4.50	1.46	2.08
400	1003	1444	21.5	4.69	4.32	1.66	2.39
500	1122	1620	22.1	4.56	4.09	1.85	2.69
600	1264	1827	22.58	4.47	3.92	2.09	3.02
700	1429	2085	22.99	4.40	3.78	2.36	3.44
800	1500	2208	24.22	4.18	3.40	2.47	3.64

Table 6.2: Flow parameters at different points in streamwise direction.

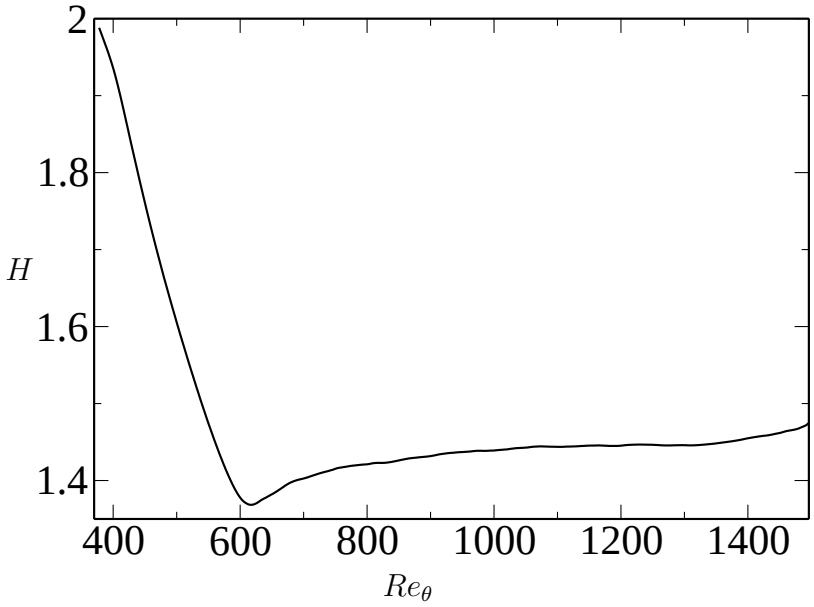

Figure 6.18: Shape factor H for the full simulation box.

6.2.1 Mean velocity profiles and flow structure

Mean velocity profiles in outer and inner scalings are shown in Figures 6.20 and 6.21 respectively. The velocities are plotted for different points in streamwise direction, corresponding to $Re_\theta = 754, 882, 1003, 1122, 1264, 1429, 1500$.

Instantaneous velocity fields (streamwise velocity fluctuations) are shown in Figures 6.22, 6.23, 6.24. The structure size in Figure 6.22 (bottom plot) is $l_x^+ \times l_y^+ \approx 500 \times 50$. In the upper plot the big structure is seen with the size in wall-normal direction approximately $l_y^+ \approx 250$.

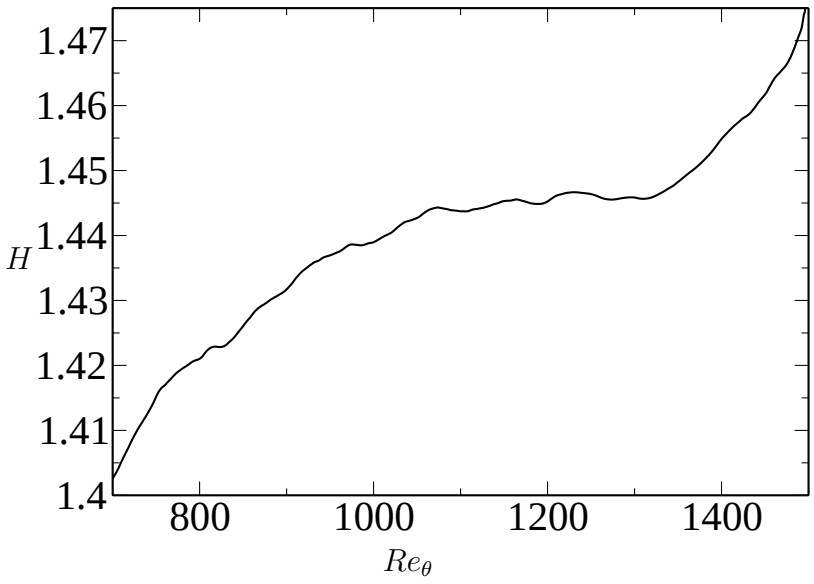

Figure 6.19: Shape factor H in the region with fully developed turbulence.

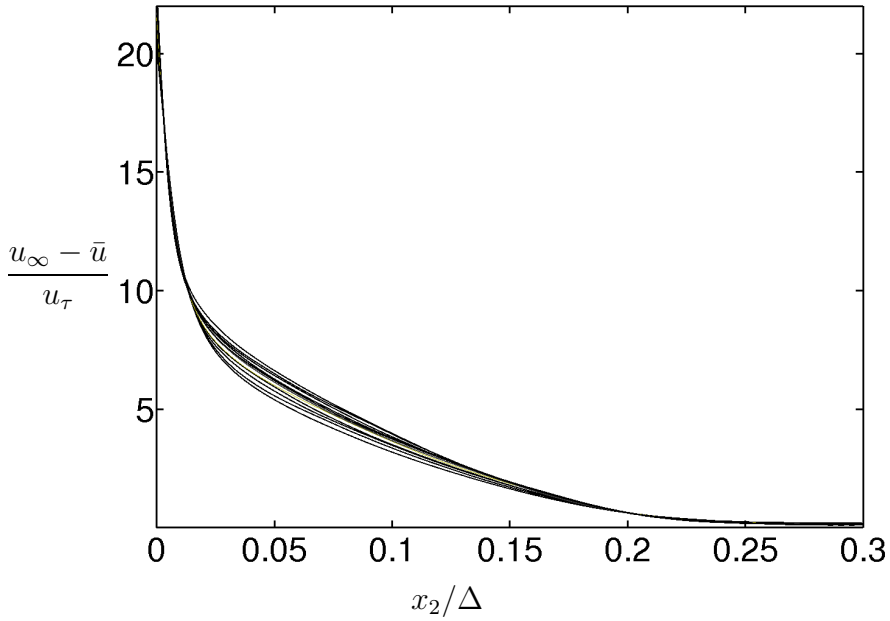

Figure 6.20: Mean velocity profiles in outer scalings at different points in streamwise direction with the corresponding Reynolds numbers: $Re_\theta = 754, 882, 1003, 1122, 1264, 1429, 1500$.

The Figures 6.23 and 6.24 show streamwise velocity fluctuations in x_1x_3 and x_2x_3

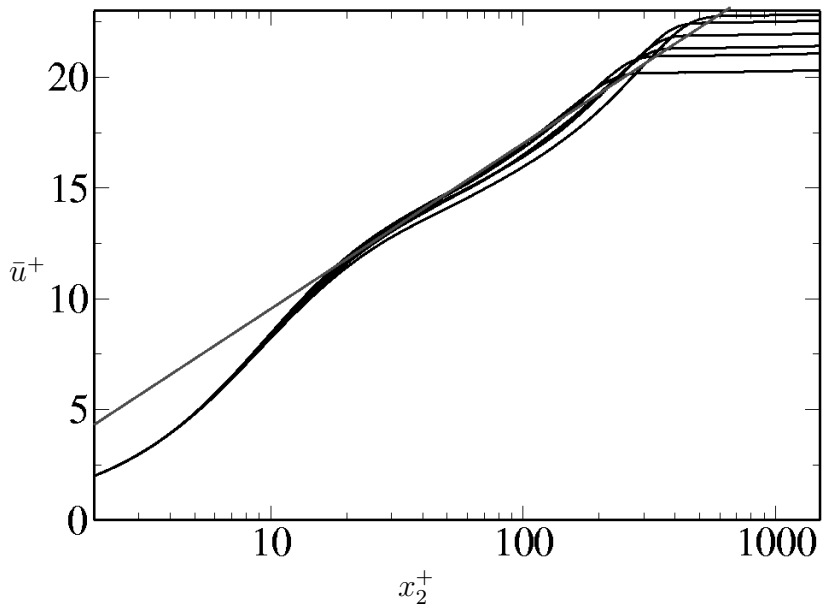

Figure 6.21: Mean velocity profiles in plus scalings at Reynolds numbers: $Re_\theta = 754, 882, 1003, 1122, 1264, 1429, 1500$.

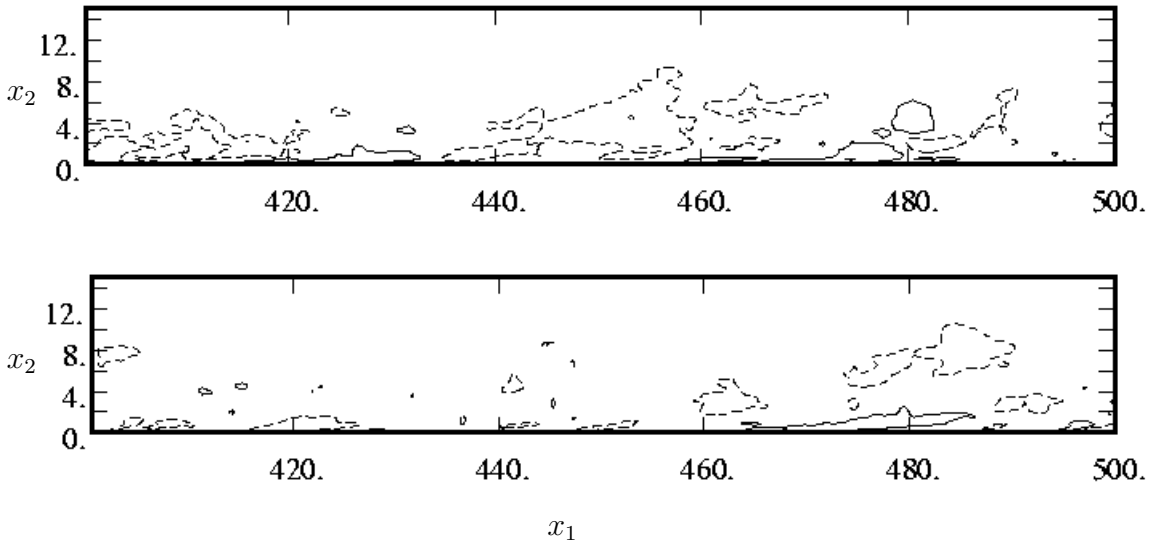

Figure 6.22: Streamwise velocity fluctuations in a plane x_1x_2. Levels of contours: --- -0.1 and —— 0.1. The sections are taken at $x_3 = -0.5, 0.5$ for upper and bottom plots respectively.

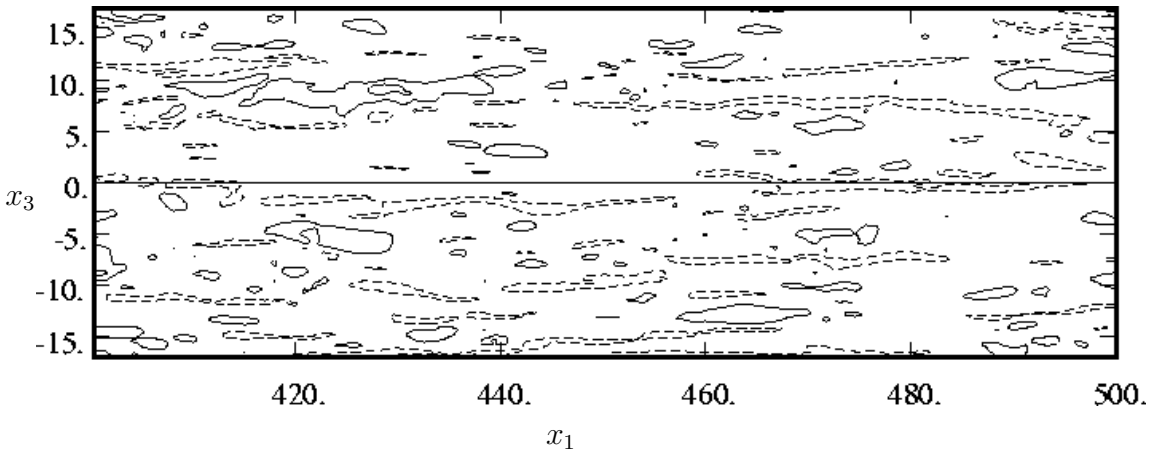

Figure 6.23: Streamwise velocity fluctuations in x_1x_3 at $x_2 = 0.3$. Levels of contours: --- -0.15 and — 0.15.

planes. In the left plot, very long, thin streaks are observed.

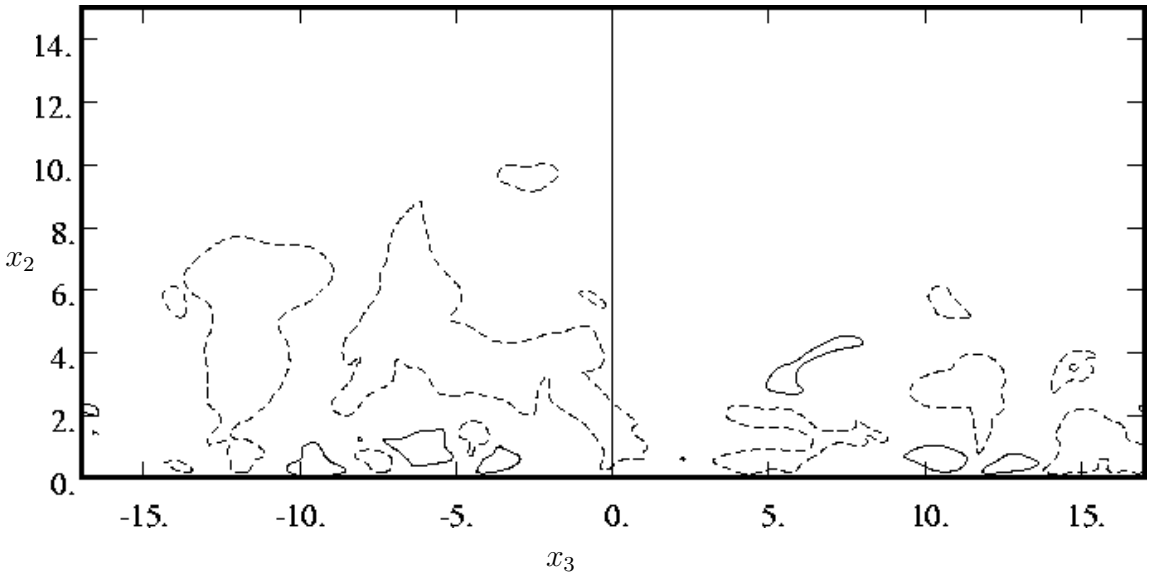

Figure 6.24: Streamwise velocity fluctuations x_2x_3 at $x = 500$ planes. Levels of contours: --- -0.15 and — 0.15.

Simulation in the case of long box ($DNS600d, e$) gives the same statistics as the simulations for smaller box ($DNS600a - c$). However, the turbulent Reynolds number achieved in this case is higher then in the simulations described in the previous section.

7 High Reynolds number case

7.1 Simulations at $Re_\theta = 2240$

For a Reynolds number of $Re_{\delta|_{x=0}} = 2000$ two simulations were performed with $N \approx 138.8$ and 231 million grid points. The basic simulation is the DNS with 138.9 million grid points ($DNS2000a, b$). The second one was done for an increased number of modes in the wall-normal direction, which is very important for the turbulent boundary layer flow.

Using equation 5.2 we can calculate the number of grid points for the bigger simulations assuming that $N_0 \approx 7.9 * 10^6$ was sufficient to resolve the flow for the low Reynolds number ($Re_{\delta^*} \approx 1100$) case. Thus, we have

$$N \approx N_0 \left(\frac{Re^1_{\delta^*}}{Re^0_{\delta^*}} \right)^{9/4} . \tag{7.1}$$

The simulations for the higher Reynolds number require large computational resources. The simulation in this case was run for $5500\delta^*/u_\infty$ time units. The statistical averaging was performed during the last 4000 time units. To obtain the statistics more than 120 CPU days of were needed using 32 CPUs of IBM computer, Regatta-H, while for the low Reynolds number case ($Re_\theta = 750$), the simulation was done in 25 CPU days.

The useful region was confined to $100 - 350\delta^*|_{x=0}$ (total length of computational box is $450\delta^*|_{x=0}$) which corresponds to Re_{δ^*} ranging from 1957 to 3240 or Re_θ

	Re_θ	Re_δ	u_∞/u_τ	$u_\tau \times 10^{-2}$	Δ	$c_f \times 10^{-3}$	θ	$\delta^\star$
100	1476	1957	20.94	4.77	20.47	4.56	0.73	0.98
150	1671	2233	21.70	4.62	24.19	4.24	0.83	1.11
200	1869	2517	22.35	4.48	28.06	4.00	0.93	1.25
250	2062	2794	22.76	4.40	31.69	3.85	1.03	1.39
300	2240	3051	23.21	4.32	35.26	3.70	1.12	1.52
350	2374	3241	23.46	4.29	37.78	3.63	1.18	1.61

Table 7.1: Flow parameters at $Re_\theta = 2240$.

from 1476 to 2374. The resolution in plus units was $\Delta x^+ \approx 15$, $\Delta z^+ \approx 11$ and $\Delta y^+ \approx 0.13 - 18$.

7.1.1 Mean velocity profiles

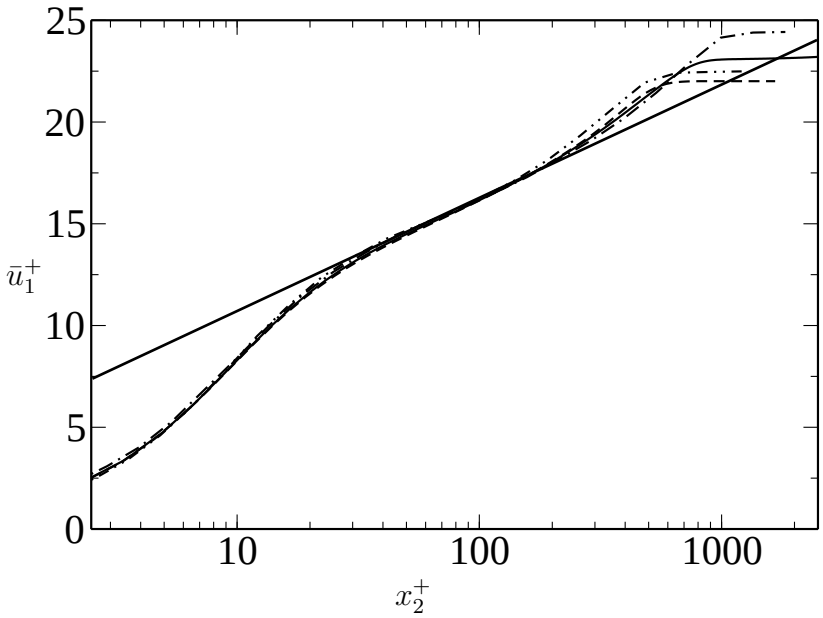

Figure 7.1: $\bar{u}_1^+$ in inner scaling. —— $Re_\theta = 2240$, - - - Spalart's DNS at $Re_\theta = 1410$, —·— $Re_\theta = 1430$, —··— $Re_\theta = 2900$ (DeGraaff & Eaton (2000)), straight line corresponds to the log-law.

As it was mentioned in the introduction the logarithmic law of the wall is one of the most celebrated analytical results in turbulence theory. However, in recent years, doubts about its validity begun to appear in the literature (see for example the papers of Barenblatt & Prostokishin (2000), George & Castillo (1997) and Zagarola et al. (1997)). It is very important to perform experiments and DNS on turbulent boundary layer flow in order to check the validity of the law. DeGraaff & Eaton (2000) measured Reynolds stresses and mean velocity profiles for a flat-plate turbulent boundary layer for different Reynolds numbers using a high-resolution laser-Doppler anemometer. They concluded that the log-law provides a reasonably accurate universal profile for the mean velocity. Österlund et al. (2000a) performed two independent experimental studies of turbulent boundary layer flow with increasing Reynolds number and came to the same conclusion.

The Reynolds number in the presented simulation is considerably higher then the highest Reynolds number in Spalart's DNS (Spalart 1988). The results from

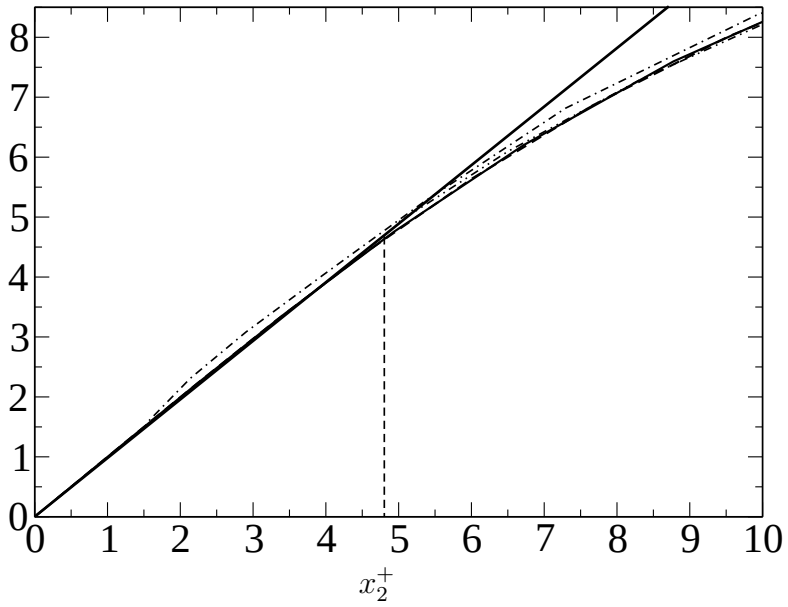

Figure 7.2: close up view of the mean velocity profiles from the Figure 7.1. — straight line corresponds to the linear law near the wall.

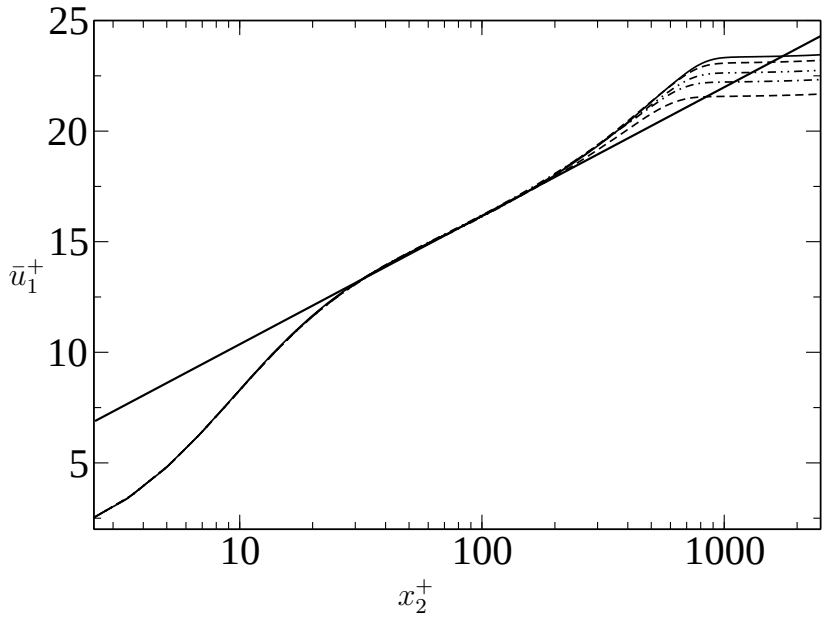

Figure 7.3: $\bar{u}_1^+$ in inner scalings for $Re_\theta = 1670, 1870, 2060, 2240, 2370$.

our DNS are compared to the experimental data (DeGraaff & Eaton 2000) and Spalart's DNS data. Mean velocity profiles in inner scalings are shown in Figures

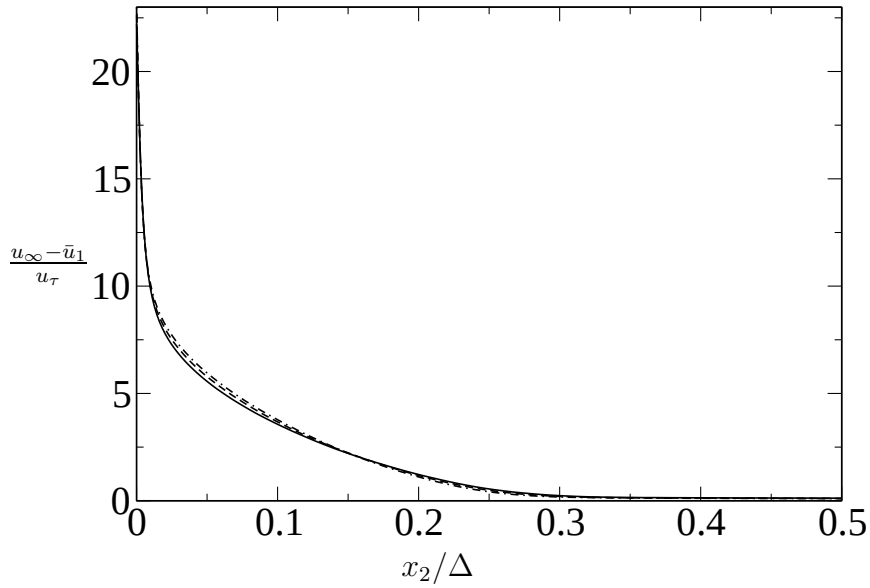

Figure 7.4: Mean velocity profiles near the wall in outer scaling at $Re_\theta = 1670, 1870, 2060, 2240, 2370$.

7.1 and 7.2 for $Re_\theta = 1430, 2900$ (experiments performed by DeGraaff & Eaton (2000)) and $Re_\theta = 1410, 2240$ (Spalart's and our DNS respectively). The straight line corresponds to the logarithmic law of the wall. Good agreement with the algebraic law is observed up to $x_2^+ = 5$. To find a self-similar profile, the boundary layer must be divided in inner and outer regions, where different scalings should be used to collapse the mean velocity properly. Outer scaling depends on the global properties of the boundary layer flow. Here the Rotta-Clauser length scale is used for scaling of this region. Figures 7.3 and 7.4 show mean velocity profiles in inner and outer scaling respectively for different Reynolds numbers measured within the streamwise directions of simulation box ($Re_\theta = 1670, 1870, 2060, 2240, 2370$). Figure 7.4 shows very good collapse of velocity profiles measured at different points in streamwise direction.

7.1.2 Flow structures

The flow structures in turbulent boundary layer flow for different Reynolds numbers are quite different (see for comparison Figures 6.11 and 7.5). In Figure 7.5 streamwise velocity fluctuations are shown for two levels: $-0.5, 0.5$. Structures in comparison to the low Reynolds number simulations are smaller in size. More fine structures are also observed in the Figures 7.6 and 7.7 in physical space.

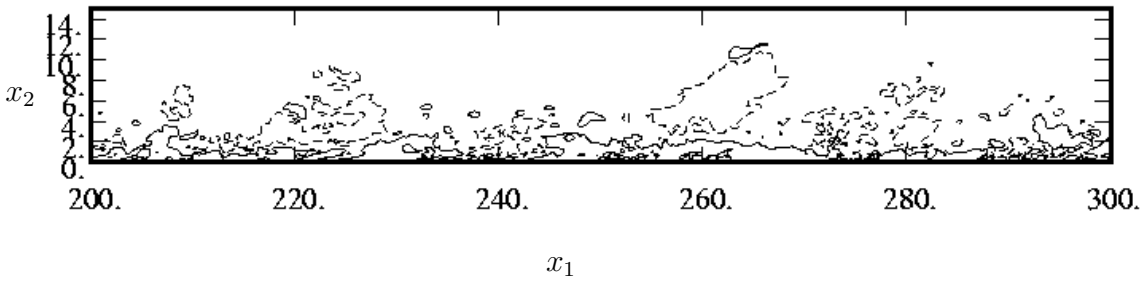

Figure 7.5: Streamwise velocity fluctuations in a plane x_1x_2. Levels of contours: -0.05 and 0.05.

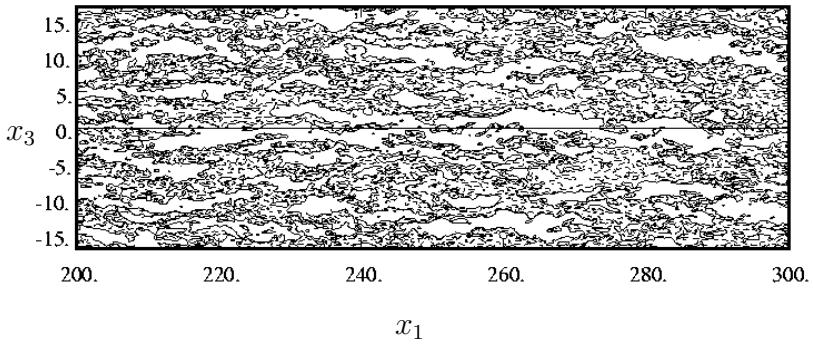

Figure 7.6: Streamwise velocity fluctuations in x_1x_3. Levels of contours: -0.05 and 0.05.

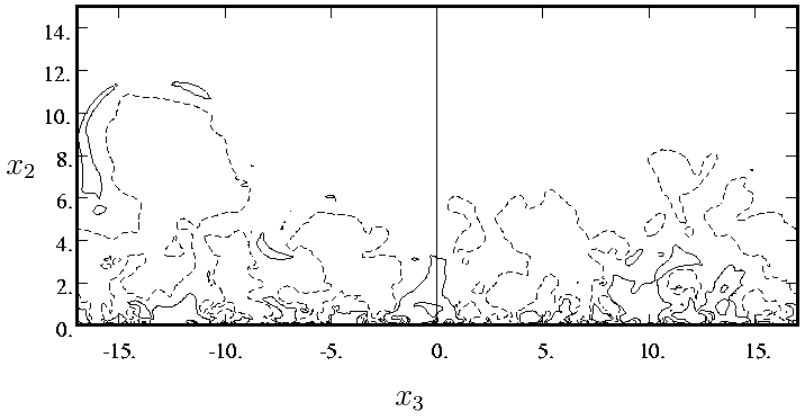

Figure 7.7: Streamwise velocity fluctuations x_2x_3 planes. Levels of contours: -0.05 and 0.05.

Streamwise, wall-normal and spanwise components of vorticity are shown in Figures 7.8, 7.9 and 7.10 respectively.

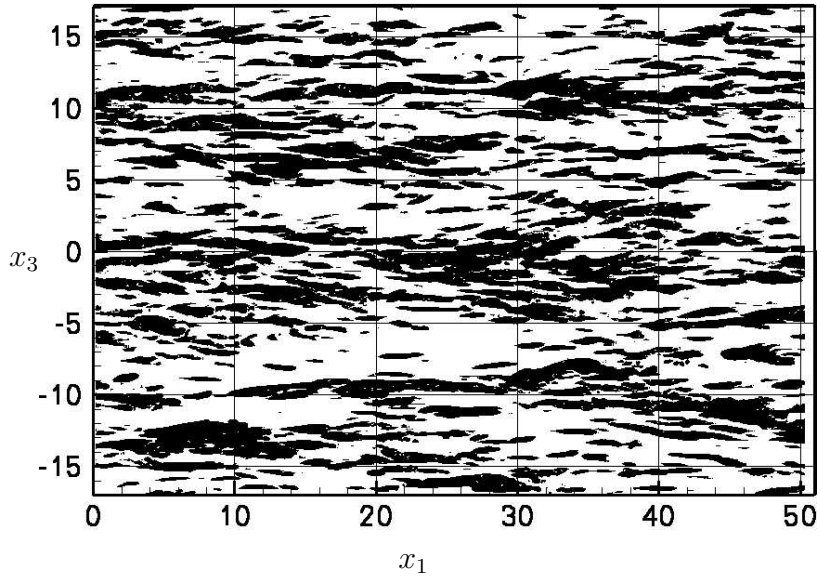

Figure 7.8: Streamwise vorticity component (ω_x) fluctuations in x_1x_3 plane.

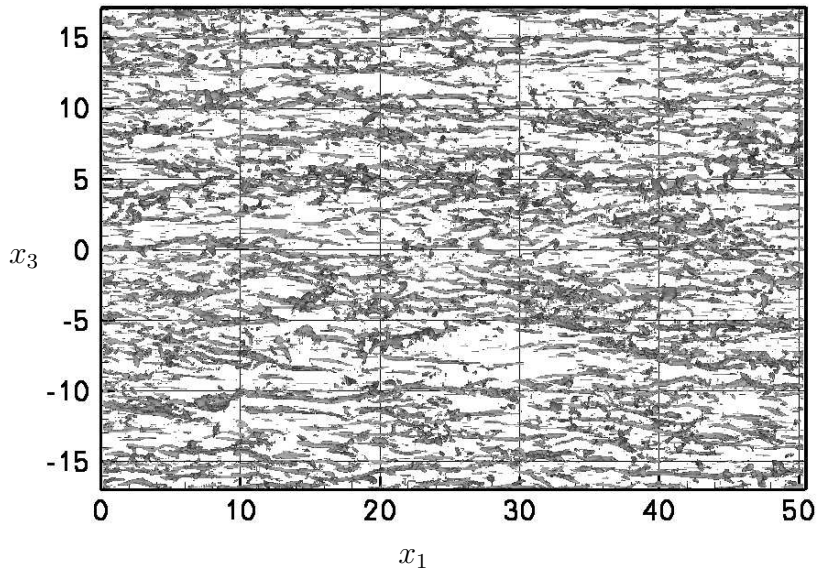

Figure 7.9: Wall-normal vorticity component (ω_y) fluctuations in x_1x_3 plane.

As it is observed from these figures, the structures in the boundary layer decreases

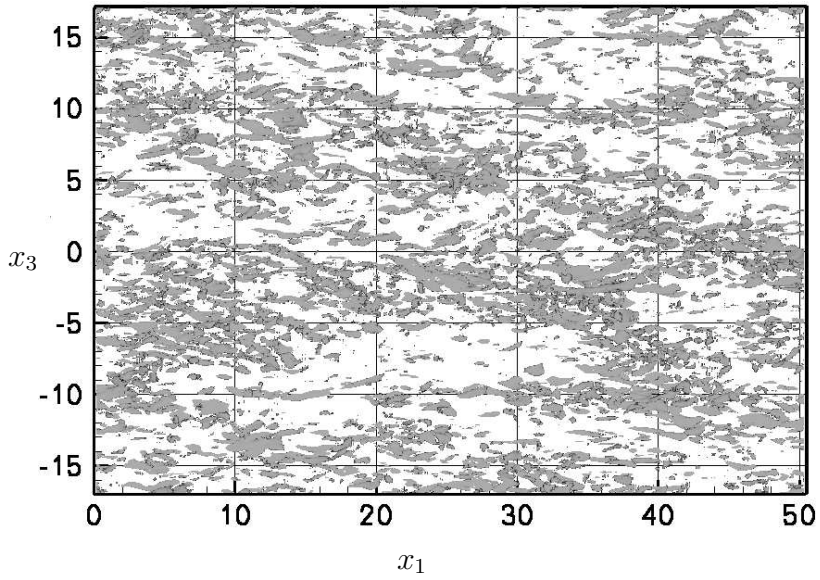

Figure 7.10: Spanwise vorticity fluctuations (ω_z) in a plane x_1x_3.

at high Reynolds number in comparison to the low Reynolds number case. More detailed discussion of the coherent structures will be given in Chapter 11.

7.2 Simulations at $Re_\theta = 2500$

DNS for Reynolds number $Re_\theta = 2500$ was done with $N \approx 270$ million grid points ($2048 \times 513 \times 256$) in a box of size $450 \times 30 \times 34$. The job was run on the Hitachi supercomputer in Munich (MPI version of the code), on 256 processors. The memory usage was $\approx 252GB$. The file of statistics which accumulates 42 physical mean variables was more then $350MB$ each simulation run. For every simulation we were getting about 30 time units. That means that we needed nearly one year to get a more or less smooth statistics. The resolution in streamwise and spanwise

$\times$	Re_θ	Re_δ	u_∞/u_τ	$u_\tau \times 10^{-2}$	θ	$\delta^\star$
100	1570	2121	21.03	4.74	0.63	0.85
150	1824	2469	21.83	4.57	0.73	0.99
200	2070	2816	22.43	4.46	0.83	1.13
250	2301	3146	23.05	4.34	0.92	1.26
300	2500	3401	23.30	4.30	0.99	1.36

Table 7.2: Flow parameters at $Re_\theta = 2500$.

directions is: $\Delta x_1^+ \approx 23$ and $\Delta x_3^+ \approx 10$. As for the resolution in wall-normal direction it is $\Delta x_2^+ \approx 0.03 - 6$. The non-dimensional timestep has been chosen to $\Delta t U_\infty/\delta^*|_{x=0} = 0.07$. In wall units this is $\Delta t u_\tau^2/\nu = 0.3$.

The logarithmic skin friction law has a form (Österlund et al. 2000a):

$$c_f = 2\left[\frac{1}{\kappa} ln(Re_\theta + C)\right]^{-2}. \tag{7.2}$$

The skin friction coefficient is compared to its analytic expression (see equation (7.2)) in Figure 7.11.

The shape factor H is displayed in Figures 7.12 and 7.13.

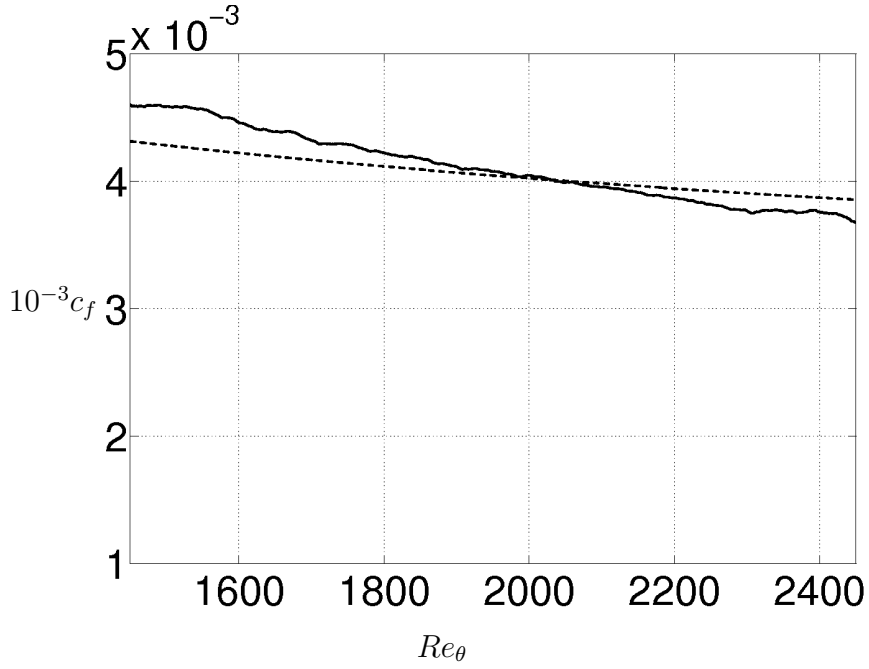

Figure 7.11: Friction coefficient c_f. --- Logarithmic skin friction law (equation (7.2)), —— DNS data.

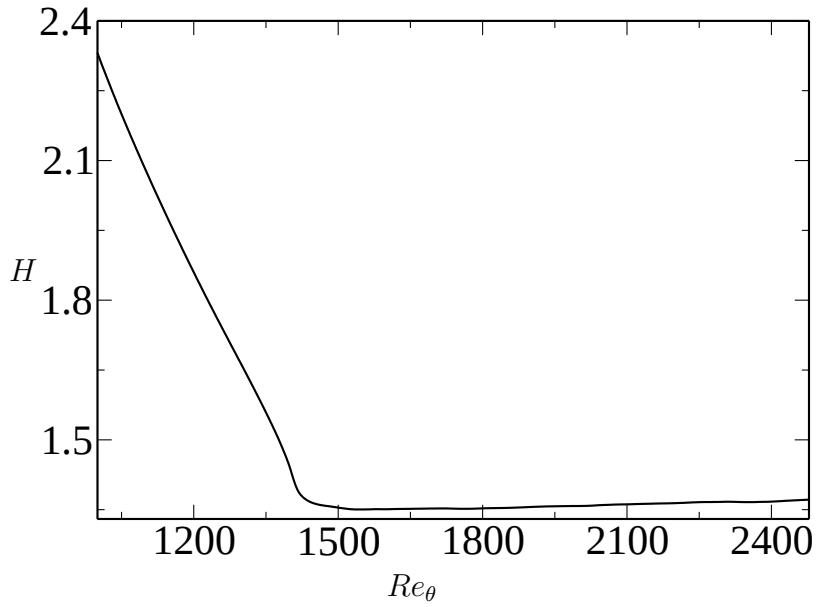

Figure 7.12: Shape factor H.

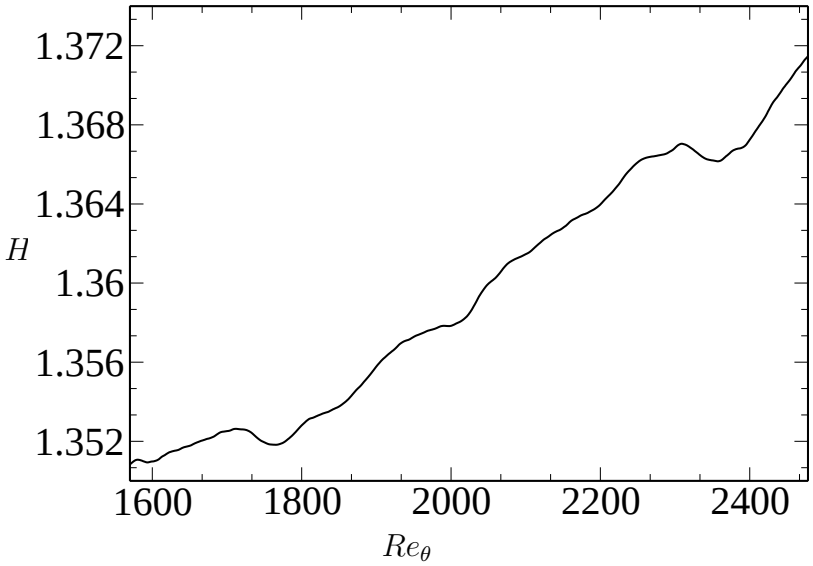

Figure 7.13: Shape factor H.

7.2.1 Mean velocity profiles

Mean velocity profiles in plus units are shown in Figure 7.14 for different points within the simulation box that corresponds to different Reynolds numbers: $Re_\theta = 1570, 1825, 2070, 2300, 2500$. As we see the mean velocity profiles show good col-

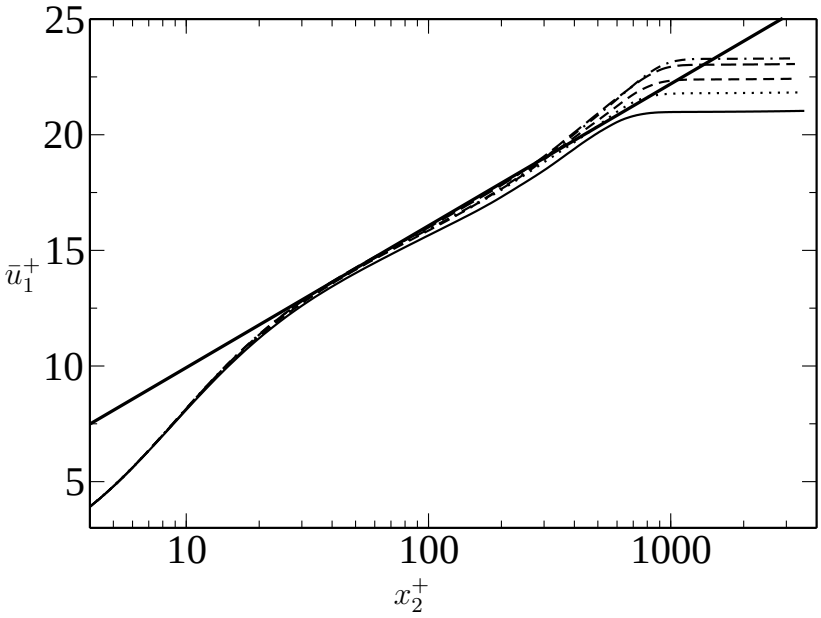

Figure 7.14: Mean velocity profiles in plus units at $Re_\theta = 2500$. Velocity profiles are taken in different points of the simulation box ($Re_\theta = 1570, 1825, 2070, 2300, 2500$).

lapse in plus units in the log region calculated in different points in streamwise directions. A small deviation is observed with the velocity profile measured in the beginning of the simulation box, at $x_1 = 100$ with Reynolds number $Re_\theta = 1570$.

Mean velocity profiles near the wall-region are shown in Figures 7.15 and 7.16. The linear law of the wall is satisfied up to $x_2 \approx 4.5$. The dashed line corresponds to the data from KTH experiments with $Re_\theta = 2513$.

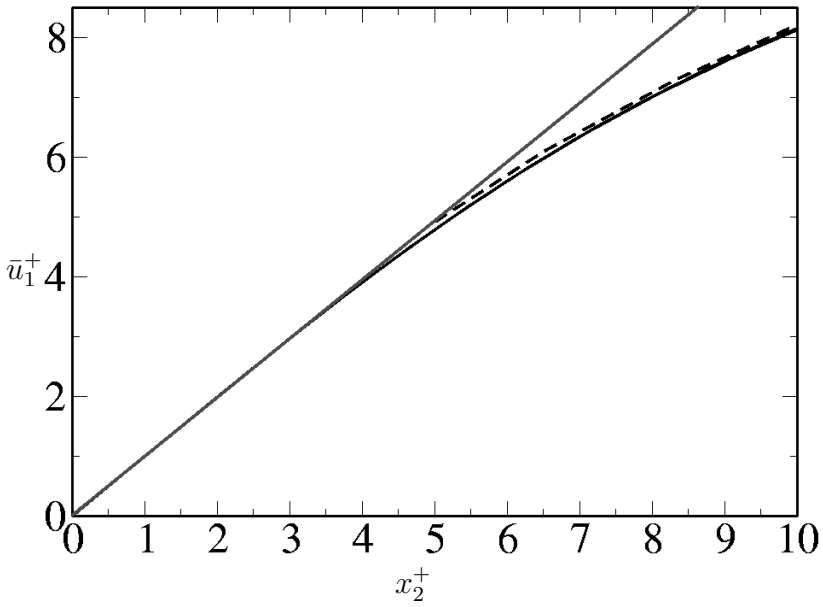

Figure 7.15: Mean velocity profiles in plus units at $Re_\theta = 2500$ near-wall region. --- line corresponds to the data from KTH experiments with $Re_\theta = 2500$.

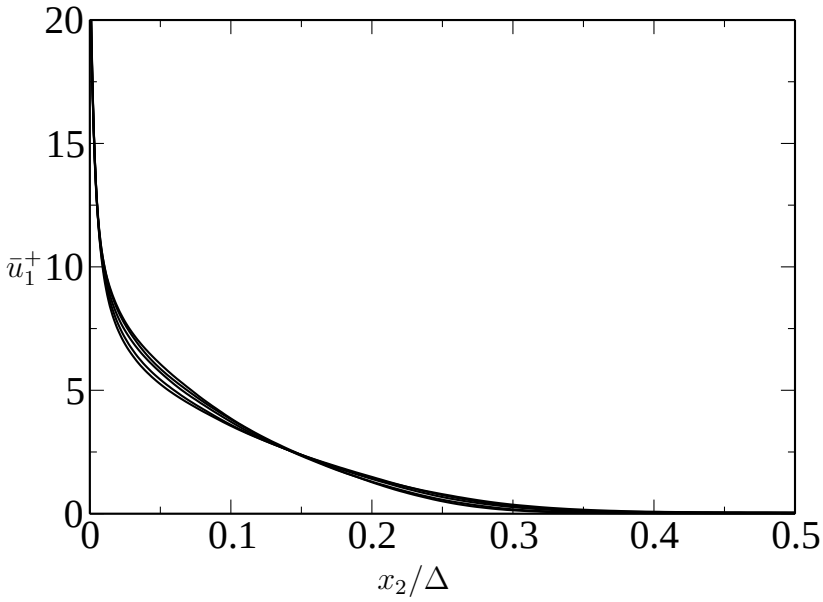

Figure 7.16: Mean velocity profiles at the same parameters as in Figure 7.15, but in outer scaling.

7.2.2 Flow structures

In this section we present instantaneous streamwise velocity fluctuations in different planes. In Figure 7.17 we display velocity contours at two different levels

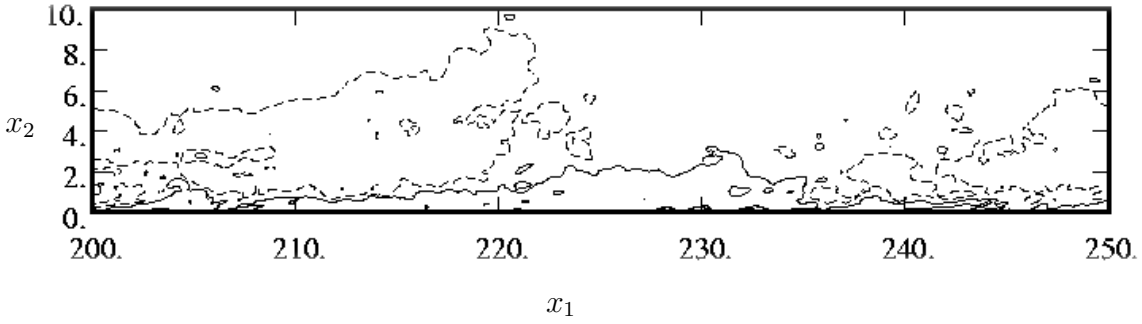

Figure 7.17: Streamwise velocity fluctuations in a plane x_1x_2. Levels of contours: -0.275 and 0.375.

$-0.275, 0.375$. The contour with the positive level is allocated near the wall with a length of $l_x^+ \approx 3250$, very long structure which increases in wall-normal direction.

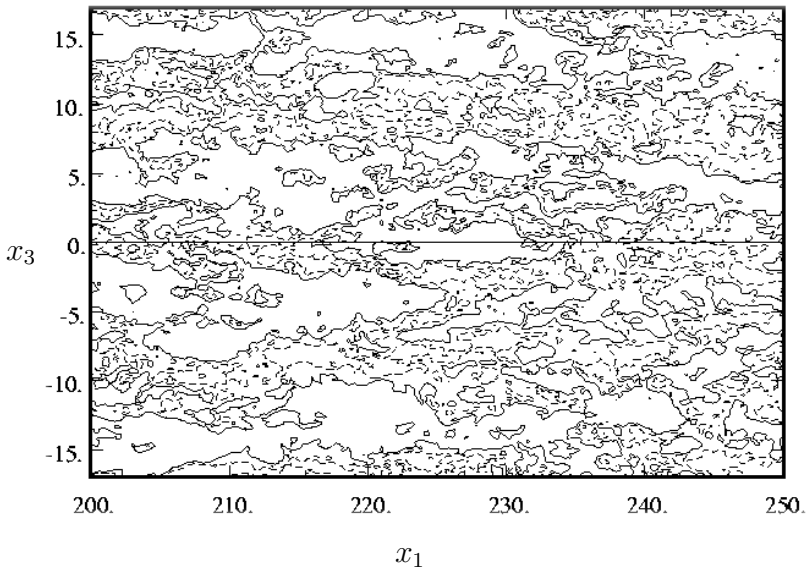

Figure 7.18: Streamwise velocity fluctuations in x_1x_3. Levels of contours: -0.175 and 0.575.

With the same parameters but in x_1x_3 and x_2x_3 planes the streamwise velocity fluctuations are presented in Figures 7.18 and 7.19. Near the wall smaller structures with positive value are dominant in the flow (right plot). The size of one of

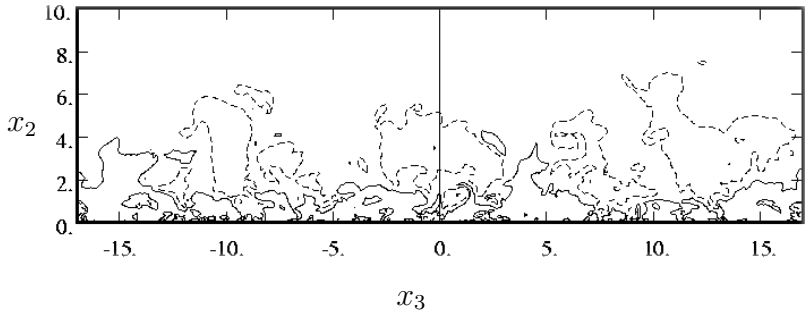

Figure 7.19: Streamwise velocity fluctuations in x_2x_3, levels of contours: -0.23 and 0.43).

such a structure is $l_z^+ \approx 590$ in spanwise direction. In the wall normal direction the bigger coherent structures start nearly in the region of $x_2^+ = 100$. The extension in this direction is more then $l_y^+ = 500$. These structures have nearly the same size in spanwise and wall-normal directions.

ω_x, ω_y and ω_z are shown in Figures 7.20, 7.21 and 7.22. The isosurfaces were plotted for nearly equal levels (negative and positive ones). In this case with higher Reynolds number the size of vorticity structures is much smaller in the physical space.

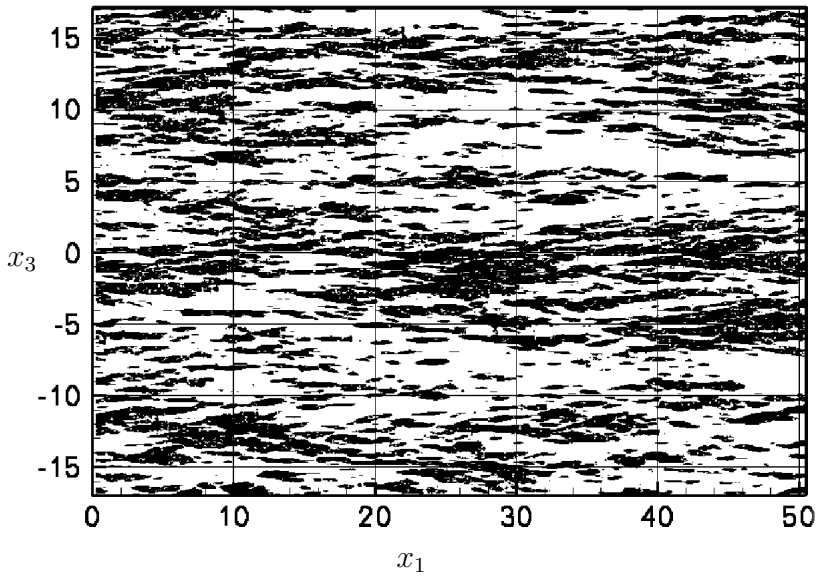

Figure 7.20: Streamwise component of vorticity (ω_x) in x_1x_3-plane at $Re_\theta = 2500$.

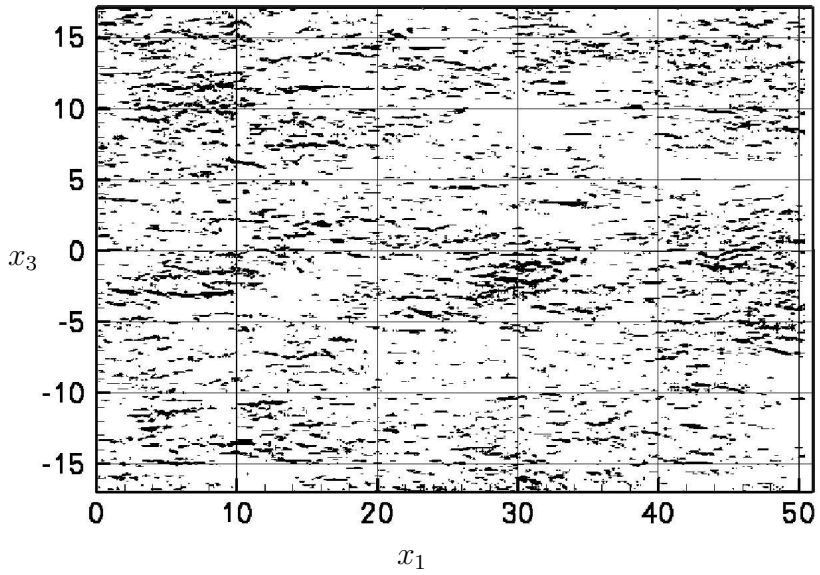

Figure 7.21: Wall-normal component of vorticity (ω_y) in x_1x_3-plane at $Re_\theta = 2500$.

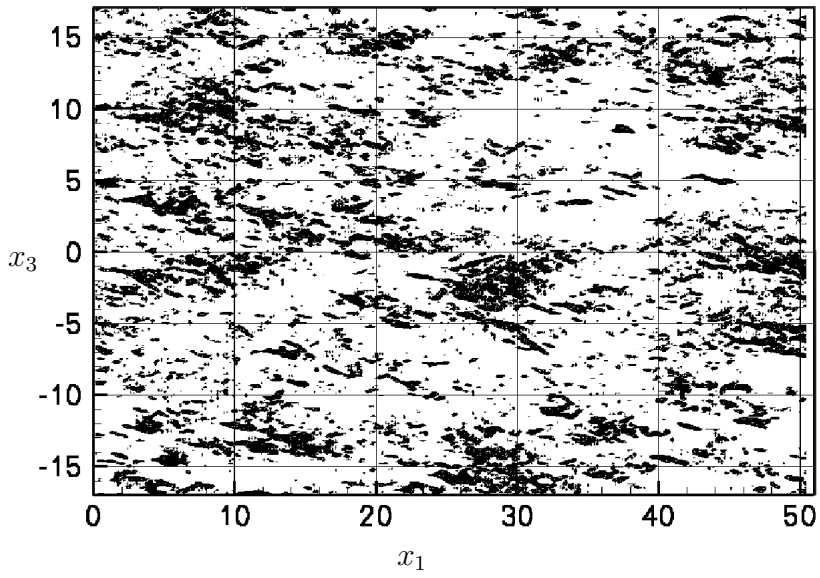

Figure 7.22: Vorticity fluctuations (ω_z) in a plane x_1x_3 at $Re_\theta = 2500$.

The aim of this part was to show the parameters of the simulations done for different Reynolds number cases. Mean velocity profiles and instantaneous velocity and vorticity fields were compared to each other for the different cases. More detailed discussion about the velocity and vorticity fields will be given in the Chapter 11. DNS at the different Reynolds numbers were done for the different numbers of grid

points. Exception from this rule was the last simulation ($DNS2500$), which was very computer time and resources consuming. In this case only one simulation was done. However, number of grid points for this case was estimated from the experience based on the previous simulations.

Part III

Statistics

8 Low Reynolds number case

8.1 Small box simulations

In this chapter the statistics of the simulation performed for the Reynolds number $Re_\theta = 810$ (simulations $DNS600a - d$) is represented. DNS results for two different simulations boxes are discussed and compared to each other: $450 \times 30 \times 34$ ($DNS600a - c$) and $1000 \times 60 \times 34$ ($DNS600d, e$).

8.1.1 One-point statistics

Fluid dynamic fields of velocity, pressure, temperature and etc. in a turbulent flow are so complex in structure that it is practically impossible to describe them individually. The knowledge of every detail of the very irregular individual flow is never required for any application, and it is the mean characteristics which are of interest. The most important, and at the same time, the simplest statistical characteristics of random fluid dynamic fields are their mean values. The mean values of the fluid dynamic variables generally are very smooth and slowly varying.

Reynolds normal stresses

First of all we compare our DNS results ($Re_\theta = 755$) to Spalart's at comparable Reynolds number ($Re_\theta = 670$). Figure 8.1 shows streamwise Reynolds normal stresses from DNS data. The peak value of $\overline{u_1 u_1}^+$ for our DNS is bigger than in Spalart's DNS. The location of the peak is the same in both cases.

The streamwise Reynolds stresses in plus and outer units are shown in Figure 8.2 for different Reynolds numbers measured in different points of the simulation box. In the paper of Klewicki, Murray & Falco (1994) the authors found an empirical fit for the peak magnitude of $\overline{u_1 u_1}$:

$$\overline{u_1 u_1}^+_{max} = 8.5 \times 10^{-9} Re_\theta^2 + 4.8 \times 10^{-4} Re_\theta + 6.86, \tag{8.1}$$

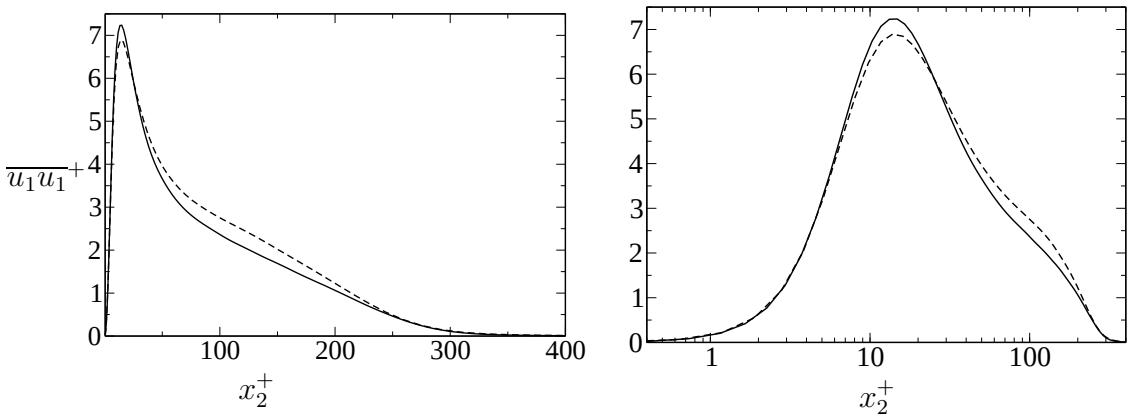

Figure 8.1: Streamwise Reynolds stresses for $Re_\theta = 755$ from our DNS (——) and $Re_\theta = 670$ from Spalart's DNS (---) in plus units for linear and linear-log axes.

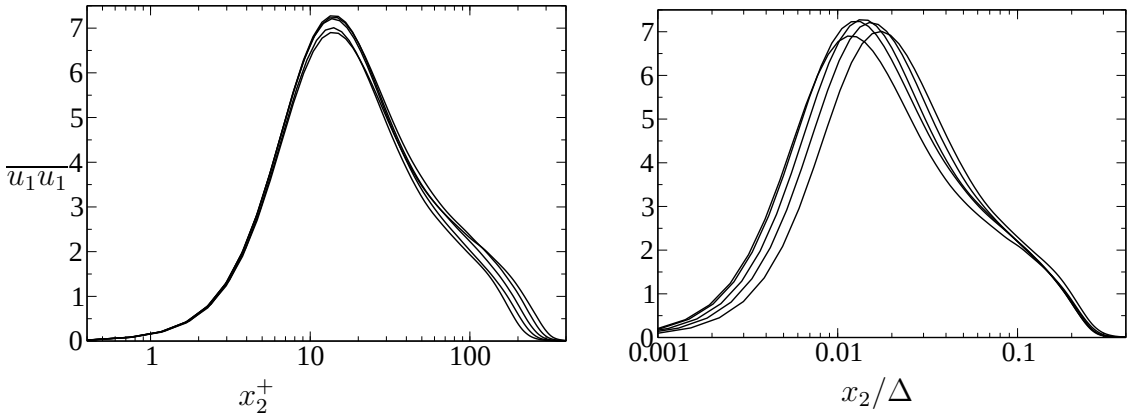

Figure 8.2: Streamwise Reynolds stresses for $Re_\theta = 470, 540, 615, 755$ from our DNS in plus and outer scalings.

In our DNS for Reynolds number $Re_\theta = 755$, the maximum and its location are the following $\overline{u_1u_1}_{max} = 7.233$ and $y^+_{max} = 14.7$. From the Equation 8.1 for this Reynolds number one gets: $\overline{u_1u_1}_{max} = 7.227$ that is very close to the DNS data. As for the peak location value Mochizuki & Nieuwstadt (1996) found the following equation:

$$y^+_{peak} = 1.7 \times 10^{-4} Re_\theta + 14.4 \tag{8.2}$$

From this equation we have: $y^+_{max} = 14.52$.

DeGraaff & Eaton (2000) introduced mixed scalings for the streamwise component of the stress tensor ($\overline{u_1u_1}/u_\tau \bar{u}_\infty$). Figure 8.3 shows streamwise Reynolds stresses in their scaling for the same parameter as in the previous figure. We see that the

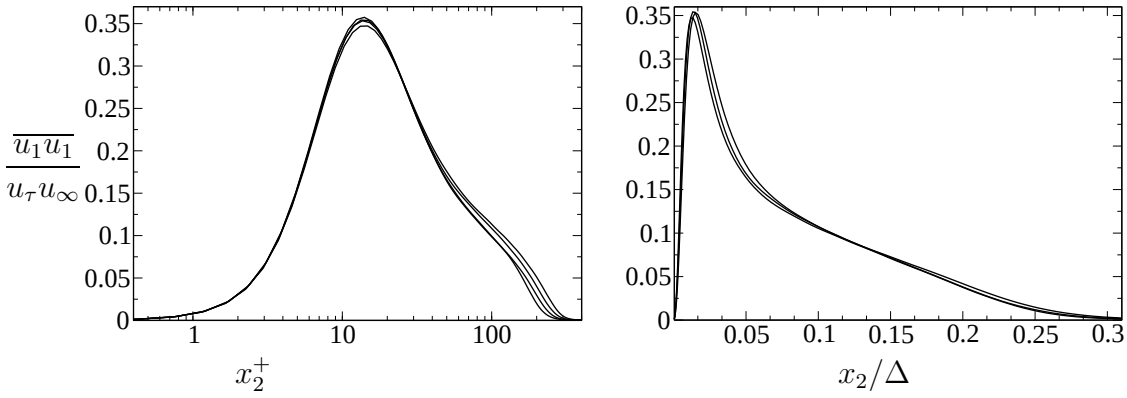

Figure 8.3: Streamwise Reynolds stresses for $Re_\theta = 470, 540, 615, 755$ from our DNS in mixed-plus and -outer scalings.

collapse is much better in this case for this Reynolds number case.

Wall-normal and spanwise Reynolds stresses

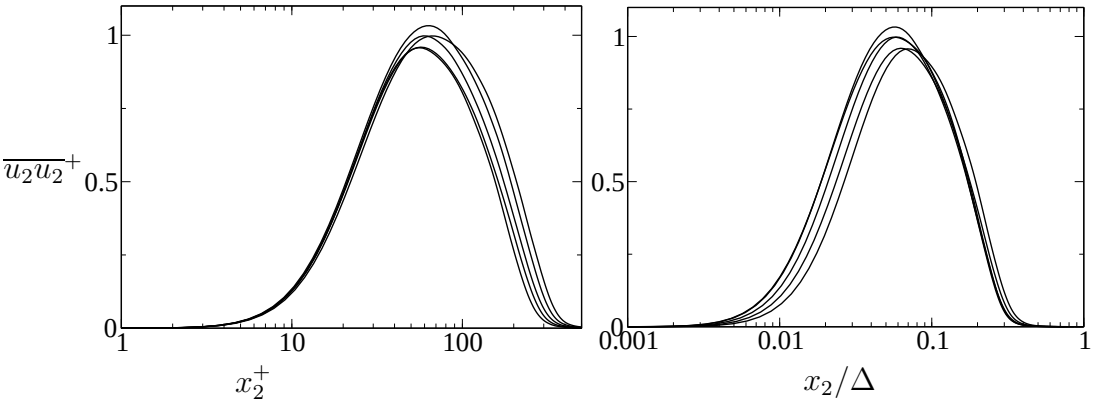

Figure 8.4: Wall-normal Reynolds stresses for $Re_\theta = 540, 615, 690, 755, 810$ from our DNS in inner-inner and inner-outer scalings.

Measurements of wall-normal stresses are very rare. The fluctuation u_2 is of great importance, because it provides the turbulence transport which makes turbulent boundary layer so different from laminar layers. Almost all the experimental data which were obtained with cross-wires, reach points further away from the wall as those obtained from a single-wire probe. Even magnitudes measured in the outer region with different probes are not in good agreement. For example, in Fernholz & Finley (1996) the authors show cross-wire measurements from different

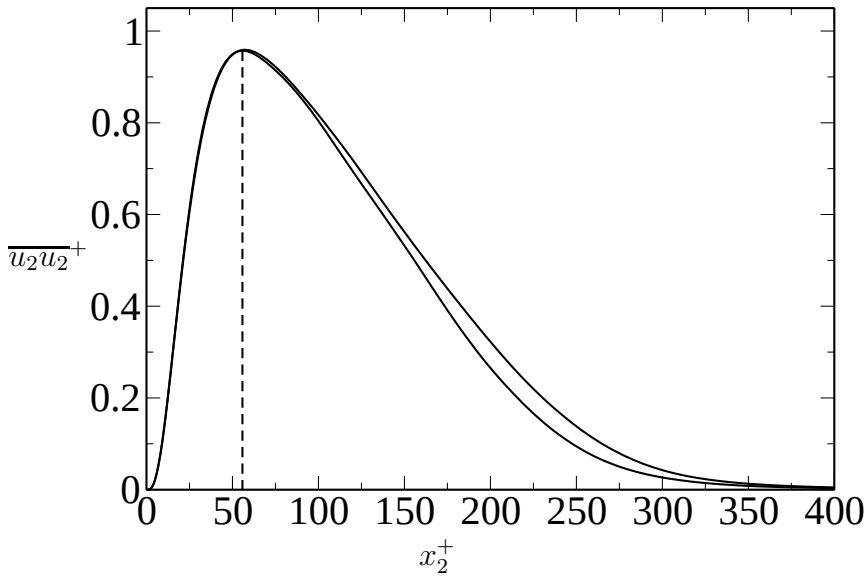

Figure 8.5: Wall-normal Reynolds stresses for $Re_\theta = 540, 615$ from our DNS in inner-inner scaling.

experiments (for the details see the paper), which suggest the location of the maximum of $\overline{u_2u_2}^+$ at

$$x_2^+(\overline{u_2u_2}^+_{max}) = 0.071 Re_\theta. \tag{8.3}$$

Figure 8.4 represents wall-normal Reynolds stresses in inner and outer scalings. The maximum location is $x_2^+ \approx 55.23$ as it is seen from Figure 8.5. The equation 8.3 gives $x_2^+ = 43.665$.

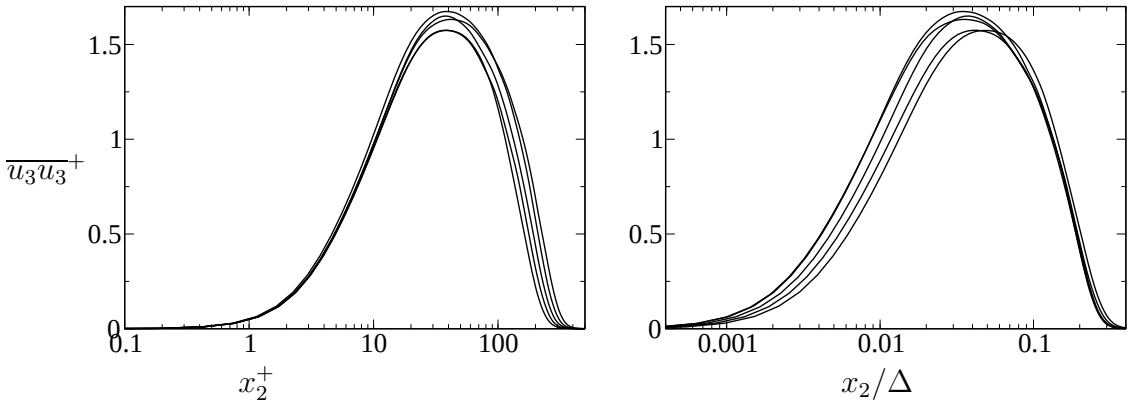

Figure 8.6: Spanwise Reynolds stresses for $Re_\theta = 540, 615, 690, 755, 810$ from our DNS in inner-inner and inner-outer scaling.

Figure 8.6 displays spanwise normal Reynolds stresses in inner and outer scaling.

The spanwise stresses measured in different points is streamwise direction do not show good collapse for the maximum value or its position.

Reynolds shear stresses

The Reynolds shear stress $-\overline{u_1 u_2}$ is a very important quantity in turbulent boundary layer flow, because it forms the main part of the total shear stress and it plays a significant role in the production of turbulent kinetic energy. Because the peak of the latter is located in the inner region, one should expect that the peak of the Reynolds shear stress will be also found in the same region. Fernholz & Finley (1996) conclude from the different experimental data that despite of a large scatter, there is no Reynolds number dependence of the peak value of $-\overline{u_1 u_2}$. They found that the peak value is between $0.8 - 1$ at a location, which depends on Reynolds number in the following manner:

$$(x_2^+)_{peak} = Re_\theta^{0.61}, \tag{8.4}$$

which gives $(x_2^+)_{peak} \approx 56.9$. In our case the peak is located closer to the wall $(x_2^+)_{peak} \approx 33.5$ which corresponds to $Re_\theta^{0.53}$ (see Figure 8.7) and the value of the peak is 0.88.

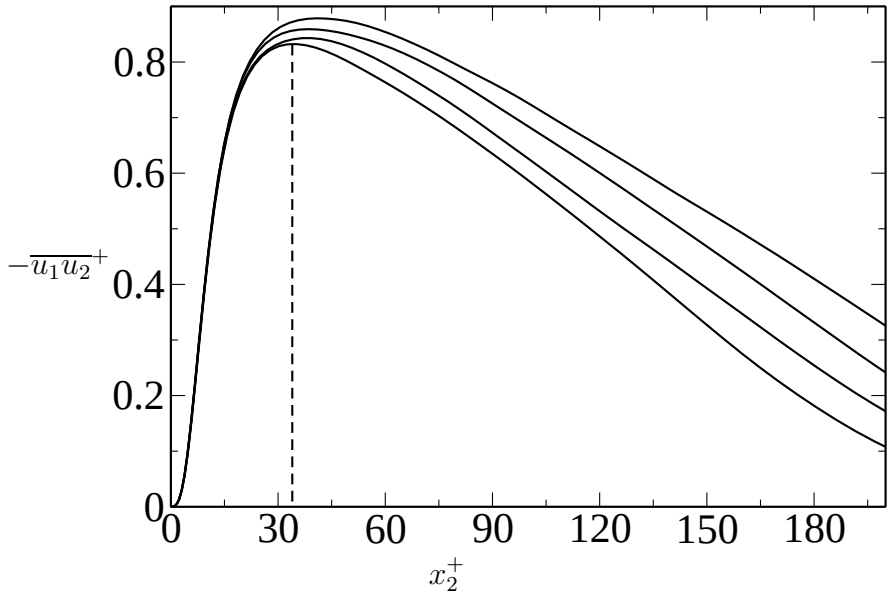

Figure 8.7: Linear plot of Reynolds shear stresses for $Re_\theta = 540, 615, 690, 755$ from our DNS in inner-inner scaling.

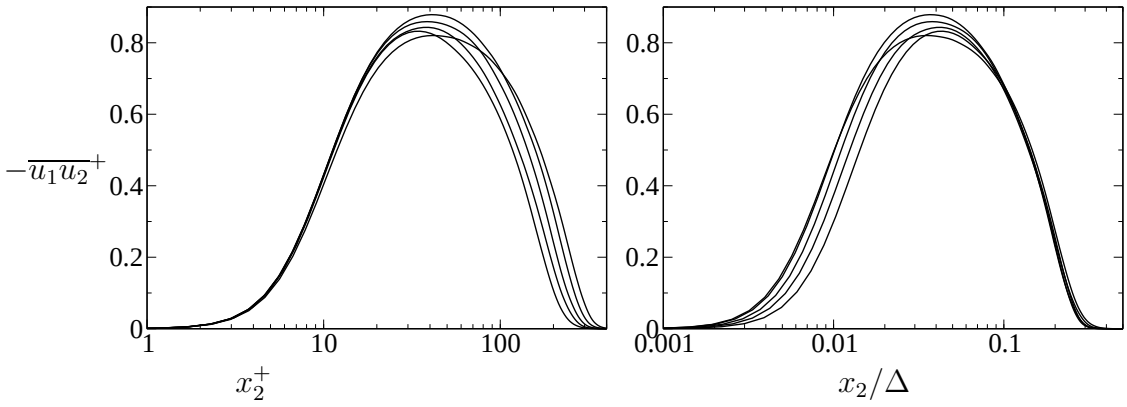

Figure 8.8: Log-linear plots Reynolds shear stresses for $Re_\theta = 540, 615, 690, 755, 810$ from our DNS in inner-inner and inner-outer scalings.

The first term of the Taylor series expansion of $\overline{u_1u_2}$ around the point $x_2 = 0$ gives the equation for it:

$$\overline{u_1u_2}^+ = A(x_2^+)^3 + ... \tag{8.5}$$

The constant A is equal to 0.0009. The result is shown in Figure 8.9.

In the boundary layer approximation total shear stress is defined by the equation (see the derivation of equation (3.8)):

$$\tau^+ \equiv \frac{du_1^+}{dx_2^+} - \overline{u_1u_2}^+ = 1. \tag{8.6}$$

As we see it is the sum of the viscous shear stress and the Reynolds shear stress. These three quantities are plotted in Figures 8.10 and 8.11. From the last figure one can see that the viscous shear and Reynolds stress cross at $x_2^+ = 10$ and $\tau/\tau_w = 0.5$ (the same results are obtained in DeGraaff & Eaton (2000)). For this Reynolds number the total shear drops below τ_w close to the wall, and the viscous stress contribution extends away further from the wall. These are low-Reynolds number effects, i.e. the viscosity is important through a substantial fraction of the inner region. The point where the viscous shear and the Reynolds shear are equal is the position of maximum energy production (Rotta 1962).

Figure 8.12 shows rms pressure fluctuations (p_{rms}^+) in plus and outer scalings. The rms pressure fluctuations has a strong rise near the wall (it has a peak at $x_2^+ \approx 28.4$) (see the left plot). The wall value rises from 2.1 to 2.52 (2.7 in Spalart's case but for high Reynolds number case). The increase away from the wall is weaker.

Rms vorticity fluctuations are shown in the Figure 8.13 for $Re_\theta = 540, 615, 690, 755$.

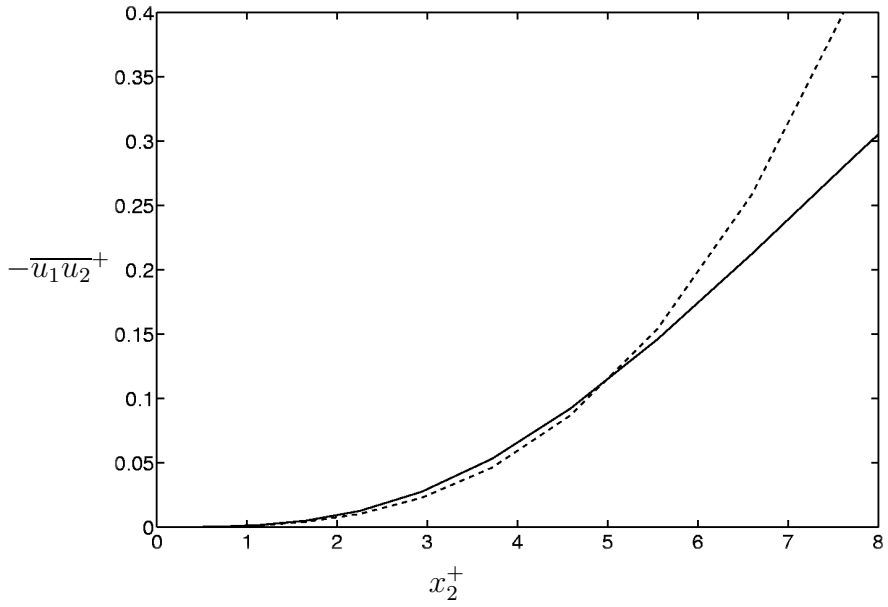

Figure 8.9: Linear plot of Reynolds shear stresses for $Re_\theta = 755$ from our DNS (solid) in inner-inner scaling. Dashed line corresponds to equation (8.5).

The spanwise rms vorticity fluctuations is considerably larger than the other components near the wall. The peak of $\omega_{z,rms}$ is 4.05. Away from the wall other two components $\omega^+_{x,rms}$ and $\omega^+_{y,rms}$ become much more equal. $\omega^+_{x,rms}$ peaks at $x_2^+ = 18.3$ with a value $(\omega^+_{x,rms})_{max} = 0.67$ (see Figure 8.13 (upper, left plot)). As for $\omega^+_{y,rms}$ it peaks at $x_2^+ = 14.8$ with a value $(\omega^+_{x,rms})_{max} = 0.79$ (see Figure 8.13 upper, right plot). All rms vorticity fluctuations show very good collapse in plus units near the wall, since the Reynolds numbers do not vary much.

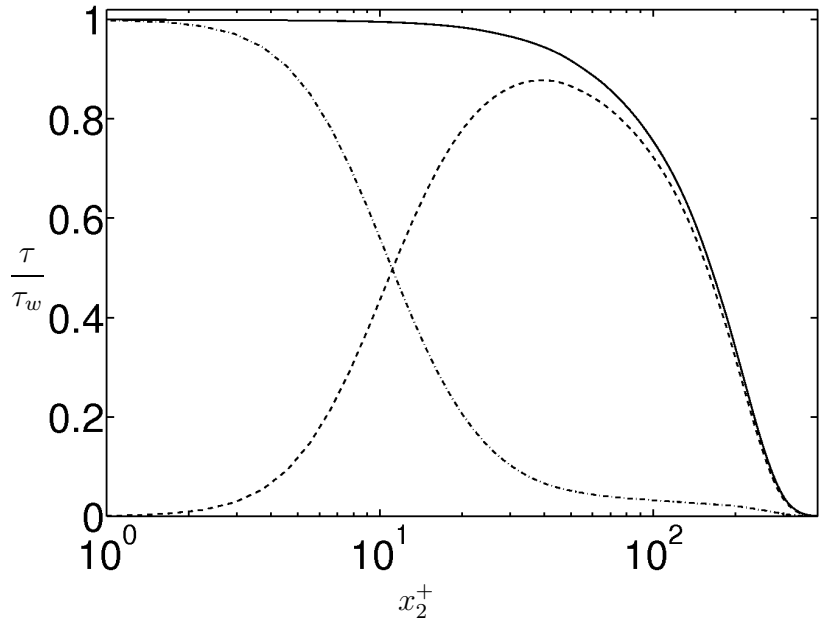

Figure 8.10: Shear stress distribution (linear-log axes) for $Re_\theta = 755$. --- viscous shear, —·— Reynolds shear, —— total shear.

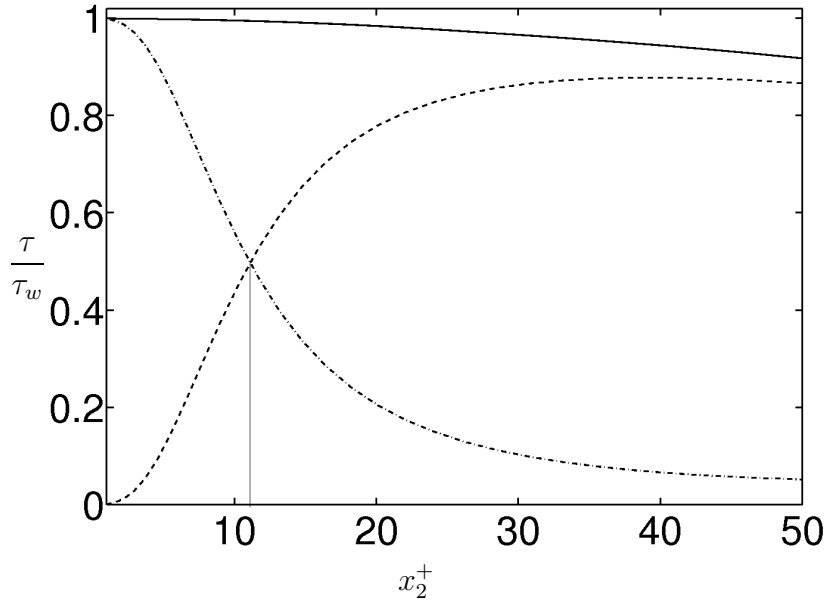

Figure 8.11: Near-wall behavior of shear stresses (Figure 8.10). --- viscous shear, —·— Reynolds shear, —— total shear.

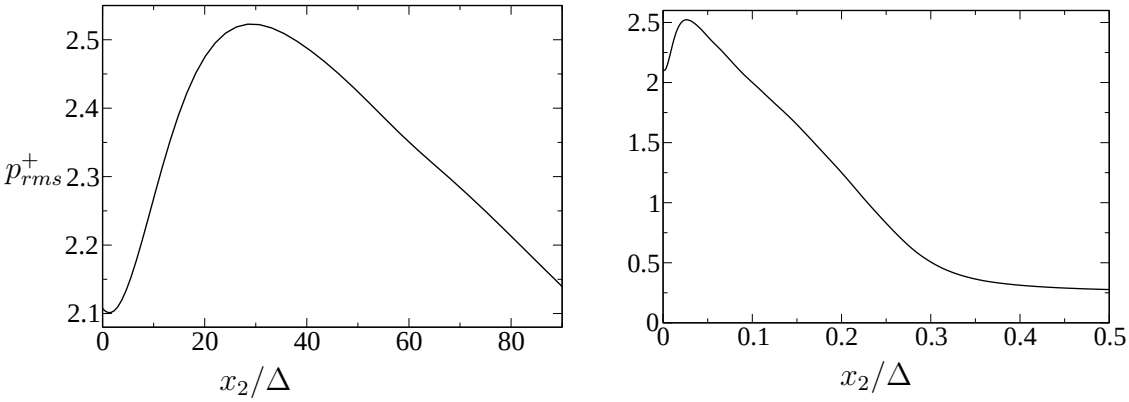

Figure 8.12: p_{rms} in inner (near-wall behavior, left plot) and in outer scalings (right plot) for $Re_\theta = 755$.

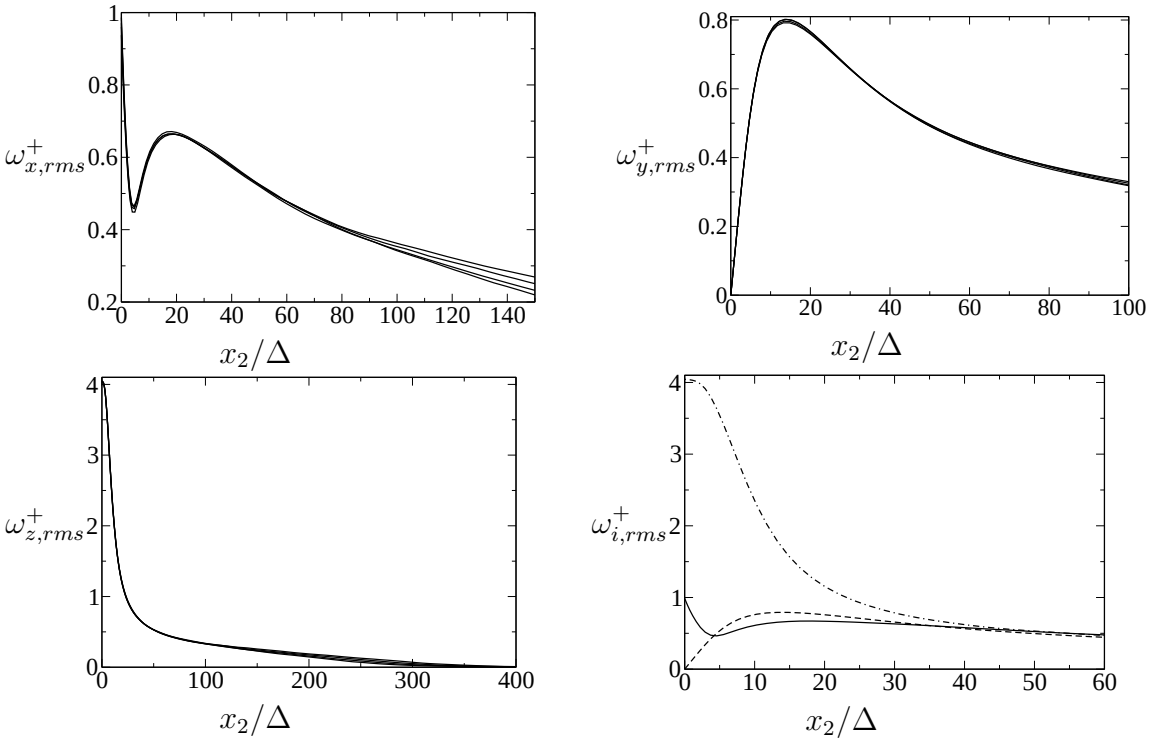

Figure 8.13: $\omega^+_{x,rms}$ (left, upper plot), $\omega^+_{y,rms}$ (right, upper plot), $\omega^+_{z,rms}$ (left, bottom plot) and $\omega^+_{i,rms}$ (right, bottom plot (—— $\omega^+_{x,rms}$, - - - $\omega^+_{y,rms}$), —·— $\omega^+_{z,rms}$) in inner (near-wall behavior) $Re_\theta = 540, 615, 690, 755$.

8.1.2 Two-point statistics

TPC functions were calculated for both cases of DNS presented in this paper. $R_{12}(x_2, r_2)$, $R_{21}(x_2, r_2)$ and $R_{22}(x_2, r_2)$ are plotted against $r_2 = x_2' - x_2$ normalized by the Reynolds stresses:

$$\mathcal{R}_{[ij]}(x_2, \boldsymbol{r}) = \frac{R_{ij}(x_2, \boldsymbol{r})}{u_i(x_2)u_j(x_2)}, \tag{8.7}$$

where [] is the index denote componentwise ratios. Note that $\mathcal{R}_{[ij]}$ is not a tensor. Normalized TPC functions $\mathcal{R}_{ij}$ do not depend on the wall-normal coordinate anymore. The last equation is the important result of the Lie group approach of TPC equations:

$$\frac{R_{ij}(x_2, \boldsymbol{r})}{u_i(x_2)u_j(x_2)} = \frac{e^{-k_4 x_2} B_{ij}(\boldsymbol{r})}{e^{-k_4 x_2} B_{ij}(0)} = F_{[ij]}(\boldsymbol{r}). \tag{8.8}$$

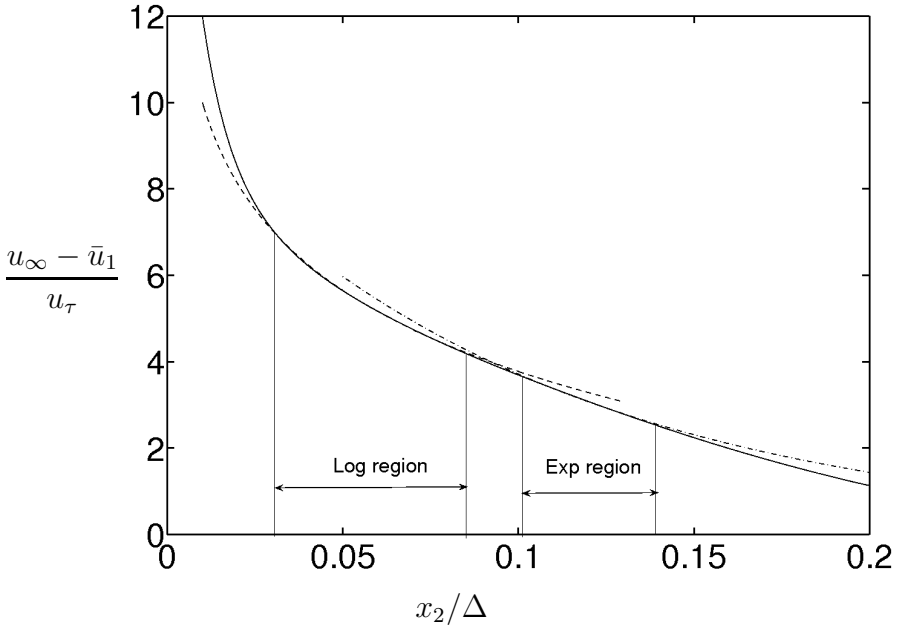

Figure 8.14: Mean velocity profile for at $Re_\theta = 1015$. —— log-law, - - - DNS, —·— exponential law.

Figure 8.14 shows the mean velocity profile.

TPC at low Reynolds number are represented as normalized $\mathcal{R}_{22}$ (Figure 8.15) and non-normalized (Figure 8.16) R_{22} functions in outer scaling for different initial points $x_2/\Delta = 0.013, 0.026, 0.052$ which in plus units correspond to $x_2^+ = 14, 28, 57$

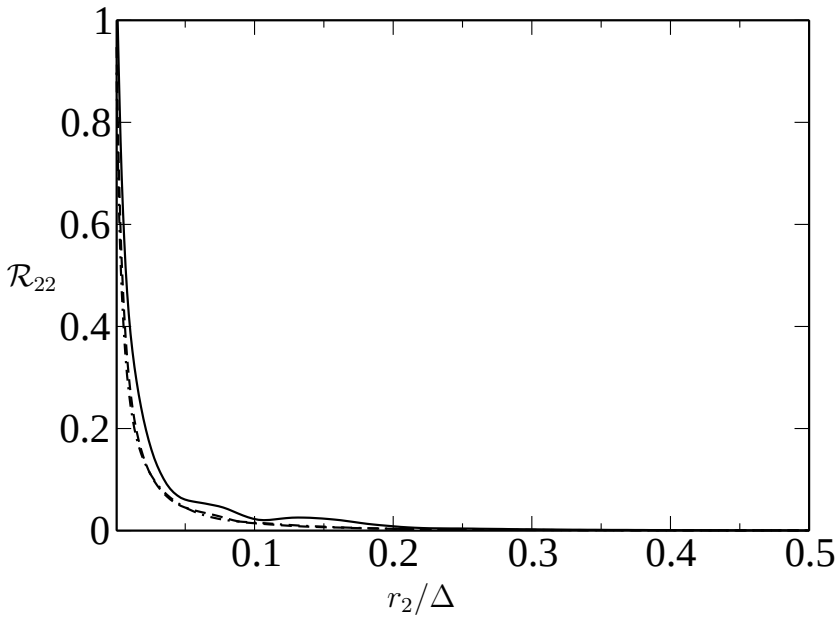

Figure 8.15: TPC functions: normalized ($\mathcal{R}_{22}(r_2)$) for $Re_\theta = 750$ at different initial points; —— $x_2/\Delta = 0.013$, - - - $x_2/\Delta = 0.026$, —·— $x_2/\Delta = 0.052$

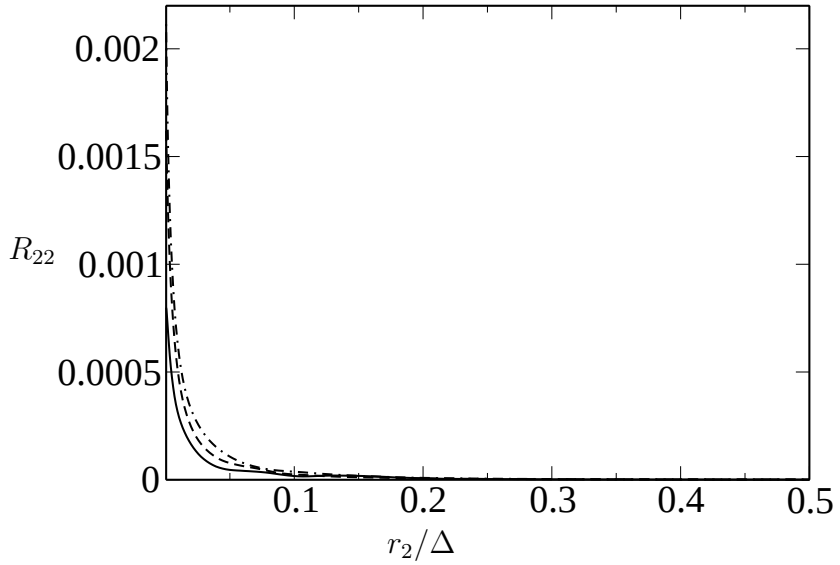

Figure 8.16: Non-normalized TPC functions ($R_{22}(x_2, r_2)$) for $Re_\theta = 750$ at different initial points; —— $x_2/\Delta = 0.013$, - - - $x_2/\Delta = 0.026$, —·— $x_2/\Delta = 0.052$

respectively. First point ($x_2^+ = 14$) is located in the buffer region, while last two ones ($x_2^+ = 28, 57$) are in the logarithmic region.

The behavior of the TPC can be explained by the following reasoning: the magnitude of R_{22} at ($x_2^+ = 14$) is smaller than for R_{22} at $x_2^+ = 28, 57$ because in the region near the wall (buffer region) the Reynolds stress is smaller (the peak for the low Reynolds number case of $\overline{u_2 u_2}^+$ is at $y^+ \approx 65$) then far from the wall. In this region the streak lifts up from the wall (this happens normally at $x_2^+ \approx 10$), oscillates and breaks down into small-scale motions. However, as it is seen from Figure 8.15 $\mathcal{R}_{22}(x_2^+ = 14)$ (solid line) decreases slower than $\mathcal{R}_{22}$ at ($x_2^+ = 28, 57$), because further away from this region bigger structures exist in the flow and consequently the more widely separated points are correlated. For the initial points $x_2^+ = 28, 57$ located further apart from the wall, large coherent structures are already developed, (because of this fact we have a larger magnitude of $\mathcal{R}_{22}$), and calculating TPC functions at larger separations, we leave the region entering the region with smaller structures (where large structures break down). This is the reason why we have small correlation distances in this region.

TPC functions were calculated also in the exponential region for the different initial points in wall-normal direction: $x_2/\Delta = 0.1, 0.12, 0.13, 0.144$ which in plus units correspond to $x_2^+ = 102, 122, 132, 146$.

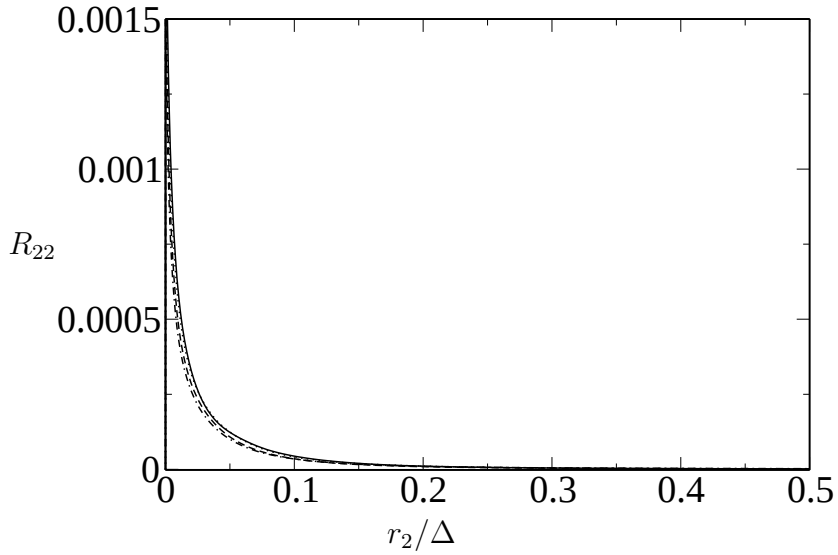

Figure 8.17: TPC functions: non-normalized ($R_{22}(r_2)$) for $Re_\theta = 750$ at different initial points in exponential region; —— $x_2/\Delta = 0.1$, ····· $x_2/\Delta = 0.12$, - - - $x_2/\Delta = 0.13$ and —·— $x_2/\Delta = 0.144$

Figure 8.18 shows normalized TPC function $\mathcal{R}_{22}(r_2)$. As it follows from equation

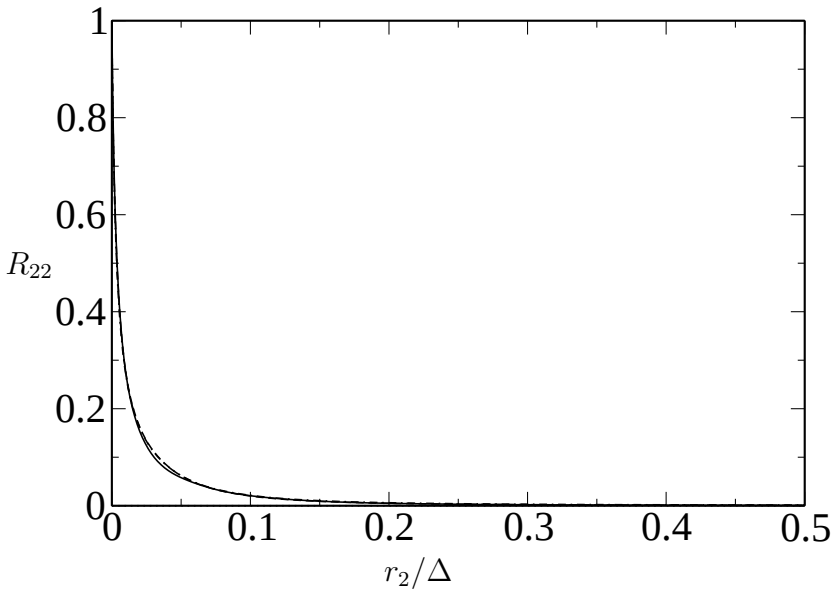

Figure 8.18: TPC functions: normalized ($\mathcal{R}_{22}(r_2)$) for $Re_\theta = 750$ at different initial points in exponential region; —— $x_2/\Delta = 0.1$, ····· $x_2/\Delta = 0.12$, - - - $x_2/\Delta = 0.13$ and —·— $x_2/\Delta = 0.144$

(8.8) normalized on Reynolds stresses TPC functions should collapse for different initial point (x_2) in wall-normal direction. Figure 8.18 shows excellent collapse of the lines for different x_2 that were taken in the exponential region of the flow (see Figure 8.14). This fact shows the validity of the results of Lie group approach (see equation (8.8)).

8.1.3 Budgets

Reynolds stress budget equations 2.23, in the case of boundary layer approximation ($\partial\bar{u}_1/\partial x_2$ is the only significant mean velocity gradient)

$$\frac{\partial}{\partial x_1} \ll \frac{\partial}{\partial x_2}, \tag{8.9}$$

can be written in the form:

$$\frac{D\overline{u_1u_1}}{Dt} = -2\overline{u_1u_2}\frac{\partial\bar{u}_1}{\partial x_2} + 2p\overline{\frac{\partial u_1}{\partial x_1}} + 0 + D_{11} - \varepsilon_{11} + \left(\frac{\partial\overline{u_1u_1u_2}}{\partial x_2}\right), \tag{8.10}$$

$$\frac{D\overline{u_2u_2}}{Dt} = 0 + 2p\overline{\frac{\partial u_2}{\partial x_2}} - 2\frac{\partial\overline{u_2p}}{\partial x_2} + D_{22} - \varepsilon_{22} + \left(\frac{\partial\overline{u_2u_2u_2}}{\partial x_2}\right), \tag{8.11}$$

$$\frac{D\overline{u_3u_3}}{Dt} = 0 + 2p\overline{\frac{\partial u_3}{\partial x_3}} + 0 + D_{33} - \varepsilon_{33} + \left(\frac{\partial\overline{u_3u_3u_2}}{\partial x_2}\right), \tag{8.12}$$

$$\frac{D\overline{u_1u_2}}{Dt} = -2\overline{u_2u_2}\frac{\partial\bar{u}_1}{\partial x_2} + \overline{p\left(\frac{\partial u_1}{\partial x_2} + \frac{\partial u_2}{\partial x_1}\right)} - \frac{\partial\overline{u_1p}}{\partial x_2} + D_{12} - \varepsilon_{12} + \left(\frac{\partial\overline{u_1u_2u_2}}{\partial x_2}\right). \tag{8.13}$$

In this approximation the kinetic energy budget equation has the following form:

$$\frac{D\overline{k}}{Dt} = -\overline{u_1u_2}\frac{\partial\bar{u}_1}{\partial x_2} + D - \varepsilon, \tag{8.14}$$

where D and ε are defined by the equations

$$\mathcal{D} \equiv T_{ii}^{(u)} + T_{ii}^{(p)} + D_{ii}$$

and

$$\varepsilon \equiv \varepsilon_{ii}$$

respectively.

Longitudinal Reynolds stress

Figure 8.19 shows the terms of equation 8.10. Production has the maximum in the region of $x_2^+ \approx 10$. In the near wall region the most important terms are dissipation (ε_{11}) and viscous diffusion (D_{11}), they balance each other. They both represent viscous effects, ε_{11} acts as a destruction of turbulent kinetic energy, while D_{11} being molecular diffusion term, is acting on turbulent stresses by spatial redistribution. Φ_{11} is almost zero near the wall, but falls down to negative values far from the wall. Pressure transport term $T_{11}^{(p)}$ is negligible in comparison to the other terms (in boundary layer approximation it is zero, third term in the rhs of the equation 8.10).

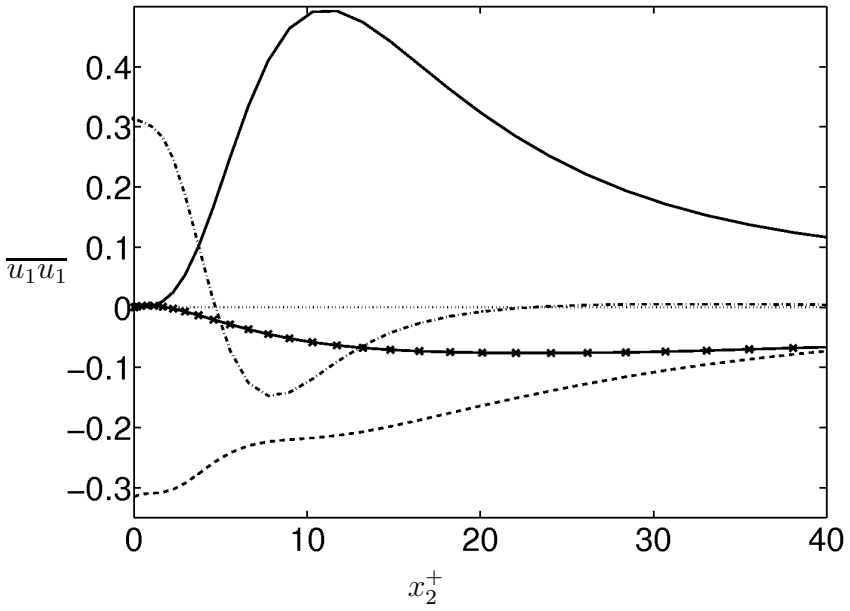

Figure 8.19: Terms in the $\overline{u_1u_1}$-budget. — P_{11}, - - - ε_{11}, —·— D_{11}, —×— Φ_{11}, ····· $T_{11}^{(p)}$.

Wall-normal Reynolds stress

In Figure 8.20 the budget of the wall-normal Reynolds stress is plotted in plus units. The velocity-pressure gradient term Π_{22} becomes very important far from the wall. Φ_{22} (pressure-rate-of-strain term) follows nearly Π_{22} away from the wall (after the point $x_2^+ \approx 15$). It means that the pressure transport term ($T_{22}^{(p)}$) has opposite behavior in the wall layer (see Figure 8.22). The pressure-rate-of-strain

term near the wall is negative, and far from the wall is positive. It has a maximum in the region of $x_2^+ \approx 35$. As for $T_{22}^{(p)}$, it is positive near the wall and almost zero far from the wall. Figure 8.21 shows near-wall behavior of the wall-normal

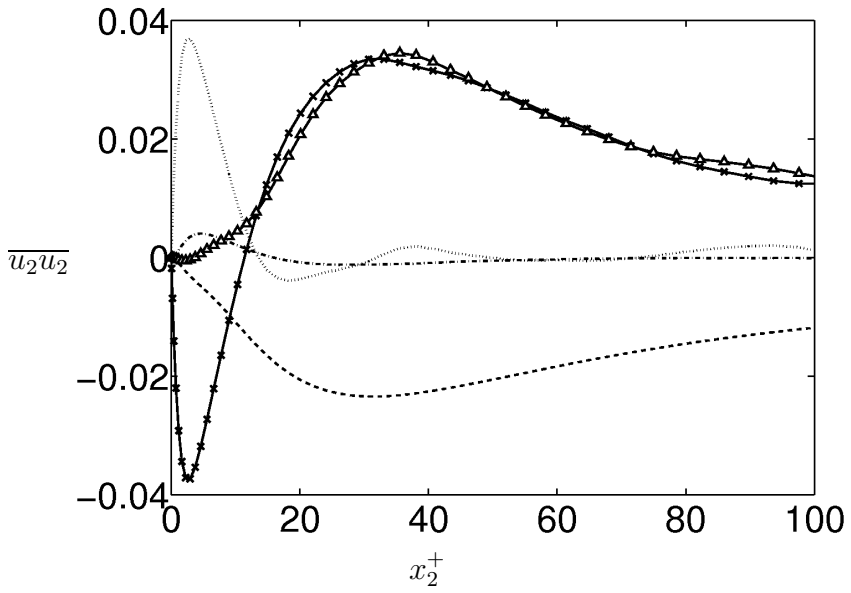

Figure 8.20: Terms in the $\overline{u_2u_2}$-budget. ····· $T_{22}^{(p)}$, --- ε_{22}, —·— D_{22}, -×- Φ_{22}, -△- Π_{22}.

shear stress budgets. The velocity-pressure gradient term (Π_{22}) in the budget equations was split-up into two terms: the pressure-rate-of-strain tensor (Φ_{22}) and the pressure transport tensor ($T_{22}^{(p)}$) (see Figure 8.22).

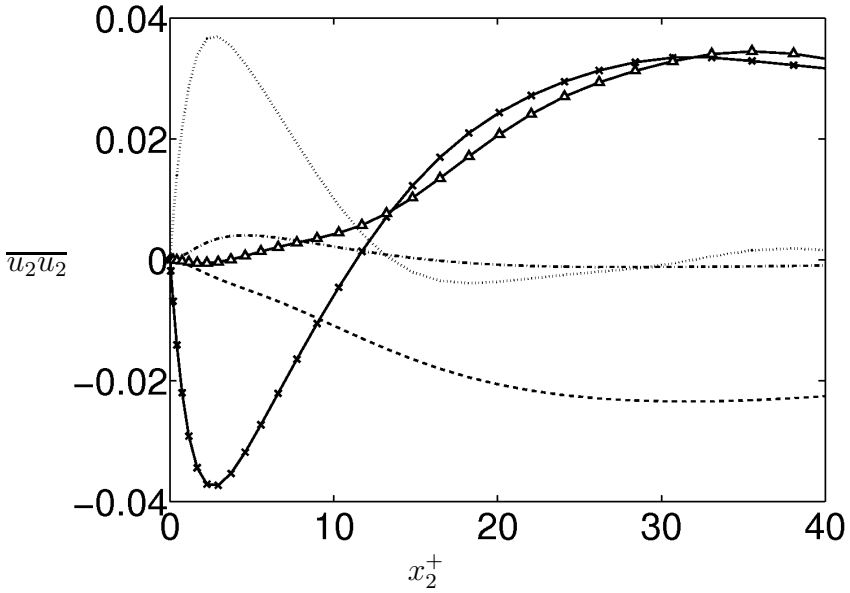

Figure 8.21: Terms in the $\overline{u_2u_2}$-budget. ····· $T_{22}^{(p)}$, - - - ε_{22}, —·— D_{22}, —×— Φ_{22}, —△— Π_{22}.

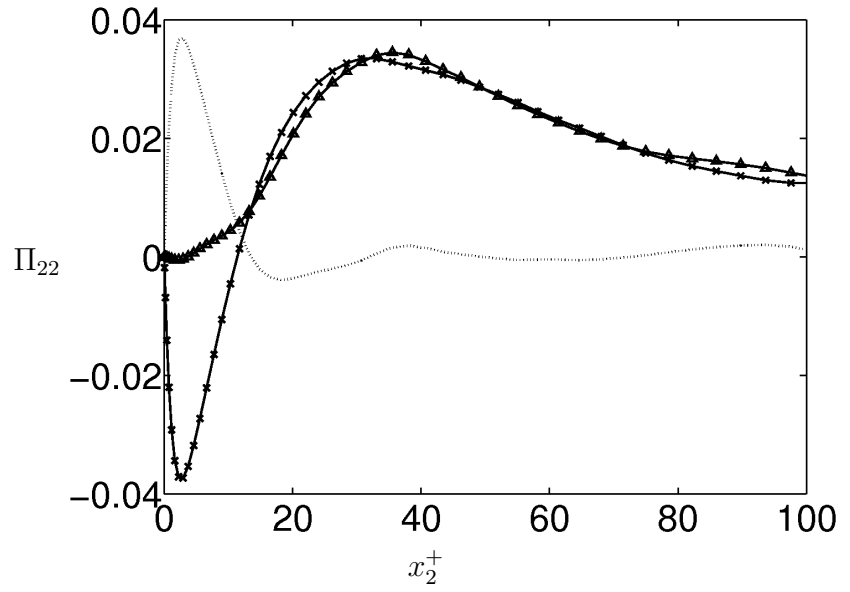

Figure 8.22: —△— $\Pi_{22} = \Phi_{22} + T_{22}^{(p)}$ at $Re_\theta = 810$. —×— Φ_{22} ····· $T_{22}^{(p)}$.

Spanwise Reynolds stress

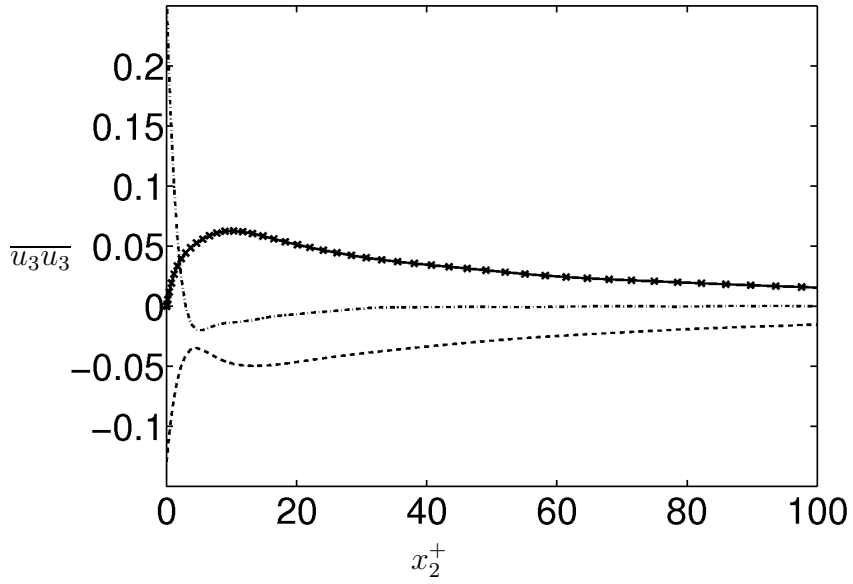

Figure 8.23: Terms in the $\overline{u_3u_3}$-budget at $Re_\theta = 810$. --- ε_{33}, —·— D_{33}, -×- Φ_{33}

In the case of the budgets of the spanwise Reynolds normal stress component the only terms we have are Φ_{33}, D_{33} and dissipation ε_{33} (see Figure 8.23). Molecular diffusion term (D_{33}) is very large near the wall. It decreases very fast away from the wall. Φ_{33} is very small near the wall, but increases away from the wall, reaches a maximum and then slowly decreases far from the wall to zero.

Reynolds shear stress

Budgets for Reynolds shear stresses are shown in Figures 8.24 and 8.25 (near-wall behavior of the budgets). ε_{12} and D_{12} are almost of the same amplitude, but with the opposite signs near the wall. Away from the wall they decrease and become almost zero. The other terms of budget equation are more important. Φ_{12} near the wall decreases to the minimum value. However, it reaches it maximum value away from the wall. $T_{12}^{(p)}$ shows similar behavior but in the opposite half of the plane.

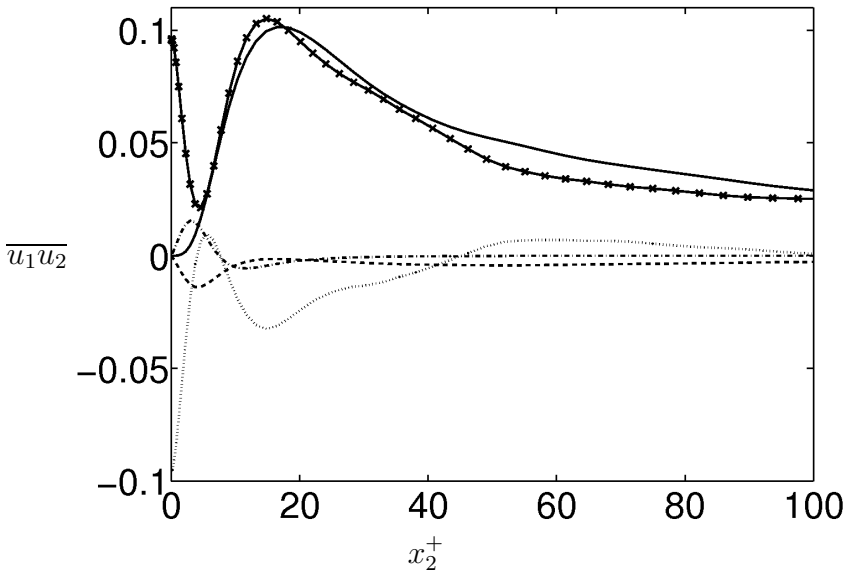

Figure 8.24: Terms in the $\overline{u_1u_2}$-budget at $Re_\theta = 810$. — P_{12}, --- ε_{12}, —·— D_{12}, ····· to $T_{12}^{(p)}$, -×- Φ_{12}.

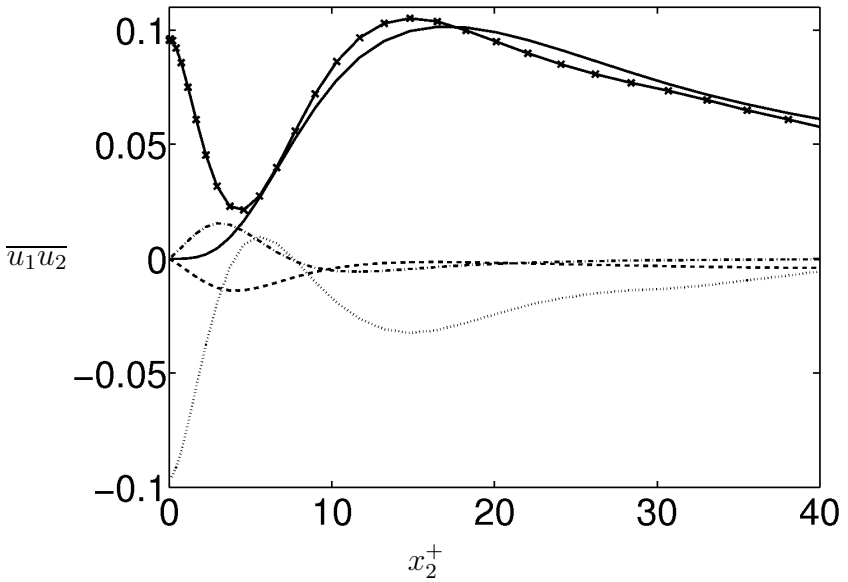

Figure 8.25: Close-up view of the Figure 8.24.

Turbulent kinetic energy budget

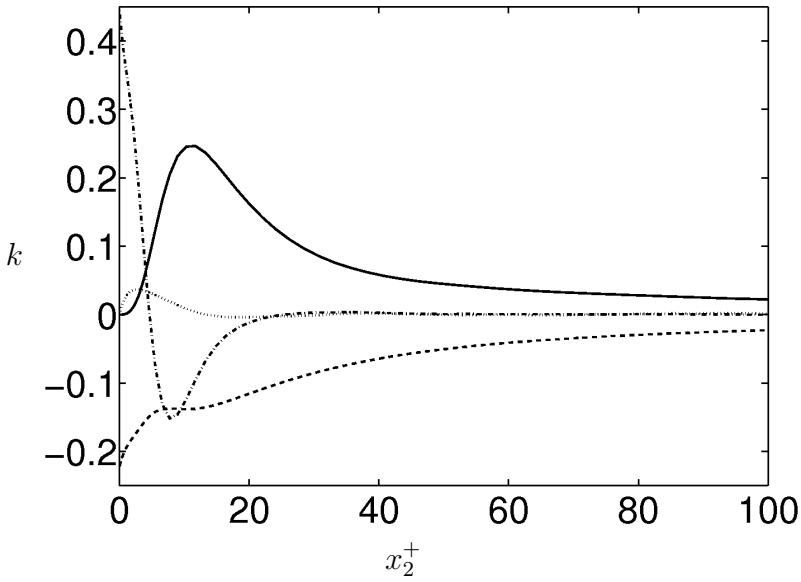

Figure 8.26: Turbulent kinetic energy budget. —— turbulent kinetic energy production ($\mathcal{P}$); - - - dissipation; —·— viscous diffusion (D_{ii}); ····· pressure transport ($T_{ii}^{(p)}$).

In Figure 8.26 the turbulent kinetic energy budgets are presented. The maximum of the turbulent production is at about $x_2^+ = 10$. The sign of the diffusion term changes in the wall layer, that means that the energy is transported towards the wall or in the direction of the outer region. For the higher x_2^+ the diffusion tends to zero (faster than dissipation and production (in the overlap region the dissipation is balanced by the production (Schlichting & Gersten 2000)). The pressure transport term ($T_{ii}^{(p)}$) is small It has small maximum near the wall and then decreases to zero far from the wall.

Figure 8.27 displays the near wall behavior of the turbulent kinetic energy budgets.

In Figure 8.28 turbulent kinetic energy is displayed together with the normal stresses. From this figure one can see that k is half the sum of the three normal stresses. The streamwise component contains the highest amount of kinetic energy, because it receives energy permanently by production, while the other two terms receive energy only by redistribution.

Figure 8.29 shows the dissipation components in plus units. The anisotropy near the wall of ε_{ij} is clearly seen from the figure while away from the wall we observe

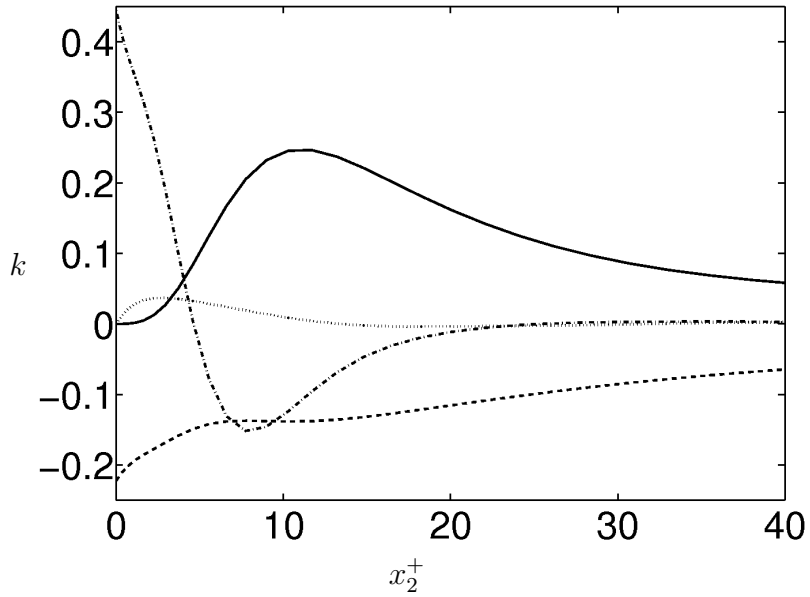

Figure 8.27: Close-up view of turbulent kinetic energy budget.—— turbulent kinetic energy production ($\mathcal{P}$); - - - dissipation; —·— viscous diffusion (D_{ii}); ····· pressure transport (T_{ii}^p).

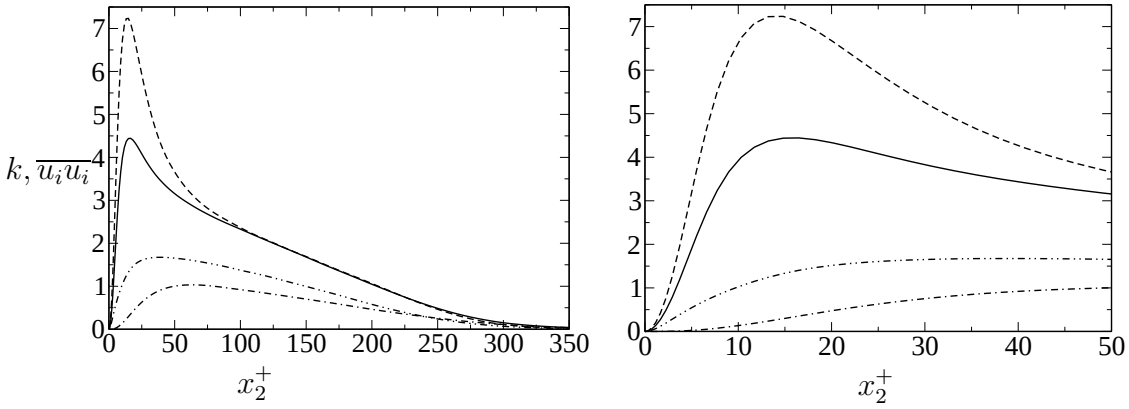

Figure 8.28: Reynolds normal stresses and turbulent kinetic energy. —— k; - - - $\overline{u_1 u_1}$; —·— $\overline{u_2 u_2}$ and —··— $\overline{u_3 u_3}$

approximate isotropy. It is also important to note that the off-diagonal element is considerably small than the trace elements.

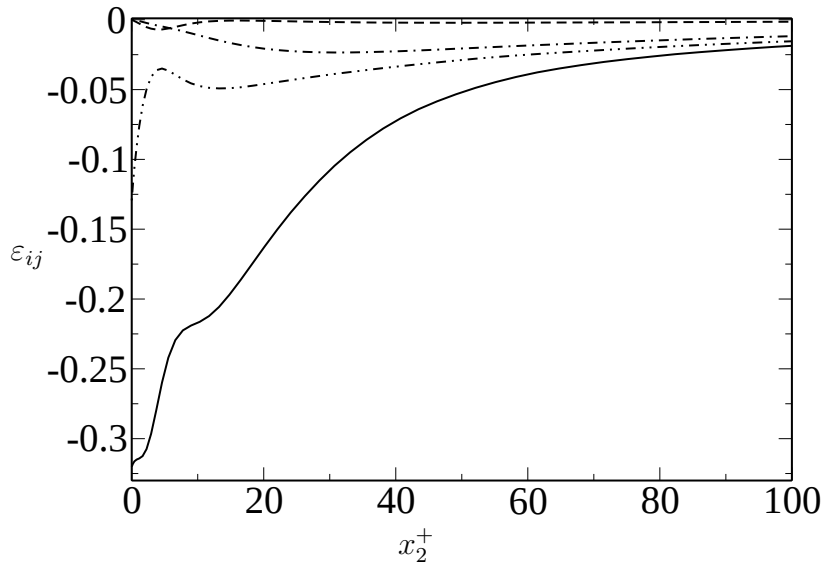

Figure 8.29: Dissipation terms: --- corresponds to ε_{12}; — ε_{11}; —·— ε_{22}, —··— ε_{33}.

8.2 Large box simulations

In this section statistics accumulated during the simulation at $Re_\theta = 1500$ in the simulation box $1000 \times 60 \times 34$ ($DNS600d, e$) is presented.

8.2.1 One-point statistics

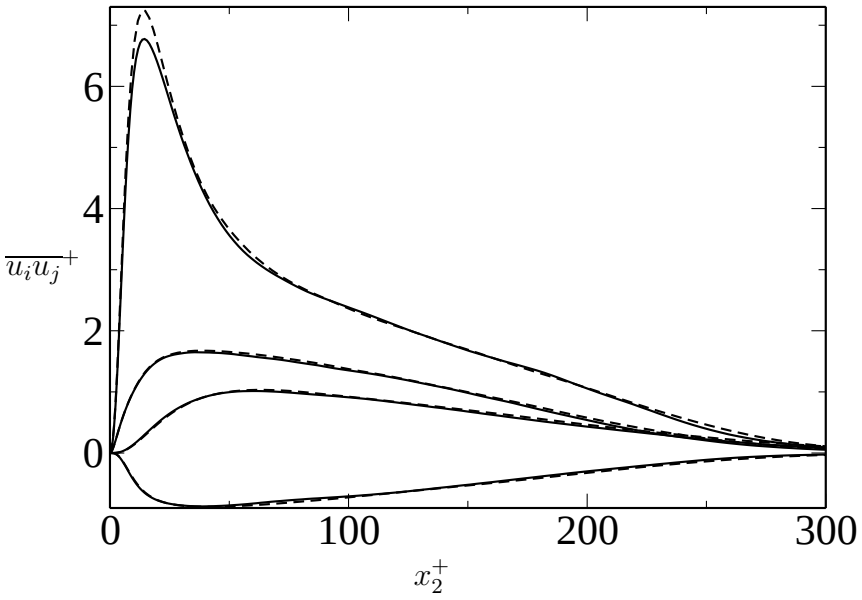

Figure 8.30: Comparison of the four Reynolds stresses for --- small and — big boxes at $x_1 = 300$.

The comparison of the Reynolds stresses in both cases of small and big simulation boxes in the low Reynolds number simulation is shown in Figure 8.30. As one can see, the only significant difference is observed for the streamwise stresses.

Figure 8.31 displays streamwise Reynolds stresses for different Reynolds numbers in inner and outer scaling. Inner scaling shows good collapse near the wall. For the outer scaling we have a less convincing collapse of the curves in the near wall region. The reason may be insufficient simulation time (during which the statistics was accumulated) in this case.

For the wall-normal Reynolds stresses, the situation is even worse. It shows very strong Reynolds number dependence. The curves collapse only near the wall in inner scaling and in the small region far from the wall in outer scaling (see Figure 8.32).

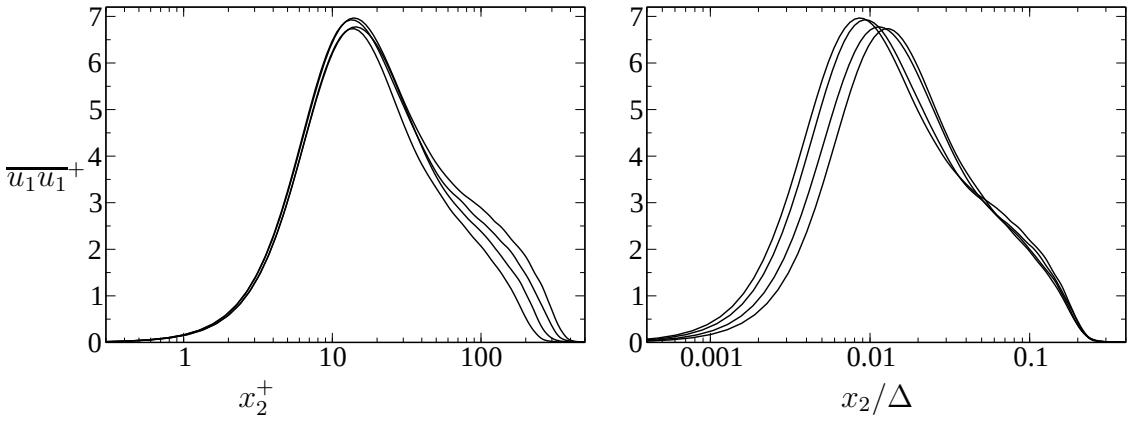

Figure 8.31: Streamwise Reynolds stresses in plus and outer scalings for $Re_\theta = 755, 882, 1003, 1122$

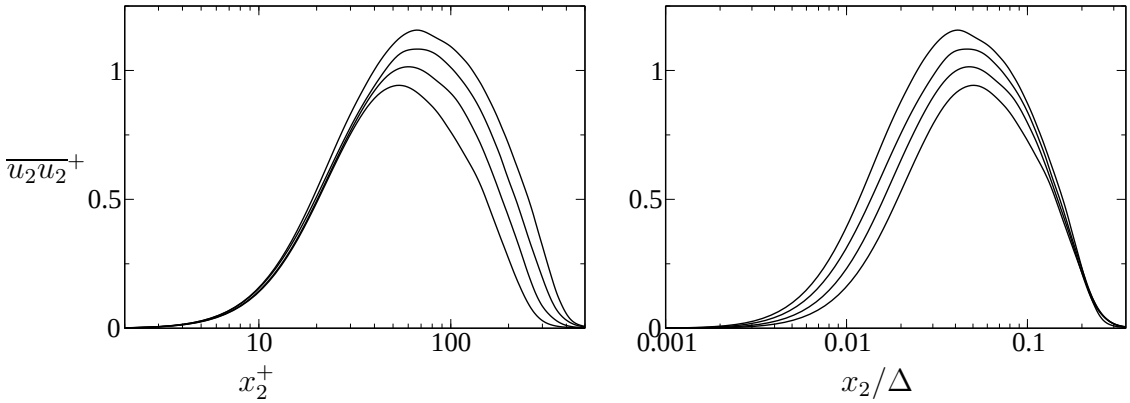

Figure 8.32: Wall-normal Reynolds stresses in inner and outer scalings for $Re_\theta = 755, 882, 1003, 1122$

Figures 8.33 and 8.34 show shear stresses distributions. Viscous shear and Reynolds shear stresses cross in the point $x_2^+ = 10$. As it was mentioned above, this point corresponds to the maximum production of the turbulent kinetic energy.

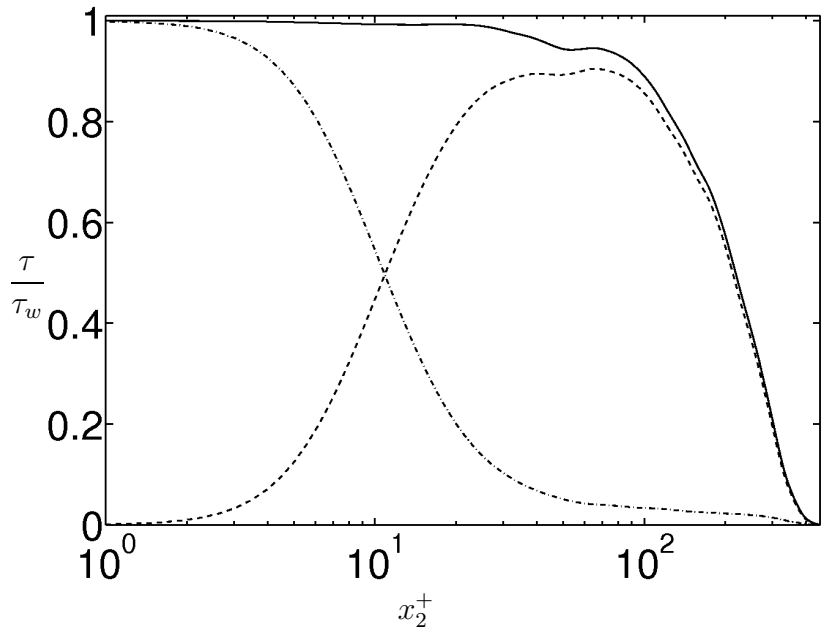

Figure 8.33: Shear stress distribution (linear-log axes) for $Re_\theta = 1500$. --- viscous shear stress, —·— Reynolds shear stress, —— total shear stress.

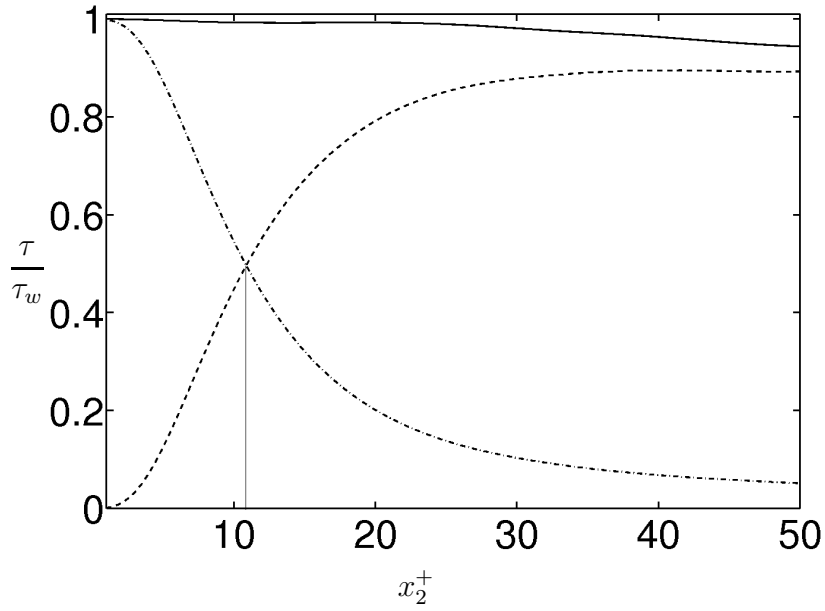

Figure 8.34: Near-wall behavior of shear stress distribution (linear-log axes) for $Re_\theta = 1500$. --- viscous shear stress, —·— Reynolds shear stress, —— total shear stress.

9 High Reynolds number case

9.1 Simulations at $Re_\theta = 2240$

9.1.1 One-point statistics

Normal stresses

Reynolds stress components are shown in Figure 9.1 from the DNS results obtained by Spalart (1988) and the present DNS for the highest Reynolds number each. Major differences are only visible far from the wall. For $\overline{u_1 u_1}^+$ the peak is slightly higher in our case. It is generally accepted that Reynolds stresses must scale on

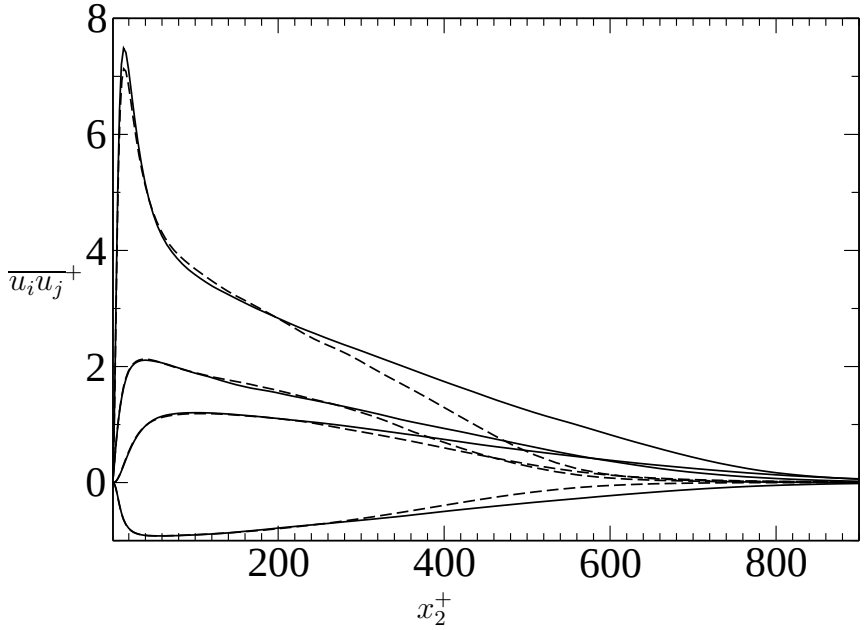

Figure 9.1: $\overline{u_i u_j}$ in inner scaling for Reynolds numbers $Re_\theta = 1410, 2240$, from Spalart's --- and our DNS —— respectively.

inner coordinates, because of the mean velocity scaling in these coordinates. How-

ever, this fact is not supported by different measurements. The profiles of $\overline{u_1u_1}^+$ show a strong peak near the wall. The magnitude and location of the peak depends on the Reynolds number. There appears to be a contradiction between different experimental data. For example, Mochizuki & Nieuwstadt (1996), plotting data from different experiments, came to the conclusion that the peak value for $\overline{u_1u_1}^+$ is constant and equal to 7.34. However, an other flat-plate data analysis shows that the peak increases with the Reynolds number (Fernholz & Finley (1996) and references therein). In order to reach Reynolds number independence near the wall some researchers tried to introduce a mixed inner-outer scaling. DeGraaff & Eaton (2000), for example, introduced mixed scalings for the streamwise component of the stress tensor ($\overline{u_1u_1}/u_\tau\bar{u}_\infty$). They performed experiments for a wide range of Reynolds numbers and plotted this component of the Reynolds stress tensor in the new scaling vs. x_2^+ and a good collapse of the near-wall peak at $x_2^+ = 14$ was obtained. However, accurate experiments on turbulent boundary layer still involve severe difficulties. Thus DNS of turbulent boundary layer is important to throw light on the problem. Note that the present DNS ($Re_\theta = 2240$) gives the peak at $x_2^+ \approx 13.87$ with a magnitude of $(\overline{u_1u_1})^+_{peak} \approx 7.48$.

The Reynolds stress streamwise component is presented in Figure 9.2 for inner (left plot) and outer (right plot) scalings at different Reynolds numbers obtained from the DNS. Apparently, a rather good collapse of the data is observed. In inner scaling a reasonable agreement between different Reynolds numbers is observed up to $x_2^+ \approx 200$. For the larger values of x_2^+ typical Reynolds number dependence of the velocity profiles is observed. The figure displays the Reynolds number dependence of the peak. The latter weakly increases with Reynolds number. The near

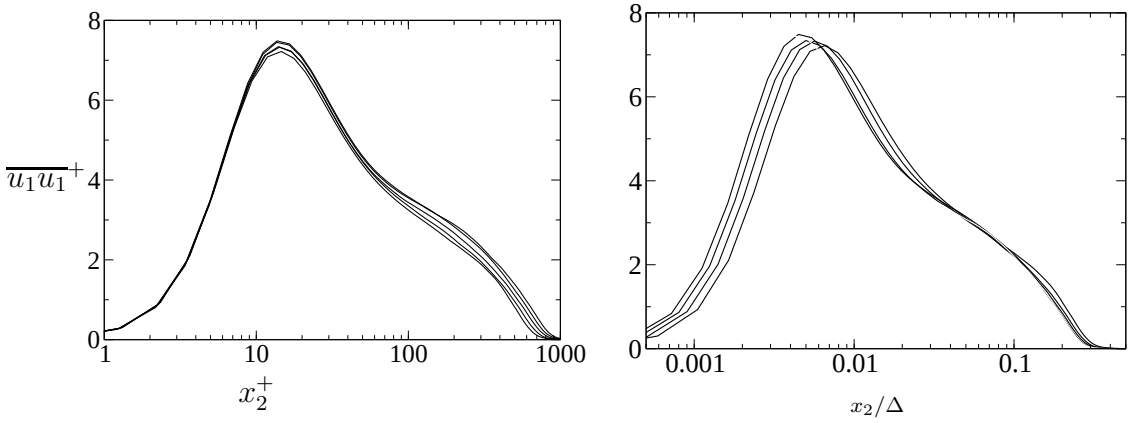

Figure 9.2: $\overline{u_1u_1}$ in inner (Left plot) and in outer scalings (Right plot) for $Re_\theta = 1670, 1870, 2060, 2240$

wall behavior is presented in Figure 9.3. The dashed line in this figure represents

the first term of the Taylor series expansion of $\overline{u_1 u_1}^+$ around $y = 0$ (Monin & Yaglom 1971),

$$\overline{u_1 u_1}^+ = 0.16(y^+)^2 + \cdots$$

which is accurate below $x_2^+ \approx 4$.

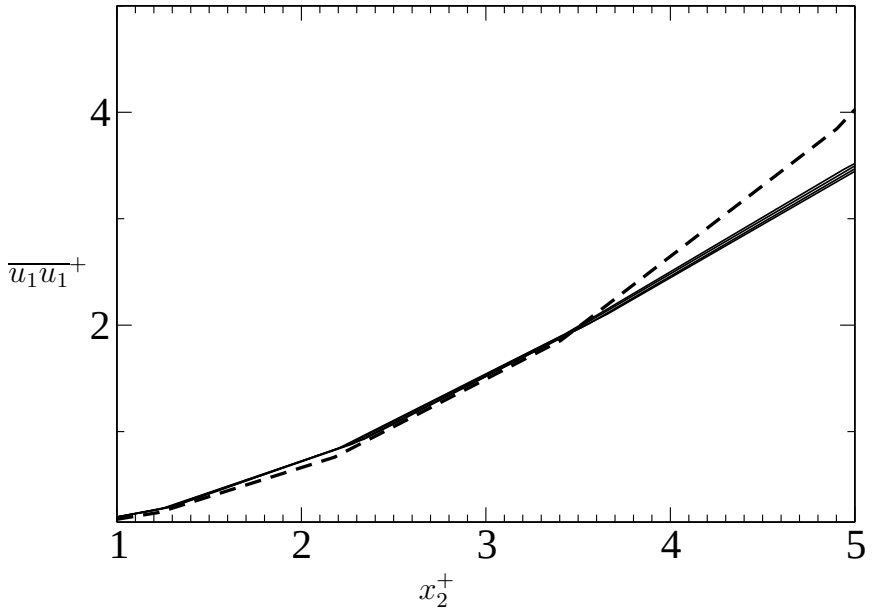

Figure 9.3: $\overline{u_1 u_1}^+$ in inner scaling very near the wall, —— DNS results, --- $0.16(y^+)^2$).

As it was mentioned above, DeGraaff & Eaton (2000) introduced a new scaling for $\overline{u_1 u_1}$. It was shown that the mixed scaling nicely collapses the data and sublayer and buffer layer profiles fall on a single curve when plotted as $\overline{u_1 u_1}/u_\tau \bar{u}_\infty$ versus x_2^+. The same result was obtained by Metzger, Klewicki, K.L. & Sadr (2001) over an extended Reynolds number range.

The streamwise Reynolds stress component for the same Reynolds numbers as in Figure 9.2, is presented in Figure 9.4 for the mixed-inner (left plot) and mixed-outer (right figure) scalings. The present result supports the validity of this new scaling. In this scaling the peak of $\overline{u_1 u_1}/u_\tau \bar{u}_\infty$ is collapsed to 0.32 a number which is also obtained by DeGraaff & Eaton (2000).

Wall-Normal and spanwise normal stresses

The wall normal component of the velocity fluctuation is very important for turbulent boundary layer flow. Measurements of this quantity are very rare. Because

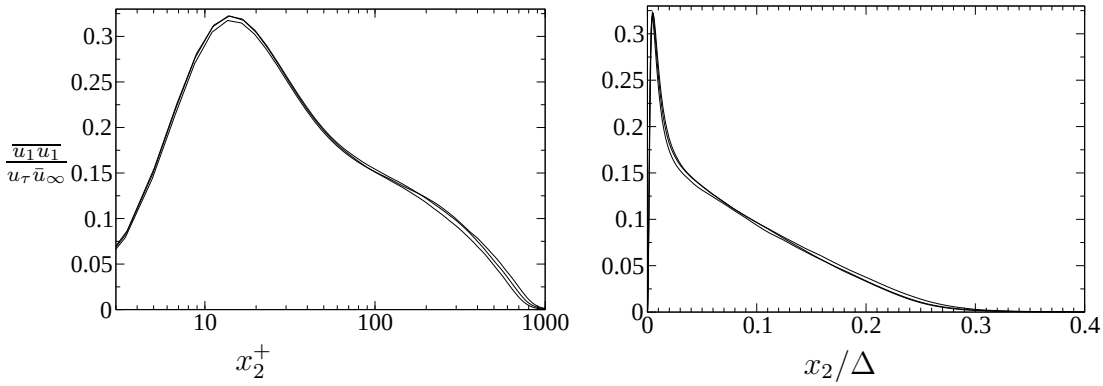

Figure 9.4: $\overline{u_1u_1}^+$ in the mixed-inner (left figure) and mixed-outer (right figure) scalings introduced by DeGraaff & Eaton (2000).

of this fact, DNS becomes a very important tool in the study of this quantity. Figure 9.5 shows the normal Reynolds stress in inner and outer scalings (top plots). $\overline{u_2u_2}^+$ peaks at $x_2^+ \approx 100$ with the value $(\overline{u_2u_2}^+)_{peak} = 1.2$. The profiles of the wall-normal Reynolds stress peaks around $x_2/\Delta \approx 0.05$. However, the peaks show a Reynolds number dependence. In the same figure the behavior of the spanwise component $\overline{u_3u_3}^+$ of the Reynolds stress tensor in both scalings is shown. The profiles of this component peaks approximately at $x_2^+ = 40$ at a magnitude of $(\overline{u_3u_3})^+_{peak} \approx 2.1$. The maximum is closer to the wall than in the case of the wall-normal Reynolds stress. It shows good collapse in inner scaling below $x_2^+ \approx 200$. In contrast in outer scaling there is no good collapse for different Reynolds numbers.

Reynolds shear stress

The formula

$$(x_2^+)_{peak} = Re_\theta^{0.61}$$

gives an empirical scaling law where the Reynolds shear stress peaks near the wall. For our Reynolds number ($Re_\theta = 2240$) this leads to the value of $x_2^+ = 110$. This is indeed different from the value obtained from our DNS. We got the peak magnitude of $-\overline{u_1u_2}^+ = 0.92$ at $x_2^+ \approx 60$. As one can see from Figure 9.6 the profile behavior is similar to that of the wall-normal Reynolds stress, but the data are more scattered. Spalart (1988) found that for $Re_\theta = 1410$ the magnitude of the peak $-\overline{u_1u_2}^+ = 0.91$ is located at $x_2^+ = 58$. DeGraaff & Eaton (2000) got from their experiments: $-\overline{u_1u_2}^+_{peak} = 0.95$ at $(x_2^+)_{peak} \approx 70$.

Figure 9.7 shows shear stress distributions in plus units.

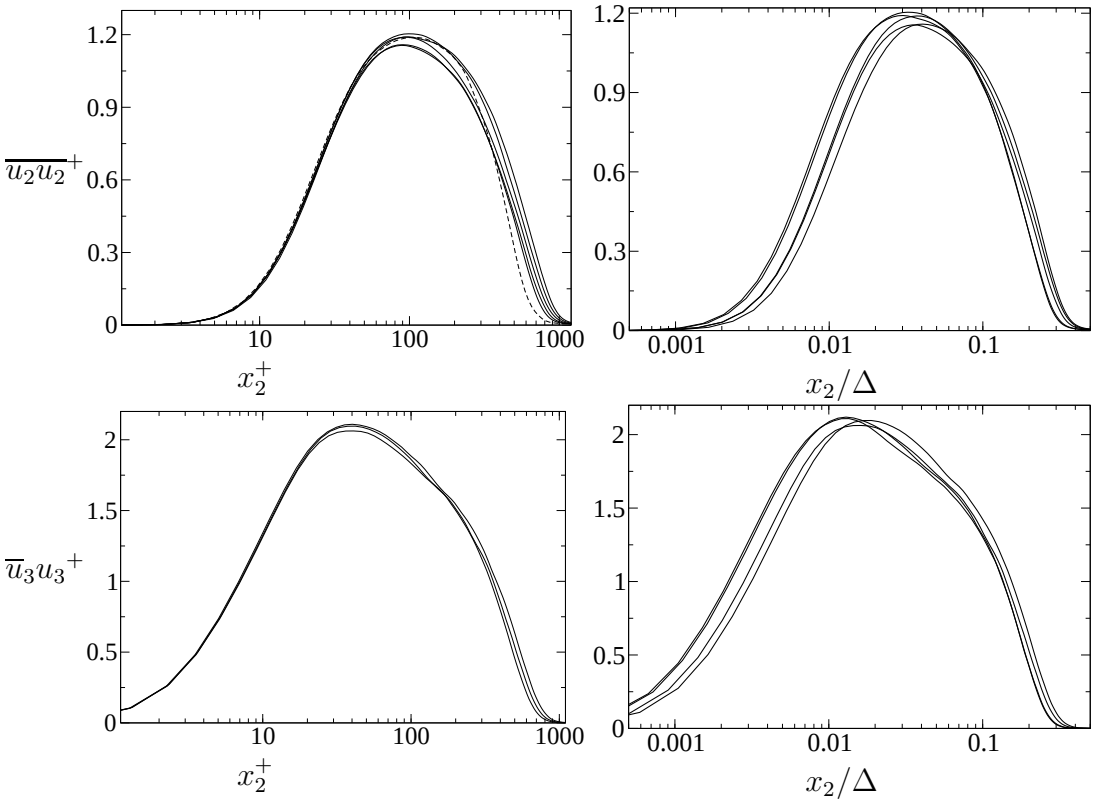

Figure 9.5: $\overline{u_2u_2}$ and $\overline{u_3u_3}$ in inner and outer scalings for Reynolds numbers $Re_\theta = 1670, 1870, 2060, 2240$.

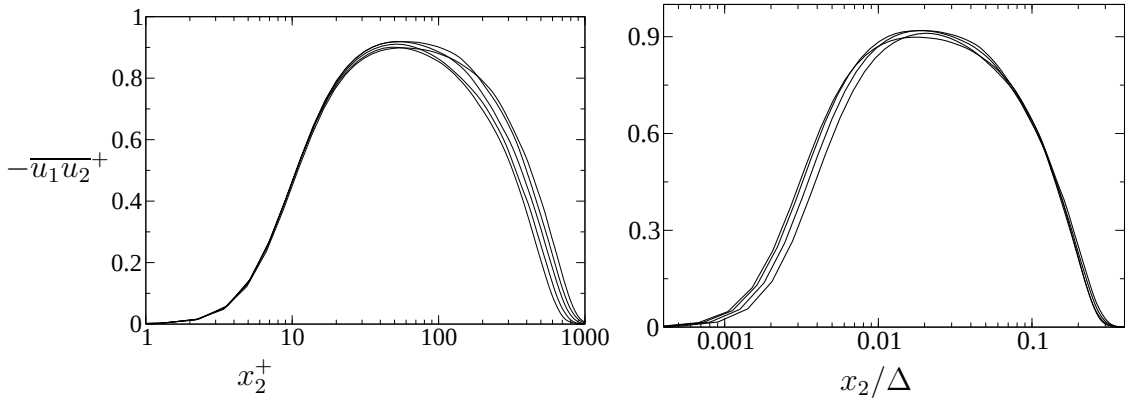

Figure 9.6: Reynolds shear stress $-\overline{u_1u_2}$ in inner (Left plot) and outer scalings (Right plot).

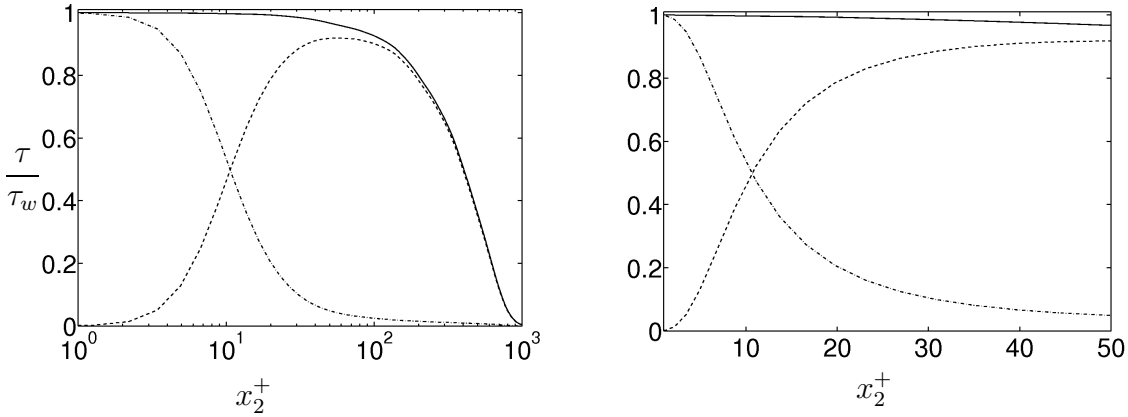

Figure 9.7: Shear stress distribution (linear-log axes) for $Re_\theta = 2240$ (left figure); Near-wall behavior on the right plot. --- viscous shear, —·— Reynolds shear, —— total shear.

9.1.2 Two-point statistics

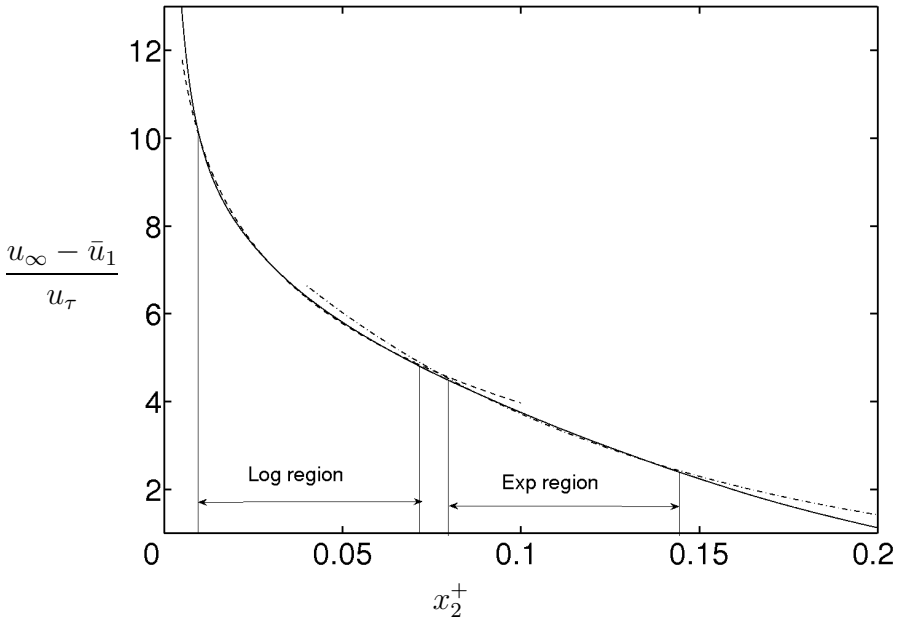

Figure 9.8: Velocity profile at $Re_\theta = 2240$. —— DNS, - - - log-law, —·— exponential law.

Figure 9.8 shows mean velocity profile in the outer scaling. DNS, exponential law and log-law are plotted together on this plot. Exponential region is in the range of $x_2^+ \approx 0.9 - 0.15$. There is the small region between log and exponential regions where both of the laws are not valid.

For the high Reynolds number case simulations TPC functions were computed for $x_2/\Delta = 0.028, 0.057, 0.085$ initial points which are located in the log region.

TPCs are represented in Figure 9.9 as normalized $\mathcal{R}_{22}$ (left plot) and non-normalized R_{22} (right plot) functions in outer scaling for different initial points $x_2/\Delta = 0.028, 0.057, 0.085$ which in the plus units correspond to $x_2^+ = 85, 173, 259$ at the high Reynolds number $Re_\theta = 2240$.

As for the exponential region, three different points were taken for the initial points for the calculation TPC functions ($x_2/\Delta = 0.095, 0.126, 0.16$). In the plus units these numbers are $x_2^+ = 266, 353, 448$.

Figure 9.10 shows non-normalized TPC functions calculated in the exponential region. In the next figure the same functions are represented, but normalized by the Reynolds stresses. From the equation (8.8) we have that normalized TPC functions

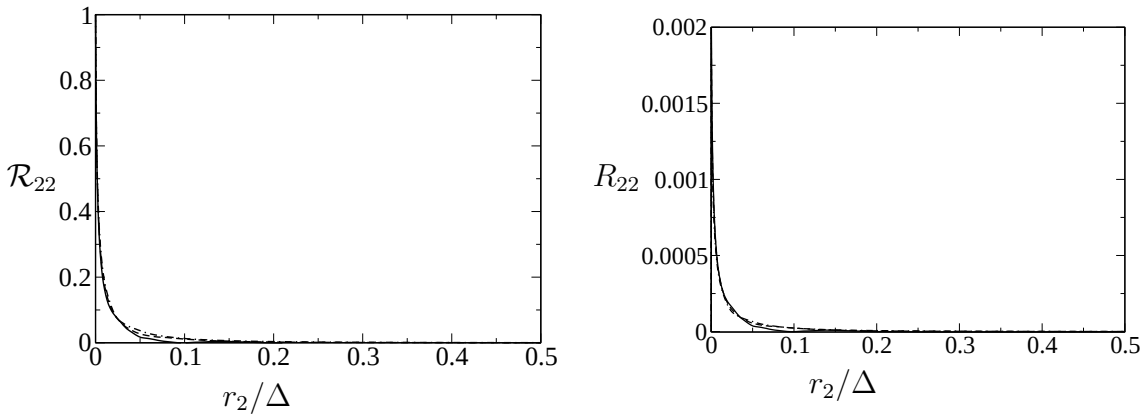

Figure 9.9: TPC functions at $Re_\theta = 2240$ at different initial points. —— $x_2/\Delta = 0.028$, - - - $x_2/\Delta = 0.057$, —·— $x_2/\Delta = 0.085$: normalized on Reynolds stress ($\mathcal{R}_{22}(r_2)$) and non-normalized ($R_{22}(x_2, r_2)$).

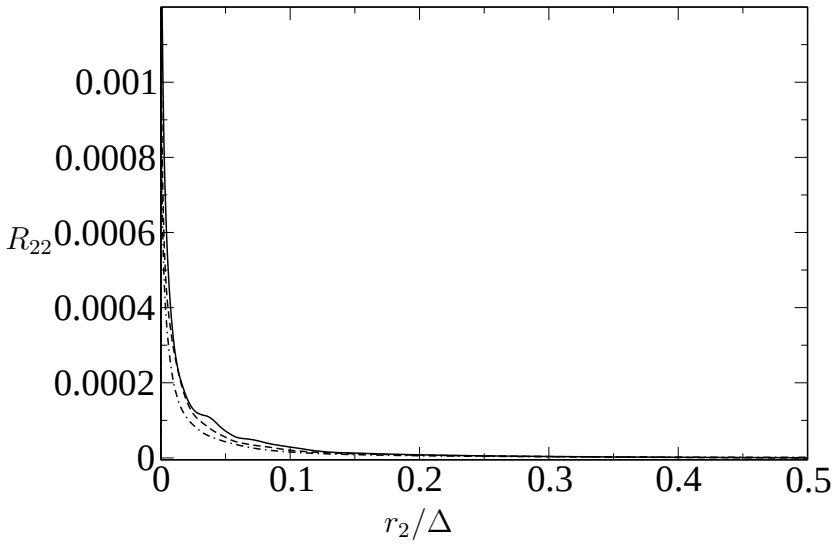

Figure 9.10: Non normalized TPC functions at $Re_\theta = 2240$ at different initial points in the exponential region. —— $x_2/\Delta = 0.095$, - - - $x_2/\Delta = 0.126$, —·— $x_2/\Delta = 0.16$:

should should collapse for the different initial points in wall-normal direction(x_2). Figure 9.11 shows that all TPC functions calculated from the different point from the wall collapse.

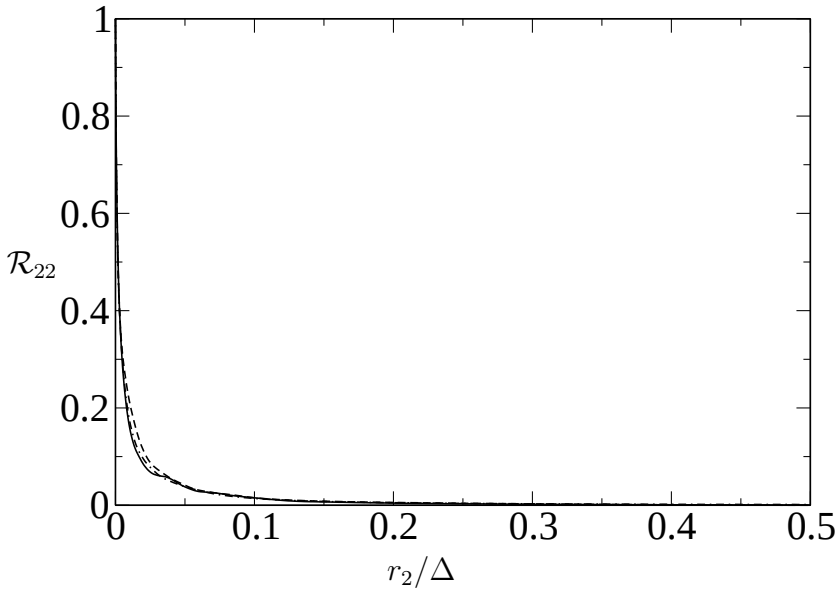

Figure 9.11: Normalized TPC functions at $Re_\theta = 2240$ at different initial points in the exponential region. —— $x_2/\Delta = 0.095$, - - - $x_2/\Delta = 0.126$, —·— $x_2/\Delta = 0.16$:

9.2 Simulations at $Re_\theta = 2500$

9.2.1 One-point statistics

Streamwise normal stresses

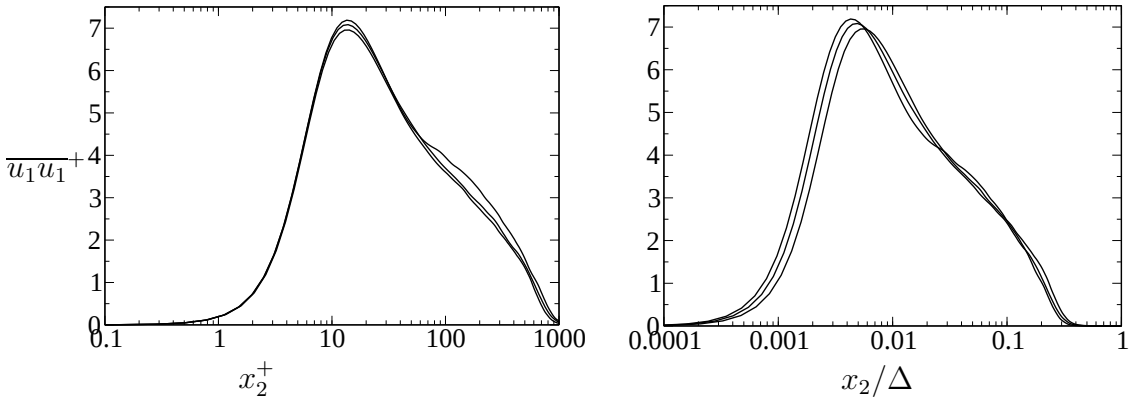

Figure 9.12: Streamwise Reynolds stresses for $Re_\theta = 1824, 2070, 2300$ in inner and outer scaling.

In Figure 9.12 streamwise Reynolds stresses are presented in inner and outer scaling. Equations (8.2) and (8.1) give the location and the peak value of $\overline{u_1u_1}^+$ respectively:

$$x_2{}^+{}_{peak} = 14.79, \qquad \overline{u_1u_1}^+_{peak} = 8.009.$$

The DNS data gives the following values:

$$x_2{}^+{}_{peak,DNS} = 13.49, \qquad \overline{u_1u_1}^+{}_{peak,DNS} = 7.189.$$

In the Figure 9.13 streamwise normal stresses are presented in the mixed-inner and mixed-outer scaling introduced by DeGraaff & Eaton (2000). Mixed-inner scaling shows better collapse than classical plus scaling. Mixed-outer scaling shows improved collapse of the stresses.

Wall-normal and spanwise normal stresses

Figure 9.14 displays wall-normal stresses in inner and outer scalings. The collapse of the lines for different Reynolds numbers (different measurement point in streamwise direction) is not satisfactory. It can be caused by the considerably smaller

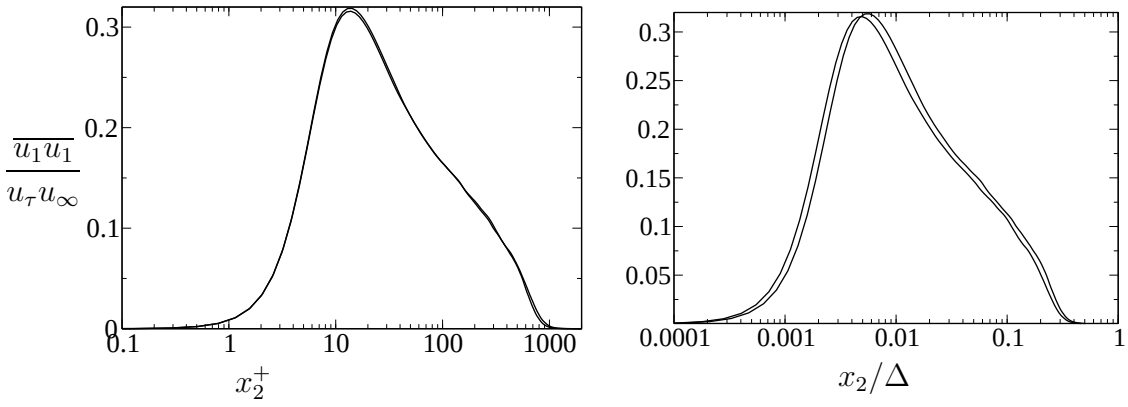

Figure 9.13: Streamwise Reynolds stresses for $Re_\theta = 1824, 2070$ in inner and outer scaling.

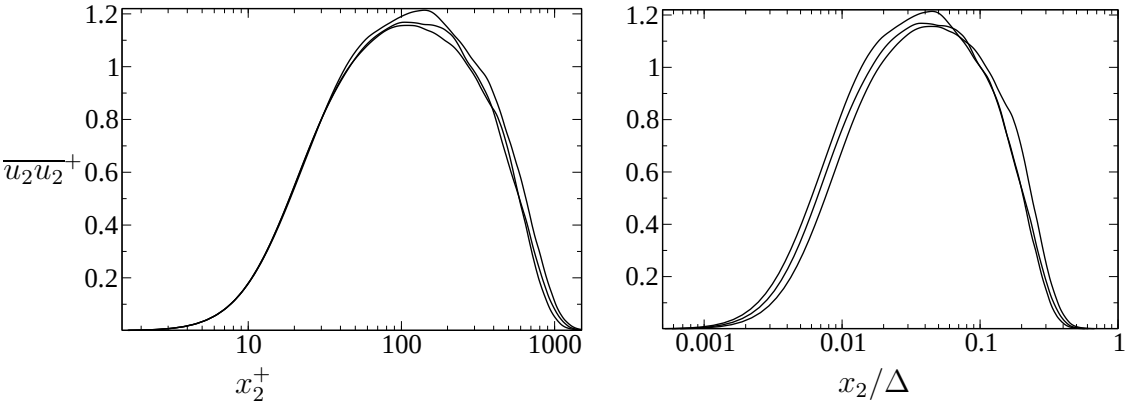

Figure 9.14: Wall-normal Reynolds stresses for $Re_\theta = 1824, 2070, 2300$ in inner and outer scaling.

simulation time in this case (statistics accumulation time was a few times less then in the previous simulations because of the required huge computer resources).

Equation (8.3) gives the following value for the location of the peak of $\overline{u_2 u_2}^+$: $(x_2^+)_{peak} \approx 146$, while DNS gives $(x_2^+)_{peak,DNS} \approx 104$, $\overline{u_2 u_2}^+_{peak} = 1.168$.

Figure 9.15 shows spanwise stresses in inner and outer scalings for three different Reynolds numbers. The peak value for the spanwise Reynolds stresses is: $\overline{u_3 u_3}_{peak} = 2.1318$ in $(x_2^+)_{peak,DNS} \approx 38.4$.

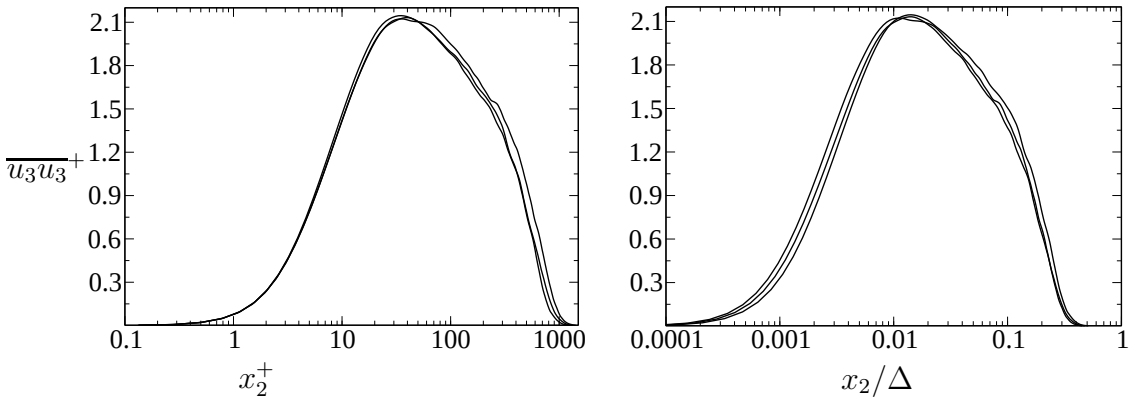

Figure 9.15: Spanwise Reynolds stresses for $Re_\theta = 1824, 2070, 2300$ in inner and outer scaling.

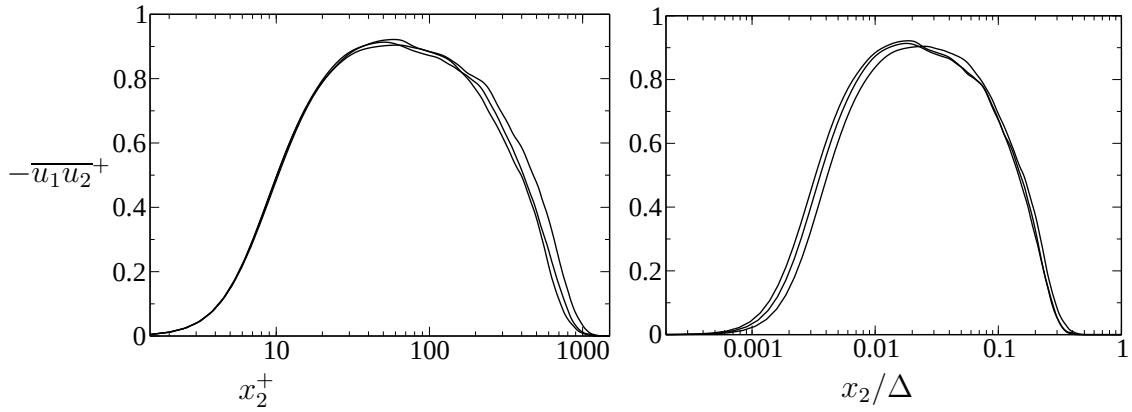

Figure 9.16: Reynolds shear stresses for $Re_\theta = 1824, 2070, 2300$ in inner and outer scaling.

Reynolds shear stresses

In Figure 9.16 Reynolds shear stresses are plotted in inner and outer scaling. In inner scaling near the wall the data show good collapse. In outer scaling away from the wall the collapse of the plots for different Reynolds numbers is not so good as in the former case. $(-\overline{u_1u_2})_{peak} = 0.91$ at $(x_2^+)_{peak,DNS} \approx 50.13$. Turbulent energy plots are shown in Figure 9.17 in plus units.

Figure 9.18 shows shear stress distributions in the whole region (left plot) and its near wall behavior (right plot). The viscous shear and Reynolds shear cross in the point $x_2^+ = 10$.

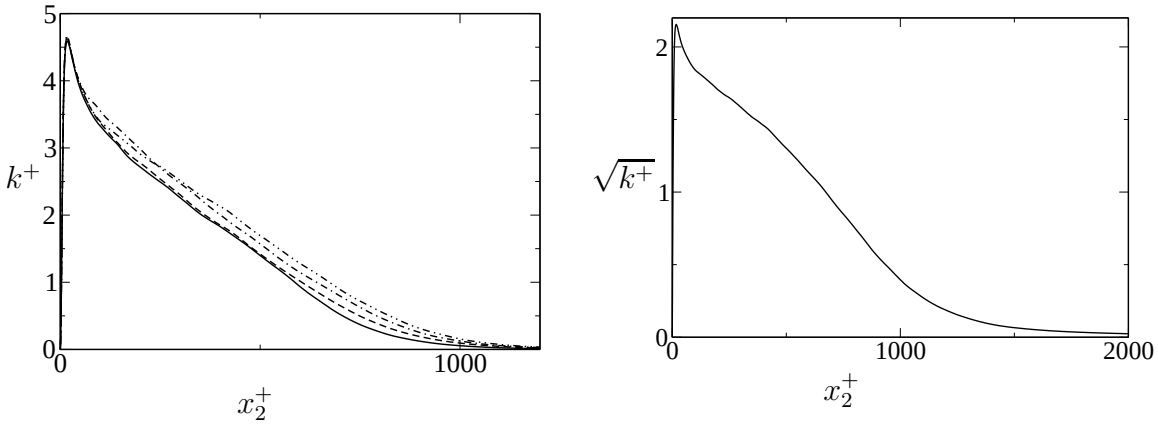

Figure 9.17: Turbulent energy in plus units at $Re_\theta = 2500$.

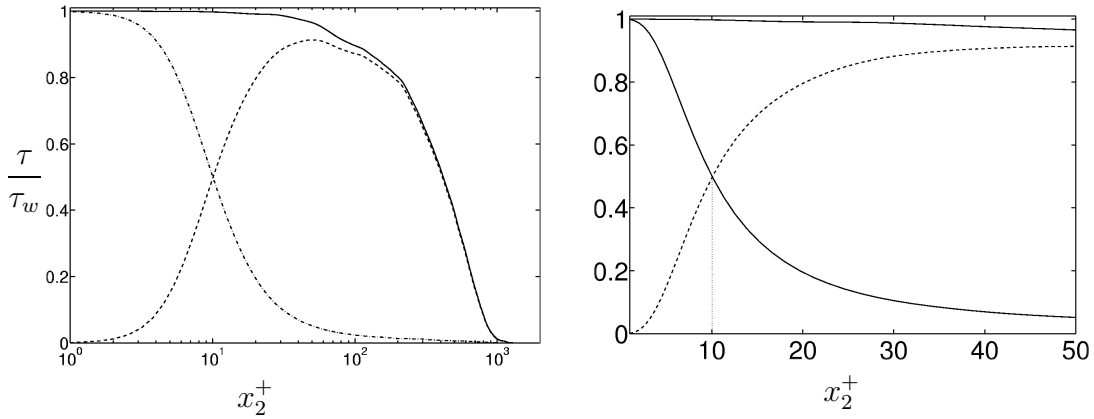

Figure 9.18: Left figure: Shear stress distribution (linear-log axes) for $Re_\theta = 2500$. --- viscous shear, —·— Reynolds shear, —— total shear; Right figure: Near wall behavior of the shear stresses at the same parameters as in the left figure.

10 Turbulent scaling laws

10.1 Scaling law validation: Exponential law

Though the new scaling laws have a rigorous derivation from Lie group analysis, it is not clear a priori that these solutions physically exist in the flow. Particularly since turbulent scaling laws only have a limited region of validity. Hence the phrase 'validation' in the present context means a comparison between theory and DNS.

$$\frac{\bar{u}_\infty - \bar{u}_1}{u_\tau} = \alpha \, \exp\left(-\beta \frac{x_2}{\Delta}\right). \tag{10.1}$$

$$\frac{\overline{u_i u_j}(x_2)}{u_\tau^2} = b_{ij} \, \exp\left(-a \frac{x_2}{\Delta}\right), \tag{10.2}$$

$$R_{ij}(x_2, \boldsymbol{r}) = e^{-k_4 x_2} B_{ij}(\boldsymbol{r}), \tag{10.3}$$

$$\overline{u_i p}(x_2, \boldsymbol{r}) = e^{-(k_3+k_4)x_2} E_i(\boldsymbol{r}), \tag{10.4}$$

$$\overline{p u_i}(x_2, \boldsymbol{r}) = e^{-(k_3+k_4)x_2} F_i(\boldsymbol{r}). \tag{10.5}$$

Equations (10.1–10.5) are the basic results from Lie group analysis performed for TPC equations.

The main aim of this chapter is to show the validity of these laws, compare DNS results of different Reynolds numbers with the theoretical ones.

The mean velocity of the turbulent boundary layer data is plotted in Figure 10.1 for $Re_\theta = 2240$. As one can see from the figure, DNS and the theoretical result 10.1 are in good agreement in the region $x_2/\Delta \approx 0.01 - 0.15$. Above this region the velocity defect law in the outer part of the boundary layer decreases more rapidly than what was derived from the theoretical result. There may be two reasons for this. First it might be the result of the low Reynolds number phenomenon in DNS while for the derivation of the theoretical results we assumed the large Reynolds number limit. Second, as it is argued in Lindgren et al. (2004) the non-parallel effects become dominant in the outer part of the wake region, which could cause the deviation from the exponential law, while the theoretical results were derived assuming a fully parallel flow. Because of these reasons, we have a relatively

small "coincidence region" of the theoretical and DNS results. The close up of mean velocity profiles is presented in Figure 10.2 at different Reynolds numbers $Re_\theta = 1670, 1870, 2060, 2240$. Good collapse of the profiles in the exponential region is observed.

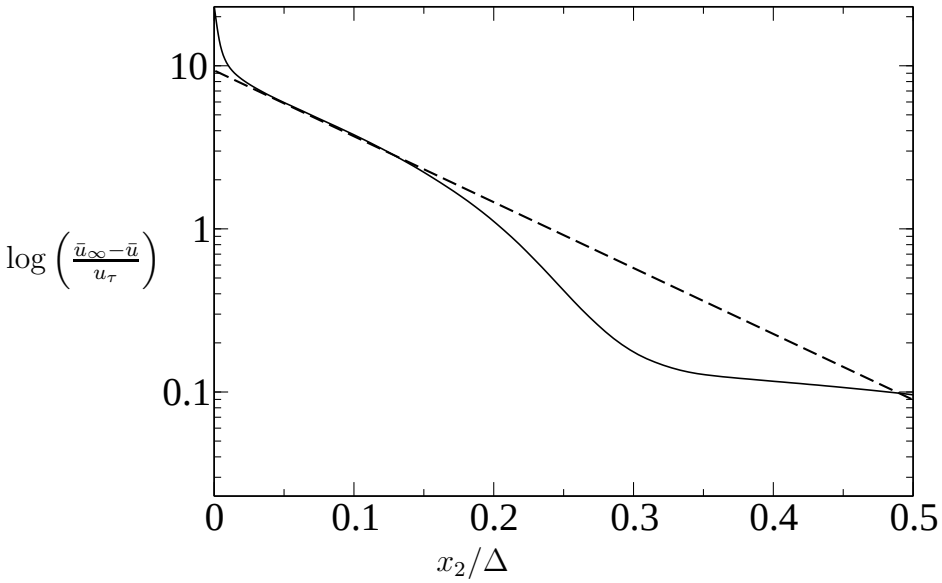

Figure 10.1: Mean velocity profile in log-linear scaling. --- theoretical result from the law (4.29). —— DNS results for the simulation $DNS2000a, b$.

In Figures 10.3 and 10.4 the mean velocity profiles from DNS ($Re_\theta = 2500$) are compared to the theoretical result. As one can see from the figure the exponential region is larger in this case than for the Reynolds number mean velocity profiles displayed in Figures 10.1 and 10.2. The exponential region covers the range $x_2/\Delta \approx 0.01 - 0.2$ which in plus units corresponds to $x_2^+ \approx 34 - 680$.

Figure 10.5 represents Reynolds stresses in log-outer scaling showing exponential regions at Reynolds number $Re_\theta = 755$ (simulations $DNS600a-c$). The difference between the exponential regions for different Reynolds stresses is expressed just in the coefficients b_{ij} (see Figure 10.1), but the coefficient in the exponent a is the same for all stresses. This fact is clearly seen from Figure 10.5. The exponential regions for $\overline{u_i u_i}$ are parallel to each other, and even have almost the same length. The exponential law covers the region $x_2/\Delta \approx 0.06 - 0.14$ ($x_2^+ \approx 66 - 155$). In the case of the wall-normal Reynolds stress, it extends up to $x_2/\Delta \approx 0.16$ ($x_2^+ = 178$).

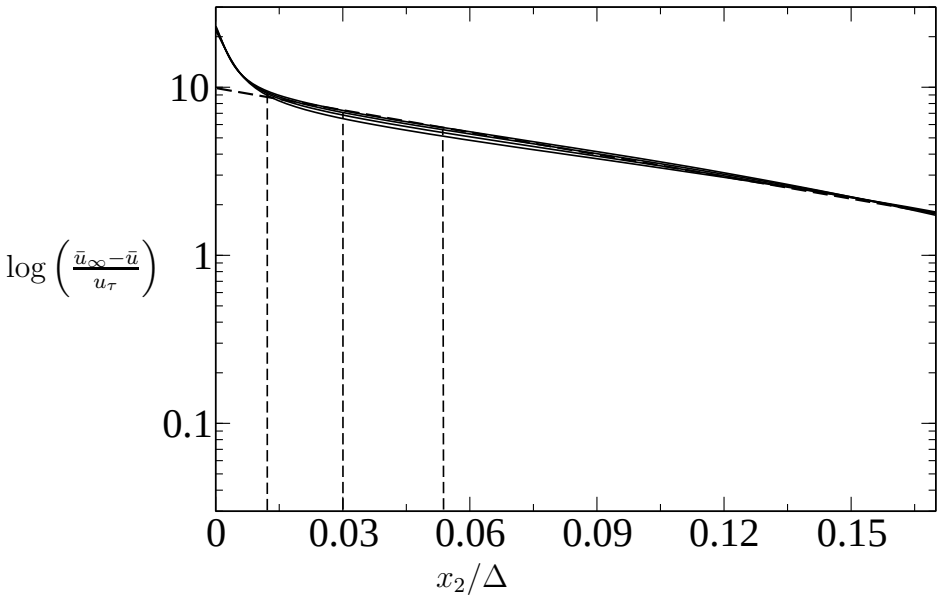

Figure 10.2: Close up plots of the mean velocity profile in log-linear scaling at different Reynolds numbers ($Re_\theta = 1670, 1870, 2060, 2240$).

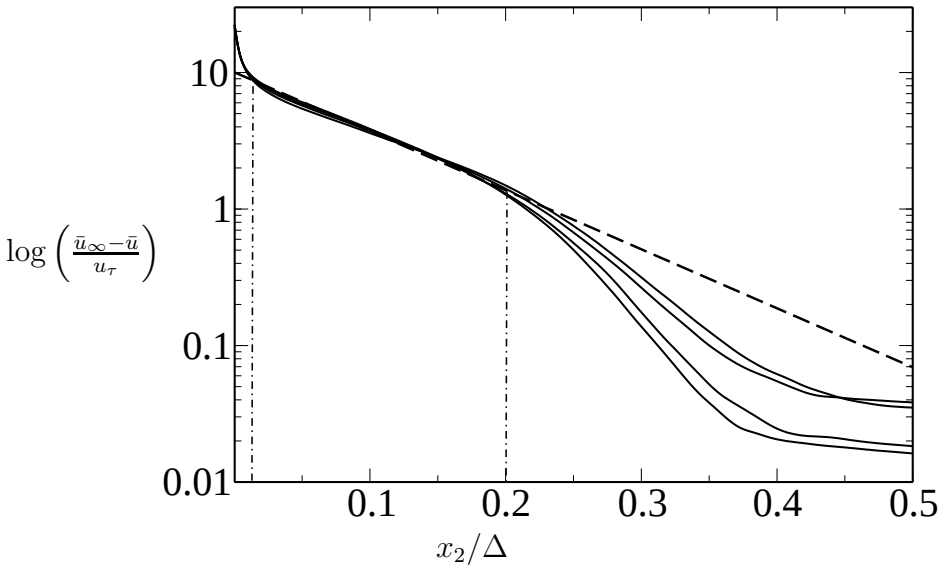

Figure 10.3: Mean velocity profile in log-linear scaling. --- theoretical result from the law (4.29). — DNS results at $Re_\theta = 1824, 2070, 2301, 2500$.

Using DNS we can find the constants in equation (10.2):

$$\begin{aligned} \overline{u_1 u_1}(x_2) &= 4.55 e^{-7.2 x_2}, \\ \overline{u_2 u_2}(x_2) &= 2.7 e^{-7.2 x_2}, \\ \overline{u_3 u_3}(x_2) &= 1.8 e^{-7.2 x_2}. \end{aligned} \tag{10.6}$$

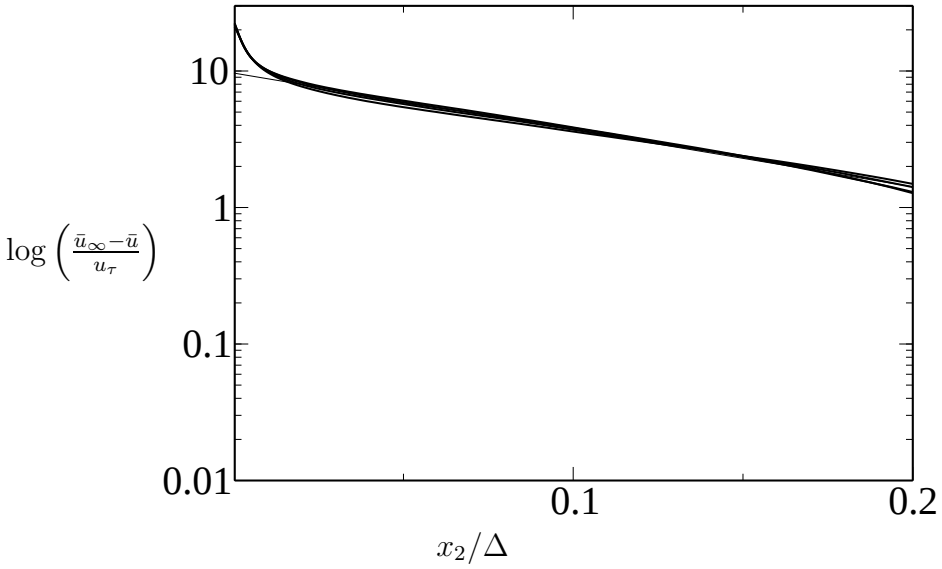

Figure 10.4: M an v

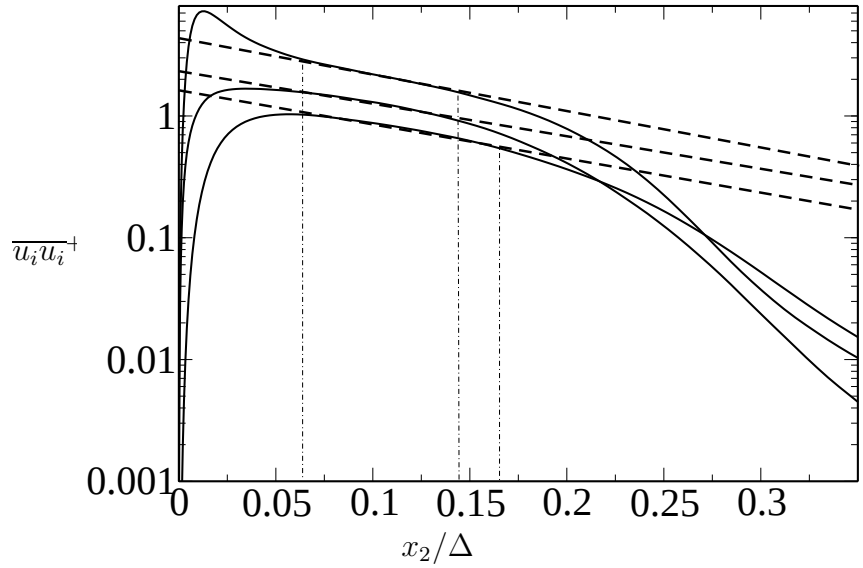

Figure 10.5: Reynolds stresses ($\overline{u_1u_1}$; $\overline{u_2u_2}$; $\overline{u_3u_3}$). —— DNS ($Re_\theta = 615, 690, 755$), - - - theoretical result.

We found that the constant in equation (10.2) is: $a = 7.2$. It validates the result of Lie group analysis.

The Reynolds stresses for Reynolds numbers $Re_\theta = 2240$ are presented in Figure

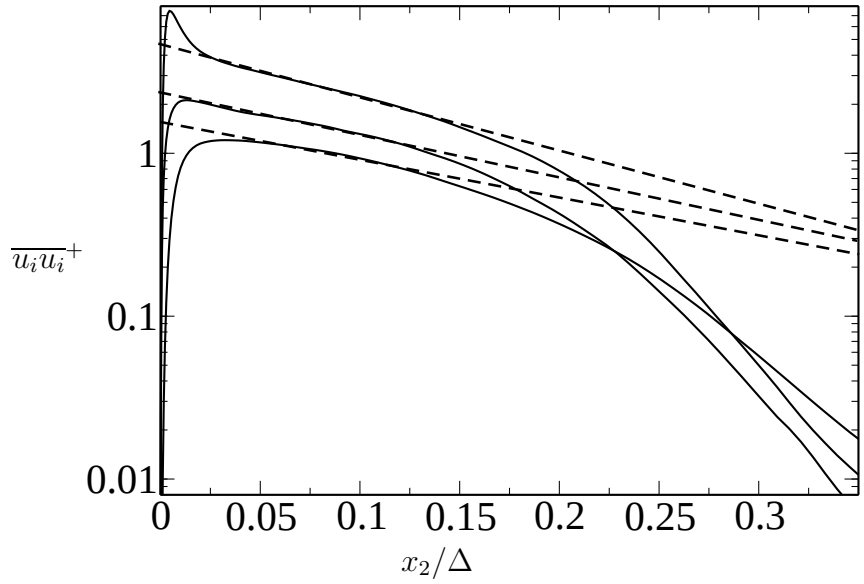

Figure 10.6: Reynolds stresses. —— DNS ($Re_\theta = 2240$), - - - theoretical results.

10.6 in log-outer scaling. The exponential region is clearly seen from the figure. The region of theoretical and DNS results coincidence covers $x_2/\Delta \approx 0.03 - 0.14$ ($x_2^+ \approx 67 - 314$) for all components of the Reynolds stress tensor. In this figure 10.6 the exponential regions are plotted together for normal Reynolds stresses. As we see the regions are almost parallel to each other as it should be according to the theoretical result. The small deviation can be caused by the simulation time which was not enough. The simulation time for this DNS case was about 5000 in the non-dimensional times. As for the Reynolds number case ($Re_\theta = 755$ (see Figure 10.5)) the simulation time was more then 30000 in the same units, and the results are excellent: the exponential regions are parallel to each other. The Reynolds normal stresses for the high Reynolds numbers $Re_\theta = 2500$ are presented in Figure 10.7 in log-outer scaling. The simulation time was even smaller in this case compared to the previous ones, because of the high Reynolds numbers which require very big numbers of grid points (about the DNS parameters see Section 7.2). The simulation time was enough to get smooth statistics, but it seems, that to get better results in the exponential regions we need to have more simulation time. However, the exponential region is clearly seen from the figure. The region of theoretical and DNS results coincidence covers $x_2/\Delta \approx 0.02 - 0.15$ ($x_2^+ \approx 62 - 472$). As we see, the exponential region in this case is much longer. This fact was expected, because the exponential law was derived in the case of infinite Reynolds number, and increasing the Reynolds number means increasing the exponential region.

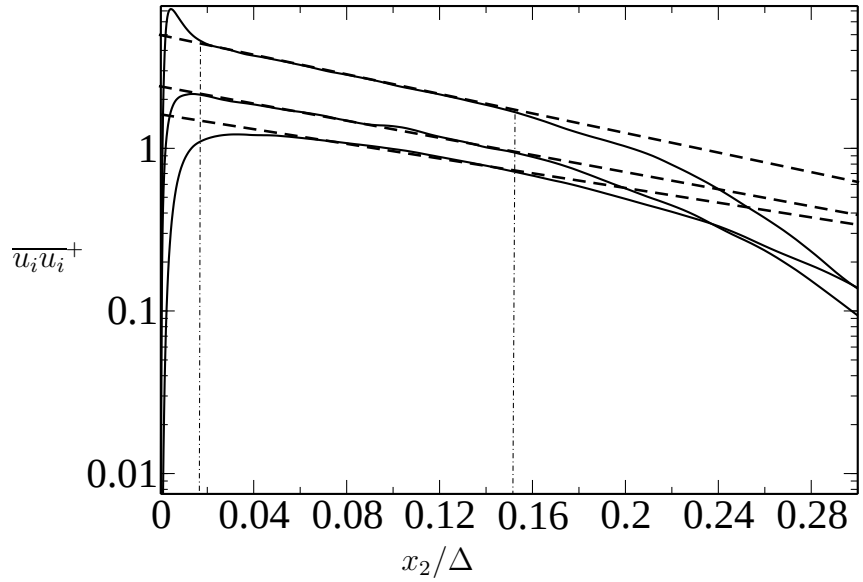

Figure 10.7: Reynolds stresses. —— DNS ($Re_\theta = 2500$), --- theoretical results.

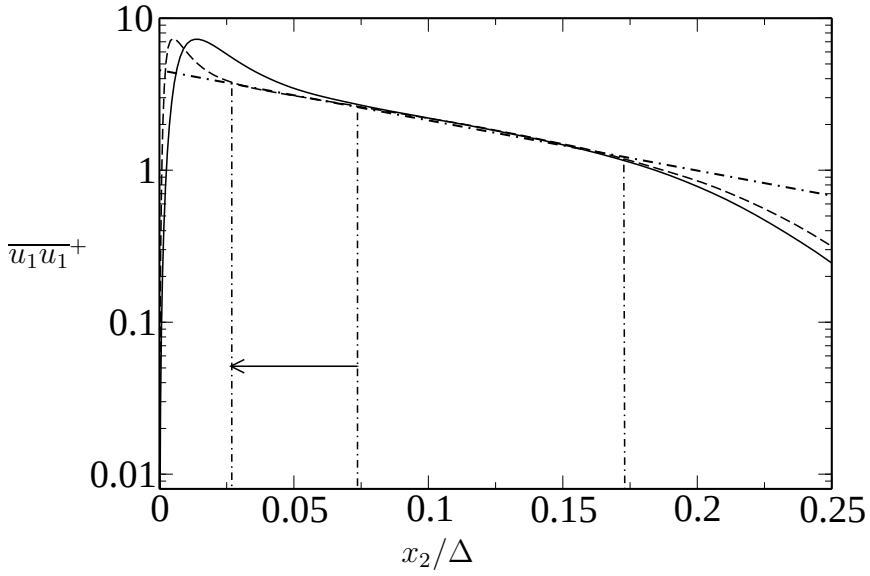

Figure 10.8: Longitudinal Reynolds stress component ($\overline{u_1 u_1}$) at Reynolds numbers: $Re_\theta = 755, 2240$ —·— DNS, —— $Re_\theta = 755$, --- $Re_\theta = 2500$.

Figure 10.8 shows the comparison of the longitudinal Reynolds stress component ($\overline{u_1 u_1}^+$) at two different Reynolds numbers $Re_\theta = 755, 2240$. The exponential region in the case of high Reynolds number is longer than in the low Reynolds number case. The arrow in the figure shows the direction of increasing of the

exponential when we increase Reynolds number. Thus, for the higher Reynolds number exponential region increases down to the wall.

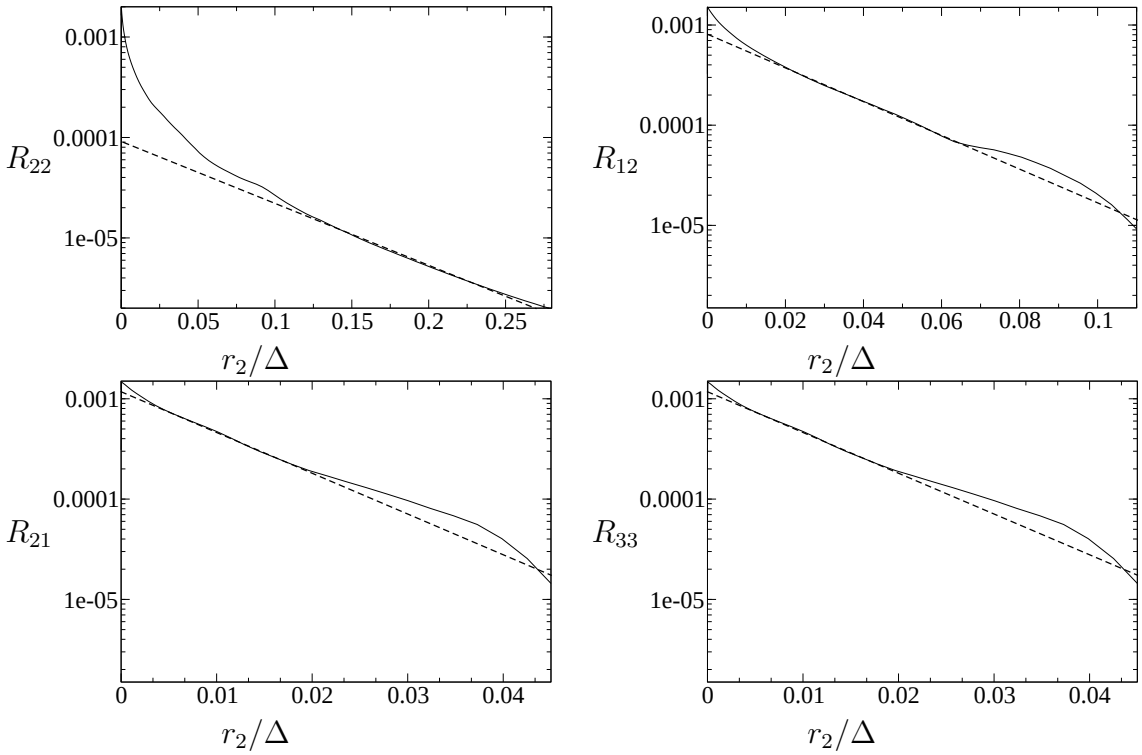

Figure 10.9: TPC functions, R_{22}, R_{12}, R_{21}, R_{33}; --- theoretical results, equation 10.3, —— DNS for $Re_\theta = 2240$.

TPC functions are represented in Figures 10.9. The region where the exponential law is valid, for different components of TPC function is different. For R_{22} the exponential law is valid in the interval $0.1 - 0.25$; For R_{12} and R_{21} these intervals are $0.02 - 0.06$ and $0.001 - 0.02$ respectively.

In Figure 10.10 DNS results are compared to the theoretical ones for the pressure-velocity correlations. The exponential region for $\overline{pu_1}$ is $x_2/\Delta \approx 0.04 - 0.18$, while the law for $-\overline{pu_2}$ is valid in the interval of $x_2/\Delta \approx 0.15 - 0.22$.

Comparison of the DNS results to the theoretical ones is very promising:

- The exponential law exists for all statistical quantities as it was predicted by the Lie group analysis;
- Increase of the Reynolds number increases the region where this law is valid;
- DNS allows us to find the constants in the formula of the exponential laws;

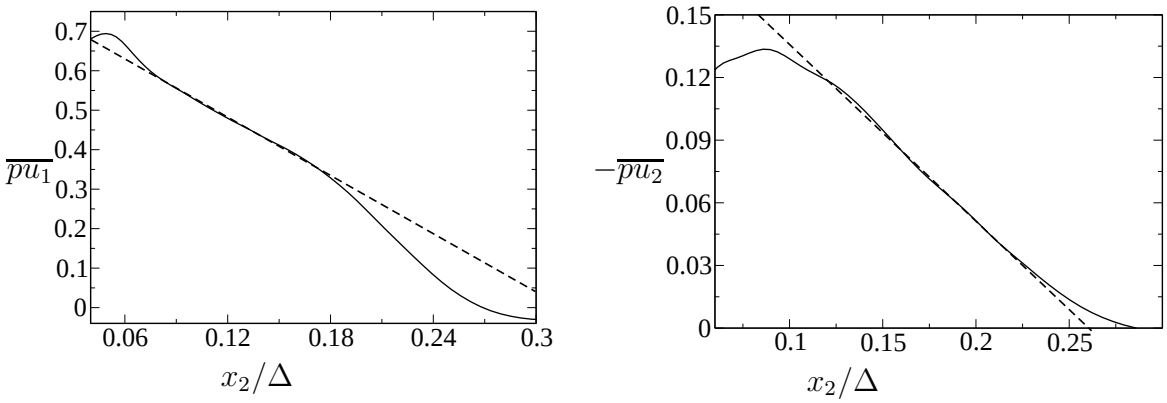

Figure 10.10: Pressure velocity correlations —— DNS ($Re_\theta = 690$), - - - theoretical result. Left figure: $\overline{pu_1}$; Right figure: $-\overline{pu_2}$;

- Statistics accumulation time is very important parameter for the validation of the exponential law.

10.2 Log-law in the overlap region

As it was mentioned in the introduction the classical theory of turbulent boundary layer flow leads to the classical log-law in the overlap region which has the form in the inner variables:

$$\bar{u}_1(x_2)^+ = \frac{1}{\kappa} ln(x_2^+) + B, \tag{10.7}$$

where κ and B are constants that have to be found from experiments and/or DNS. Here we would like to repeat the derivation of the log-law from Lie group analysis performed first by Oberlack (2001). In equation (4.23) the assumption $c_1 = c_2$ leads to the following ordinary differential equation:

$$\frac{dx_2}{c_1 x_2 + c_4} = \frac{d\bar{u}_1}{c_5}, \tag{10.8}$$

The solution to the equation is:

$$\bar{u}_1 = \frac{c_5}{c_1} ln(c_1 x_2 + c_4) + C_1, \tag{10.9}$$

where C_1 is the integration constant. c_1, c_4, c_5 are group constants. This equation can be rewritten in the following form using inner scaling:

$$\bar{u}_1(x_2)^+ = \frac{1}{\kappa} ln(x_2^+ + A^+) + B, \tag{10.10}$$

where A^+ is the additional constant in the logarithm.

To check the validity of the law is important for turbulence modeling (Buschmann & Gad-el Hak 2003). The authors discussed both, the classical logarithmic and the power low developed during the past few years. In the introduction the authors state that if the classical, Reynolds number independent log-law is fallible, the implications can be far reaching. Flow modelers, heavily rely on similarity principles to model turbulence quantities and close statistical equations. Practically all models are calibrated to reproduce the law of the wall in simple flows and failure of this universal law will guarantee the failure of Reynolds averaged models. It means that it is very important to prove whether the log-law is correct or not. In the paper of Buschmann & Gad-el Hak (2003) the authors concluded that the examined data do not indicate any statistically significant preference toward either law.

In the recent paper by Österlund et al. (2000a) the authors performed two independent experimental investigations of the behavior of turbulent boundary layers with different Reynolds numbers $Re_\theta = 2500 - 27000$. The experiments were performed

in two facilities, the minimum turbulence level wind tunnel at Royal Institute of Technology (KTH) and the National Diagnostic Facility wind tunnel at Illinois Institute of Technology. The aim of the experiments was to understand the characteristics of the overlap region between inner and outer region of the boundary layer flow. They state that no significant Reynolds number dependence for the parameters describing the overlap region using the classical logarithmic relation were found and that the data analysis shows the viscous influence to extend within the buffer layer up to $x_2^+ \approx 200$ instead of the previously assumed value $x_2^+ \approx 50$. The parameters of the log-law are constant: $\kappa = 0.38, B = 4.1$. The authors explain the result with the low Reynolds number effects in previous experiments.

Equation (10.10) has an additional constant in the logarithmic function in comparison to the classical one, and as it was found in (Lindgren et al. 2004) it gives a small modification of the innermost part of the log-law. They found that the modified log-law is valid down to about $x_2^+ = 100$ (in the paper (Österlund et al. 2000a) found the limit is $x_2^+ = 200$).

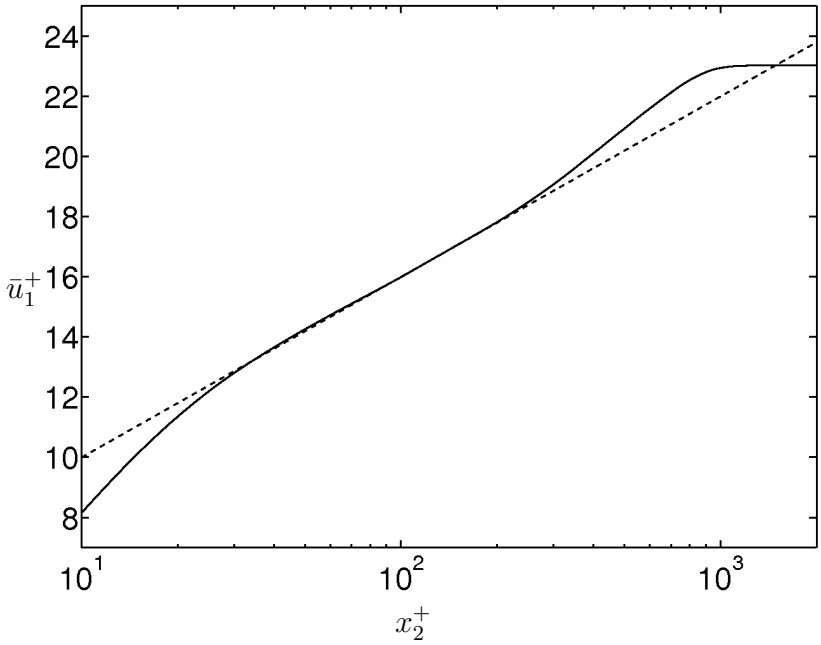

Figure 10.11: Mean velocity profile in inner scaling at $Re_\theta = 2500$. —— experiments and DNS data; - - - theoretical results (equation (10.7)).

Figure 10.11 shows comparison of the DNS results to the theoretical one (equation (10.7)). The constants for the log-law are: $\kappa = 0.383$ and $B = 4.1$. In Figure 10.12 the same velocity profile is shown but in normal scaling. The logarithmic region is located in the range of $x_2^+ \approx 30 - 220$.

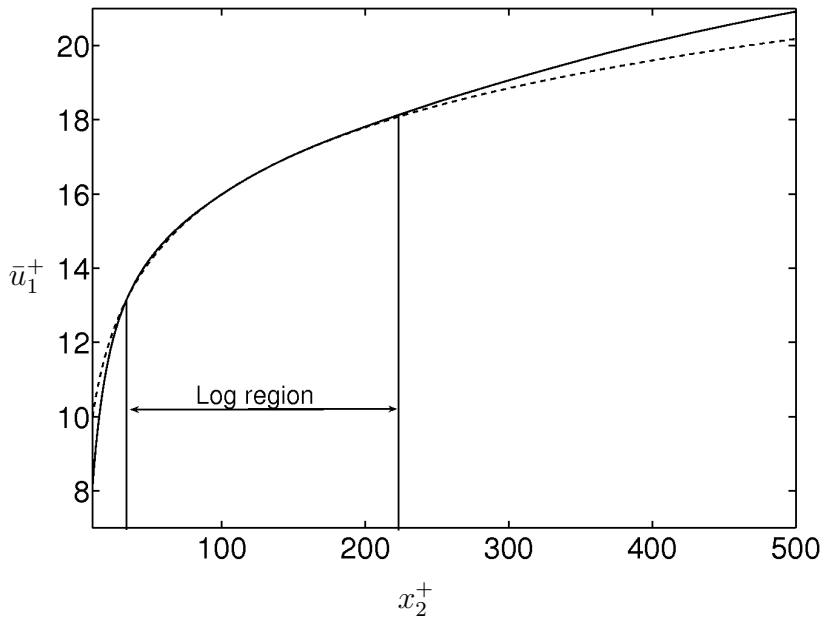

Figure 10.12: Mean velocity profile in inner scaling at $Re_\theta = 2500$. Parameters from Figure 10.11.

Figures 10.13 and 10.14 show mean velocity profile for modified log-law (see equation 10.10) for log and normal scaling. The constants for the logarithmic law are: $\kappa = 0.383$, $B = 4.0$ and $A = -0.13$. As it is seen from these figures, the log-region extends very little in comparison with the classical log-law.

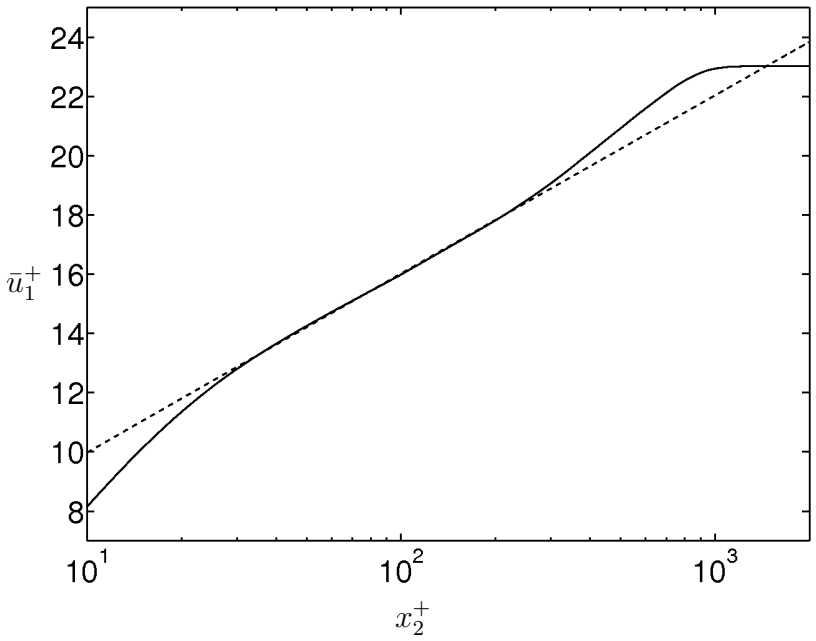

Figure 10.13: Mean velocity profile in inner scaling at $Re_\theta = 2500$ for the modified log-law. —— experiments and DNS data; - - - theoretical results (equation (10.10))

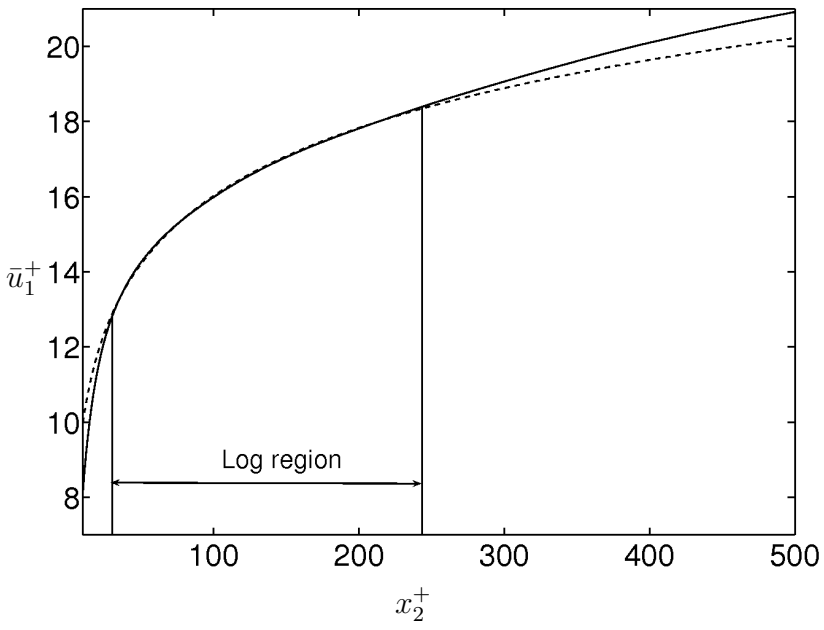

Figure 10.14: Mean velocity profile in inner scaling. Parameters from Figure 10.13.

Part IV

Coherent Structures and Wavelets

11 Coherent structures

Laboratory and numerical experiments have shown that, whatever their space dimension, geometry or Reynolds number, turbulent flows exhibit self-organization, that leads to the formation of **coherent structures**, which play an essential role in the flow dynamics, and should be taken into account in turbulence modeling (Hussain 1983).

It is a well-established fact that in a turbulent boundary layer there exist structures, so-called 'coherent structures' or 'organized structures', that are recognized to be an important component of the velocity and pressure fields. A coherent structure was described by Robinson (1991) as 'a three-dimensional region of the flow over which at least one fundamental flow variable exhibits significant correlation with itself or with another flow variable over a range of space and/or time that is significantly larger than the smallest local scales of the flow'.

The organized large-scale structures in turbulent boundary layers have been studied extensively for over five decades (see paper by Schoppa & Hussain (2002) and references therein). A comprehensive review of this development can be found in Robinson (1991). There is the broad evidence that a vortical structure qualitatively similar to the "horseshoe vortex" proposed by Theodorsen (1952) does exist in wall bounded turbulence. At low Reynolds number, Smith (1984) reported the existence of hairpin loops and proposed an organized alignment of these structures in the streamwise direction.

Nevertheless, the generation mechanism and dynamics of near-wall coherent structures are poorly understood.

Extensive experimental study of coherent structures in turbulent boundary layer flow was done by Adrian & Tomkins (2000), Adrian (2000), Christensen & Adrian (2001), Hommema & Adrian (2002) and Tomkins & Adrian (2003). Particle image velocimetry (PIV) was used to study the structure in the outer region of ZPG turbulent boundary layer flow. Experiments were performed at three Reynolds numbers in the range $930 < Re_\theta < 6845$. The authors found that the boundary layer is densely populated by velocity fields associated with hairpin vortices (hairpin represents cane, hairpin, horseshoe, or omega-shaped vortices). It was found that in the outer layer, hairpin vortices occur in streamwise-aligned packets that

propagate with small velocity dispersion (Adrian & Tomkins 2000). They found that individual packets grow upward in the streamwise direction at a mean angle of approximately 12^o.

The amount of information in turbulence obtained through the application of new experimental and computational tools is growing immensely in the last decades. There are different tools in fluid dynamics to investigate turbulent flows: PIV (particle image velocimetry) which gives 2D velocity vector fields, hodography PIV, DNS - 3D fields of all possible flow quantities, LES, large eddy simulations.

All these tools provide new information about the scales, kinematics and dynamics of turbulence. A huge amount of information initiates the development of new methods of extracting this information and post-processing of data. Adrian (2000) states that the fluctuating field taken from Reynolds decomposition may not constitute the best method for visualizing the turbulent mechanics of the flow. In the paper by Chakraborty & Adrian (2005) the authors analyse the different popular vortex identification criteria. A new measure of spiraling compactness of material orbits in vortices is introduced. In a long-studied field such as fluid mechanics a fundamental question about the vortex identification still has no clear answer. There is no single definition of the vortex universally accepted.

In the paper by Carlier & Stanislas (2005), the authors studied the coherent structures taking part in the generation and preservation of wall turbulence. The Reynolds number in their experiments were up to $Re_\theta = 19000$. Ganapathisubramani, Hutchins, Hambleton, Longmire & Marusic (2005) used two-point correlations to identify coherent structures in the flow. PIV measurements were done of a turbulent boundary layer at moderate Reynolds number ($Re_\tau \sim 1100$). The results obtained with this technique are consistent with an earlier study in which packets of hairpin vortices were identified in the log region. A low-Reynolds-number ZPG incompressible turbulent boundary layer was investigated using a volumetric imaging technique by Delo, Kelso & Smits (2004). The Reynolds number based on momentum thickness was 700. The authors found that in the outer portion of the boundary layer, structures were observed to lie along lines in the x_1x_3-plane, inclined to the streamwise direction in the range ± 50.

Jeong & Hussain (1994) proposed a definition of a vortex in an incompressible flow was proposed in terms of the eigenvalues of the symmetric tensor $\boldsymbol{S}^2 + \boldsymbol{\Omega}^2$, where $\boldsymbol{S}$ and $\boldsymbol{\Omega}$ are the symmetric and antisymmetric parts of velocity gradient tensor. Haller (2005) defined a vortex as a set of fluid trajectories along which the strain acceleration tensor is indefinite over directions of zero strain.

The regions of vorticity in turbulent flows have been identified in terms of filaments, sheets, and blobs. Quasi-streamwise vortices (Robinson 1991), 'hairpin'

vortices in wall turbulence ((Smith 1984), (Adrian & Tomkins 2000) and (Head & Bandyopadhyay 1981)) are important examples of coherent structures that approximate vortex filaments.

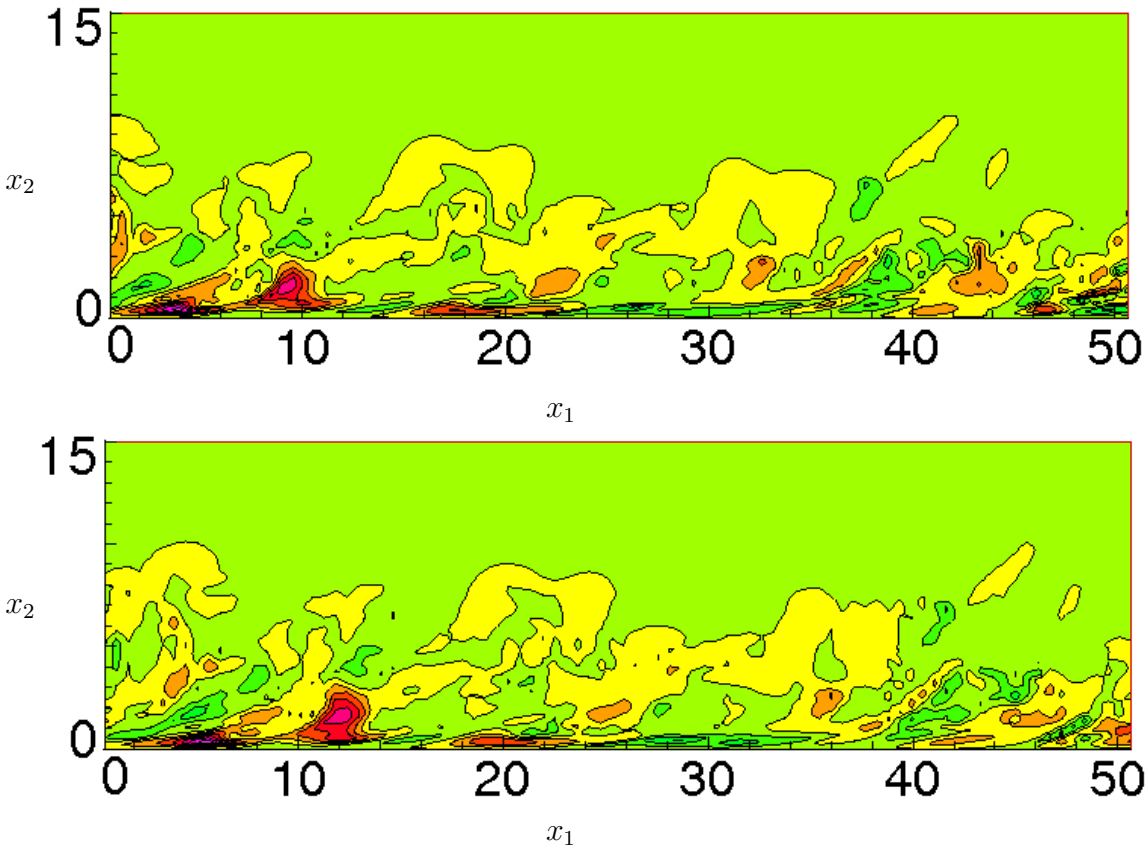

Figure 11.1: Wall-normal component of vorticity (ω_y) component for different time at $Re_\theta = 810$.

Figures 11.1 and 11.2 shows contours of wall-normal component of vorticity (ω_y) component at $Re_\theta = 810$ developing in time (time intervals are 5 in nondimensional units).

Figure 11.3 shows wall-normal component of vorticity in x_1x_2 plane. Four coherent structures are compared to each other. First three coherent structures are almost with the same angle oriented to the axes x_1, $52°, 50°$ and $49°$ respectively. The last one, which is located near the wall is inclined to the streamwise direction with $20°$ degree.

Figures 11.4, 11.5 and 11.6 show streamwise, wall-normal and spanwise vorticity components respectively near the entrance into the simulation box. The plots are

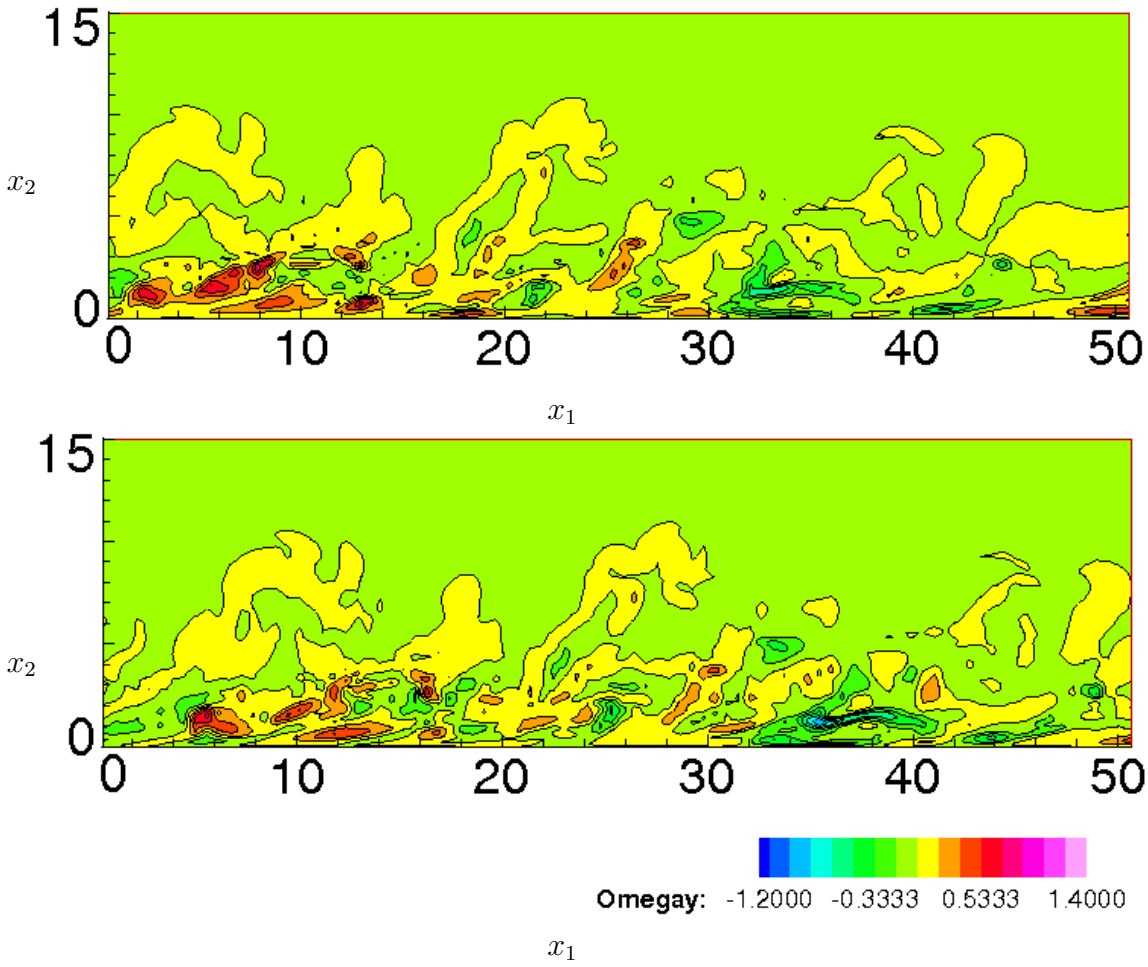

Figure 11.2: For the caption see Figure 11.1

done with the same parameters (contour levels, number of contours, etc.) for each component.

Figure 11.7 shows the time evolution of spanwise vorticity in a vertical plane aligned in streamwise direction. In this case the time intervals are approximately 30 in nondimensional units.

Spanwise velocity field ($3D$ case) isosurfaces $(-0.13, 0.14)$ for different Reynolds numbers are shown in Figures 11.8, 11.9 and 11.10.

Figure 11.11 shows streamwise vorticity fluctuations at $Re_\theta = 810$ in different planes from the wall: $x_2 = 1, 5$ or $x_2^+ \approx 28, 140$. From these figures it can be seen that structures of positive and negative vorticity in the lower slice $x_2 = 1$

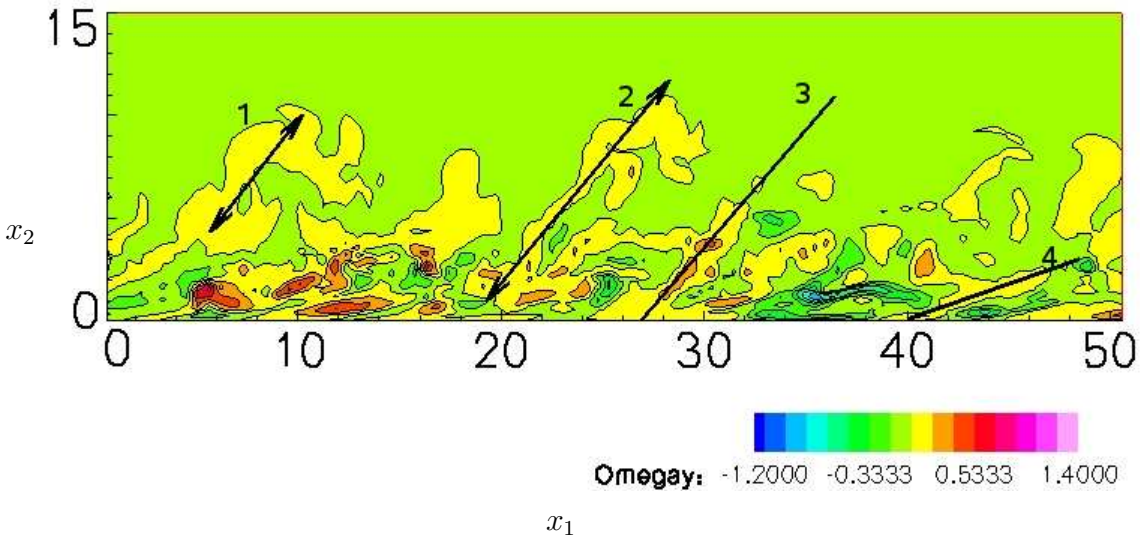

Figure 11.3: Wall-normal vorticity component (ω_θ) at $Re_\theta = 810$.

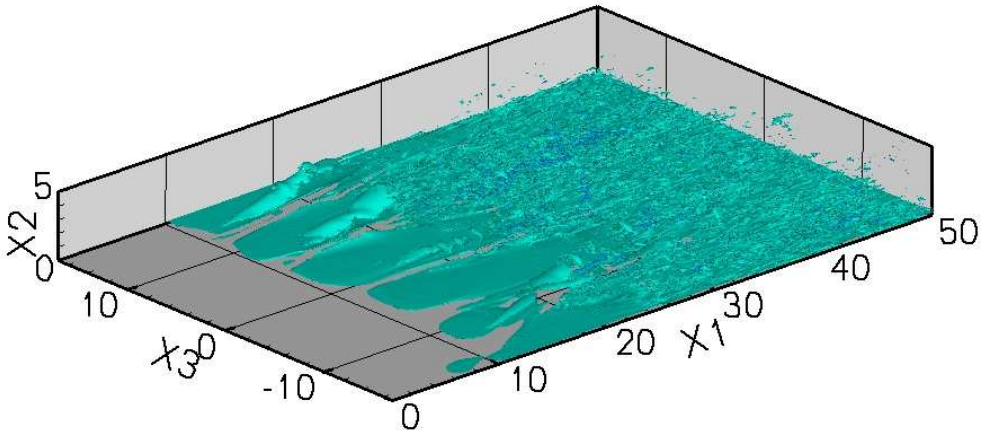

Figure 11.4: Streamwise vorticity fluctuations at $Re_\theta = 2500$.

(viscous wall layer) are equally populated, than in the upper slice (outer region), where the big vortical structures with one sign are dominant. The length of the biggest structure in the plane $x_2^+ \approx 28$ (left plot in Figure 11.11) is approximately $l_x^+ = 280$. In the plane $x_2^+ \approx 140$ the vortical structures are more wide and longer.

Figure 11.12 shows wall-normall vorticity fluctuations at $Re_\theta = 810$ (at $x_2^+ \approx 28, 140$ left and right plots respectively). Streaks of wall-normal component of vorticity are $l_x^+ \approx 540$ long. There are mostly pairs of the streaks (with the

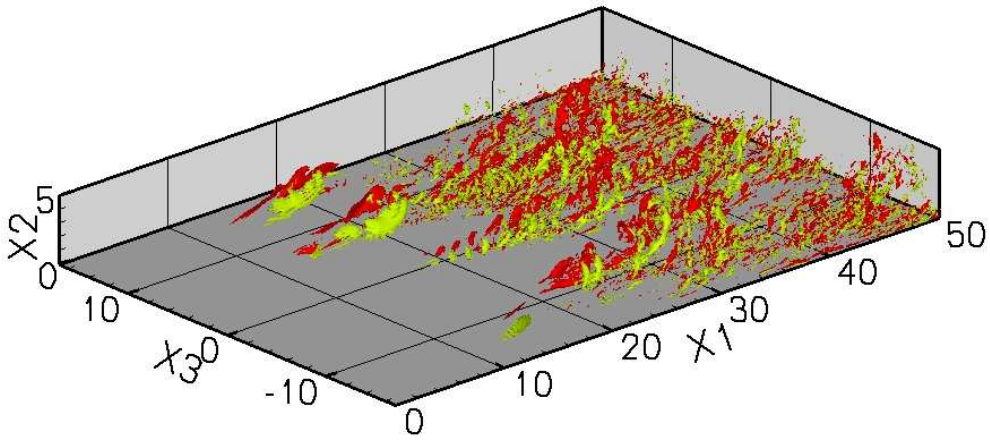

Figure 11.5: Wall-normal vorticity fluctuations at $Re_\theta = 2500$.

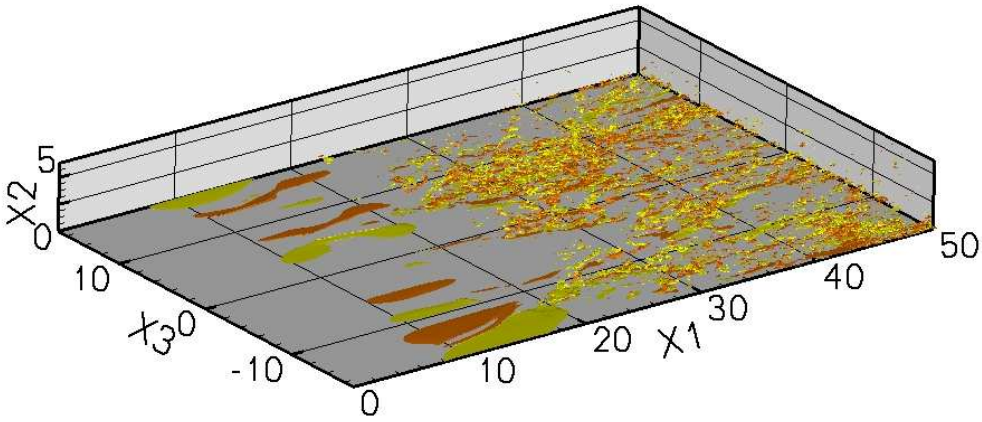

Figure 11.6: Spanwise (bottom plot) vorticity fluctuations at $Re_\theta = 2500$.

positive and negative vorticity) living together near the wall at $x_2^+ \approx 28$. As for the slice at $x_2^+ \approx 140$ the streaks with the same levels of vorticity as on the left plot are shorter and a few of them exist in this region.

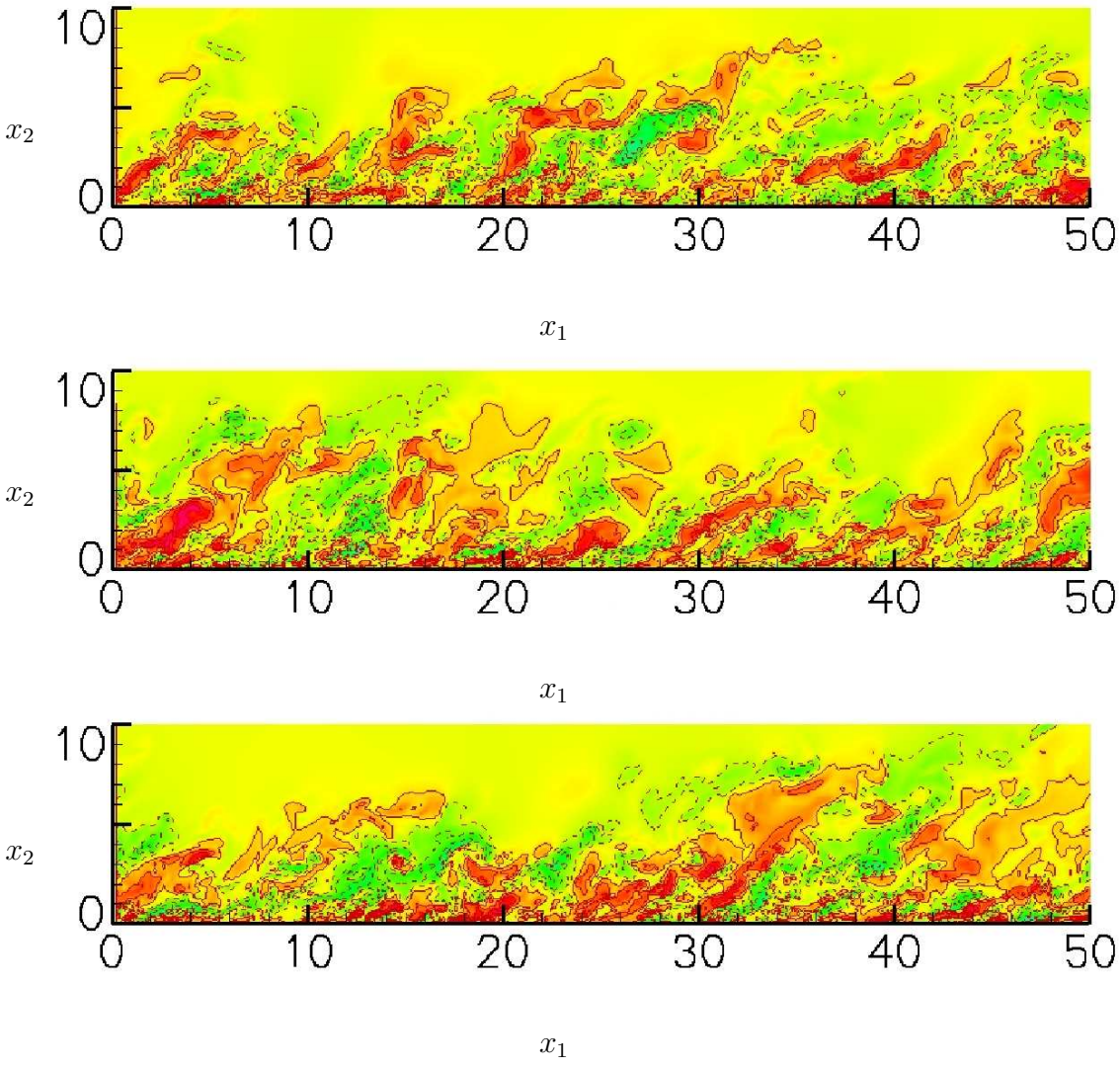

Figure 11.7: Spanwise vorticity fluctuations at different instants of time at $Re_\theta = 2500$.

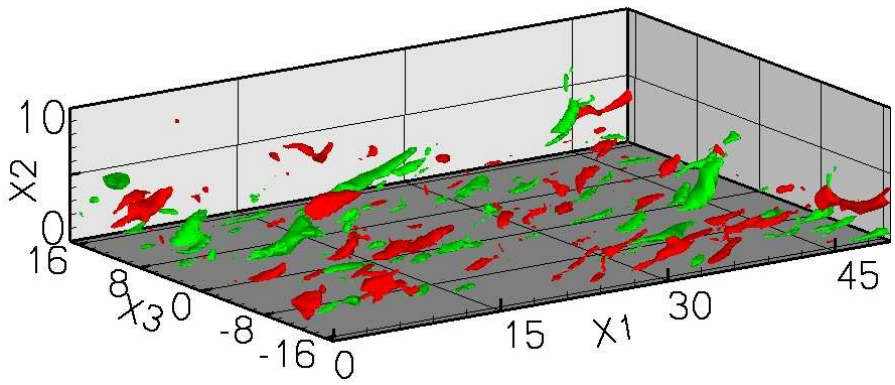

Figure 11.8: Spanwise velocity field ($3D$ case) isosurfaces $(-0.13, 0.14)$ at $Re_\theta = 755$

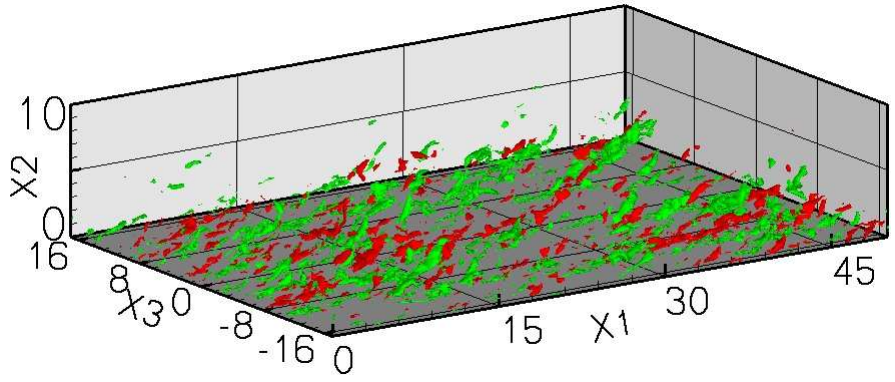

Figure 11.9: Spanwise velocity field ($3D$ case) isosurfaces $(-0.13, 0.14)$ at $Re_\theta = 2240$

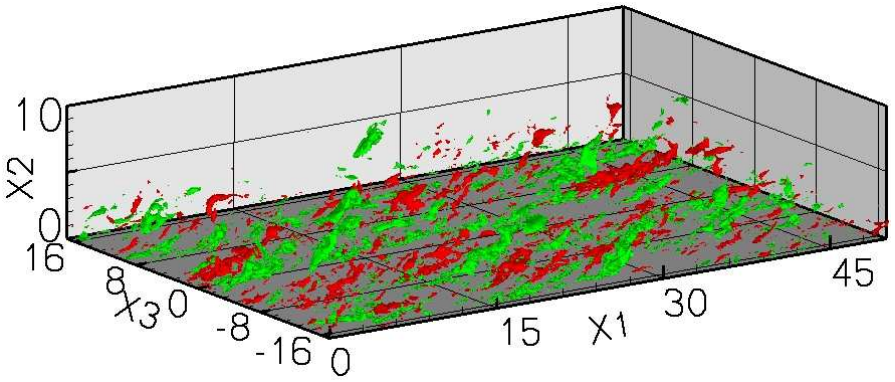

Figure 11.10: Spanwise velocity field ($3D$ case) isosurfaces $(-0.13, 0.14)$ at $Re_\theta = 2500$

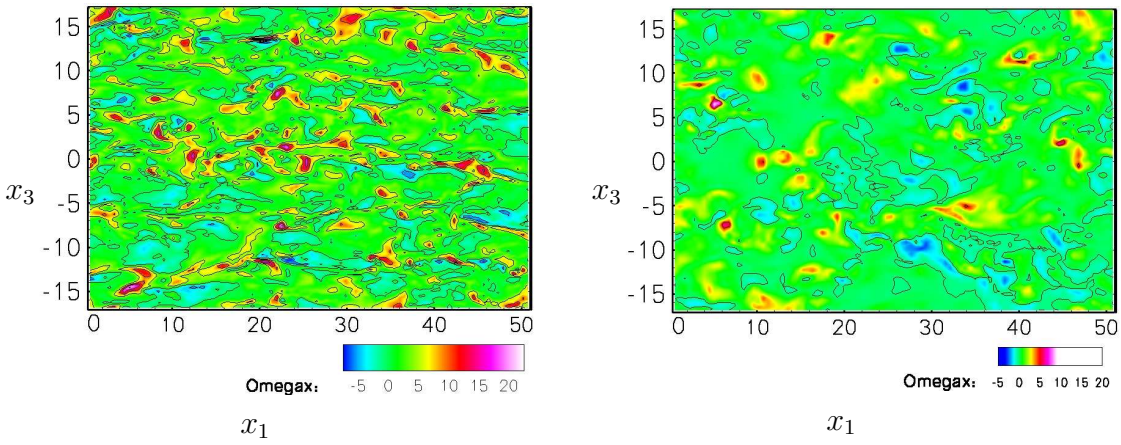

Figure 11.11: Streamwise vorticity fluctuations at $Re_\theta = 810$ in different planes from the wall: $x_2 = 1$ (left plot) and $x_2 = 5$ (right plot). The distances in the plus units are $x_2^+ = 28$ and $x_2^+ = 140$ respectively.

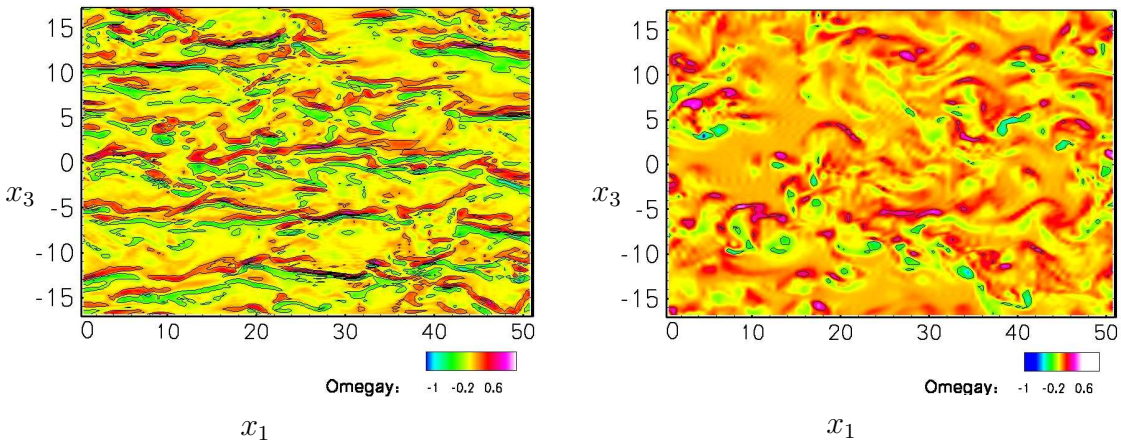

Figure 11.12: Wall-normal vorticity fluctuations at $Re_\theta = 810$ in different planes from the wall: $x_2 = 1$ (left plot) and $x_2 = 5$ (right plot). The distances in the plus units are $x_2^+ = 28$ and $x_2^+ = 140$ respectively.

12 Wavelet analysis

The FFT had a far-reaching impact on society (for the discussion of Fourier transformation see for example the book by Hubbard (1998)). However the FFT has limits of usage. The building blocks of a Fourier analysis are sine and cosine functions, which oscillate for all time.It hides information about time. The information about time is not destroyed, but is buried deeply within the phases. In theory one can extract this time information by calculating the phases from the Fourier coefficients. In practice, computing them with enough precision is impossible. The fact that information about one instant of a signal is dispersed throughout all the frequencies of the entire transform is a serious drawback. A local characteristic of the signal becomes a global characteristic of the transformation.

The information in one part of a signal, whether real or erroneous, it necessarily spreads throughout the entire transform. To analyse a signal in both time and frequencies, Gabor (1946) for example used the windowed Fourier transform. This method imposes painful compromises. The smaller your window, the better you can locate sudden changes. However the blinder you become to the lower frequency components of your signal. These low frequencies just will not fit into your window. Because all of these problems of Fourier transform, researchers have spent a lot of time to find a new tool which could decompose signals simultaneously by time and by frequency.

Wavelets are an extension of Fourier analysis. The basic approach is the same. The coefficients tell us in what way the analysing function (sines and cosines, or wavelets) needs to be modified in order to reconstruct a signal. However squeezing and stretching the wavelets to change their frequency changed everything. Wavelets automatically adapt to the different components of the signal, using a small window to look at short, high-frequency components and a large window to look at long-lived, low-frequency components. The procedure is called multiresolution. For this reason wavelets have been called a **mathematical microscope**.

There exist a lot of books and articles about wavelets and their application. Some of them are listed here, for example the book by Hubbard (1998) which is a wonderful introduction to the wavelet theory. The review written by Marie Farge (Farge 1992) for Annual Reviews of Fluid Mechanics is very useful to understand

wavelet application to turbulence. In Farge, Schneider & Kevlahan (1999), Farge, Pellegrino & Schneider (2001) the authors introduced a new method of coherent vortex extraction from two- and three-dimensional homogeneous turbulent flows. A method (coherent vortex simulation) was used to compute three-dimensional turbulent mixing layers in Schneider, Farge, Pellegrino & Rogers (2005). A similar study was made by Farge, Schneider, Pellegrino, Wray & Rogally (2003) for isotropic homogeneous turbulence.

The common goals of wavelet decomposition are the signal or image clearance or simplification, which are parts of de-noising or compression. There are many papers published in oceanography and earth studies. One of the most popular successes of the wavelets is the compression of FBI fingerprints. Another application of wavelet analysis is a classification of Magnetic Resonance Spectra. Other fields that are making use of wavelets include astronomy, acoustics, neurophysiology, music, speech discriminations, fractals, human vision, and etc. (for details see (Graps 1995)).

Continuous wavelet transform (CWT) is defined as the sum over all time/space of the signal multiplied by scaled, shifted versions of the wavelet function Ψ:

$$C(scale, position) = \int_{-\infty}^{\infty} f(t)\Psi(scale, position, t)dt, \tag{12.1}$$

where C are many wavelet coefficients, which are functions of scale and position. The coefficients C represent how closely is the wavelet correlated with this section of the signal. The higher is wavelet coefficient (C), the more similarity exists between signal and wavelet. We could make a plot on which the x_1-axis represents position along the signal (time/space), the x_2-axes represents scale, and the color at each x_1x_2 point represents the magnitude of the wavelet coefficients C.

There is a correspondence between wavelet scales and frequency:

- Low scale $a \Rightarrow$ Compressed wavelet $\Rightarrow$ Rapidly changing details $\Rightarrow$ High frequency ω.
- High scale $a \Rightarrow$ Stretched wavelet $\Rightarrow$ Slowly changing, coarse details $\Rightarrow$ Low frequency ω.

To calculate the wavelet coefficients at every possible scale is a very difficult task, and it generates a large amount of data. It turns out that if we choose scales and positions based on powers of two, then our analysis will be much more efficient and just as accurate. Such an analysis is called as the discrete wavelet transform (DWT). An efficient way to implement this scheme using filters was developed by Mallat (1989).

One-dimensional wavelet analysis is based on one scaling function Φ and one wavelet Ψ. The following figure shows these functions of the *db*10 wavelet (Daubechies 1992). This family of wavelets has no explicit expression.

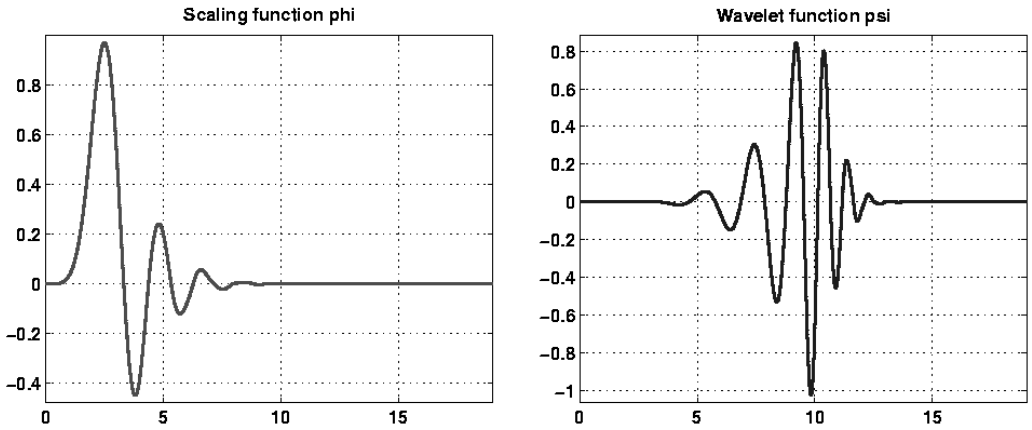

Figure 12.1: db10 wavelet Φ and Ψ functions.

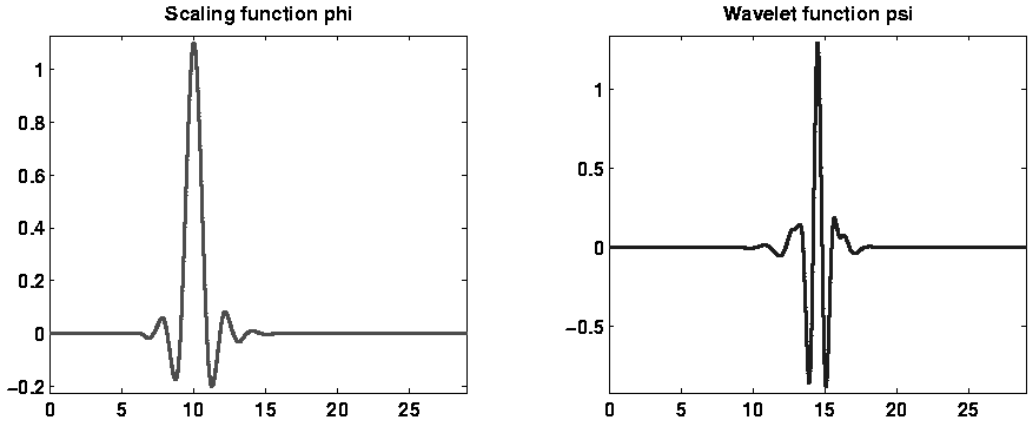

Figure 12.2: Coif5 wavelet Φ and Ψ functions.

In general the CWT of a function $u(t)$ (with zero mean and finite energy) is defined as

$$\tilde{u}(a,t) = \int_{-\infty}^{\infty} \left[u(t') \frac{1}{\sqrt{a}} \Psi^{\star} \left(\frac{t-t'}{a} \right) \right], dt' \tag{12.2}$$

where $\tilde{u}(a,t)$ is the wavelet coefficient at time t and scale a (the same as in equation (12.1)).

The dilatation measure a acts as a zoom, so large features of the original signal appear at large values of a, while short-duration events will appear at small a. The value of the wavelet transform as an analytical tool is based on two statements. First, it is based on the existence of the inverse transform (which expresses the fact that no information is lost in the transform) and the second, the energy of the signal is conserved in the time-frequency domain. Thus, the squared wavelet coefficients provide an instantaneous power spectrum, useful for transient or intermittent signals.

In wavelet analysis there are **approximations** (high-scale, low-frequency components) and **details** (low-scale, high-frequency components) of the signal. On the

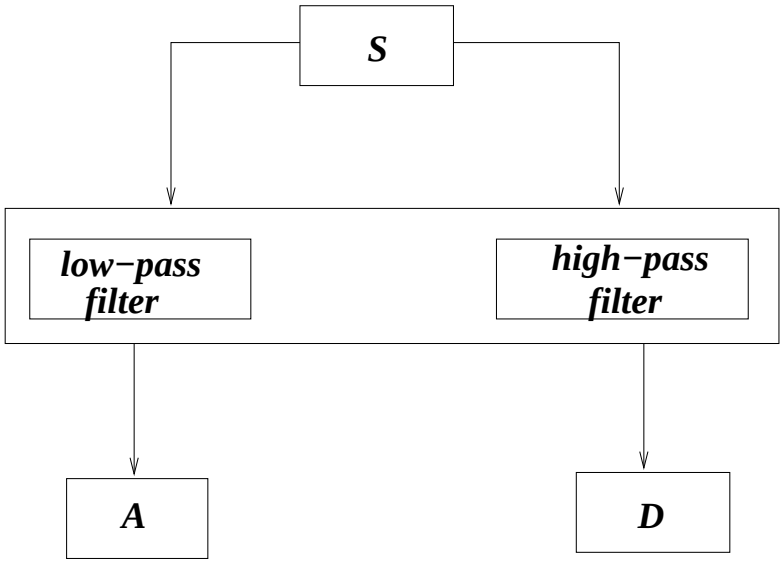

Figure 12.3: The filtering of the signal.

basic level (see Figure 12.3), the original signal, S, passes through the low-pass and high-pass filters and gives two signals.

12.1 One-dimensional wavelet analysis at low Reynolds number

A one-dimensional wavelet analysis of the velocity field was done in streamwise and spanwise directions for different wall-normal positions at $Re_\theta = 1150$. The points in this direction were taken in different regions of boundary layer flow: viscous sublayer, buffer layer, viscous wall layer, log region and exponential region (see table 12.1 and Figure 12.4).

	viscous sublayer	buffer	log region	exponential region	outer region
x_2	0.13	0.30	2.35	7.65	9.45
x_2^+	3.3	8.2	65.4	212.7	261.8
x_2/Δ	0.002	0.005	0.04	0.13	0.16

Table 12.1: Points in different regions in wall-normal direction.

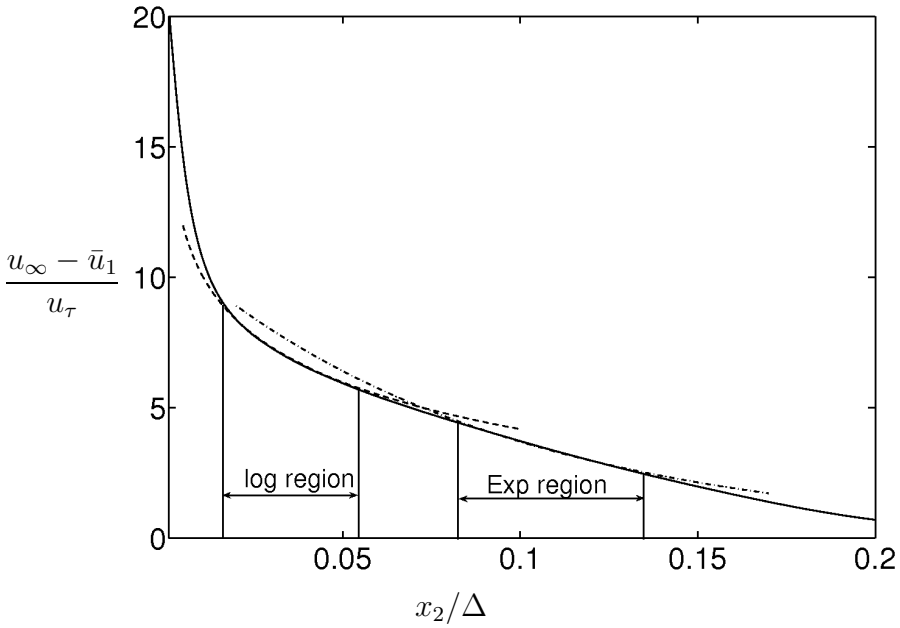

Figure 12.4: Log-law and exponential law. --- DNS.

Several wavelet analyses of $u - \bar{u}$, i.e. the streamwise fluctuations of the velocity field in streamwise direction for different distance from the wall have been conducted: $y = 0.1, 0.3, 1, 1.44, 3$ (see table 12.1). The turbulent signal was analysed using discrete ($db10$) (see Figure 12) and continuous ($coif5$) (see Figure 12) wavelet

transformations. In DWT we split up the turbulent signal (streamwise velocity fluctuation $u_1 = u_1 - \bar{u}_1$ in our case) up to fifth level:

$$S = A_5 + D_1 + D_2 + D_3 + D_4 + D_5.$$

Figure 12.5 shows DWT and CWT of the streamwise velocity fluctuation at $x_2 = 0.1$ from the wall, which in plus units corresponds to $x_2^+ = 3.3$ (viscous sublayer). As one can see from the figure (top plot, DWT) details of the signal $d_1 - d_3$ have nearly equal magnitudes (generally speaking, they are magnitudes of wavelet coefficients C (see equation (12.1))), but different frequencies. As it was mentioned the figure containing the CWT represents the coefficients of the wavelet decompositions (the x_1-axis represents position along the signal (time/space), the x_2-axes represents the scale, and the color at each x_1x_2 point represents the magnitude of the wavelet coefficients C). In Figure 12.5 (bottom plot) dark color means wavelet coefficient with small amplitudes. In the beginning of the box $x_1 = 0 - 100$ (transitional region), we have a big white zone which increases in x_2 direction (big scales), that means that in this region we have mainly big scales. Moving in the streamwise direction we have similar regions of periodicity of black and white colors. This fact means self-similar behavior of the signal in x_1 direction. Figure 12.6 shows the wavelet decomposition of the signal in the buffer layer $x_2^+ = 8.27$. In this case details of the signal have different amplitudes but still are very close to each other. The CWT is very similar to the previous one, but similar structures are more pronounced. We still have a big white zone near the entrance into the box. The magnitudes of the wavelet transformation coefficients become smaller for small scales, that results in weaker correlation between wavelet and the corresponding region of the signal. In the middle of the CWT plot, the big regions with high correlations (big magnitudes of C) between wavelets and signal are observed, that means in this region (buffer, and also in the viscous sublayer (see Figure 12.5, bottom plot)) region the corresponding scales are dominant in the flow.

For the log-region $x_2^+ = 65.4$ (Figure 12.7) the DWT shows that the signal details have different magnitudes. For example, $d_1 \approx 0.05$, $d_2 \approx 0.05$, but $d_3, d_4, d_5 \approx 0.1$ have nearly the same magnitude of wavelet coefficients. The CWT shows that there are no dominant scales anymore. All scales are 'at work' in the log-region. The picture of the CWT of the signal differs significantly from the pictures for the viscous sublayer and buffer layer.

For the exponential region $x_2^+ \approx 212.7$ the DWT and CWT are presented in Figure 12.8. In the transition region ($x_2 = 0 - 100$) bigger scales are dominant, the magnitude of small scales are approximately zero (d_1, d_2). The white color (high correlation between different scales) is less pronounced for large scales. The wavelet transform shows a self-similar character of the signal.

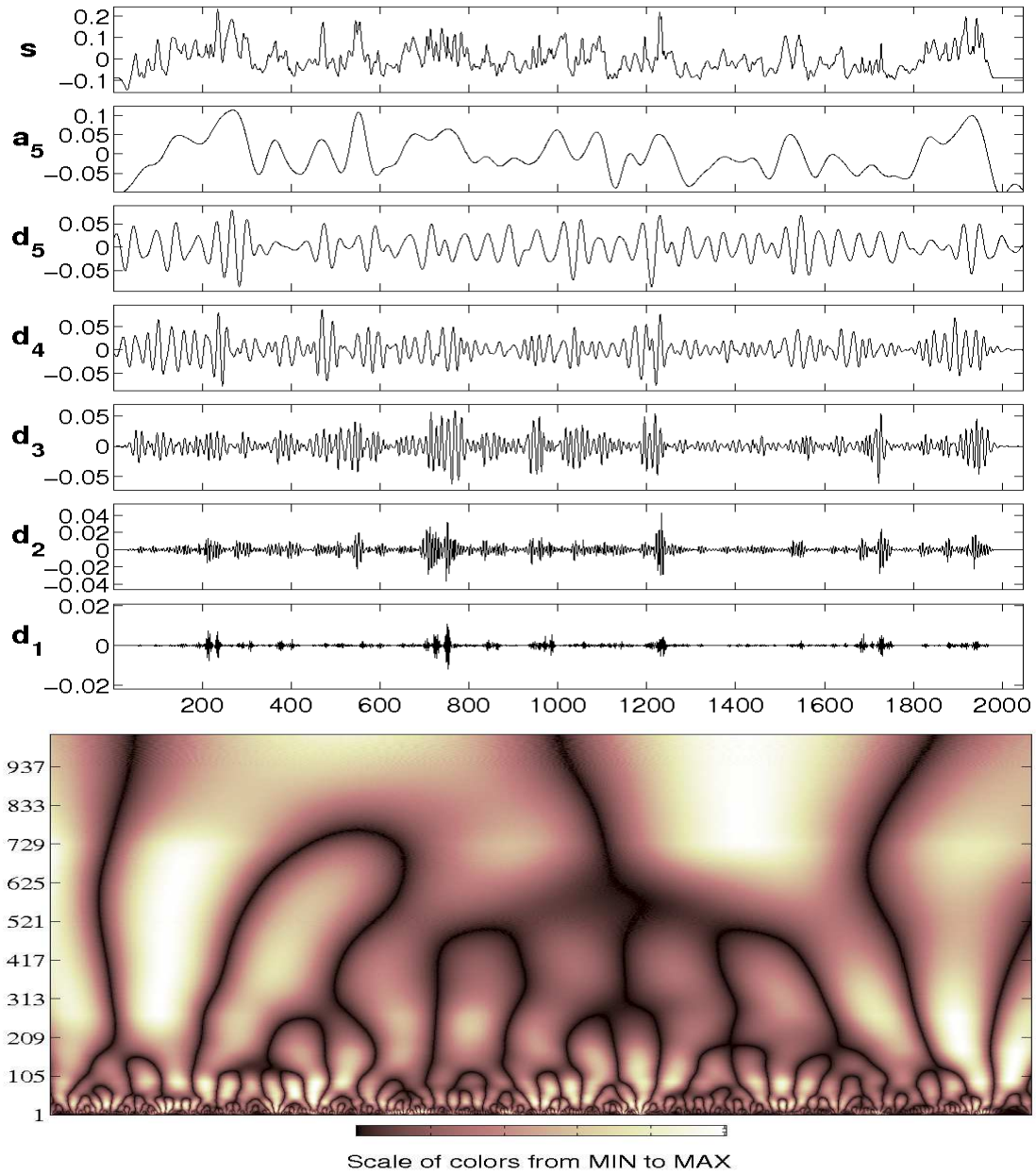

Figure 12.5: $db10$ DWT and $coif5$ CWT (bottom plot) of u_1 signal in streamwise direction for $Re_\theta = 810$. The position in wall-normal direction is $x_2 = 0.1$ or $x_2^+ = 3.3$.

In the outer region $x_2^+ = 261.8$, the turbulent signal shows different behavior from all previous cases. Magnitudes of all details are small. In the region $x_1 = 0 - 400$

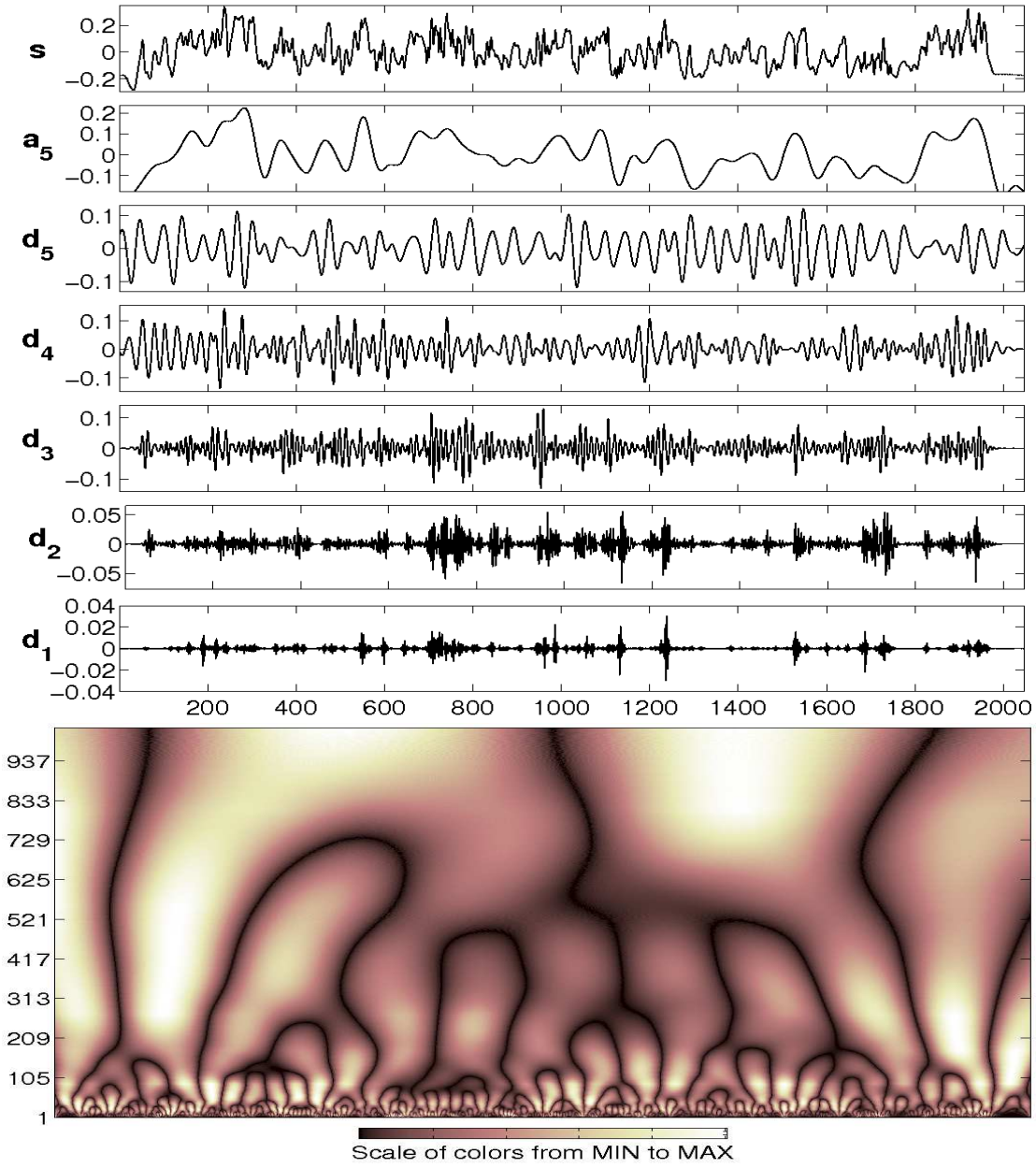

Figure 12.6: *db*10 DWT of u_1 signal in streamwise direction for $Re_\theta = 810$. The position in wall-normal direction is $x_2 = 0.3$ or $x_2^+ = 8.27$.

magnitudes of almost all details are very small.

Thus, the wavelet analysis of the turbulent signal allows to study its behavior in different regions of the turbulent boundary layer. This analysis helps us to separate

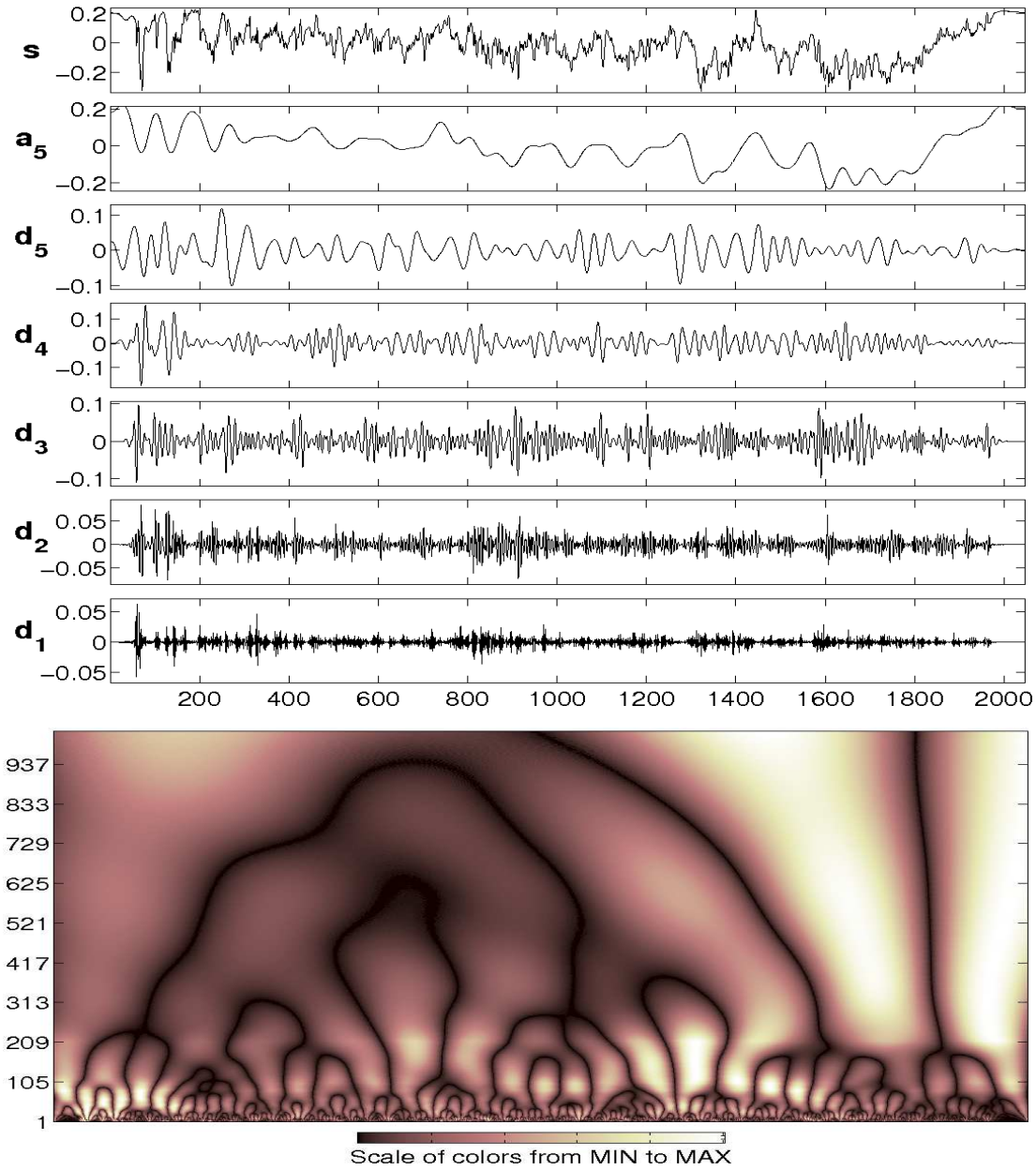

Figure 12.7: *db*10 DWT of u_1 signal in streamwise direction for $Re_\theta = 810$. The position in wall-normal direction is $x_2 = 2.35$ or $x_2^+ = 65.4$.

out different scales from the signal and study them separately; It allows to show in which region what scales are dominant and allows to determine the size of the transitional region.

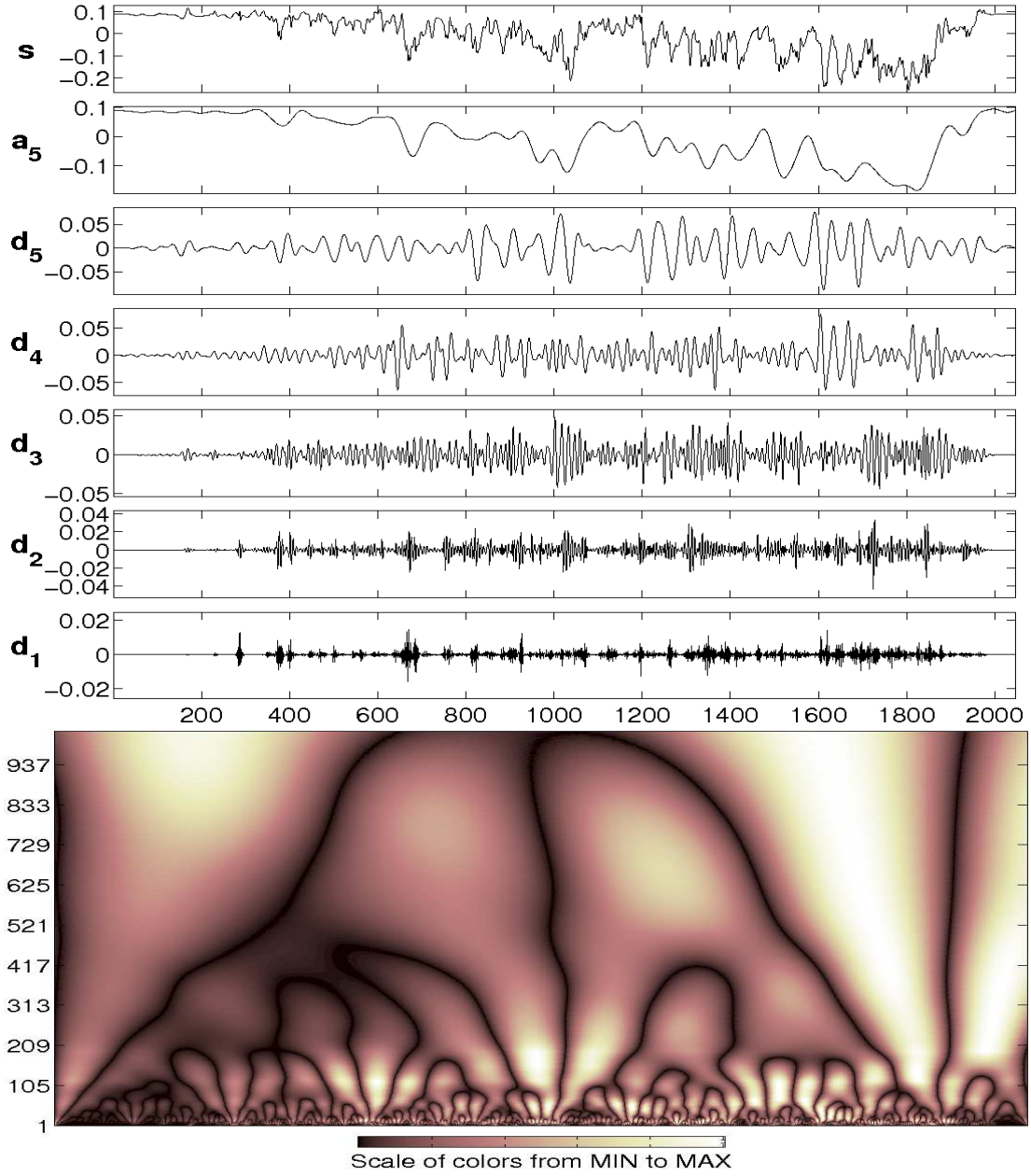

Figure 12.8: *db*10 DWT of u_1 signal in streamwise direction for $Re_\theta = 810$. The position in wall-normal direction is $x_2 = 7.65$ or $x_2^+ = 212.7$.

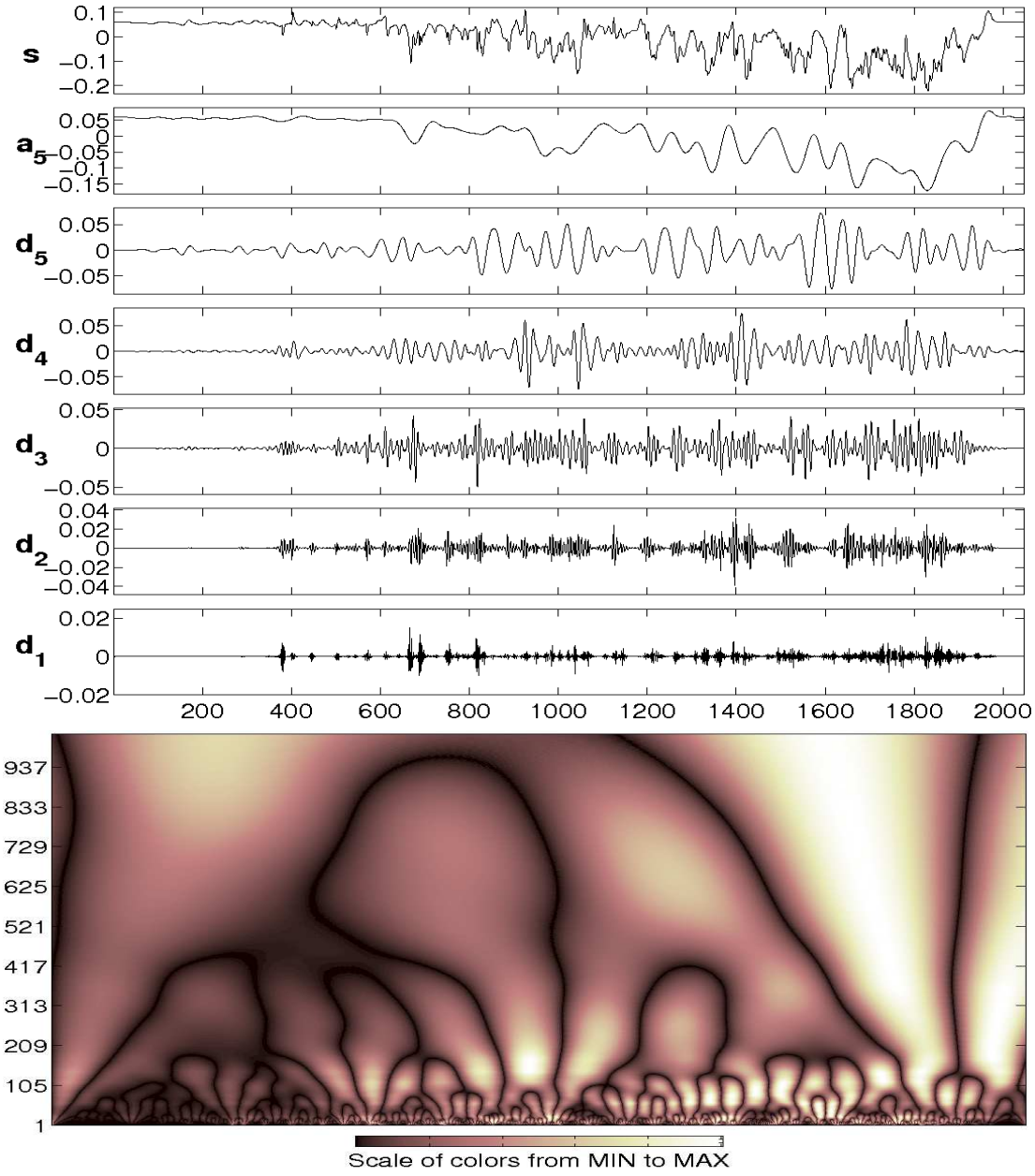

Figure 12.9: *db*10 DWT of u_1 signal in streamwise direction for $Re_\theta = 810$. The position in wall-normal direction is $x_2 = 9.45$ or $x_2^+ = 261.8$.

12.2 One-Dimensional wavelet analysis at high Reynolds number

A wavelet analysis (discrete and continuous) of streamwise velocity fluctuation was done in the case of high Reynolds number ($Re_\theta = 2500$) number case. The turbulent signal was taken from four different regions of the flow: viscous sublayer, buffer layer, log-region and exponential region (for details see table 12.2 and Figure 12.10).

	viscous sublayer	buffer	log-region	exponential region	outer region
y	0.02	0.1	0.7	3	5
y^+	2	12.5	62.9	315	535
y/Δ	0.0007	0.004	0.02	0.1	0.17

Table 12.2: Points in different regions in wall-normal direction.

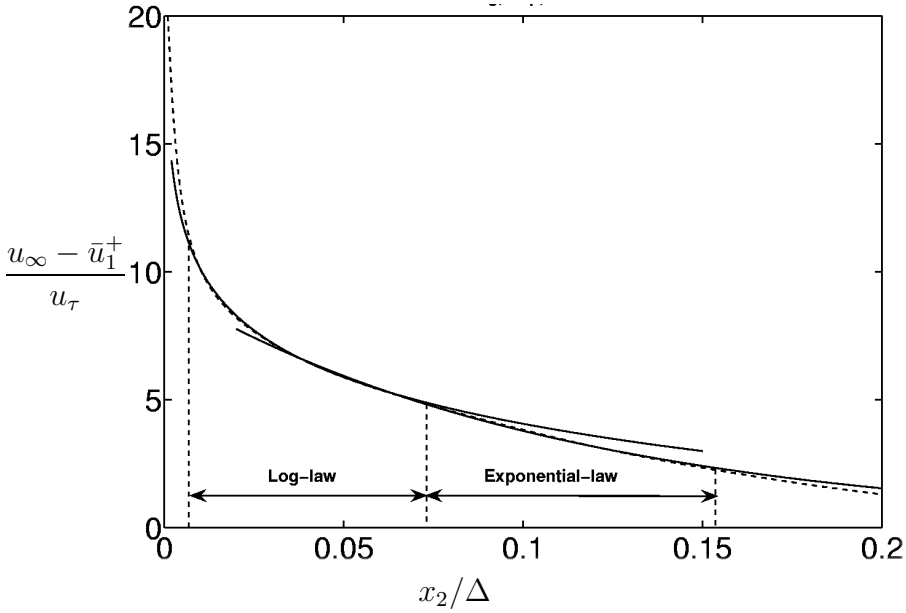

Figure 12.10: Log-law, exponential law. --- DNS.

In the viscous sublayer (Figure 12.11) the behavior of the signal is different from that in the low Reynolds number case (see Figure 12.5). The amplitudes of the small scales (d_1, d_2, d_3) are zero near the entrance into the simulation box ($x_2 = 0 - 200$). From the CWT plot one can see that there are only three regions in the upper part of the plot (big scales) with large zones of high correlations between

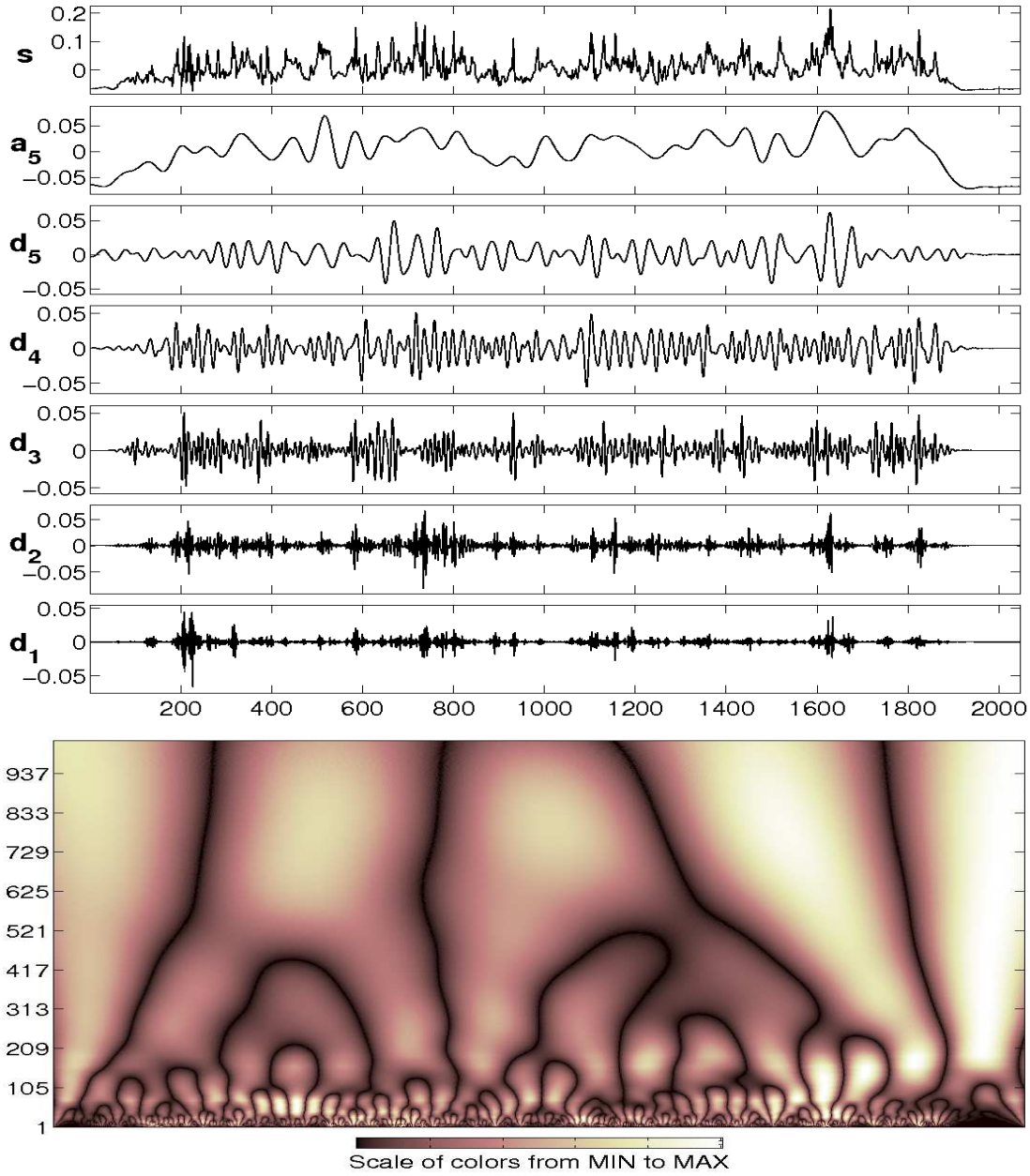

Figure 12.11: *db*10 DWT of u_1 signal in streamwise direction for $Re_\theta = 2500$. The position in wall-normal direction is $x_2 = 0.02$ or $x_2^+ = 2$.

wavelet and the signal. In streamwise direction at points $x_1 \approx 1000$ and $x_1 \approx 1600$ in the region of small scales $1 - 300$ we can observe two very similar structures. Such structures exist down to the small scales too. The amplitudes of the details $d_1 - d_5$ are the same.

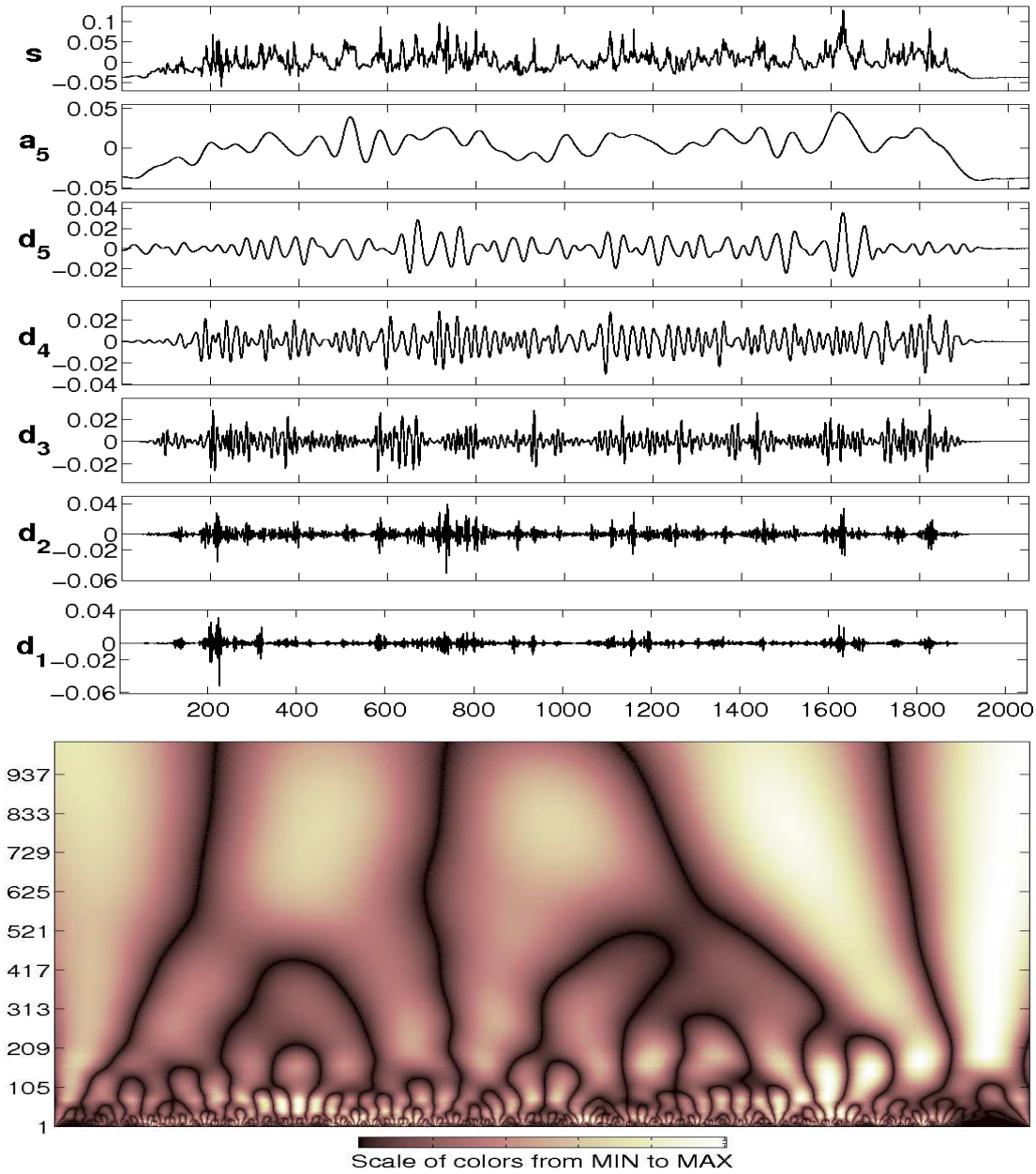

Figure 12.12: *db*10 DWT of u_1 signal in streamwise direction for $Re_\theta = 2500$. The position in the wall-normal direction is $x_2 = 0.1$ or $x_2^+ = 12.5$.

In the buffer layer $x_2^+ \approx 12.5$ (Figure 12.12) we have similar situation comparing the result of CWT. The details have different amplitudes. We still have three big regions but with lower correlations in this case. In the region $x_1 = 0 - 400$ we have two highly correlated regions for small and moderate scales.

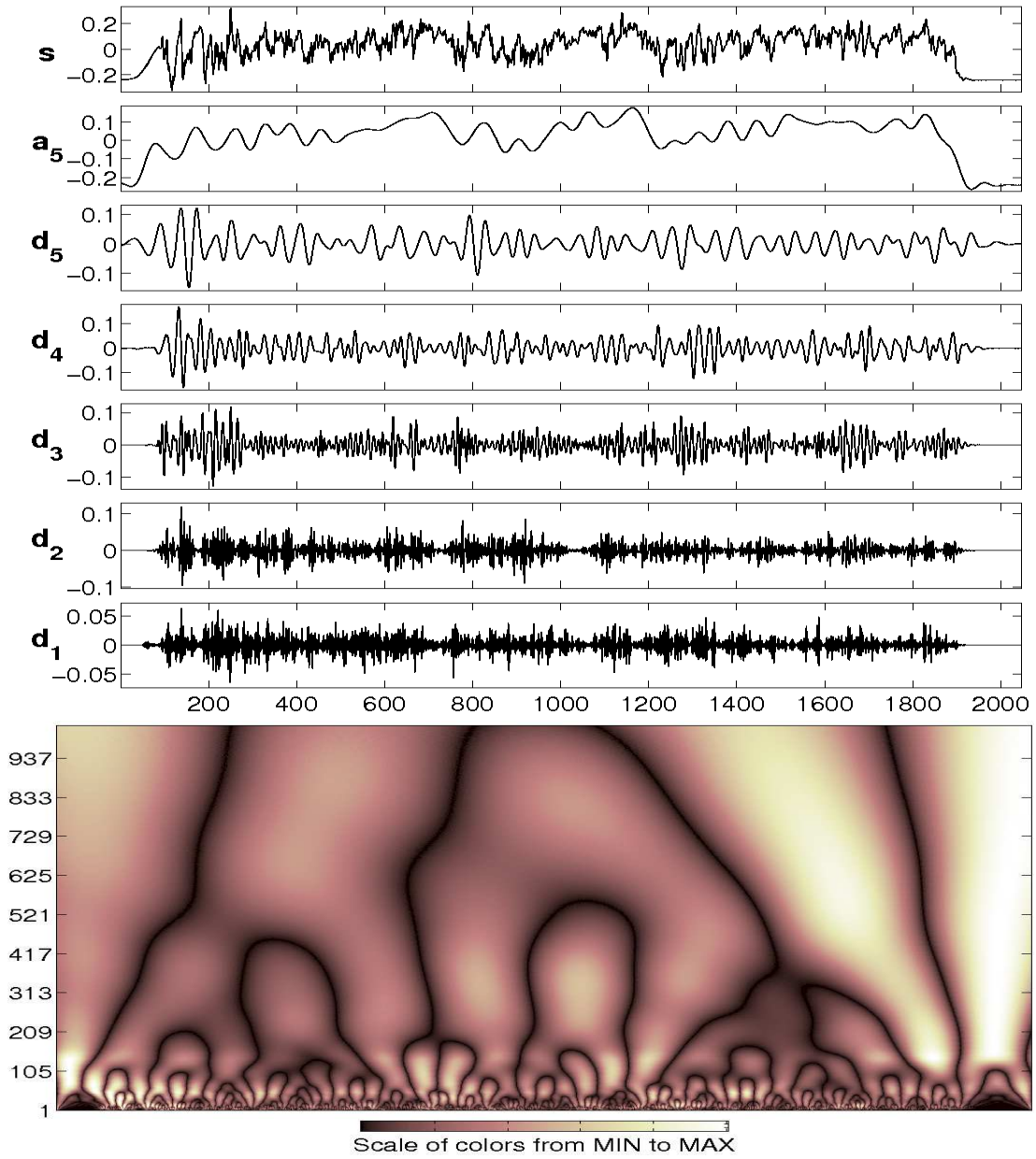

Figure 12.13: *db*10 DWT of u_1 signal in streamwise direction for $Re_\theta = 2500$. The position in wall-normal direction is $x_2 = 0.7$ or $x_2^+ = 62.9$.

The next signal (see Figure 12.13) of the streamwise velocity fluctuation analysed by wavelets was taken in the log-region ($x_2^+ = 62$). In this case d_1 has the smaller amplitude, than d_2, d_3, d_4 and d_5. In this region amplitudes of details are bigger then in the previos case (see Figure 12.12). The structures with different scales

have the same importance in this region as it is seen from the CWT plot.

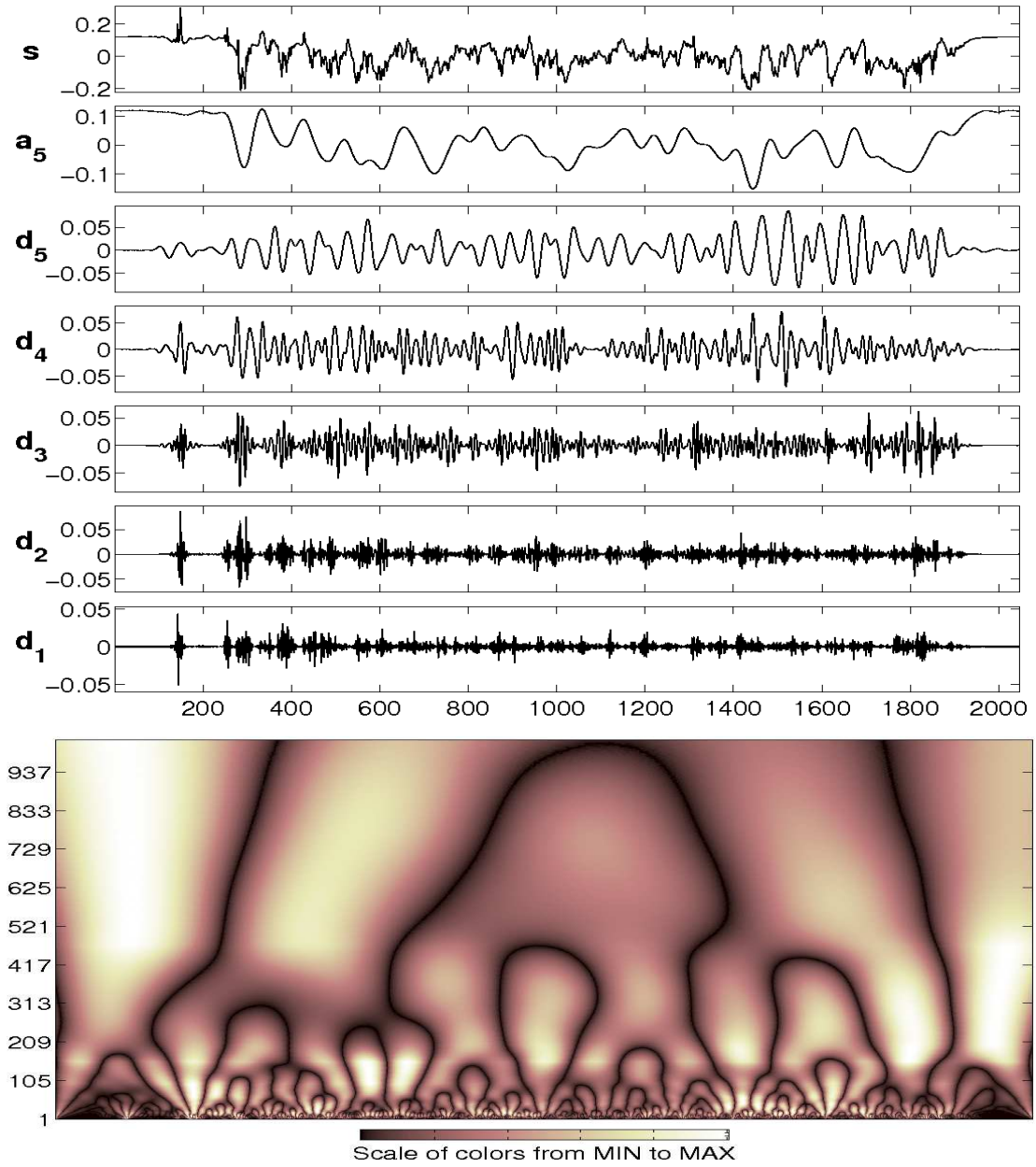

Figure 12.14: *db*10 DWT of u_1 signal in streamwise direction for $Re_\theta = 2500$. The position in the wall-normal direction is $x_2 = 3$ or $x_2^+ = 315$.

As for the exponential region, the signal was analysed at $x_2 = 315$ (see Figure 12.14). In the exponential region details of the signal (DWT) show interesting

behavior. Their amplitudes for $x_1 = 0 - 300$ are zero, only d_1, d_2 and d_3 show small waves in the region of $x_1 = 100$. These two stand alone waves are seen in the CWT plot for moderate and big scales (see the bottom plot in Figure 12.14). The amplitudes of details are smaller than in the log-region.

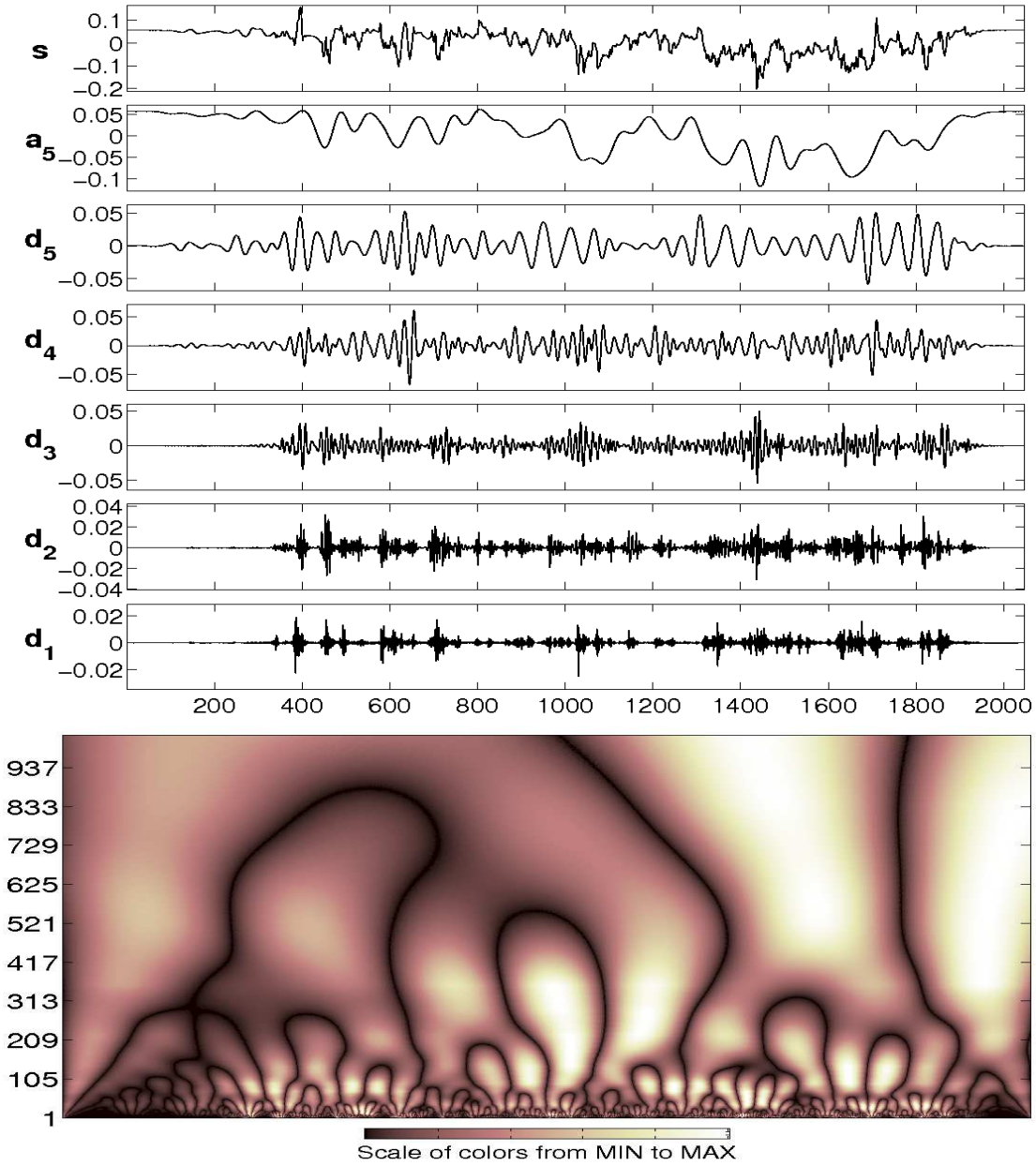

Figure 12.15: *db*10 DWT of u_1 signal in streamwise direction for $Re_\theta = 2500$. The position in the wall-normal direction is $x_2 = 5$ or $x_2^+ = 535$.

The picture of the wavelet decomposition of the signal in the outer region differs from that of the exponential region. In this case for $x_1 = 0-400$ wavelet coefficients are almost zero or very small (Figure 12.15). From the CWT we see that in this region only moderate scales show wavelet coefficients with higher magnitude. In the point $x_1 = 400$ one can observe highly correlated (wavelet coefficients with big magnitude) structures of the signal for small scales $(1 - 100)$. The whole picture (the bottom plot in Figure 12.15) is divided into two region with the similar structures (see d_5 in the regions $x_1 = 400$ and $x_1 = 1100$).

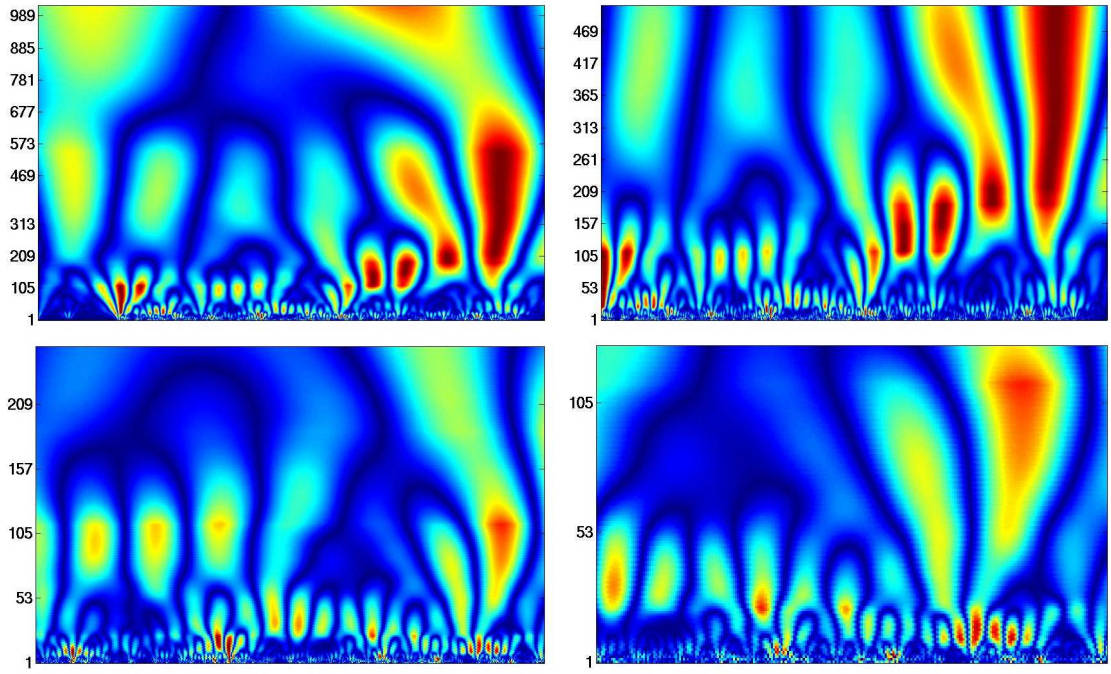

Figure 12.16: $db10$ DWT of u_1 signal in streamwise direction for $Re_\theta = 2500$.

Figure 12.16 shows CWT of streamwise velocity fluctuation signal u_1. On the first plot (top, left) the whole region of the space and scales is shown. The coherent and similar structures are clearly seen from this plot. In the meadle of the plot we have four big area with the high magnitude of wavelet coeffients. It means that these scales are dominant in the flow. On the next plots we have smaller regions (the size was reduced two times comparing to the previos one) from the first plot. The self-similarity and fractal structure of the signal are observed. All, four plots are similar to each other that means going to the small scales and distances the turbulent signal keeps the same characteristics.

The wavelet analyses makes it possible to extract more extensive and detail information from the turbulent signal than it is possible with the classical methods.

The results presented in the thesis are preliminary. The wavelet decomposition of streamwise velocity fluctuations was done only in one direction. We are planning to prefrom 2D and 3D wavelet analyses (that was beoynd the frames of this thesis) for velocity and vorticity fields in the nearly future.

13 Results and discussions

In the present work a Lie group analysis of the TPC equations is presented in the case of ZPG turbulent boundary layer flow using the parallel flow assumption ($\bar{u}_1 \equiv \bar{u}_1(x_2)$). It is shown that the Lie group analysis helps to gain more insight into the description of the turbulent flow. This method provides a systematical procedure to derive symmetries from a set of differential equations.

The following results were obtained:

- The new exponential scaling law for the mean velocity profile, TPC functions, velocity-pressure correlations and Reynolds stresses were found in the mid-wake region of flat-plate boundary layers:

$$\frac{\bar{u}_\infty - \bar{u}_1}{u_\tau} = \alpha \exp\left(-\beta \frac{x_2}{\Delta}\right), \frac{\overline{u_i u_j}(x_2)}{u_\tau^2} = b_{ij} \exp\left(-a \frac{x_2}{\Delta}\right);$$

- A New, third scaling group $\boldsymbol{G}_{s3}$ (that is a characteristic feature only of the one-dimensional turbulent boundary layer flow) was found in the TPC equations in contrast to the Navier-Stokes and Euler equations which have one and two scaling groups, respectively.

The one of the main aims of the present work was to validate the new exponential laws. For this reason DNS of a flat plate turbulent boundary layer with ZPG was performed at three different Reynolds numbers:

- $Re_\theta = 750, Re_{\delta^+} = 1110$; $\Delta x^+ \approx 16, \Delta z^+ \approx 5.5, \Delta y^+ \approx 0.04 - 5$
- $Re_\theta = 2240, Re_{\delta^+} = 3100$; $\Delta x^+ \approx 15, \Delta z^+ \approx 11, \Delta y^+ \approx 0.13 - 18$
- $Re_\theta = 2500, Re_{\delta^+} = 3400$; $\Delta x^+ \approx 12, \Delta z^+ \approx 10, \Delta y^+ \approx 0.03 - 6$

All possible classical statistical quantities were accumulated during the simulations as well as instantaneous velocity, vorticity and pressure fields. A huge amount of DNS data was collected as a result of numerical simulations. Part of these data were analysed and presented in the thesis.

The DNS results for the mean velocity, TPC and Reynolds stresses were compared to the theoretical ones. The numerical simulations show good agreement with the

theoretical results. Classical and modified log-laws were compared to the DNS results. The comparison with the DNS shows that for the Reynolds numbers reached in our simulations the classical log-law describes the mean velocity profile behavior more precisely for the inner part of log-law.

As it was mentioned above, a Lie group analysis was performed for the parallel boundary layer flow which forms an approximation for the two-dimensional flow. The results are in good agreement with the DNS simulations of the flow. However, there is region in the flow (beyond the exponential region) where the velocity decreases faster than the exponential law. This effect needs to be investigated further. Thus, the next step in the study of ZPG turbulent boundary layer flow should be the symmetry analysis for real, two-dimensional flow ($\bar{u}_1 \equiv \bar{u}_1(x_1, x_2)$).

Another part that needs to be investigated in the future is the behavior of the exponential law in the outer part of the boundary layer flow, i.e. in the viscous superlayer. The current analytical research implies the large Reynolds number limit. This fact means that we need higher Reynolds numbers in numerical simulations. To increase the Reynolds number in numerical simulations and to collect smooth statistics as well as instantaneous velocity and pressure fields for the dynamical study of the processes in the flow is the next step in the investigation.

14 Bibliography

Abe, H., Kawamura, H., Matsuo, Y. (2001): Direct numerical simulation of a fully developed turbulent Channel flow respect to the reynolds number dependence. *Journal of fluids Engineering 123*, 382–393.

Adrian, C. K. L. Z.-C., R.J. (2000): Analysis and intepretation of instantaneous turbulent velocity fields. *Experiments in Fluids 29*, 277–290.

Adrian, M. C., R.J., Tomkins, C. (2000): Vortex organization in the outer region of the turbulent boundary layer. *J.Fluid Mech. 422*, 1–54.

Baikov, G. R., V.A., Ibragimov, N. (1993): Approximate groups of transformation. *Differential equations 29*, 10, 1487–1504.

Barenblatt, C. A., G.I., Prostokishin, V. (2000): Self-similar intermediate structures in turbulent boundary layers at large Reynolds numbers. *J.Fluid Mech. 410*, 263–283.

Bertolotti, H. T., F.P., Spalart, P. (1992): Linear and nonlinear stability of the Blasius boundary layer. *J.Fluid Mech. 242*, 441–474.

Bluman, G., Anco, S. (2002): *Symmetry and integration methods for differential equations.*, vol. 154 of *Applied mathematical sciences*. Springer-Verlag.

Buschmann, M., Gad-el Hak, M. (2003): Debate concerning the mean-velocity profile of a turbulent boundary layer. *AIAA Journal 41*, 4, 565–572.

Cantwell, J., Brian (2002): *Introduction to symmetry analysis*. Cambridge texts in applied mathematics, Cambridge University Press.

Canuto, H. M. Q. A., C., Zang, T. (1988): *Spectral Methods in Fluid Dynamics*. Springer, New-York.

Carlier, J., Stanislas, M. (2005): Experimental study of eddy structures in a turbulents boundary layer using particle image velocimetry. *J. Fluid Mech. 535*, 143–188.

Carminati, J., Vu, K. (2000): Symbolic Computation and differential equations: Lie symmetries. *J.Sym. Comp. 29*, 95–116.

Castillo, L., Johansson, T. (2002): The effects of the upstream conditions on a low Reynolds number turbulent boundary layer with zero pressure gradient. *Journal of Turbulence* .

Chakraborty, B. S., P., Adrian, R. (2005): On the relationships between local vortex identification schemes. *J. Fluid Mech. 535*, 189–214.

Chong, P. A., M.S., Cantwell, B. (1990): A general classification of three dimensional flow fields. *Phy. Fluids A 2*, 765–777.

Christensen, K., Adrian, R. (2001): Statistical evidence of hairpin vortex packets in wall turbulence. *J. Fluid Mech. 431*, 433–443.

Coleman, G., Kim, J., Spalart, P. (2000): A numerical study of strained three-dimensional wal-bounded turbulence. *J. Fluid Mech. 416*, 75–116.

Coles, D. (1956): The law of the wakein the turbulent boundary layer. *J. Fluid Mech. 1*, 191-226.

Daubechies, I. (1992): *Ten lectures on wavelets*. SIAM.

Davidson, P. (2004): *Turbulence, an introduction for scientists and engineers*. Oxford University Press.

DeGraaff, D., Eaton, J. (2000): Reynolds-number scaling of the flat-plate turbulent boundary layer. *J.Fluid Mech. 422*, 319–349.

Delo, C., Kelso, R., Smits, A. (2004): Three-dimensional structure of a low-Reynolds-number turbulent boundary layer. *J. Fluid Mech. 512*, 47–83.

Farge, M. (1992): Wavelet transforms and their applications to turbulence. *Annu. Rev. Fluid. Mech. 24*, 395–457.

Farge, M., Pellegrino, G., Schneider, K. (2001): Coherent vortex extraction in 3D turbulent flows using orthogonal wavelets. *Phys. Rev. Letters 87*, 5, 45011–45014.

Farge, M., Schneider, K., Kevlahan, N. (1999): Non-Gaussianity and coherent vortex simulation for tho-dimensional turbulence unisng and adaptive orthonormal wavelet basis. *Phys. Fluids 11*, 2187–2201.

Farge, M., Schneider, K., Pellegrino, G., Wray, A., Rogally, B. (2003): Coherent vortex extraction in three-dimensional homogeneous turbulence: Comparion between CVS-wavelet and POD-Fourier Decompositions. *Phys. Fluids 15*, 2886–2896.

Fernholz, H., Finley, P. (1996): The incompressible zero-pressure-gradient

turbulent boundary layer: An assessment of the data. *Prog. Aerospace Sci. 32*, 25–311.

Fernholz, H., Krause, E., Nockemann, M., Schrober, M. (1995): Comparative measurements in the canonical boundary alyer at $Re_{\delta_2} < 6 \times 10^4$ on the wall of german-dutch windtunnel. *Phys. Fluids 7*, 6, 1275–1281.

Foias, C., Manley, O., Rosa, R., Temam, R. (2001): *Navier-Stokes Equations and Turbulence*, vol. 83 of *Encyclopedia of mathematics and its application*. Cambridge University Press.

Gabor, D. (1946): Theory of communications. *Journ. Inst. Elect. Eng. 93*, 3, 429–457.

Ganapathisubramani, B., Hutchins, N., Hambleton, W., Longmire, E., Marusic, I. (2005): Investigation of large-scale coherence in a turbulent boundary layer using two-point correlations. *J. Fluid Mech. 524*, 57–80.

George, W., Castillo, L. (1997): Zero-pressure-gradient turbulent boundary layer. *Appl. Mech. Rev. 50*, 689–729.

Gottlieb, D., Orszag, S. (1977): *Numerical analysis of spectral methods: Theory and applications.*, vol. 28 of *Regional Conference Series in Applied Mathematics*. SIAM, Philadelphia.

Graps, A. (1995): An introduction to Wavelets. *IEEE Computational Science and Engineering 2*, 2.

Haller, G. (2005): Ad objective definition of a vortex. *Journal of Fluid Mechanics 525*, 1–26.

Head, M., Bandyopadhyay, P. (1981): New aspects of turbulent boundary layer structure. *J. Fluid Mech. 107*, 287–338.

Hommema, S., Adrian, R. (2002): Similarity of apparently random structures in the outer region of wall turbulence. *Experiments in Fluids 33*, 5–12.

Honkan, A., Andreopoulos, Y. (1997): Vorticity, strain-rate and dissipation characteristics in the near-wall region of turbulent boundary layers. *J. Fluid Mech. 350*, 29–96.

Hubbard, B. B. (1998): *The world accourding to wavelets*. A K Peters, Natick, Massachusetts, second edition edn..

Hussain, A. (1983): Coherent structures - reality and myth. *Physics of Fluids 26*, 10, 2816–2850.

Ibragimov, H., N (1996): *CRC handbook of Lie group analysis of differential equations.*, vol. 3. CRC press.

Jeong, J., Hussain, F. (1994): On the identification of a vortex. *J. Fluid Mech. 285*, 69–94.

Jimenez, J. (2003): Computing high-Reynolds-number turbulence: will simulations ever replace experiments? *Journal of Turbulence 4*.

Jones, M., Nishizawa, C. M., N., Marusic, I. (2002): Scaling of the turbulent boundary layer at high Reynolds numbers. In: *IUTAM symposium on Reynolds number scaling in turbulent flow*, Princeton, University NJ, USA.

Kähler, C. (2004): *The significance of coherent flow structures for the turbulent mixing in wall-bounded flows*. Ph.D. thesis, Mathematich-Naturwissenschaftlichen Fakultäten der George-August Universität zu Göttingen.

Kármán, T. v. (1930): Mechanische ähnlichkeit und turbulenz. *Nach. Ges. Wiss. Göttingen 86*.

Khujadze, G., Oberlack, M. (2002): DNS and scaling laws from new symmetry groups of turbulent boundary layer with zero pressure gradient. In: *Proceedings of ETC9*.

Khujadze, G., Oberlack, M. (2003a): DNS of zero pressure gradient turbulent boundary layer flow. Hessischer Hochleistungsrechner-HHLR Nutzer-Kolloquium, Darmstadt, Germany.

Khujadze, G., Oberlack, M. (2003b): Symmetries, Scaling laws and DNS of Turbulent Boundary layer flow. In: *Proceedings of ITI Conference on Turbulence*, Bad Zwischenahn, Germany.

Khujadze, G., Oberlack, M. (2003c): Symmetries, Scaling Laws and DNS of Turbulent Boundary Layer Flow. In: *Proc. of the Int. Symposium on Turbulence, Heat and Mass Transfer-4*, Antalya, Turkey.

Khujadze, G., Oberlack, M. (2004a): DNS and Scaling laws from new symmetry groups of ZPG turbulent boundary layer flow. *Theoretical and Computational Fluid Dynamics 18*, 391–411.

Khujadze, G., Oberlack, M. (2004b): *DNS and Scaling Laws from the New Symmetry Groups of ZPG Turbulent Boundary Layer*, Springer-Verlag, chap. New Results in Numerical and Experimental Fluid Mechanics IV, Notes on Numerical Fluid Mechanics and Multidisciplinary Design.

Khujadze, G., Oberlack, M. (2004c): DNS of ZPG Turbulent Boundary Layer Flow. ITI meeting, Darmstadt, Germany.

Khujadze, G., Oberlack, M. (2004d): Similarity of two-point correlations in turbulent boundary layer flow. In: *Proc. of the Tenth European Turbulence Conference*, K. Andresson, ed., Norway, Trondheim.

Khujadze, G., Oberlack, M. (2005a): *DNS and New Scaling Laws of ZPG Turbulent Boundary layer flow*, Springr-Verlag, chap. Progress in Turbulence.

Khujadze, G., Oberlack, M. (2005b): Numerical simulation and Lie group analysis of turbulent boundary layer flow. Die Gesellschaft für Angewandte Mathematik und Mechanik e.V. (GAMM-2005).

Kim, J., Moin, P., Moser, R. (1987): Turbulence statistics in fully developed channel flow. *J.Fluid Mech. 177*, 133–166.

Klebanoff, P. (1955): Characteristics of turbulence in a boundary laer with zero pressure gradient. Tech. Rep. TR-1247, NACA.

Klewicki, J., Murray, J., Falco, R. (1994): Vortical motion contributions to stress transport in turbulent boundary layers. *Phys. Fluids 6*, 277–286.

Knobloch, K., Fernholz, H. (2002): Statistics, correlations and scaling in a canonical, incompressible turbulent boundary layer with $Re_{\delta_2} \leq 1.15 \times 10^5$. In: *IUTAM symposium on Reynolds number scaling in turbulent flow*, Princeton, University NJ, USA.

Kreiss, O. (1972): dssdfsdfds. *J.Fluid Mech.* , 133–166.

Lesieur, M. (1990): *Turbulence in fluids. Stochastic and numerical modelling.* Kluwer, Dordrecht.

Lie, S. (2004): *Lie group analysis. Classical heritage*, ALGA Publications, chap. 1.

Lindgren, B. (2002): *Flow facility and experimental studies of wall-bounded turbulent shear flows.* Ph.D. thesis, Royal Institute of Technology, Department of Mechanics.

Lindgren, B., Österlund, J. M., Johansson, A. V. (2004): Evaluation of scaling laws derived from Lie group symmetry methods in zero pressure-gradient turbulent boundary layers. *J.Fluid Mech. 502*, 127–152.

Lundbladh, A., Berlin, S., Skote, M., Hildings, C., Choi, J., Kim, J., Henningson, D. (1999): An efficient spectral method for simulation of incompressible flow over a flat plate. Tech. Rep. 1999:11, KTH, Stokholm.

Lundbladh, A., Henningson, D., Johansson, A. (1992): An efficient spectral integration method for the solution of the Navier-Stokes equations. Tech. Rep. FFA-TN 1992-28, Aeronautical Research Institute of Sweden, Bromma.

Mallat, S. (1989): A theory for multiresolution signal decomposition: the wavelet representation. *IEEE Trans. Pattern Anal. Mach. Intell. 11*, 7, 674–693.

Mallat, S. (1998): *a wavelet tour of signal processing*. Academic Press.

Mansour, N., J., K., Moin, P. (1987): Reynolds-stress and dissipation-rate budgets in a turbulent channel flow. *J. Fluid Mech. 194*, 15–44.

Metzger, M., Klewicki, J., K.L., B., Sadr, R. (2001): Scaling the near-wall axial turbulent stress in the zero pressure gradient boundary layer. *Physics of Fluids 13*, 1819–1821.

Millikan, C. (1939): A critical discussion of turbulent flows in channels and circular tubes. In: *Proc. 5th Int. Congr. Applied Mechanics*, Cambridge.

Mochizuki, S., Nieuwstadt, F. (1996): Reynolds-number-dependence of the maximum in the streamwise velocity fluctuations in wall turbulence. *Exps. Fluids* , 21, 218–226.

Moin, P., Mahesh, K. (1998): Direct numerical simulation: A tool in turbulence research. *Annu. Rev. Fluid Mech. 30*, 539–578.

Monin, A., Yaglom, A. (1971): *Statistical fluid mechanics*. MIT press.

Moser, R., Kim, J., Mansour, N. (1999): Direct numerical simulation of turbulent channel flow up to $Re_\tau = 590$. *Physics of Fluids 11*, 943–945.

Murlis, J., Tsai, H., Bradshow, P. (1982): The structure of turbulent boundary layers at low Reynolds numbers. *J. Fluid Mech. 122*, 13–56.

Na, Y., Moin, P. (1998): Direct numerical simulation of a separated turbulent boundary layer. *J. Fluid Mech. 374*, 379–405.

Nagib, H., Christophorou, C., Monkewitz, P., Österlund, J. (2002): Higher Reynolds number boundary layer dataon a flat plate in the NDF. In: *IUTAM symposium on Reynolds number scaling in turbulent flow*, Princeton, University, NJ, USA.

Nikuradse, J. (1932): Gesetzmäßigkeit der turbulenten Strömung in glatten Rohren. *Forsch. Arb. Ing.-Wes. H. 356*.

Nördstrom, J., Nordin, N., Henningson, D. (1999): The fringe region technique and the fourier method used in the direct numerical simulation of spatially evolving viscous flows. *SIAM J. Sci. Comput. 20*, 1365–1393.

Oberlack, M. (2000): Asymptotic Expansion, Symmetry Groups and Invariant Solutions of Laminar and Turbulent Wall-Bounded Flows. *Z.Angew.Math.Mech 80*, 11-12, 791–800.

Oberlack, M. (2001): A unified approach for symmetries in plane parallel turbulent shear flows. *J.Fluid Mech. 427*, 299–328.

Oberlack, M. (2002): *Theories of turbulence, (CISM Courses and Lectures)*, SpringerWien, New-York, vol. 442, chap. 5.

Oberlack, M., Khujadze, G. (2003): Skalengesetze zur Beschreibung turbulenter wandnaher Strömungen. Thema FORSCHUNG, Panta rhei - alles fliest, vol. 2, p. 64.

Oberlack, M., Khujadze, G. (2005): Symmetry methods in turbulent boundary layer theory (New wake region scaling laws and boundary layer growth). In: *'One Hundred Years of Boundary layer Research'*, H.J.Heinemann, ed., Springer-Verlag.

Oberlack, M., Peters, N. (1993): Closure of the Two-Point Correlation Equation as a Basis of Reynolds Stress Models. In: *Near-Wall Turbulent Flows*, R. So, C. Speziale, B. Launder, eds., Elsevier Science Publisher, 85–94.

Oertel, H. (2004): *Prandtl's essentials of fluid mechanics*, vol. 158 of *Applied Mathematical Sciences*. Springer, second edition edn..

Olver, P. (1993): *Applications of Lie groups to Differential equations*, vol. 107 of *Graduate Texts in Mathematics*. Springer, New-York.

Orszag, S. (1972): Comparison of pseudospectral and spectral approximations. *Stud. Appl. Math. 51*, 253–259.

Österlund, J. (1999): *Experimental studies of zero pressure-gradient turbulent boundary-layer flow, Doctoral thesis Royal Institute of technology*. Ph.D. thesis, Royal Institute of technology (KTH), Stokholm, Sweden.

Österlund, J., Johansson, A., Nagib, H. (2000b): Comment on 'a note on the intermediate region in turbulent boundary layers'[Phy.Fluids 12, 2159]. *Phys. Fluids 12*, 2360–2363.

Österlund, J., Johansson, A., Nagib, H., Hites, M. (2000a): A note on the overlap region in turbulent boundary layers. *Phys. Fluids 12*, 1, 1–4.

Peyret, R. (2002): *Spectral methods for incompressible viscous flow*, vol. 148 of *Applied mathematical sciences*. Springer, New-York.

Pope, S. (2000): *Turbulent flows*. Cambridge Univ. Press.

Prandtl, L. (1904): Über Flüssigkeitsbewegungen bei sehr kleiner Reibung. *Verhandlg. III Intern. Math. Kongr. Heidelberg* , 484–491.

Prandtl, L. (1932): Zur turbulenten Strömung in Rohren und Längs Platten. *Ergeb. Aerodyn. Versuchsants* , 18–29.

Preston, J. (1958): The minimum Reynolds number for a turbulent boundary layer and the selection of the transition device. *J.Fluid Mech. 3*, 373–384.

Reynolds, O. (1894): On the dynamical theory of turbulent incompressible voscous fluids and the determination of the criterion. *Phil. Trans. R. Soc. Lond. A186*, 123–61.

Richardson, L. (1922): *Weather prediction by numerical Process*. Cambridge University Publishers.

Robinson, S. (1991): Coherent motions in the turbulent boundary layer. *Annu. Rev. Fluid. Mech. 23*, 601–639.

Rogallo, R. (1981): Numerical Experiments in homogeneous turbulence. Tech. Rep., NASA TM-81315.

Rotta, J. (1962): Turbulent boundary layers in incompressible flow. In: *Prog. Aeronaut. Sci.*, Pergamon Press LTD., vol. 2, 1–220.

Schlichting, H., Gersten, K. (2000): *Boundary layer theory*. Springer.

Schneider, K., Farge, M., Pellegrino, G., Rogers, M. (2005): Coherent vortex simulation of three-dimensional turbulent mixing layers using orthogonal wavelets. *J. Fluid. Mech.* .

Schoppa, W., Hussain, F. (2002): Coherent structure generation in near-wall turbulence. *Journal of Fluid Mechanics 453*, 57–108.

Seo, C. L. J. T., J., Hangan, H. (2004): Reynolds stress in turbulent boundary layers at high Reynolds number. *Journal of Turbulence* .

Skote, M. (2001): *Studies of turbulent boundary layer flow through direct numerical simulation*. Ph.D. thesis, Royal Institute of Technology (KTH), Stockholm, Sweden.

Skote, M., Haritonidis, J., Henningson, D. (2002): Varicose instabilities in turbulent boundary layers. *Phys. Fluids 14*, 2309–2323.

Skote, M., Henningson, D. (2002): Direct numerical simulation of separating turbulent boundary layers. *J. Fluid Mech. 471*, 107–136.

Skote, M., Henningson, D., Henkes, R. (1998): Direct numerical simulation of self-similar turbulent boundary layers in adverse pressure gradients. *Flow, Turbulence and Combustion 60*, 47–85.

Smith, C. (1984): A synthesized model of near-wall behavior in turbulent boundary layers. In: *8th Szmp. on Turbulence*, Rolla, Missouri, Univ. Missouri-Rolla, 299–325.

Spalart, P. (1986): Numerical study of sink-flow boundary layers. *J. Fluid Mech. 172*, 307–328.

Spalart, P. (1988): Direct simulation of a turbulent boundary layer up to $R_\theta = 1410$. *J. Fluid Mech. 187*, 61–98.

Spalart, P., Coleman, G. (1997): Numerical study of a separation bubble with heat transfer. *European J. of Mech. B/Fluids 16*, 169.

Spalart, P., Watmuff, J. (1993): Experimental and numerical study of a turbulent boundary layer with pressure gradients. *J. Fluid Mech. 249*, 337–371.

Sreenivasan, K. (1989): The turbulent boundary layer. *Frontiers in experimental Fluid Mech. 46*, 97–120.

Theodorsen, T. (1952): Mechanism of turbulence. In: *2nd Midwestern Conf. on Fluid Mech.*, Columbus, Ohio, Ohio state University, 1–19.

Tomkins, C., Adrian, R. (2003): Spanwise structure and scale growth in turbulent boundary layers. *J. Fluid Mech. 490*, 37–74.

Yaglom, I. (1988): *Felix Klein and Sophus Lie: Evolution of the idea of symmetry in the Nineteenth Century.* Birkhauser,Boston,Basel.

Zagarola, M., Perry, A., Smits, A. (1997): Log laws or power laws: the scaling in the overlap region. *Phys. Fluids 9*, 2094–2100.

Zhou, A. R. B. S., J., Kendall, T. (1999): Mechanisms for generating coherent packets of hairpin vortices in channel flow. *J. Fluid Mech. 387*, 353–396.

Part V

Appendix

A Spectral method: velocity-vorticity formulation

The incompressible Navier-Stokes equations can be formulated in several different ways. The one chosen here is a velocity-vorticity formulation. The reason behind using this formulation rather than the more usual one (velocity and pressure) is that it is thereby possible to avoid the difficulty of solving for the pressure. Unlike for the velocity, there is no evolution equation for the pressure and it is indirectly determined from the continuity equation. In incompressible flows the pressure adjusts itself to the velocity field instantaneously, implying infinite wave speed. This often causes problems (Canuto & Zang 1988).

The original algorithm (Lundbladh et al. 1992) has been developed for the incompressible flow equations in a channel flow geometry.

The starting point is the non-dimensional incompressible Navier-Stokes equations in a rotating reference frame

$$\frac{\partial u_i}{\partial t} = -\frac{\partial p}{\partial x_i} + e_{ijk}(\omega_k + 2\Omega_k) - \frac{\partial}{\partial x_i}\frac{u_j u_j}{2} + Re\nabla^2 u_i + F_i \tag{A.1}$$

$$\frac{\partial u_i}{\partial x_i} = 0 \tag{A.2}$$

with boundary conditions at the flat plate and the free-stream boundary. $(\omega_1, \omega_2, \omega_3) = (\chi, \omega, \theta)$ are streamwise, wall-normal and spanwise vorticities. $(x_1, x_2, x_3) = (x, y, z)$ and $(u_1, u_2, u_3) = (u, v, w)$. Ω_k is the angular velocity of the coordinate frame around axis k. F_i is the body force which is used for numerical purposes.

The Reynolds number is defined as $Re = U_\infty \delta^*/\nu$, where U_∞ and δ^* are the undisturbed streamwise free-stream velocity and the displacement thickness correspondingly at $x = 0$ and $t = 0$. The domain size in physical space is x_L, y_L, z_L.

A Poisson equation for the pressure reads:

$$\nabla^2 p = \frac{\partial H_i}{\partial x_i} - \nabla^2 \frac{u_j u_j}{2} \tag{A.3}$$

where $H_i = e_{ijk}(\omega_k + 2\Omega_k) + F_i$.

From equations A.1 and A.3 one can get the following equation for the wall-normal velocity component:

$$\frac{\partial \nabla^2 v}{\partial t} = \left(\frac{\partial^2}{\partial x^2} + \frac{\partial^2}{\partial z^2}\right) H_2 - \frac{\partial}{\partial y}\left(\frac{\partial H_1}{\partial x} + \frac{\partial H_3}{\partial z}\right) + \frac{1}{Re}\nabla^4 v \tag{A.4}$$

For numerical purposes this equation has to be rewritten in the following way

$$\begin{aligned} \frac{\partial \phi}{\partial t} &= h_v + \frac{1}{Re}\nabla^2 \phi \\ \nabla^2 v &= \phi \end{aligned} \tag{A.5}$$

where

$$h_v = \left(\frac{\partial^2}{\partial x^2} + \frac{\partial^2}{\partial z^2}\right) H_2 - \frac{\partial}{\partial y}\left(\frac{\partial H_1}{\partial x} + \frac{\partial H_3}{\partial z}\right) \tag{A.6}$$

Using the same mathematics for the normal vorticity one gets

$$\frac{\partial \omega}{\partial t} = h_\omega + \frac{1}{Re}\nabla^2 \omega \tag{A.7}$$

where

$$h_\omega = \frac{\partial H_1}{\partial z} - \frac{\partial H_3}{\partial x}. \tag{A.8}$$

Note that the equations for ϕ, v, ω have similar form and can be solved using the same numerical routine. Once normal velocity and normal vorticity are found, the other components can be found from the incompressibility constraint.

CURRICULUM VITAE

FIRST NAME:	**GEORGE**
SECOND NAME:	**KHUJADZE**
PERMANENT ADDRESS:	Abastumani Astrophysical Observatory (ABAO), Center for Plasma Physics, 2a, Ave. A. Kazbegi, 0160 Tbilisi, Georgia
Telephone/Fax:	+995 32 383510 / +995 32 375228
e-mail:	**khujadze@astro-ge.org**
Date and place of birth:	24 January 1969, Kutaisi, Georgia
Nationality:	Georgian
MARITAL STATUS:	Married
Children:	One daughter
PRESENT ADDRESS:	Group of fluid dynamics, Department of mechanical engineering, Technische Universität Darmstadt, Petersenstrasse 13, 64287 Darmstadt, Germany
Telelphone/Fax:	+49 6151 164952 / +49 6151 167060
e-mail:	**khujadze@hyhy.tu-darmstadt.de**
HOME ADDRESS:	Michaelisstrasse 16 B, 64293, Darmstadt Germany
Telephone:	+49 6151 9519378

EDUCATION

Graduated from:	Department of Theoretical Physics Tbilisi State University, Georgia
Entered:	1986
Finished:	1993
Diploma:	MSc. in Physics and Physics Teaching, Specialization of Theoretical Physics.

POSITIONS

2001–	**Research Scientist**, Technische Universität Darmstadt, Germany
1998–2001:	**Senior Research Scientist**, Center for Plasma Astrophysics, ABAO, Tbilisi, Georgia
1996–1998:	**Research Scientist**, Center for Plasma Astrophysics, ABAO, Tbilisi, Georgia
1995-1996:	**Assistent Researcher** Department of Physics, Kutaisi Technical University, Kutaisi Georgia